

WL-TR-1997-7039

Numerical Algorithms in a Lagrangian Hydrocode

G. R. Johnson
R. A. Stryk
T. J. Holmquist
S. R. Beissel

Alliant Techsystems Inc.
600 Second Street N. E.
Hopkins, MN 55345

CONTRACT No. F08635-92-C-0006

JUNE 1997

FINAL REPORT for June 1992 - May 1997

19970722 186

DTIC QUALITY INSPECTED 4

Approved for public release; distribution is unlimited.

WRIGHT LABORATORY, ARMAMENT DIRECTORATE
Air Force Materiel Command United States Air Force Eglin Air Force Base

NOTICE

When Government drawings, specifications, or other data are used for any purpose other than in connection with a definitely Government-related procurement, the United States Government incurs no responsibility or any obligation whatsoever. The fact that the Government may have formulated or in any way supplied the said drawings, specifications, or other data, is not to be regarded by implication, or otherwise as in any manner construed, as licensing the holder, or any other person or corporation; or as conveying any rights or permission to manufacture, use, or sell any patented invention that may in any way be related thereto.

This technical report has been reviewed and is approved for publication.

FOR THE COMMANDER

Albert F. Young
ALBERT F. YOUNG

Chief, Munitions Assessment Division

Even though this report may contain special release rights held by the controlling office, please do not request copies from the Wright Laboratory, Armament Directorate. If you qualify as a recipient, release approval will be obtained from the originating activity by DTIC. Address your request for additional copies to:

DTIC-OCP
Defense Technical Information Center
8725 John J Kingman Road, Suite 0944
Fort Belvoir, VA 22060-6218

If your address has changed, if you wish to be removed from our mailing list, or if your organization no longer employs the addressee, please notify WL/MNSI, Eglin AFB FL 32542-6810, to help us maintain a current mailing list.

Do not return copies of this report unless contractual obligations or notice on a specific document requires that it be returned.

REPORT DOCUMENTATION PAGE

Form Approved
OMB No. 0704-0188

Public reporting burden for this collection of information is estimated to average 1 hour per response, including the time for reviewing instructions, searching existing data sources, gathering and maintaining the data needed, and completing and reviewing the collection of information. Send comments regarding this burden estimate or any other aspect of this collection of information, including suggestions for reducing this burden, to Washington Headquarters Services, Directorate for Information Operations and Reports, 1215 Jefferson Davis Highway, Suite 1204, Arlington, VA 22202-4302, and to the Office of Management and Budget, Paperwork Reduction Project (0704-0188), Washington, DC 20503.

1. AGENCY USE ONLY (Leave blank)

2. REPORT DATE
June 1997

3. REPORT TYPE AND DATES COVERED
Final Jun 1992-May 1997

4. TITLE AND SUBTITLE
Numerical Algorithms in a Lagrangian Hydrocode

5. FUNDING NUMBERS
C: F08635-92-C-0006
PE: 63602F

6. AUTHOR(S)
G. R. Johnson, R. A. Stryk, T. J. Holmquist, S. R. Biessel

PR: 2502
TA: 07
WU: 21

7. PERFORMING ORGANIZATION NAME(S) AND ADDRESS(ES)

Alliant Techsystems Inc
600 Second Street N. E.
Hopkins, MN 55345

8. PERFORMING ORGANIZATION REPORT
NUMBER

9. SPONSORING/MONITORING AGENCY NAME(S) AND ADDRESS(ES)
Wright Laboratory, Armament Directorate
Munitions Assessment Division (MNSI)
Eglin AFB, FL 32542-6810
Program Manager: W. H. Cook (904)882-8302x3430

10. SPONSORING/MONITORING AGENCY
REPORT NUMBER
WL-TR-1997-7039

11. SUPPLEMENTARY NOTES

12a. DISTRIBUTION/AVAILABILITY STATEMENT

Approved for public release; distribution is unlimited.

12b. DISTRIBUTION CODE

13. ABSTRACT (Maximum 200 words)

This report documents the numerical algorithms used in an explicit Lagrangian finite element hydrocode. One, two, and three dimensional implementations of the numerical solution of the conservation equations are covered. Triangular and tetrahedral continuum elements and shell elements are described. SPH (Smooth Particle Hydrodynamics) techniques are discussed. Slideline techniques are explained. Material models are presented for constitutive behavior and equation of state behavior for several categories of materials. This report is a comprehensive presentation of the numerical techniques used in a current production hydrocode.

14. SUBJECT TERM

Hydrocode Computational Mechanics

15. NUMBER OF PAGES

193

16. PRICE CODE

17. SECURITY CLASSIFICATION OF
REPORT
UNCLASSIFIED

18. SECURITY CLASSIFICATION
OF THIS PAGE
UNCLASSIFIED

19. SECURITY CLASSIFICATION
OF ABSTRACT
UNCLASSIFIED

20. LIMITATION OF ABSTRACT
UL

PREFACE

This report on the numerical algorithms in a Lagrangian hydrocode was prepared by Alliant Techsystems Inc., 600 Second Street N.E., Hopkins, MN 55343, for the Armament Directorate, Wright Laboratory, Eglin Air Force Base, FL 32542, under Contract F08630-92-C-0006.

This effort was conducted during the period from June 1992 through May 1997. The authors would like to thank W.H. Cook, WL/MNSI program manager, for many helpful technical discussions.

TABLE OF CONTENTS

| Section | | Page |
|---------|--|------|
| 1 | INTRODUCTION | 1 |
| 2 | EPIC CODE STRUCTURE | 3 |
| 3 | FINITE ELEMENT ALGORITHMS | 9 |
| 3.1 | 1D Cartesian Geometry | 9 |
| 3.1.1 | Equations of Motion | 11 |
| 3.1.2 | Contact Interfaces | 12 |
| 3.1.3 | 1D Cartesian Elements | 13 |
| 3.1.4 | Nonreflective Boundary Elements | 19 |
| 3.2 | 1D Cylindrical Geometry | 19 |
| 3.3 | 1D Spherical Geometry | 21 |
| 3.4 | 2D Axisymmetric Geometry | 22 |
| 3.4.1 | Equations of Motion | 24 |
| 3.4.2 | Sliding Interfaces | 25 |
| 3.4.3 | Erosion | 35 |
| 3.4.4 | Triangular Elements | 38 |
| 3.4.5 | Quad Elements | 46 |
| 3.4.6 | Bending Shell Elements | 50 |
| 3.4.7 | Membrane Shell Elements | 59 |
| 3.4.8 | Nonreflective Boundary Elements | 61 |
| 3.5 | 2D Axisymmetric Geometry with Spin | 63 |
| 3.6 | 2D Plane Strain Geometry | 65 |
| 3.7 | 2D Plane Stress Geometry | 66 |
| 3.8 | 3D Geometry | 67 |
| 3.8.1 | Equations of Motion | 68 |
| 3.8.2 | Sliding Interfaces | 70 |
| 3.8.3 | Erosion | 74 |
| 3.8.4 | Tetrahedral Elements | 77 |
| 3.8.5 | Brick Elements | 87 |
| 3.8.6 | Bar Elements | 97 |
| 3.8.7 | Bending Shell Elements | 100 |

TABLE OF CONTENTS (CONTINUED)

| Section | Page |
|---|------|
| 3.8.8 Membrane Shell Elements | 112 |
| 3.8.9 Nonreflective Boundary Elements | 112 |
| 4 SPH ALGORITHMS | 117 |
| 4.1 2D Axisymmetric Geometry | 117 |
| 4.1.1 Smoothing Functions | 119 |
| 4.1.2 Strain Rates | 122 |
| 4.1.3 Forces | 125 |
| 4.1.4 Artificial Viscosity | 127 |
| 4.1.5 Material Interfaces | 129 |
| 4.2 2D Plane Strain Geometry | 130 |
| 4.3 3D Geometry | 131 |
| 5 LINKING OF FINITE ELEMENTS AND SPH NODES | 135 |
| 6 MATERIAL MODELS | 139 |
| 6.1 Solid Materials | 139 |
| 6.1.1 Johnson-Cook Strength Model | 141 |
| 6.1.2 Modified Johnson-Cook Strength Model | 142 |
| 6.1.3 Zerilli-Armstrong Strength Model for FCC Metals | 142 |
| 6.1.4 Zerilli-Armstrong Strength Model for BCC Metals | 142 |
| 6.1.5 Bodner-Partom Strength Model | 142 |
| 6.1.6 MTS Strength Model | 144 |
| 6.1.7 Steinberg-Guinan-Lund Strength Model | 146 |
| 6.1.8 2D Orthotropic Model | 147 |
| 6.1.9 Internal Energy | 150 |
| 6.1.10 Artificial Viscosity | 150 |
| 6.1.11 Mie-Gruneisen Equation of State | 151 |
| 6.1.12 Johnson-Cook Fracture Model | 152 |
| 6.1.13 Modified Johnson-Cook Fracture Model | 154 |
| 6.1.14 Fragmentation Model | 155 |
| 6.2 Explosive Materials | 160 |
| 6.2.1 Gamma Law Model | 160 |

TABLE OF CONTENTS (CONCLUDED)

| Section | Page |
|--|------|
| 6.2.2 JWL Model | 161 |
| 6.3 Crushable/Concrete Materials | 162 |
| 6.3.1 Modified Osborn Model | 162 |
| 6.3.2 Holmquist-Johnson-Cook Model | 164 |
| 6.4 Liquid Materials | 167 |
| 6.5 Brittle Materials | 167 |
| 6.5.1 Johnson-Holmquist JH-1 Model | 168 |
| 6.5.2 Johnson-Holmquist JH-2 Model | 173 |
| 6.6 Reactive Explosive Materials | 182 |
| 6.6.1 Tarver Ignition and Growth Model | 182 |
| 6.6.2 Mader Forest Fire Model | 186 |
| 6.7 RDG Strength and Fracture Model | 186 |
| 7 REFERENCES | 187 |

LIST OF ILLUSTRATIONS

| Figure | | Page |
|--------|--|------|
| 1 | Partial Hierarchy Chart for EPIC Subroutines | 4 |
| 2 | Description of the 1D Cartesian Element | 10 |
| 3 | Description of the 1D Cylindrical Element | 20 |
| 4 | Description of the 2D Axisymmetric Triangular Element | 23 |
| 5 | Determination of the 2D External Interfaces | 26 |
| 6 | Description of the 2D Sliding Interface Searching Algorithm | 27 |
| 7 | Description of the 2D Sliding Interface Contact Algorithm | 31 |
| 8 | Description of the 2D Erosion Algorithm | 37 |
| 9 | Description of the 2D Quad Element | 47 |
| 10 | Description of the 2D Bending Shell Element | 52 |
| 11 | Stresses, Forces, and Moments for the 2D Bending Shell Element | 53 |
| 12 | Normal Stress Iteration Algorithm for 2D and 3D Bending Shells, and Plane Stress Geometry | 57 |
| 13 | Accuracy Assessment for Bending Shells | 60 |
| 14 | Description of the 2D Nonreflective Boundary Element | 61 |
| 15 | Description of the 2D Axisymmetric Triangular Element with Spin | 63 |
| 16 | Description of the 3D Tetrahedral Element | 68 |
| 17 | Description of the 3D Sliding Interface Contact Algorithm | 71 |
| 18 | Description of the 3D Erosion Algorithm | 75 |
| 19 | Description of the 3D Brick Element | 88 |
| 20 | Description of the 3D Bar Element | 98 |
| 21 | Description of the 3D Bending Shell Element | 101 |
| 22 | Description of the Geometry and Velocities for the 3D Bending Shell Element | 102 |
| 23 | Description of the Mass Distribution for the 3D Bending Shell Element . . . | 103 |
| 24 | Description of the Stresses for the 3D Bending Shell Element | 104 |
| 25 | Description of the Forces and Moments for the 3D Bending Shell Element . | 105 |
| 26 | Description of the 3D Nonreflective Boundary Element | 113 |
| 27 | EPIC Code Structure for Standard Elements and SPH Nodes | 118 |
| 28 | SPH Characteristics | 118 |

LIST OF ILLUSTRATIONS (CONCLUDED)

| Figure | | Page |
|--------|---|------|
| 29 | 2D B-Spline and Quadratic Smoothing Functions and Their Derivatives . . . | 120 |
| 30 | Equivalent Strain Rates in Radially Stretching Cross-Sections With a Uniform Arrangement of SPH Nodes | 124 |
| 31 | Equivalent Strain Rate Versus Dimensionless Smoothing Distance for an Interior SPH Node in a Radial Stretching Cross-Section | 126 |
| 32 | Material Interface With SPH Nodes | 129 |
| 33 | SPH Node Attachment to a Standard Grid | 136 |
| 34 | SPH Node Sliding on a Standard Grid | 137 |
| 35 | Description of the SPH Node Generation Algorithm | 138 |
| 36 | Description of the Johnson-Cook Fracture Model | 153 |
| 37 | Description of Fracture Strains at Large Tensile Pressure-Stress Ratios for the Johnson-Cook Fracture Model | 155 |
| 38 | Fragment Characteristics | 156 |
| 39 | Description of the Pressure-Volume Relationship for the Osborn Concrete Model | 163 |
| 40 | Description of the Holmquist-Johnson-Cook (HJC) Concrete Model | 165 |
| 41 | Description of the Original Johnson-Holmquist (JH-1) Ceramic Model | 169 |
| 42 | Examples of Material Responses with the JH-1 Ceramic Model | 172 |
| 43 | Description of the Improved Johnson-Holmquist (JH-2) Ceramic Model | 175 |
| 44 | Strength, Damage, and Fracture Under a Constant Pressure and Strain Rate for the JH-2 Model | 177 |
| 45 | Description of Incremental Bulking Pressure for the JH-2 Model | 178 |
| 46 | Examples of Material Responses with the JH-2 Ceramic Model | 180 |

SECTION 1

INTRODUCTION

This report documents the numerical algorithms in the EPIC hydrocode. The EPIC code was conceived in the early 1970s and has undergone significant development since that time. The first two technical publications for the 2D and 3D versions of EPIC are given in References 1 and 2, and the first two contract reports are given in References 3 and 4. Although most of the numerical algorithms in EPIC have been published as technical papers and/or reports, there has not been a recent publication that contains all of the important algorithms within a single report.

In Section 2 of this report there is a description of the structure of the EPIC code. This is included to show where and how the numerical algorithms fit into the computational framework.

Section 3 represents the main portion of this report and contains all of the finite element algorithms. This contains several 1D, 2D and 3D geometry options, and each of these geometries contains multiple element types. The contact, sliding and erosion algorithms are also included in this section.

The SPH (Smooth Particle Hydrodynamics) algorithms are presented in Section 4, and the linking together of SPH nodes and standard finite elements is presented in Section 5.

The report concludes with Section 6, which describes the numerous material models available in EPIC.

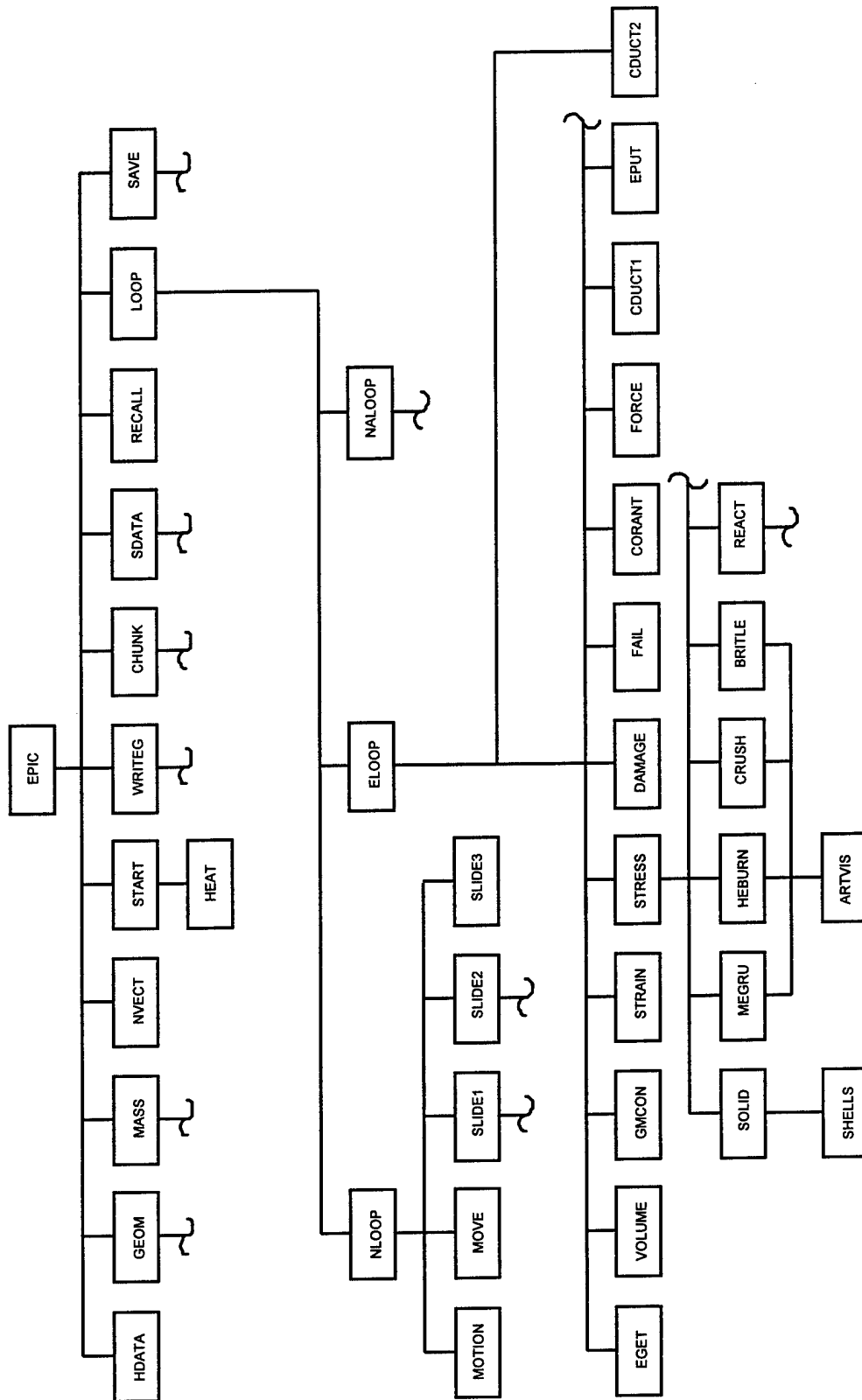
SECTION 2

EPIC CODE STRUCTURE

This section provides an overview of the structure of the EPIC code. Figure 1 shows a hierarchy chart of some of the key subroutines in the EPIC code. Because there are hundreds of subroutines in the code it is not possible to include all of them in a single figure. In general, however, the flow of the code can be described by Figure 1. In most instances the calling sequence goes from left to right.

The following provides a brief description of the functions of the subroutines shown in Figure 1:

| | |
|--------|---|
| EPIC | Calls the first layer of subroutines. |
| HDATA | Reads the input file. |
| GEOM | Generates the initial geometry. |
| MASS | Computes nodal masses. |
| NVECT | Groups node arrays into blocks to allow for vectorized computational loops. |
| START | Assigns initial velocities and explosive detonation points and times. |
| HEAT | Computes nodal heat conduction quantities from element heat conduction parameters. |
| WRITEG | Writes output file for the Preprocessor and computes initial integration time increment. |
| CHUNK | Computes data (velocity, position, energy, momentum, etc.) for user-specified chunks of elements. |
| SDATA | Computes data (velocity, position, energy, momentum, etc.) for the entire system. |



01.pct
T19616

Figure 1. Partial Hierarchy Chart for EPIC Subroutines

| | |
|--------|--|
| RECALL | Reads the restart file for restart runs. |
| LOOP | Calls the three primary subroutines for each computational cycle. |
| SAVE | Writes the restart file for subsequent postprocessing and restart runs. |
| NLOOP | Calls the subroutines that govern the velocities and positions of the nodes. This is the first of three primary subroutines/functions in the computational cycle. |
| MOTION | Updates the velocities of the nodes through the equations of motion. |
| MOVE | Updates the displacements of the nodes through the equations of motion. |
| SLIDE1 | Calls subroutines to update the velocities and displacements of the nodes for 1D contact interfaces. |
| SLIDE2 | Calls subroutines to update the velocities and displacements of the nodes for 2D sliding interfaces. |
| SLIDE3 | Calls the subroutines to update the velocities and displacements of the nodes for 3D sliding interfaces. |
| ELOOP | Calls the subroutines that compute the element quantities. This is achieved by computing with blocks of elements that have the same material and element type. This is the second of the primary subroutines/functions in the computational cycle. |
| EGET | Gathers nodal data (velocities and displacements) and transforms it into element data such that the element computations can be vectorized. |
| VOLUME | Computes volumetric strains and strain rates. |
| GMCON | Computes geometry factors that are used for strain rate, force and heat conduction computations. |

| | |
|---------|---|
| STRAIN | Computes normal and shear strain rates. |
| STRESS | Calls the subroutines that compute the stresses in the elements. |
| SOLID | Computes the maximum allowable Von Mises stress for most of the material models that exhibit strength. Also calls some additional subroutines for more complicated strength models. |
| SHELLS | Performs iterative strain rate and stress computations for shells with bending capability. |
| MEGRU | Computes pressure, internal energy and sound velocity for solids (metals). |
| ARTVIS | Computes artificial viscosity. |
| HEBURN | Computes pressure, internal energy and sound velocity for explosives that use a programmed burn algorithm. |
| CRUSH | Computes pressure, internal energy and sound velocity for crushable (concrete) materials. |
| BRITTLE | Computes pressure, internal energy and sound velocity for brittle (ceramic) materials. |
| REACT | Calls subroutines to compute burn fractions, pressure and sound velocity for reactive explosives. |
| DAMAGE | Computes damage for fracture. |
| FAIL | Totally fails highly distorted elements that have exceeded a user-specified strain. |
| CORANT | Computes the allowable integration time increment for the next computational cycle. |

| | |
|--------|--|
| FORCE | Computes nodal forces that result from the stresses in the elements. |
| CDUCT1 | Computes heat flow across the elements for the heat conduction option. |
| EPUT | Scatters the element forces to the corresponding nodes. |
| CDUCT2 | Redefines element temperatures and internal energies based on temperatures and internal energies of the nodes. Used only for the heat conduction option. |
| NALoop | Calls the subroutines that compute SPH nodal quantities. This is the third of the primary subroutines/functions in the computational cycle. The subroutines called by NALoop are similar to those called by ELoop. |

SECTION 3

FINITE ELEMENT ALGORITHMS

This section provides a description of the algorithms for the finite elements in the EPIC Code. For 1D geometry, the algorithm for Cartesian geometry is presented in detail. The other 1D options for cylindrical and spherical geometry only include descriptions of those features that are different from the Cartesian geometry.

The baseline 2D geometry is the axisymmetric case, and this is presented in detail. The other 2D geometries (axisymmetric with spin, plane strain and plane stress) only include descriptions of those features that are different from the axisymmetric geometry. There is only one geometric option for 3D geometry and it is presented in detail. The material models to determine stresses are not presented in this section, but are presented in Section 6.

An attempt has been made to keep the nomenclature consistent for the various algorithms, but this is not always possible because this work has been performed by several different people over the course of many years. The general philosophy is to have the nomenclature in this report be similar to that which exists in the code.

A final comment is that the numbering of the equations begins with Equation 1 at the beginning of each subsection.

3.1 1D CARTESIAN GEOMETRY

A description of the 1D Cartesian geometry is shown in Figure 2. The z coordinate is the coordinate of interest and the element is defined by nodes i and j , with node i having a higher z coordinate than node j ($z_i > z_j$). The algorithm is for 1D uniaxial strain (not uniaxial stress); therefore the cross-sectional area is always $A \equiv 1.0$.

The mass at node i , for an individual element, is

$$M_i = \rho_o V_o / 2 \tag{1}$$

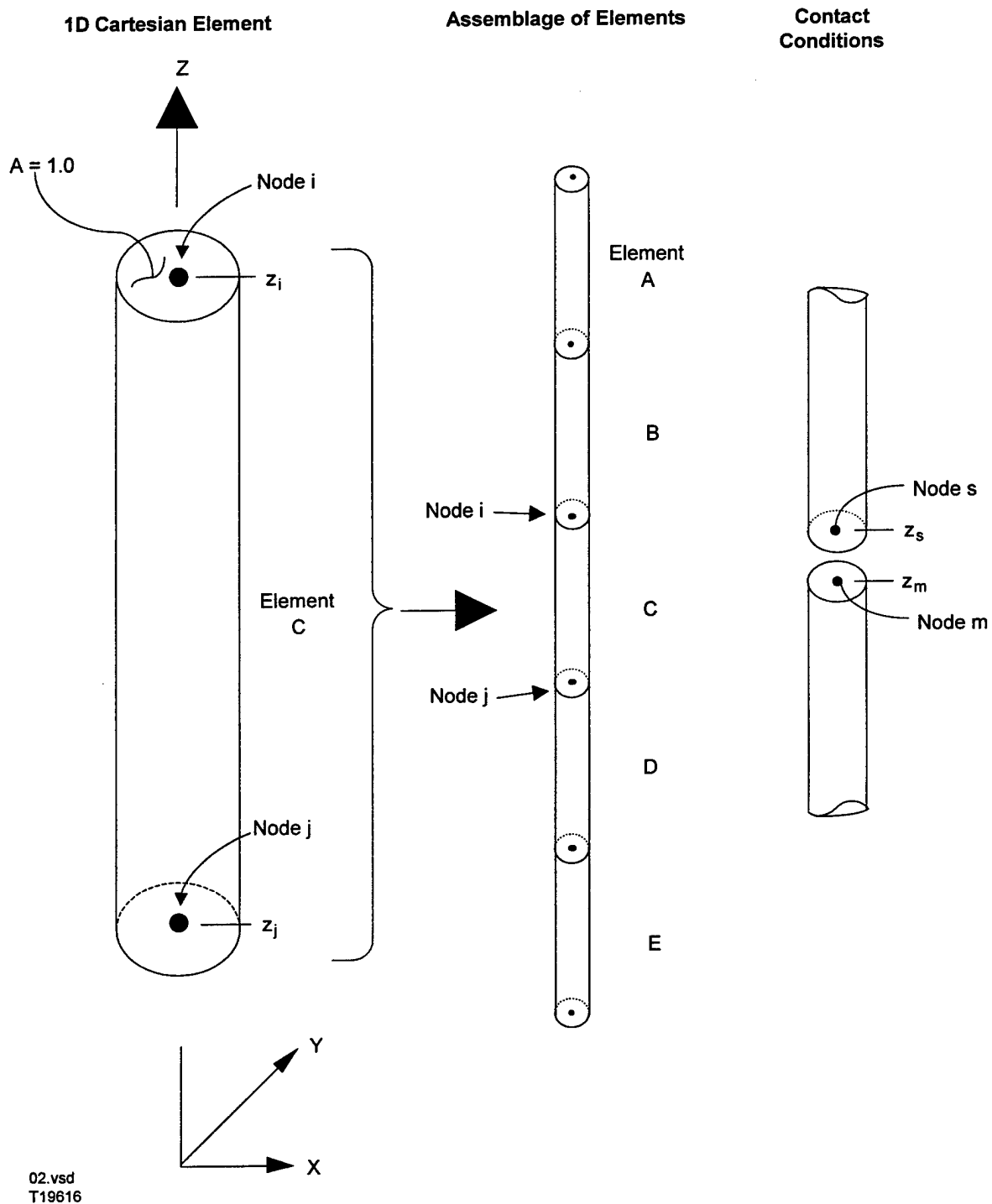


Figure 2. Description of the 1D Cartesian Element

where ρ_0 is the initial density of the material and the initial volume is

$$V_o = A(z_i - z_j) = z_i - z_j \quad (2)$$

for $A \equiv 1.0$.

When element C is incorporated into an assemblage of elements, as shown in Figure 2, then the total mass at node i contains the individual element masses from both elements B and C. The total mass at node i is

$$\bar{M}_i = \sum M_i \quad (3)$$

3.1.1 Equations of Motion

The acceleration, velocity and position of node i are determined as follows:

$$\ddot{z}_i^t = \bar{F}_z^i / \bar{M}_i \quad (1)$$

$$\dot{z}_i^{t+} = \dot{z}_i^{t-} + \ddot{z}_i^t \bar{\Delta t} \quad (2)$$

$$z_i^{t+\Delta t} = z_i^t + \dot{z}_i^{t+} \Delta t \quad (3)$$

In Equation 1 the acceleration is \ddot{z}_i^t at time = t. \bar{F}_z^i is the net z direction force on node i, and this is the sum of the individual element forces on node i. These forces are obtained from the element computations in the previous cycle of integration. This will be explained in greater detail in subsection 3.1.3. \bar{M}_i is the total mass at node i, as given in Equation 3 of subsection 3.1.

The updated velocity in Equation 2 is constant for the interval between time = t and time = t + Δt . The constant velocity for the previous time increment is \dot{z}_i^{t-} and $\bar{\Delta t}$ is the average of the two integration time increments about time = t.

The integration time increment is limited to

$$\Delta t = C_t \left[h / \left(\sqrt{g^2} + \sqrt{g^2 + c_s^2} \right) \right] \quad (4)$$

where $g^2 = C_Q Q / \rho$, $h = z_i - z_j$ is the height of the element and c_s is the sound velocity of the material (References 1 and 5). Q is the artificial viscosity and C_Q is a constant for the artificial viscosity. These are described in Section 6. The Courant sound speed fraction, C_t , must be less than unity ($C_t \leq 1.0$) to ensure numerical stability. $C_t = 0.9$ is a typical value.

3.1.2 Contact Interfaces

Contact interfaces can be handled in a straightforward manner in 1D. The user must specify two nodes for each interface. Node s is designated as the slave node and it is the node above (higher z coordinate) master node m . The slave and master designations are used for convenience and do not cause a bias in the results.

After the equations of motion have been applied, a check is made to determine if there is interference ($z_m \geq z_s$). If there is no interference, then there is no contact and the surfaces are free.

If there is contact, it is necessary to adjust the positions and velocities of the two nodes. The center of mass of the two nodes is

$$\bar{z} = (M_s z_s + M_m z_m) / (M_s + M_m) \quad (1)$$

where M_s and M_m are the masses of the interface nodes, and z_s and z_m are the corresponding z coordinates.

The movements of the two nodes, to the center of mass are

$$\Delta z_s = \bar{z} - z_s \quad (2)$$

$$\Delta z_m = \bar{z} - z_m \quad (3)$$

and the corresponding velocity changes are

$$\Delta \dot{z}_s = \Delta z_s / \Delta t \quad (4)$$

$$\Delta \dot{z}_m = \Delta z_m / \Delta t \quad (5)$$

The updated positions and velocities then become

$$z_s^{\text{new}} = z_s^{\text{old}} + \Delta z_s \quad (6)$$

$$z_m^{\text{new}} = z_m^{\text{old}} + \Delta z_m \quad (7)$$

$$\dot{z}_s^{\text{new}} = \dot{z}_s^{\text{old}} + \Delta \dot{z}_s \quad (8)$$

$$\dot{z}_m^{\text{new}} = \dot{z}_m^{\text{old}} + \Delta \dot{z}_m \quad (9)$$

This formulation conserves momentum and provides consistency between the velocities and positions. If there was contact during the previous cycle, then the velocities of the two contact nodes are identical. If there was a gap during the previous cycle then there will continue to be a closing velocity (but only for one cycle).

3.1.3 1D Cartesian Elements

There are three primary features to all of the element algorithms. The first is to obtain the strains, strain rates and rotational rates. From these, the stresses and pressures are obtained through a variety of material models. Then, equivalent nodal forces must be determined from the stresses.

The volumetric strain and the volumetric strain rate are as follows:

$$\epsilon_v = V / V_0 - 1 \quad (1)$$

$$\dot{\epsilon}_v = (\epsilon_v^{t+\Delta t} - \epsilon_v^t) / \Delta t \quad (2)$$

In Equation 1, V and V_0 are the current and initial element volumes; and in Equation 2, $\epsilon_v^{t+\Delta t}$ and ϵ_v^t are the volumetric strains at time $t + \Delta t$ and time t . The volumetric strains and strain rates are based on the initial configuration, as opposed to the shear and deviator strain rates which are based on the current configuration.

A more common notation is to represent the z velocity by \dot{v} , instead of \dot{z} . The z velocities in the element are then assumed to vary in a linear manner, such that

$$\dot{v} = \alpha_1 + \alpha_2 z \quad (3)$$

where α_1 and α_2 are geometry and velocity constants.

Substituting the two nodal velocities (\dot{v}_i and \dot{v}_j) and the two nodal positions (z_i and z_j) into Equation 3 gives two equations and two unknowns (α_1 and α_2). The strain rate in the z direction can then be determined from

$$\dot{\epsilon}_z = \frac{\partial \dot{v}}{\partial z} = \alpha_2 = (\dot{v}_i - \dot{v}_j) / (z_i - z_j) \quad (4)$$

All of the other strain rate components are zero.

$$\dot{\epsilon}_x = \dot{\epsilon}_y = \dot{\gamma}_{xy} = \dot{\gamma}_{xz} = \dot{\gamma}_{yz} = 0 \quad (5)$$

where $\dot{\epsilon}_x$ and $\dot{\epsilon}_y$ are the other two normal strain rates and $\dot{\gamma}_{xy}$, $\dot{\gamma}_{xz}$ and $\dot{\gamma}_{yz}$ are the three shear strain rates.

Some of the constitutive models require an equivalent strain rate, and this is expressed as

$$\bar{\epsilon} = \sqrt{\frac{2}{9} \left[(\dot{\epsilon}_x - \dot{\epsilon}_y)^2 + (\dot{\epsilon}_x - \dot{\epsilon}_z)^2 + (\dot{\epsilon}_y - \dot{\epsilon}_z)^2 + \frac{3}{2} (\dot{\gamma}_{xy}^2 + \dot{\gamma}_{xz}^2 + \dot{\gamma}_{yz}^2) \right]} \quad (6)$$

which reduces to $\bar{\epsilon} = 2\dot{\epsilon}_z / 3$ for the special case of 1D Cartesian geometry.

The constitutive models also require deviator strain rates, which are expressed as

$$\dot{\epsilon}_x = \dot{\epsilon}_x - \dot{\epsilon}_{ave} \quad (7)$$

$$\dot{\epsilon}_y = \dot{\epsilon}_y - \dot{\epsilon}_{ave} \quad (8)$$

$$\dot{\epsilon}_z = \dot{\epsilon}_z - \dot{\epsilon}_{ave} \quad (9)$$

where $\dot{\epsilon}_{ave} = (\dot{\epsilon}_x + \dot{\epsilon}_y + \dot{\epsilon}_z) / 3$. Note that the sum of the deviator strain rates is $\dot{\epsilon}_x + \dot{\epsilon}_y + \dot{\epsilon}_z = 0$.

The stresses in the elements are determined from the strains, strain rates, temperatures, pressures, internal energies, and material constants. The three normal stresses are generally expressed as

$$\sigma_x = s_x - (P + Q) \quad (10)$$

$$\sigma_y = s_y - (P + Q) \quad (11)$$

$$\sigma_z = s_z - (P + Q) \quad (12)$$

where s_x , s_y and s_z are the normal deviator stresses, P is the hydrostatic pressure and Q is the artificial viscosity. These are described in detail in Section 6. The shear stresses are $\tau_{xy} = \tau_{xz} = \tau_{yz} = 0$ for 1D geometry.

Trial values of the deviator stresses at time $t + \Delta t$ are

$$s_x^{t+\Delta t} = s_x^t + 2G\dot{\epsilon}_x\Delta t \quad (13)$$

$$s_y^{t+\Delta t} = s_y^t + 2G\dot{\epsilon}_y\Delta t \quad (14)$$

$$s_z^{t+\Delta t} = s_z^t + 2G\dot{\epsilon}_z\Delta t \quad (15)$$

In Equation 13, the first term (s_x^t) is the deviator stress at the previous time and the second term ($2G\dot{\epsilon}_x\Delta t$) is the incremental stress due to the incremental strain ($\dot{\epsilon}_x\Delta t$) during that time increment, where G is the elastic shear modulus.

Equations 13–15 assume an elastic response of the material. If the strength of the material is exceeded, then plastic flow (or fracture) will occur. The Von Mises yield criterion is used to determine an equivalent stress, $\bar{\sigma}$, that can be compared to the uniaxial tensile (or compressive) strength of the material. The general form of the equivalent stress is

$$\bar{\sigma} = \sqrt{\frac{1}{2} \left[(\sigma_x - \sigma_y)^2 + (\sigma_x - \sigma_z)^2 + (\sigma_y - \sigma_z)^2 + 6(\tau_{xy}^2 + \tau_{xz}^2 + \tau_{yz}^2) \right]} \quad (16)$$

Using deviator stresses (instead of total stresses) and setting the shear stresses to zero (for 1D response), the equivalent stress can be simplified to

$$\bar{\sigma} = \sqrt{\frac{3}{2}(s_x^2 + s_y^2 + s_z^2)} \quad (17)$$

If $\bar{\sigma}$ is not greater than the equivalent tensile strength of the material, σ , the final deviator and shear stresses are as given in Equations 13–15. If $\bar{\sigma}$ is greater than σ , then the stresses in Equations 13–15 are multiplied by the factor $(\sigma / \bar{\sigma})$. When the reduced deviator and shear stresses are put into Equation 17, the result is always $\bar{\sigma} = \sigma$. This is known as the radial return algorithm. The various material strength models for σ are presented in Section 6.

During plastic flow it is sometimes necessary to determine the equivalent plastic strain for strain hardening effects on the strength of the material, or to determine if the material has failed. The first step in this process is to adjust the total strain rates to plastic strain rates by subtracting out the elastic portion of the strain rates.

$$\dot{e}_x^p = \dot{e}_x - (s_x^{t+\Delta t} - s_x^t) / 2G\Delta t \quad (18)$$

$$\dot{e}_y^p = \dot{e}_y - (s_y^{t+\Delta t} - s_y^t) / 2G\Delta t \quad (19)$$

$$\dot{e}_z^p = \dot{e}_z - (s_z^{t+\Delta t} - s_z^t) / 2G\Delta t \quad (20)$$

Again, the plastic shear strain rates are zero for 1D geometry. The expression for the 1D equivalent plastic strain rate is

$$\bar{\dot{e}}_p = \sqrt{\frac{2}{9}[(\dot{e}_x^p - \dot{e}_y^p)^2 + (\dot{e}_x^p - \dot{e}_z^p)^2 + (\dot{e}_y^p - \dot{e}_z^p)^2]} \quad (21)$$

The equivalent plastic strain, \bar{e}_p , is then obtained by integrating $\bar{\dot{e}}_p$ with respect to time:

$$\bar{e}_p^{t+\Delta t} = \bar{e}_p^t + \bar{\dot{e}}_p \Delta t \quad (22)$$

After the element stresses are obtained, it is necessary to determine concentrated forces to act on the concentrated masses at the nodes. These nodal forces are used in the equations of motion for

the subsequent integration cycle. The net z forces on nodes i and j, for an individual element, are simply

$$F_z^i = -\sigma_z A = -\sigma_z \quad (23)$$

$$F_z^j = \sigma_z A = \sigma_z \quad (24)$$

for $A \equiv 1.0$. Note that $F_z^i + F_z^j \equiv 0$ for each element, and this ensures equilibrium for the system. This results in conservation of momentum if there are no external forces or restraints. The final net force on node i is

$$\bar{F}_z^i = \sum F_z^i \quad (25)$$

It is also possible to add external forces through applied pressures.

The heat conduction algorithm assumes the temperature varies linearly between nodes such that

$$T = \alpha_3 + \alpha_4 z \quad (26)$$

where T is the temperature in the element, and α_3 and α_4 are geometry and nodal temperature constants.

Substituting the two nodal temperatures (T_i and T_j) and the two nodal positions (z_i and z_j) into Equation 26 gives two equations and two unknowns (α_3 and α_4). The temperature gradient is then

$$\frac{\partial T}{\partial z} = \alpha_4 = (T_i - T_j) / (z_i - z_j) \quad (27)$$

The instantaneous heat flow is

$$q_z = -k \frac{\partial T}{\partial z} = -k (T_i - T_j) / (z_i - z_j) \quad (28)$$

where k is the thermal conductivity of the element material.

The incremental increase in thermal energy at the nodes can be obtained by integrating the heat flow with respect to area and time.

$$\Delta Q_i = q_z A \Delta t + \Delta Q_e / 2 \quad (29)$$

where $A \equiv 1.0$ is the area, Δt is the integration time increment, and ΔQ_e is the internal energy generated in the element during the previous time increment.

After Equations 26–29 have been applied to all elements, the updated temperatures of the nodes have the form

$$T_i^{t+\Delta t} = T_i^t + \sum \Delta Q_i / \bar{M}_i c_{pi} \quad (30)$$

where $T_i^{t+\Delta t}$ and T_i^t are the temperature of the nodes at times $t+\Delta t$ and t , $\sum \Delta Q_i$ is the sum of the incremental heat contributed by all elements that contain node i , \bar{M}_i is the total mass of node i , and c_{pi} is the specific heat of node i .

The internal energy in an element can be used to compute element pressures. To account for the flow of internal energy through the grid, the element temperature is assumed to be the average of the nodal temperatures.

$$\bar{T} = (T_i + T_j) / 2 \quad (31)$$

The internal energy (per initial volume) is given by

$$E_s = (\bar{T} - T_o) \rho_o c_p \quad (32)$$

where T_o is the initial temperature (where $E_s = 0$), ρ_o is the initial density and c_p is the specific heat of the element material.

The integration time increment must also be bounded to ensure that the computations remain stable for heat conduction (References 6 and 7). The heat conduction portion requires

$$\Delta t \leq \rho c_p h^2 / 4k \quad (33)$$

where $h = z_i - z_j$ is the length of the element and the other terms recently have been defined. This is analogous to the time increment restriction for wave propagation in Equation 4 of subsection 3.1.1. Unless h is very small, the wave propagation restriction is much more severe than the heat conduction restriction.

3.1.4 Nonreflective Boundary Elements

Nonreflective boundary elements have been available for many years (References 8 and 9), and have been used to provide nonreflective damping for the modeling of infinite bodies such as soil or water. They are intended primarily to absorb elastic waves, but they are also effective for other applications (Reference 10). The nonreflective boundary elements are incorporated as single-node, infinitely-thin, massless elements. The damping force at node i resists the velocity and is expressed as

$$F_z^i = -\sigma_d A \dot{z}_i = -\rho_o c_s A \dot{z}_i \quad (1)$$

where the damping stress on the boundary is $\sigma_d = \rho_o c_s$, $A \equiv 1.0$ is the area and \dot{z}_i is the nodal velocity. The initial density is ρ_o and the longitudinal sound velocity is

$$c_s = \sqrt{(K_1 + 4G/3)/\rho_o} \quad (2)$$

where K_1 is the elastic bulk modulus and G is the elastic shear modulus.

3.2 1D CYLINDRICAL GEOMETRY

The element for 1D cylindrical geometry is shown in Figure 3. Again, the z coordinate is the coordinate of interest and the element is defined by nodes i and j , with $z_i > z_j$. Only a $\Delta\theta$ segment of the element is shown in Figure 3, such that the effect of the hoop stress, σ_θ , can be illustrated.

The nodal masses for the 1D cylindrical geometry are different from the 1D Cartesian geometry.

$$M_i = \alpha_i \rho_o V_o \quad (1)$$

$$M_j = \alpha_j \rho_o V_o \quad (2)$$

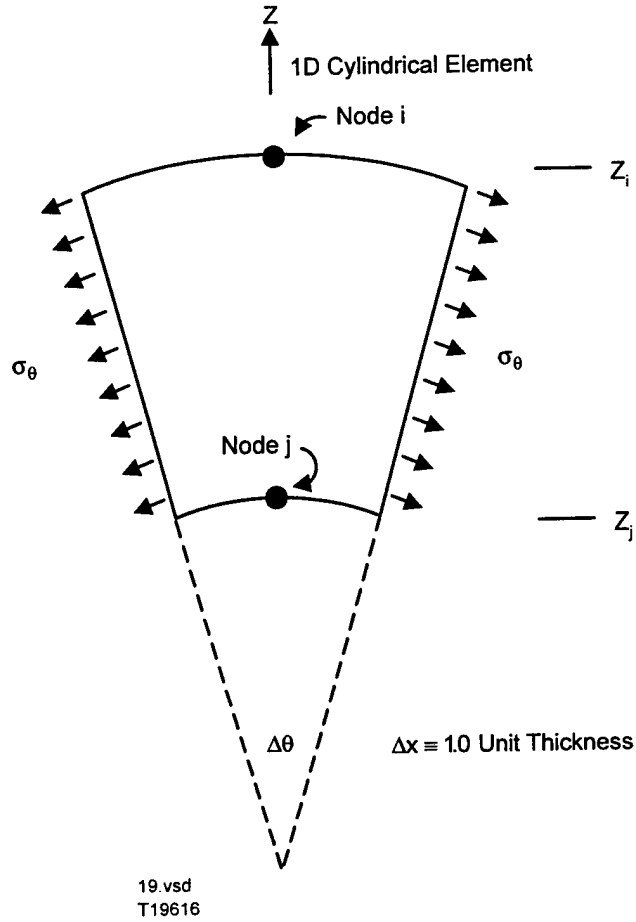


Figure 3. Description of the 1D Cylindrical Element

where ρ_0 is the initial density of the material and the initial volume is

$$V_0 = \pi(z_i^2 - z_j^2)\Delta x \quad (3)$$

where $\Delta x \equiv 1.0$ is a unit thickness normal to the plane of the element in Figure 3.

The distribution of the total element mass is determined by α_i and α_j . The larger radius of node i requires a larger mass on node i to conserve the CG position of the element.

$$\alpha_i = (2z_i / 3 + z_j / 3) / (z_i + z_j) \quad (4)$$

$$\alpha_j = 1.0 - \alpha_i \quad (5)$$

The strain rate in the z direction is identical to that of the 1D Cartesian element in Equation 4 of subsection 3.1.3. Also, the through-thickness strain rate remains $\dot{\epsilon}_x \equiv 0$. The hoop strain rate for this geometry is dependent on the z velocities.

$$\dot{\epsilon}_\theta = \dot{z} / z = (\dot{z}_i + \dot{z}_j) / (z_i + z_j) \quad (6)$$

This hoop strain rate, $\dot{\epsilon}_\theta$, can be substituted for $\dot{\epsilon}_y$ in the 1D Cartesian strain rate equations in subsection 3.1.3. Also, the hoop stress, σ_θ , can be substituted for σ_y , for the 1D Cartesian stresses.

The nodal forces depend on both σ_z and σ_θ .

$$F_z^i = -2\pi\sigma_z\bar{z} - \pi\sigma_\theta(z_i - z_j) \quad (7)$$

$$F_z^j = 2\pi\sigma_z\bar{z} - \pi\sigma_\theta(z_i - z_j) \quad (8)$$

The forces on nodes i and j are not equal and opposite as they are for the 1D Cartesian geometry, and this is due to the hoop stress, σ_θ , that acts in the same direction on both nodes. The area for the σ_z stresses is taken at the center of the element at $\bar{z} = (z_i + z_j) / 2$, and this provides equal and opposite forces from the σ_z stress.

The heat conduction formulation and nonreflective boundary elements are very similar to those of the 1D Cartesian geometry. The primary difference is that the area, A , is a function of z for the 1D cylindrical geometry.

3.3 1D SPHERICAL GEOMETRY

The element for 1D spherical geometry is similar to that of 1D cylindrical geometry shown in Figure 3. The difference is that the spherical geometry does not have a unit thickness normal to the figure, but rather has a $\Delta\theta$ and a σ_θ acting in the two directions normal to the z axis.

The nodal masses are

$$M_i = \alpha_i \rho_o V_o \quad (1)$$

$$M_j = \alpha_j \rho_o V_o \quad (2)$$

where ρ_o is the initial density of the material and the initial volume is

$$V_o = 4\pi(z_i^3 - z_j^3)/3 \quad (3)$$

The distribution of mass to the nodes (to conserve the CG position of the element) is provided by α_i and α_j .

$$\alpha_i = \frac{z_i^4 - \left(\frac{4}{3}\right)z_j z_i^3 + \left(\frac{1}{3}\right)z_j^4}{\frac{4}{3}(z_i^4 - z_j z_i^3 - z_i z_j^3 + z_j^4)} \quad (4)$$

$$\alpha_j = 1.0 - \alpha_i \quad (5)$$

The nodal forces are

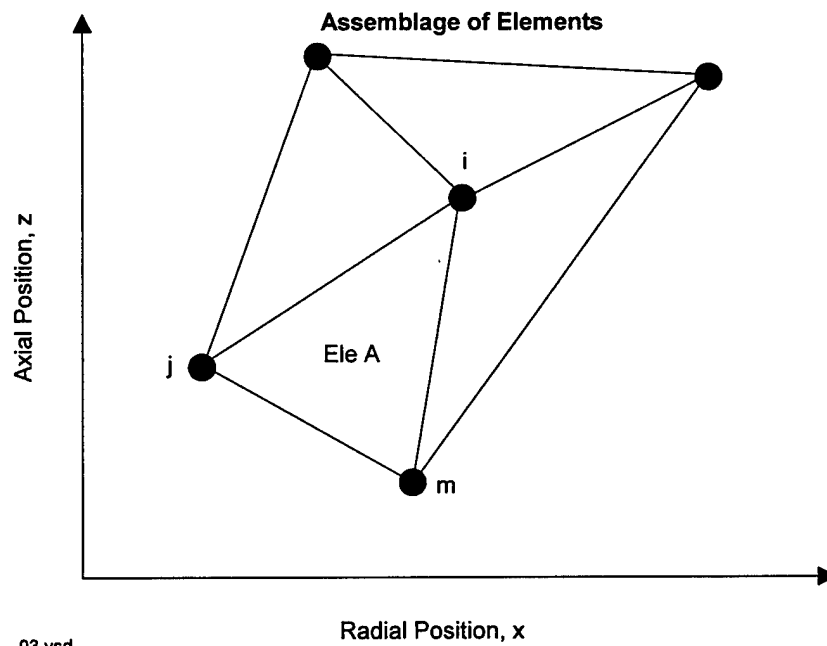
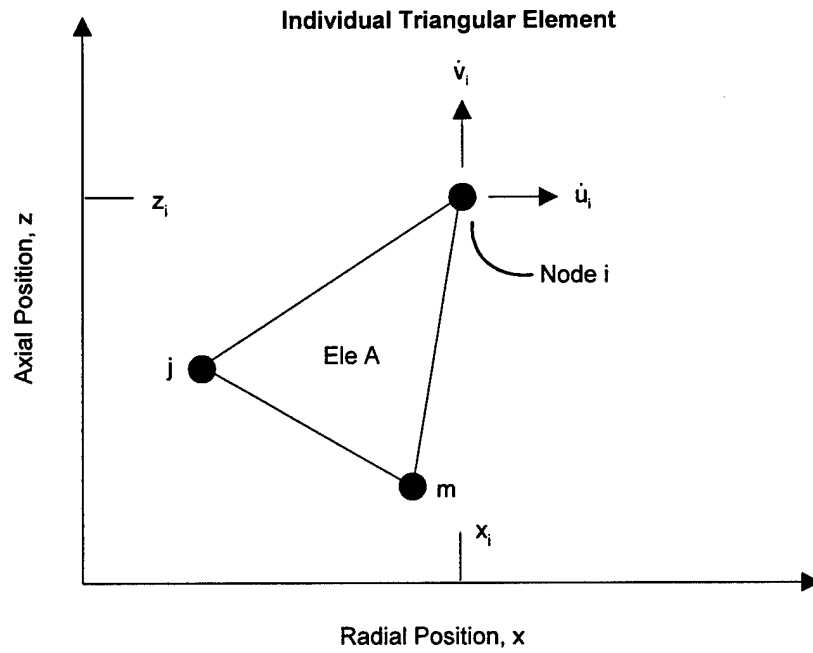
$$F_z^i = -4\pi\sigma_z \bar{z}^2 - 4\pi\sigma_\theta \bar{z}(z_i - z_j) \quad (6)$$

$$F_z^j = 4\pi\sigma_z \bar{z}^2 - 4\pi\sigma_\theta \bar{z}(z_i - z_j) \quad (7)$$

Again, the area for the σ_z stresses is taken at $\bar{z} = (z_i + z_j)/2$. Other features of this geometry are analogous to the 1D Cartesian and cylindrical geometries.

3.4 2D AXISYMMETRIC GEOMETRY

A description of 2D axisymmetric geometry is shown in Figure 4. This figure shows triangular elements, but quad elements, bending shell elements, membrane shell elements, and nonreflective boundary elements are also available. The early developments of this work are reported in References 1, 3, and 11.



03.vsd
T19616

Figure 4. Description of the 2D Axisymmetric Triangular Element

3.4.1 Equations of Motion

The radial (x) and axial (z) accelerations, velocities, and positions of node i are determined as follows:

$$\ddot{x}_i^t = \bar{F}_x^i / \bar{M}_i \quad (1)$$

$$\ddot{z}_i^t = \bar{F}_z^i / \bar{M}_i \quad (2)$$

$$\dot{x}_i^{t+} = \dot{x}_i^{t-} + \ddot{x}_i^t \bar{\Delta t} \quad (3)$$

$$\dot{z}_i^{t+} = \dot{z}_i^{t-} + \ddot{z}_i^t \bar{\Delta t} \quad (4)$$

$$x_i^{t+\Delta t} = x_i^t + \dot{x}_i^{t+} \Delta t \quad (5)$$

$$z_i^{t+\Delta t} = z_i^t + \dot{z}_i^{t+} \Delta t \quad (6)$$

Equations 1 and 2 provide the radial and axial accelerations at time = t. \bar{F}_x^i and \bar{F}_z^i are the net x and z direction forces on node i. Looking at the lower portion of Figure 4, these forces would come from the four elements that contain node i. The forces are obtained from the element computations in the previous cycle of integration. \bar{M}_i is the total mass at node i, and it contains a fraction of the mass of all elements that contain node i. Although Figure 4 shows only triangular elements, a node can have various element types attached to it. This means it is possible for an individual node to have masses and forces from different element types. The specific algorithms for masses and forces are provided in subsections 3.4.4–3.4.8.

The updated velocities in Equations 3 and 4 are constant for the interval between time = t and time = t+Δt. The constant velocities for the previous time increment are \dot{x}_i^{t-} and \dot{z}_i^{t-} , and $\bar{\Delta t}$ is the average of the two integration time increments about time = t.

The integration time increment is limited to

$$\Delta t = C_t \left[h / \left(\sqrt{g^2} + \sqrt{g^2 + c_s^2} \right) \right] \quad (7)$$

where $g^2 = C_Q Q / \rho$, h is a characteristic length of the element (described later for each element type), and c_s is the sound velocity of the material (References 1 and 5). Q is the artificial viscosity and C_Q is a constant for the artificial viscosity. These are described in Section 6. The Courant sound speed fraction, C_t , must be less than unity ($C_t \leq 1.0$) to ensure numerical stability. $C_t = 0.9$ is a typical value.

For 2D bending shell elements there is also a rotational degree of freedom on each node. The rotational velocity of node i is updated in a similar manner as the translational velocities in Equations 1–4. The updated acceleration and velocity are as follows:

$$\ddot{\theta}_i^t = \overline{M}_y^i / I_y \quad (8)$$

$$\dot{\theta}_i^{t+} = \dot{\theta}_i^{t-} + \ddot{\theta}_i^t \overline{\Delta t} \quad (9)$$

where \overline{M}_y^i is the net moment on node i , I_y is the rotational mass moment of inertia, and $\overline{\Delta t}$ is the average integration time increment. The rotational displacement, θ_i , is not required.

3.4.2 Sliding Interfaces

The 2D sliding algorithm allows the two surfaces (master and slave) to be determined automatically, or to be input by the user. This subsection describes the automated approach in detail. It is similar to that reported in Reference 12, but it has been improved to eliminate the order dependence. There are three primary steps in the automated sliding interface algorithm; the interface determination algorithm, the searching algorithm and the contact algorithm.

Interface Determination Algorithm — After the finite element grid has been assembled (using three-node triangles or four-node quads), it is necessary to determine the surface nodes and the surface line segments. The surface nodes are designated as slave nodes, and the surface line segments are designated as master segments (composed of two master nodes). The left portion of Figure 5 shows a simple illustration for an impact problem. The assemblage of master segments forms a membrane around the outer surfaces of the bodies through which the slave nodes cannot pass. As the slave nodes contact the master segments, momentum is transferred from the slave nodes to the master nodes. Note that every surface node is both a slave node and a master segment node. This is different from the earlier sliding algorithms, and therefore requires special treatment.

The right portion of Figure 5 shows how the number of slave nodes and master segments can be significantly reduced by the user, if the user has some knowledge about the region of interaction. Although this is not required, it can often be a simple way to reduce the number of slave nodes and master segments in a problem. This, in turn, leads to reduced CPU time.

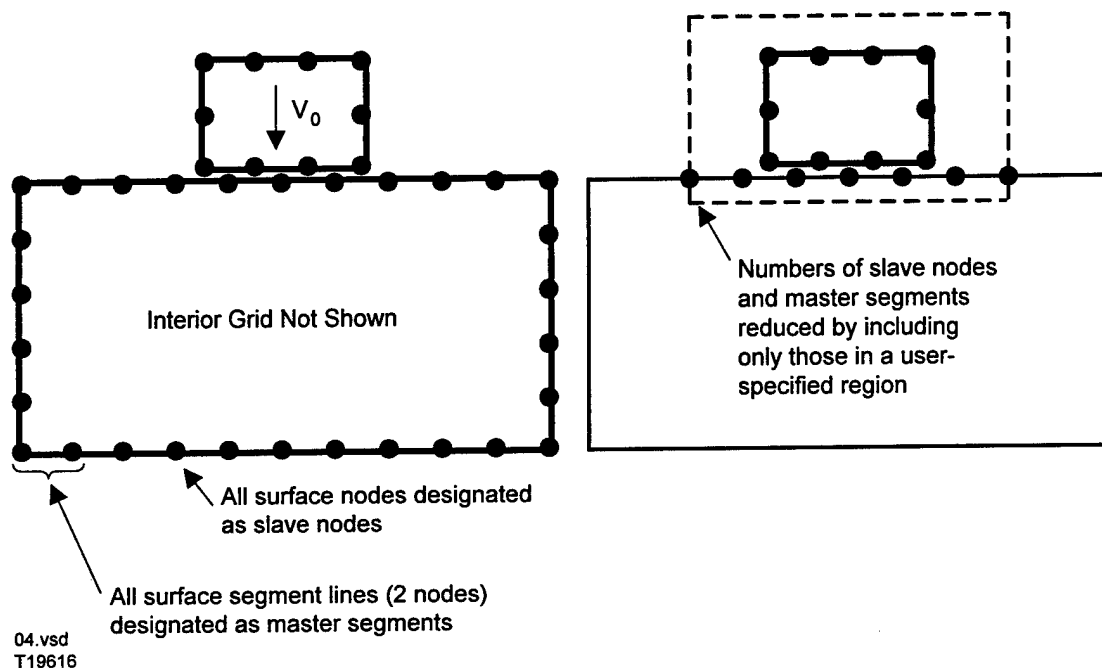


Figure 5. Determination of the 2D External Interfaces

The master segments can be obtained by comparing every line segment of every element with every line segment of every other element. If there is no matching line segment (with the same two nodes), then that segment is on the surface and is designed a master segment. Likewise, every node that forms a master segment is also a slave node. The final description of the interfaces consists of a list of slave nodes and a list of master segments that are defined by two master nodes. The pairs of master nodes (M_1 , M_2) are ordered such that the exterior surface is to the left, and the interior is to the right, when viewing node M_1 from node M_2 .

Searching Algorithm — After the nodal equations of motion (velocities and positions) have been updated, it is necessary to check all of the slave nodes to determine if they have interacted with any of the master segments that form the master surface. A summary of the searching algorithm is shown in Figure 6. The master nodes are M_1 and M_2 , and the slave node is N_s . The first check for each slave node is to determine which master segment (or segments) are candidates for interaction. A bucket sort algorithm (Reference 13) is used to limit the number of

master segments that must be considered for each slave node. If one of the two master nodes on a segment is also the slave node, then that master segment is no longer considered for that slave node. The box test in Figure 6 indicates that slave node N_s can be associated with master segment M_1-M_2 only if it is contained within a rectangular box that extends a distance, δ_{ref} , beyond the master segment, M_1-M_2 .

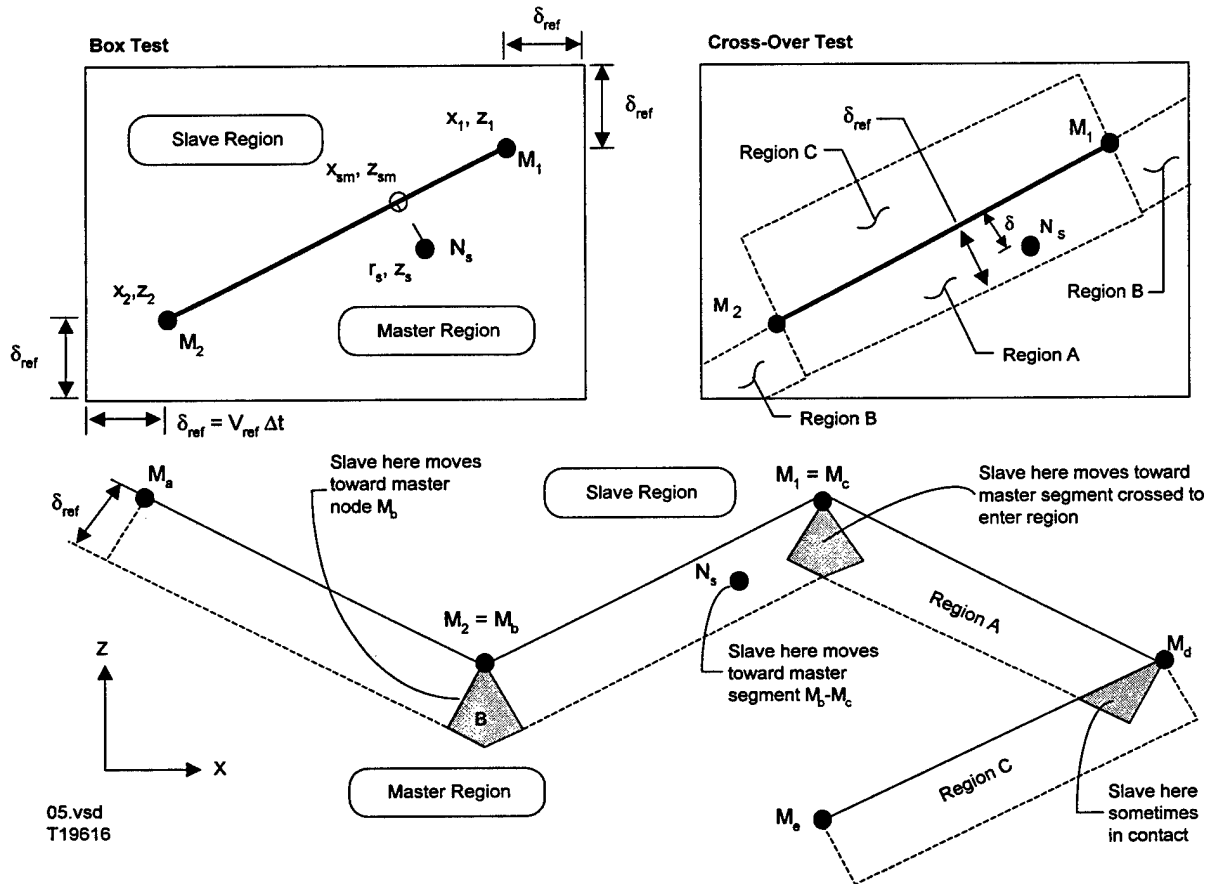


Figure 6. Description of the 2D Sliding Interface Searching Algorithm

The reference distance is simply

$$\delta_{ref} = V_{ref} \Delta t \quad (1)$$

where V_{ref} is the maximum relative velocity (between a slave node and a master segment) that can be experienced during the course of the problem, and Δt is the integration time increment. V_{ref} can be specified by the user or it can be computed by the preprocessor based on the maximum relative velocity for the initial condition. It can generally be set to about 1.5 times the

maximum relative velocity in the initial condition. For explosives it can generally be set to the detonation velocity.

If the slave node passes the box test, it is then subjected to the cross-over test. This test is performed to determine if the slave node has crossed over the master segment. The distance between the slave node and the master segment is given by

$$\delta = -(Ax_s + Bz_s + C) \quad (2)$$

where $A = (z_2 - z_1)/\ell$, $B = (x_1 - x_2)/\ell$, $C = (x_2z_1 - x_1z_2)/\ell$, and $\ell = \sqrt{(x_1 - x_2)^2 + (z_1 - z_2)^2}$.

The x and z coordinates of master nodes M_1 and M_2 are x_1 , x_2 , z_1 , z_2 , and the coordinates of slave node N_s are x_s and z_s . A and B are the direction cosines normal to the master segment and ℓ is the length of the segment. If $0 \leq \delta \leq \delta_{\text{ref}}$, then the slave node has touched or crossed over the master segment line (or the extension of the line), and it remains a candidate for interaction with that master segment. If the slave node fails either the box test or the cross-over test, then it cannot interact with that master segment.

If the slave node passes both the box test and the cross-over test, then it must be determined if it falls within the normal projection of master segment M_1-M_2 (Region A), or if it falls within the extended region of the master segment (Region B). Even after a slave node has found a master segment (by passing both the box test and the cross-over test), the search must continue for the remaining master segments, because it is possible for a slave node to find multiple candidate master segments.

It is also necessary to check if the slave node has not crossed over the master segment, but is within Region C ($-\delta_{\text{ref}} < \delta < 0$), as shown in Figure 6. This condition can be used to offset a Region A condition for an adjacent segment, as will be shown later.

After the slave node has searched for all the master segments, there are the following possibilities:

- If the slave node is within Region A for only one master segment and is not within Region C for an adjacent segment, then it interacts with master segment M_b-M_c , as shown in the lower portion of Figure 6.

- If a slave node is within Region A for only one master segment and is within Region C for an adjacent segment, then it may or may not be in contact with the master surface. This condition occurs in the shaded area near node M_d , as shown in the lower portion of Figure 6. If the slave node passed through segment M_c-M_d , then it is designated to interact with that segment. If it did not pass through segment M_c-M_d , then it is not in contact with the master surface.
- If the slave node is within Region A for two adjacent master segments, then it interacts with whichever segment it crossed to arrive at its current position. This possibility is illustrated in the shaded area near node M_c , in the lower portion of Figure 6. If it passed through line M_b-M_c to reach its position in the shaded area, then it interacts with master segment M_b-M_c . Likewise, if it passed through line M_c-M_d , then it interacts with that segment.
- If the slave node is within Region B for only one segment, then it does not interact with any master segment. This condition can exist at a convex corner on the master surface. The node can be crossed over the extension of a master segment (Region B), but it may not be crossed over the adjacent master segment.
- If the slave node is within Region B for two adjacent master segments, then it interacts only with the single node that is common for those two segments. This possibility is illustrated in the shaded area near node M_b , in the lower portion of Figure 6.
- Another situation can exist that is not illustrated in Figure 6. Under some circumstances, where three or more distinct bodies meet at a corner, it is possible for a slave node to pass through two or more master segments that are not attached to one another. When this occurs, the slave node is associated with the master segment that has the greatest crossover. If the crossover with other master segments is significant ($\delta > 0.1 \delta_{ref}$) then the complete searching and contact procedure is repeated for that cycle, with the result being that the secondary crossover now becomes the primary crossover and is adjusted accordingly.

After the searching is completed, there are three possibilities for each slave node:

- The slave node has found a master segment M_1-M_2 with which it must interact.
- The slave node has found a single master node with which it must interact.
- The slave node has not crossed over any portion of the master surface, and therefore has no interaction with the master surface.

The searching algorithm is applied every cycle. In some instances, the CPU searching time can be reduced by performing the bucket sort algorithm every N cycles instead of every cycle. This requires the buckets to be expanded in size such that all the candidate master segments are available to the slave node for all N cycles. This is accomplished by using the reference velocity concept of Equation 1. This approach provides greater CPU savings for lower reference velocities because the buckets do not need to be expanded as much as they are for higher reference velocities. This approach cannot be used with erosion, however, because the lists of slave nodes and master segments change from cycle to cycle during erosion.

Contact Algorithm — The contact algorithm adjusts the positions and velocities of the slave nodes and the master surface nodes. This is done after the equations of motion have been updated in the standard manner, and after the searching has been completed. Conservation of momentum can be attained by considering each slave node to interact with its master segment (or single master node) in a single pass (without subsequent interactions). However, subsequent interactions generally will be required to have each slave node placed exactly on the master surface, and to have the normal velocity of the slave node equal to the normal velocity of the master surface at the slave node position.

A summary of the contact algorithm is shown in Figure 7. The general approach is to have each slave node interact with its master segment ($M_1 - M_2$) or master node (if it is in a concave corner). The velocity and position changes for the master and slave nodes are performed during the course of several iterations. Multiple iterations are required to achieve a good velocity and position match of the slave node with the master segment. For a single slave node on a single master segment, it is possible to obtain an exact match in one iteration. However, when subsequent slave nodes interact with the same master segment, or an adjacent segment, then the match of the previous slave node is altered.

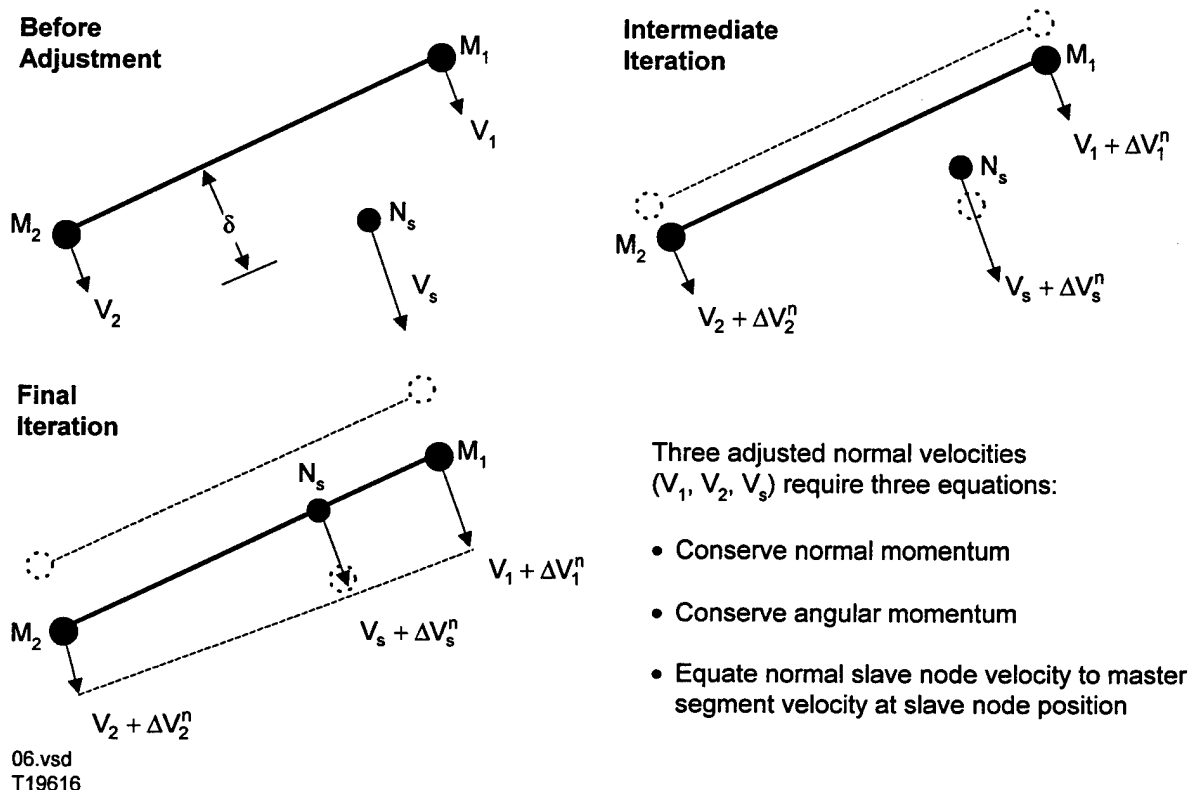


Figure 7. Description of the 2D Sliding Interface Contact Algorithm

Furthermore, only a portion of the required velocity and position changes are made during each iteration. If the entire position movement would be made during the first iteration, then it would be possible for some slave nodes to be separated from the master segment after the first iteration. Because the contact algorithm is exercised only when there is interference, if the slave node is free from the surface, then it will not be considered for subsequent iterations.

An alternative approach would be to consider the slave node (and the corresponding master segment) to be adjusted for all subsequent iterations, if it was in contact for the first iteration. The problem with this approach is that this would not allow a slave node to be released from the master surface if it is in contact during the first iteration. For some complex contact interfaces, a slave node needs to be free to separate from the master surface, even if it was in contact during the first iteration.

The following algorithm considers a contact/sliding interface with no friction, although frictional effects can be added straightforwardly using the general approach described in Reference 14, and presented in subsection 3.8.2. The basic approach is to consider each slave node interacting with

its master segment. The normal velocities of the slave node and the two master nodes are V_s^n , V_1^n , and V_2^n , where the superscript n indicates the iteration number. The objective of the algorithm is to adjust these normal velocities by conserving linear momentum, conserving angular momentum, and equating the normal velocity of the slave node to the normal velocity of the master segment at the slave node location.

The relationship between the normal velocity changes (based on conservation of linear and angular momentum) is as follows:

$$\Delta V_1^n = -R_1 M_s \Delta V_s^n / M_{M1} \quad (3)$$

$$\Delta V_2^n = -R_2 M_s \Delta V_s^n / M_{M2} \quad (4)$$

where ΔV_1^n and ΔV_2^n are the normal velocity changes to master nodes M_1 and M_2 during the n^{th} iteration; R_1 and R_2 are the fractions of momentum transferred from the slave node to the master nodes; M_s , M_{M1} , and M_{M2} are the masses at the slave node and the two master nodes; and ΔV_s^n is the normal velocity change to the slave node during the n^{th} iteration.

R_1 and R_2 are simply:

$$R_1 = \sqrt{(x_{sm} - x_2)^2 + (z_{sm} - z_2)^2} / \ell \quad (5)$$

$$R_2 = 1.0 - R_1 \quad (6)$$

where $x_{sm} = x_s + A\delta$ and $z_{sm} = z_s + B\delta$ are the coordinates of the slave node when projected back to the master segment.

Now, if the normal velocity of the slave node is equated to the normal velocity of the master segment (at the slave node location), and the relationships of Equations 3 and 4 are substituted, the normal velocity change to the slave node is:

$$\Delta V_s^{n+1} = \frac{\alpha(V_m^n - V_s^n)}{(1 + R_1^2 M_s / M_{M1} + R_2^2 M_s / M_{M2})} \quad (7)$$

where $\alpha = 1.0$ for an exact match and $V_m^n = V_2^n + R_1(V_1^n - V_2^n)$ is the master normal velocity at the projected slave node location.

In Equation 7, it is possible to substitute

$$\delta / \Delta t = (V_m^n - V_s^n) \quad (8)$$

which gives

$$\Delta V_s^{n+1} = \frac{\alpha(\delta / \Delta t)}{(1 + R_1^2 M_s / M_{M1} + R_2^2 M_s / M_{M2})} \quad (9)$$

where δ is the normal deflection from Equation 2 and Δt is the integration time increment. The use of Equations 8 and 9, instead of Equation 7, allows the algorithm to be self-correcting when the previous cycle does not provide a perfect velocity and position match.

As was noted previously, it is necessary to perform only a fraction of the velocity and position change during each iteration. This generally keeps the slave node in a crossed-over position for intermediate iterations, as shown in Figure 7, such that subsequent iterations can gradually move it toward the master segment. However, if the slave node moves free during an intermediate iteration, then it is not adjusted during the next iteration. The expression used for α is taken as

$$\alpha = \alpha_1 \alpha_2 \quad (10)$$

The first factor is based on the iteration number.

$$\alpha_1 = \frac{1}{\sqrt{N - n + 1}} \quad (11)$$

where N is the total number of iterations and n is the current iteration number. Note that $\alpha_1 = 1$ when $n = N$.

The second factor is based on the number of slave nodes that act on node N_s , when it (N_s) is a master node. This is expressed as

$$\alpha_2 = \frac{\sum R_m}{\sum R_m + \sum R_s} \quad (12)$$

where $\sum R_s$ is the sum of R_1 and R_2 (from Equations 5 and 6) that node s receives from other slave nodes when it (N_s) is acting as a master node. $\sum R_m$ is a similar sum on the master surface. This is required to keep nodes from being adjusted too much when they are both a slave and a master.

Note that if slave node N_s is never a master node, then $\sum R_s = 0$ and $\alpha_2 = 1.0$. This means that the basic algorithm can be used for the following three categories:

- Automatic
- Symmetric
- Nonsymmetric.

For automatic sliding all of the surfaces are automatically designated as slave nodes and master surfaces and the user does not need to specify the interfaces. This is the recommended option.

For symmetric sliding both sides of the interface are designated as master surfaces and slave nodes. This gives a symmetric interface that is not order dependent and is not dependent on which side is master or slave. This option provides the same results as the automatic option if all of the interacting surfaces are designated as master surfaces and slave nodes.

The nonsymmetric option is the traditional option where one side is the master surface and the other side is slave nodes. Generally, the master surface should have the denser and stronger material, an equal or greater node spacing than the slave nodes, and should not have a convex surface toward the slave nodes. This is the condition that exists for an SPH node, or a standard node whose elements have eroded, that interacts with a master surface.

After the slave velocity change has been determined from Equation 9, then the x and z velocity changes to the slave node are then transferred back into the system coordinates

$$\Delta \dot{u}_s^{n+1} = A \Delta V_s^{n+1} \quad (13)$$

$$\Delta \dot{v}_s^{n+1} = B \Delta V_s^{n+1} \quad (14)$$

The velocity changes $(\Delta \dot{u}_1^{n+1}, \Delta \dot{v}_1^{n+1}, \Delta \dot{u}_2^{n+1}, \Delta \dot{v}_2^{n+1})$ to the master nodes are performed in a manner similar to that of Equations 13 and 14, where ΔV_1^n , and ΔV_2^n are obtained by substituting ΔV_s^n into Equations 3 and 4.

After the velocity changes have been made to all nodes on the sliding interface, then the positions of the nodes must be updated in a manner that is consistent with the velocity changes. The updated nodal positions for all nodes on the sliding interface are

$$x_i^{n+1} = x_i^n + \sum \Delta \dot{u}_i^{n+1} \Delta t \quad (15)$$

$$z_i^{n+1} = z_i^n + \sum \Delta \dot{v}_i^{n+1} \Delta t \quad (16)$$

where $\sum \Delta \dot{u}_i^{n+1}$ and $\sum \Delta \dot{v}_i^{n+1}$ are the sum of all master and slave velocity changes made to node i. During this process there is no arbitrary movement of nodes, but rather total consistency between the velocity changes and position changes. Because the velocity and position changes are made after all the interface nodes are processed, there is no order dependence.

The application of the preceding algorithm, for all slave nodes, completes a single iteration. Subsequent iterations are performed in a similar manner. The number of iterations has little effect on the CPU time because the iterations require much less time than the searching.

3.4.3 Erosion

For many problems it is necessary to allow highly distorted material to be eroded away. This is done to simulate the actual phenomenon that occurs for erosion problems, and to delete the highly distorted elements from the computation. This algorithm is reported in References 15 and 16. It is only available for triangular elements.

The algorithm which follows should be applied only to problems where erosion is the primary mode of penetration. Figure 8 shows a master surface defined as a set of consecutively linked nodes (M1, M2 ... M15, M16). The slave nodes are always to the left of the master surface when moving from the beginning of the master surface (node M1) to the end of the master surface (node M16). The slave nodes can be randomly ordered and are not allowed to penetrate through the master surface.

The master surface is allowed to erode by totally failing triangular elements which have one, two or three sides on the master surface. Totally failed elements cannot develop any stresses or pressures; they essentially disappear except that mass is retained at the nodes.

The procedure begins by putting a flag on the nodes which are on the master surface. Then the three nodes of each element are examined to determine if the element is on the master surface. If two or three of the nodes on the specific element are flagged, then that element is on the master surface and it may be totally failed if it meets one of the failure criteria.

The five elements in Figure 8 (elements A, B, C, D, E) have two or three consecutive nodes on the master surface, and have one, two or three sides on the master surface. The following describes the criteria necessary to totally fail these elements and to redefine the master surface and the slave nodes.

- Element A has one side (M1–M2) on the master surface and one side (M1–N1) on the rotational axis of symmetry. If the equivalent plastic strain or volumetric strain of element A exceeds a specified eroding strain, the element is totally failed. The previous master surface (M1, M2, M3 ...) is then replaced by an updated master surface (N1, M2, M3 ...). Also, node M1 is designated as a slave node to the updated master surface.
- Element B has one side (M3–M4) on the master surface. If the equivalent plastic strain or volumetric strain of element B exceeds a specified eroding strain, the element is totally failed. The previous master surface (... M2, M3, M4, M5 ...) is then replaced by an updated master surface (... M2, M3, N2, M4, M5 ...) There are no new slave nodes to be designated for this case.
- Element C has two sides (M5–M6, M6–M7) on the master surface. If the equivalent plastic strain or volumetric strain of element C exceeds a specified eroding strain, the element is totally failed. The previous master surface (... M4, M5, M6, M7, M8 ...) is then replaced by an updated master surface (... M4, M5, M7, M8 ...). Also, node M6 is designated as a slave node to the updated master surface.

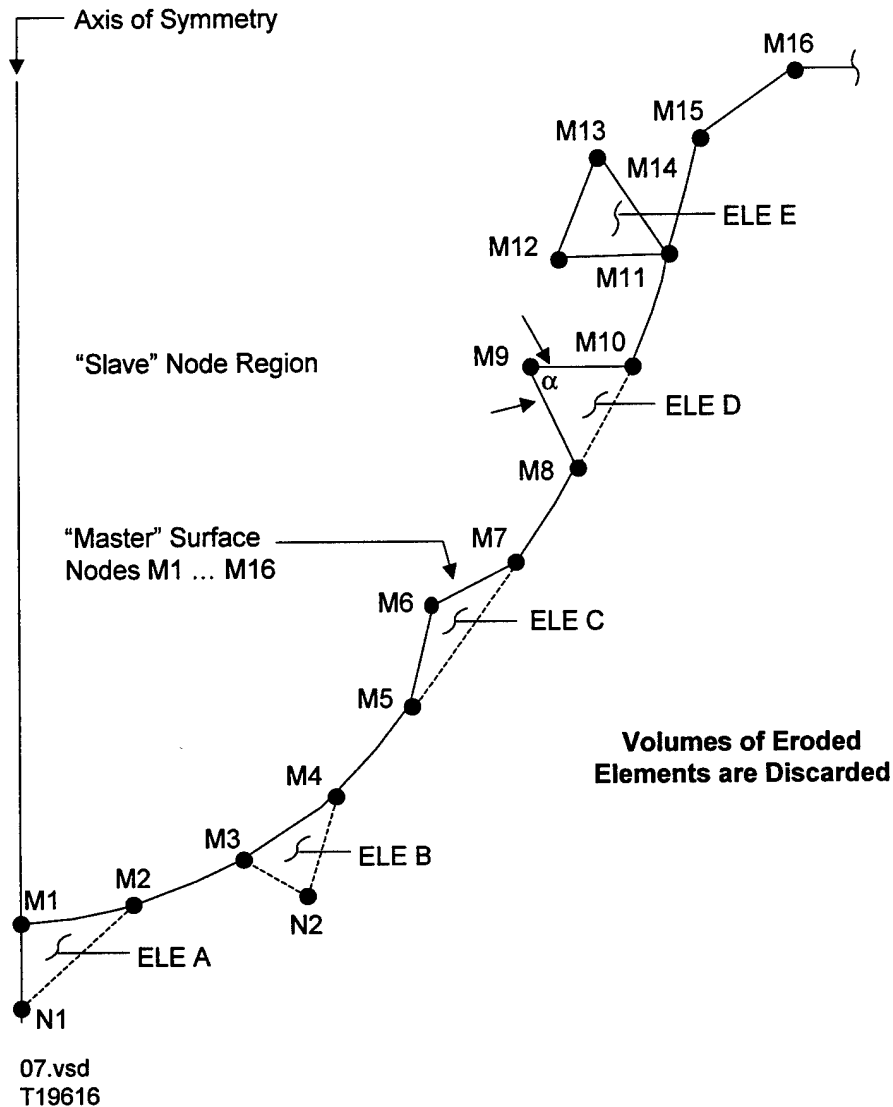


Figure 8. Description of the 2D Erosion Algorithm

- Element D also has two sides (M8–M9, M9–M10) on the master surface. If the angle α , defined by the two master sides, is less than a specified angle, the element is totally failed. The previous master surface (... M7, M8, M9, M10, M11 ...) is then replaced by an updated master surface (... M7, M8, M10, M11 ...). Also, node M9 is designated as a slave node to the updated master surface. This criterion tends to give a smoothed master surface, by eliminating intruding elements which have not exceeded the previous eroding strain criterion.
- Element E has three sides (M11–M12, M12–M13, M13–M14) on the master surface. This conditions exists because node M11 is identical to node M14. Under these

conditions, element E is always totally failed. The previous master surface (... M10, M11, M12, M13, M14, M15 ...) is replaced by an updated master surface (... M10, M11, M15 ...). Also, nodes M12 and M13 are designated as slave nodes to the updated master surface. This criterion also tends to give a smoothed master surface.

For axisymmetric geometry, when the master nodes are deleted from the master surface and designated as slave nodes, the outward radial velocity of the slave node is redefined to be a fraction of the axial velocity of that node. This is done to move the slave nodes initially on the axis of symmetry, away from the axis, as would be expected during an actual eroding penetration process.

To ensure that there is no cross-over of material between the two surfaces (such as a projectile and a target), a two-step approach (two separate sliding interfaces) is used with the standard (not automatic) sliding algorithm. For the first interface, all of the projectile nodes and the eroded target nodes are slave to the master surface in the target. For the second interface, all of the nodes in the center of the target, and the eroded projectile nodes, are slave to the master surface on the projectile. The eroded nodes are therefore restrained from passing through either the projectile or the target. The automatic sliding algorithm handles both surfaces automatically.

3.4.4 Triangular Elements

The axisymmetric triangular element algorithm follows the same sequence as the 1D Cartesian element. The element is geometrically defined by nodes i , j , and m (counterclockwise) as shown in Figure 4. This algorithm is reported in References 1, 3, and 11. The coordinates of node i are designated x_i and z_i , and the corresponding velocities are designated \dot{u}_i and \dot{v}_i (which are identical to \dot{x}_i and \dot{z}_i used previously).

The algorithm that follows is for a single triangular element. The arrangement of the elements, however, can have a significant effect on the computed response (References 16, 17, and 18). The crossed triangle arrangement (four triangles within a quad), in the lower portion of Figure 4, generally provides good accuracy. A slashed triangle arrangement (two triangles within a quad) can produce significant inaccuracies. There are also some mixed (average volumetric strain, or average pressure) algorithms that provide improved accuracy for various arrangements of elements (Reference 16).

The mass at node i , for an individual element, is

$$M_i = \alpha_i \rho_o V_o \quad (1)$$

where ρ_o is the initial density of the material and V_o is the initial volume of the element. The fraction of the element mass that is assigned to node i is

$$\alpha_i = \frac{1}{4} + \frac{1}{12} \left(\frac{x_i}{\bar{x}} \right) \quad (2)$$

where the average radial coordinate is

$$\bar{x} = (x_i + x_j + x_m) / 3 \quad (3)$$

The initial volume is

$$V_o = 2\pi\bar{x}A_o \quad (4)$$

where A_o is the initial cross-sectional area.

When element A is incorporated into an assemblage of elements, as shown in Figure 4, then the total mass at node i contains individual element masses from all elements that contain that node. The total mass at node i is

$$\bar{M}_i = \sum M_i \quad (5)$$

The volumetric strain and strain rate are obtained in the same manner as used for the 1D Cartesian element.

$$\epsilon_v = V / V_o - 1 \quad (6)$$

$$\dot{\epsilon}_v = (\epsilon_v^{t+\Delta t} - \epsilon_v^t) / \Delta t \quad (7)$$

In Equation 6, V and V_o are the current and initial element volumes; and in Equation 7, $\epsilon_v^{t+\Delta t}$ and ϵ_v^t are the volumetric strains at time $t + \Delta t$ and time t . The volumetric strains and strain rates

are based on the initial configuration, as opposed to the shear and deviator strain rates which are based on the current configuration.

The strain rates are obtained from the current geometry of the element and the velocities of the nodes. If it is assumed that the lines connecting the nodes remain straight, the displacements and velocities within each element must vary in a linear manner. Then the velocities within the element can be expressed as

$$\dot{u} = \alpha_1 + \alpha_2 x + \alpha_3 z \quad (8)$$

$$\dot{v} = \alpha_4 + \alpha_5 x + \alpha_6 z \quad (9)$$

where $\alpha_1 \dots \alpha_6$ are geometry and velocity-dependent constants. It is possible to solve for $\alpha_1, \alpha_2, \alpha_3$ by substituting the radial velocities and coordinates of nodes i, j, m into Equation 8. This gives three equations and three unknowns such that Equation 8 can be expressed in terms of the element geometry and nodal velocities.

$$\dot{u} = \frac{1}{2A} \left[(a_i + b_i x + c_i z) \dot{u}_i + (a_j + b_j x + c_j z) \dot{u}_j + (a_m + b_m x + c_m z) \dot{u}_m \right] \quad (10)$$

where $a_i = x_j z_m - x_m z_j$, $b_i = z_j - z_m$, $c_i = x_m - x_j$, and A is the cross-sectional area of the element in the x - z plane. The axial velocities are identical to Equation 10 except the radial velocities are replaced by the axial velocities. Another geometry constant for triangular elements is the minimum altitude of the triangle, h . This is used for the integration time increment in Equation 7 of subsection 3.4.1.

After the velocities are obtained, it is possible to determine the normal strain rates $(\dot{\epsilon}_x, \dot{\epsilon}_z, \dot{\epsilon}_\theta)$, the shear strain rate $(\dot{\gamma}_{xz})$ and the localized rotational spin rate of the element in the x - z plane (ω_{xz}) .

$$\dot{\epsilon}_x = \frac{\partial \dot{u}}{\partial x} = \frac{1}{2A} [b_i \dot{u}_i + b_j \dot{u}_j + b_m \dot{u}_m] \quad (11)$$

$$\dot{\epsilon}_z = \frac{\partial \dot{v}}{\partial z} = \frac{1}{2A} [c_i \dot{v}_i + c_j \dot{v}_j + c_m \dot{v}_m] \quad (12)$$

$$\dot{\epsilon}_\theta = \frac{\bar{u}}{\bar{x}} = (\dot{u}_i + \dot{u}_j + \dot{u}_m) / (x_i + x_j + x_m) \quad (13)$$

$$\dot{\gamma}_{xz} = \frac{\partial \dot{u}}{\partial z} + \frac{\partial \dot{v}}{\partial x} \quad (14)$$

$$\omega_{xz} = \frac{1}{2} \left(\frac{\partial \dot{v}}{\partial x} - \frac{\partial \dot{u}}{\partial z} \right) \quad (15)$$

It can be seen that Equations 11, 12, 14, and 15 are derivatives of linear functions and are therefore constant within the element. Equation 13 involves averages of the nodal velocities and the three radii (\bar{u} and \bar{x}), so it is not necessarily constant.

The other two shear strain rate components are zero ($\dot{\gamma}_{x\theta} = \dot{\gamma}_{z\theta} = 0$) for axisymmetric geometry with no spin about the z axis of rotation. These become nonzero when spin is included, and this is described in subsection 3.5.

The equivalent strain rate ($\bar{\dot{\epsilon}}$) and deviator strain rates ($\dot{\epsilon}_x, \dot{\epsilon}_z, \dot{\epsilon}_\theta$) are determined in an identical manner as shown previously for 1D geometry.

$$\bar{\dot{\epsilon}} = \sqrt{\frac{2}{9} \left[(\dot{\epsilon}_x - \dot{\epsilon}_z)^2 + (\dot{\epsilon}_x - \dot{\epsilon}_\theta)^2 + (\dot{\epsilon}_z - \dot{\epsilon}_\theta)^2 + \frac{3}{2} (\dot{\gamma}_{xz}^2 + \dot{\gamma}_{x\theta}^2 + \dot{\gamma}_{z\theta}^2) \right]} \quad (16)$$

$$\dot{\epsilon}_x = \dot{\epsilon}_x - \dot{\epsilon}_{ave} \quad (17)$$

$$\dot{\epsilon}_z = \dot{\epsilon}_z - \dot{\epsilon}_{ave} \quad (18)$$

$$\dot{\epsilon}_\theta = \dot{\epsilon}_\theta - \dot{\epsilon}_{ave} \quad (19)$$

where $\dot{\epsilon}_{ave} = (\dot{\epsilon}_x + \dot{\epsilon}_z + \dot{\epsilon}_\theta) / 3$. Note that the sum of the deviator strain rates is $\dot{\epsilon}_x + \dot{\epsilon}_z + \dot{\epsilon}_\theta = 0$.

The stresses in the elements are determined from the strains, strain rates, temperatures, pressures, internal energies, and material constants. This is identical to the 1D algorithm, except that a shear stress is also present. The three normal stresses are generally expressed as

$$\sigma_x = s_x - (P + Q) \quad (20)$$

$$\sigma_z = s_z - (P + Q) \quad (21)$$

$$\sigma_\theta = s_\theta - (P + Q) \quad (22)$$

where s_x , s_z , and s_θ are the normal deviator stresses, P is the hydrostatic pressure and Q is the artificial viscosity. These are described in detail in Section 6. The nonzero shear stress is τ_{xz} and the two zero shear stresses for this geometry are $\tau_{x\theta}$ and $\tau_{z\theta}$.

Trial values of the deviator stresses at time $= t + \Delta t$ are

$$s_x^{t+\Delta t} = s_x^t + 2G\dot{\epsilon}_x \Delta t - 2\tau_{xz}^t \omega_{xz} \Delta t \quad (23)$$

$$s_z^{t+\Delta t} = s_z^t + 2G\dot{\epsilon}_z \Delta t + 2\tau_{xz}^t \omega_{xz} \Delta t \quad (24)$$

$$s_\theta^{t+\Delta t} = s_\theta^t + 2G\dot{\epsilon}_\theta \Delta t \quad (25)$$

In Equation 23 the first term (s_x^t) is the radial stress at the previous time and the second term ($2G\dot{\epsilon}_x \Delta t$) is the incremental stress due to the incremental strain ($\dot{\epsilon}_x \Delta t$) during that time increment, where G is the elastic shear modulus. The third term ($2\tau_{xz}^t \omega_{xz} \Delta t$) is due to shear stresses from the previous time increment, which now act as normal stresses due to the new orientation of the element caused by an incremental rotation ($\omega_{xz} \Delta t$) during the time increment. The axial stress has the same form as the radial stress, and the tangential (hoop) stress is also similar except there is no contribution from rotated shear stresses.

The trial value of the shear stress is formulated in similar manner.

$$\tau_{xz}^{t+\Delta t} = \tau_{xz}^t + G\dot{\gamma}_{xz} \Delta t + (\sigma_x^t - \sigma_z^t) \omega_{xz} \Delta t \quad (26)$$

Equations 23–26 assume an elastic response of the material. If the strength of the material is exceeded, then plastic flow (or fracture) will occur. The Von Mises yield criterion is used to determine an equivalent stress, $\bar{\sigma}$, that can be compared to the uniaxial tensile (or compressive) strength of the material. The general form of the equivalent stress is

$$\bar{\sigma} = \sqrt{\frac{1}{2} \left[(\sigma_x - \sigma_z)^2 + (\sigma_x - \sigma_\theta)^2 + (\sigma_z - \sigma_\theta)^2 + 6(\tau_{xz}^2 + \tau_{x\theta}^2 + \tau_{z\theta}^2) \right]} \quad (27)$$

Using deviator stresses (instead of total stresses), Equation 27 can be rewritten as

$$\bar{\sigma} = \sqrt{\frac{3}{2} (s_x^2 + s_z^2 + s_\theta^2) + 3(\tau_{xz}^2 + \tau_{x\theta}^2 + \tau_{z\theta}^2)} \quad (28)$$

If $\bar{\sigma}$ is not greater than the equivalent tensile strength of the material, σ , the final deviator and shear stresses are as given in Equations 23–26. If $\bar{\sigma}$ is greater than σ , then the stresses in Equations 23–26 are multiplied by the factor $(\sigma / \bar{\sigma})$. When the reduced deviator and shear stresses are put into Equation 28, the result is always $\bar{\sigma} = \sigma$. This is known as the radial return algorithm. The various material strength models for σ are presented in Section 6.

During plastic flow, it is sometimes necessary to determine the equivalent plastic strain for strain hardening effects on the strength of the material or to determine if the material has failed. The first step in this process is to adjust the total strain rates to plastic strain rates by subtracting out the elastic portion of the strain rates.

$$\dot{\epsilon}_x^p = \dot{\epsilon}_x - (s_x^{t+\Delta t} - s_x^t + 2\omega_{xz}\tau_{xz}^t\Delta t) / 2G\Delta t \quad (29)$$

$$\dot{\epsilon}_z^p = \dot{\epsilon}_z - (s_z^{t+\Delta t} - s_z^t - 2\omega_{xz}\tau_{xz}^t\Delta t) / 2G\Delta t \quad (30)$$

$$\dot{\epsilon}_\theta^p = \dot{\epsilon}_\theta - (s_\theta^{t+\Delta t} - s_\theta^t) / 2G\Delta t \quad (31)$$

$$\dot{\gamma}_{xz}^p = \dot{\gamma}_{xz} - [\tau_{xz}^{t+\Delta t} - \tau_{xz}^t - \omega_{xz}(s_x^t - s_z^t)\Delta t] / G\Delta t \quad (32)$$

Again, the other two plastic strain rates ($\dot{\gamma}_{x\theta}^p$ and $\dot{\gamma}_{z\theta}^p$) are zero for this geometry. The general expression for the equivalent plastic strain rate is

$$\bar{\dot{\epsilon}}_p = \sqrt{\frac{2}{9} \left[(\dot{\epsilon}_x^p - \dot{\epsilon}_z^p)^2 + (\dot{\epsilon}_x^p - \dot{\epsilon}_\theta^p)^2 + (\dot{\epsilon}_z^p - \dot{\epsilon}_\theta^p)^2 + 3(\dot{\gamma}_{xz}^p{}^2 + \dot{\gamma}_{x\theta}^p{}^2 + \dot{\gamma}_{z\theta}^p{}^2) \right]} \quad (33)$$

The equivalent plastic strain, $\bar{\epsilon}_p$, is then obtained by integrating $\dot{\bar{\epsilon}}_p$ with respect to time.

$$\bar{\epsilon}_p^{t+\Delta t} = \bar{\epsilon}_p^t + \dot{\bar{\epsilon}}_p \Delta t \quad (34)$$

After the element stresses are obtained, it is necessary to determine concentrated forces to act on the concentrated mass at the nodes. This is done by obtaining the concentrated forces which are statically equivalent to the distributed stresses in the elements. The radial and axial forces acting on node i of an element are

$$F_x^i = -\pi \bar{x} [b_i \sigma_x + c_i \tau_{xz}] - \frac{2}{3} \pi A \sigma_\theta \quad (35)$$

$$F_z^i = -\pi \bar{x} [c_i \sigma_z + b_i \tau_{xz}] \quad (36)$$

Note that $F_x^i + F_x^j + F_x^m \equiv 0$ for each element, and this ensures equilibrium for the system. This results in conservation of momentum if there are no external forces or restraints. The final net forces on node i are

$$\bar{F}_x^i = \sum F_x^i \quad (37)$$

$$\bar{F}_z^i = \sum F_z^i \quad (38)$$

It is also possible to add external forces through applied pressures.

The heat conduction algorithm can be obtained straightforwardly from the 1D heat conduction algorithm (subsection 3.1.3) and the strain rate equations in this subsection. It is reported in Reference 7. Substituting temperatures for velocities in Equation 10 gives

$$T = \frac{1}{2A} [(a_i + b_i x + c_i z)T_i + (a_j + b_j x + c_j z)T_j + (a_m + b_m x + c_m z)T_m] \quad (39)$$

The instantaneous heat flows in the x and z directions can then be obtained from

$$q_x = -k \frac{\partial T}{\partial x} = -k (b_i T_i + b_j T_j + b_m T_m) / 2A \quad (40)$$

$$q_z = -k \frac{\partial T}{\partial z} = -k(c_i T_i + c_j T_j + c_m T_m) / 2A \quad (41)$$

The incremental increase in thermal energy at the nodes can be obtained by integrating the heat flow with respect to area and time.

$$\Delta Q_i = \pi \bar{x} (q_x b_i + q_z c_i) \Delta t + \alpha_i \Delta Q_e \quad (42)$$

$$\Delta Q_j = \pi \bar{x} (q_x b_j + q_z c_j) \Delta t + \alpha_j \Delta Q_e \quad (43)$$

$$\Delta Q_m = \pi \bar{x} (q_x b_m + q_z c_m) \Delta t + \alpha_m \Delta Q_e \quad (44)$$

Note that the internal energy generated in the element during the previous time increment, ΔQ_e , is distributed to the nodes through α_i , α_j , α_m as defined by Equation 2. The energy is distributed to the nodes in the same manner as the mass is distributed.

After Equations 39–44 have been applied to all elements, the updated temperatures of the nodes have the form

$$T_i^{t+\Delta t} = T_i^t + \sum \Delta Q_i / \bar{M}_i c_{pi} \quad (45)$$

where $T_i^{t+\Delta t}$ and T_i^t are the temperatures of the nodes at times $t+\Delta t$ and t , $\sum \Delta Q_i$ is the sum of the incremental heat contributed by all elements that contain node i , \bar{M}_i is the total mass of node i , and c_{pi} is the specific heat of node i .

The internal energy in an element can be used to compute element pressures. To account for the flow of internal energy through the grid, the element temperature is assumed to be the average of the nodal temperatures.

$$\bar{T} = (T_i + T_j + T_m) / 3 \quad (46)$$

The internal energy (per initial volume) is given by

$$E_s = (\bar{T} - T_o) \rho_o c_p \quad (47)$$

where T_o is the initial temperature (where $E_s = 0$), ρ_o is the initial density and c_p is the specific heat of the element material.

The integration time increment must also be bounded to ensure that the computations remain stable for heat conduction (References 6 and 7). The heat conduction portion requires

$$\Delta t \leq \rho c_p h_{\min}^2 / 4k \quad (48)$$

where h_{\min} is the minimum altitude of the element and the other terms recently have been defined. This is analogous to the time increment restriction for wave propagation in Equation 4 of subsection 3.4.1. Unless h_{\min} is very small, the wave propagation restriction is much more severe than the heat conduction restriction.

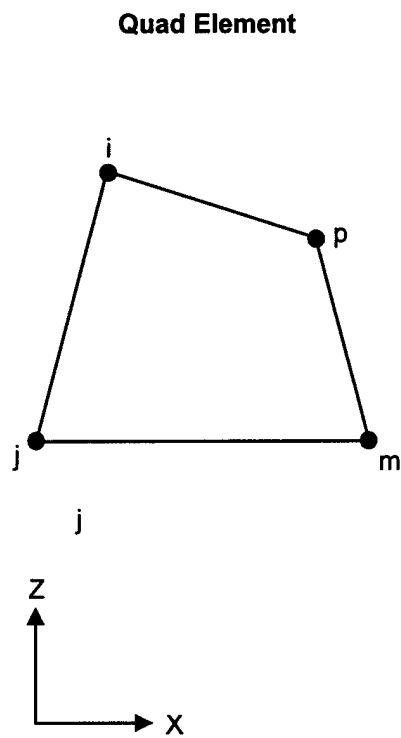
3.4.5 Quad Elements

The quad element algorithm is summarized in Figure 9. It is simply an average of the components of two quads composed of two triangles each.

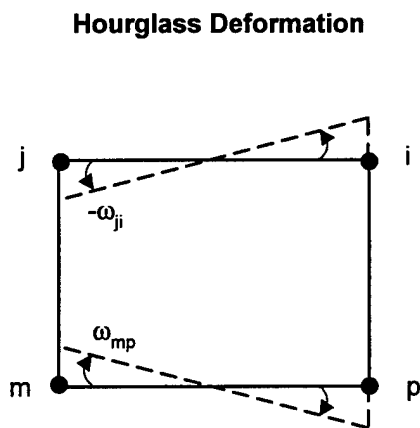
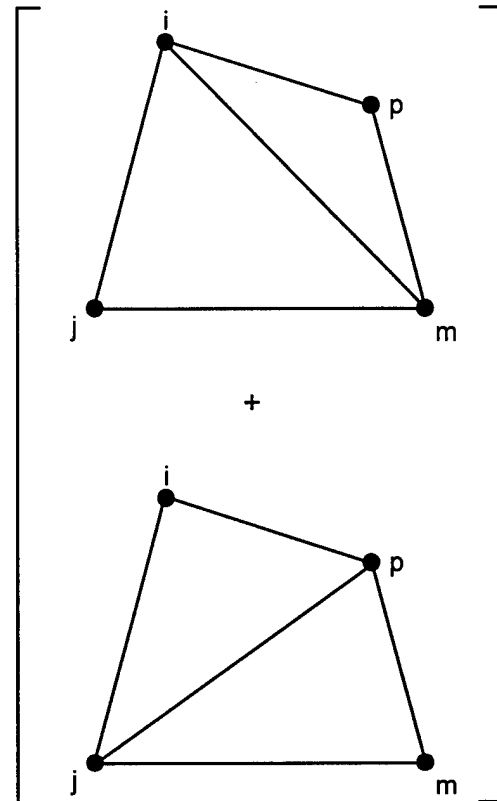
The mass at node i is half the mass of node i from triangular elements ijm , imp , and ijp .

$$M_i = \rho_o [\alpha_i^{ijm} V_o^{ijm} + \alpha_i^{imp} V_o^{imp} + \alpha_i^{ijp} V_o^{ijp}] / 2 \quad (1)$$

where ρ_o is the initial density of the material in the quad element, α_i^{ijm} is the fraction of the mass of triangle ijm that is distributed to node i , and V_o^{ijm} is the initial volume of triangle ijm . Refer to Equations 1–4 in subsection 3.4.4.



$$= \frac{1}{2}$$



20.vsd
T19616

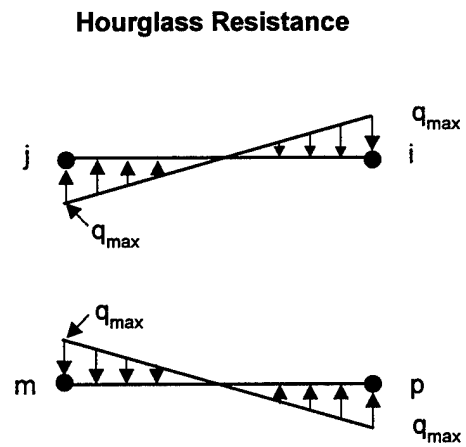


Figure 9. Description of the 2D Quad Element

The strain rate in the x direction is

$$\dot{\epsilon}_x = \frac{1}{2A} \left[z_{jp} (\dot{u}_i - \dot{u}_m) + z_{mi} (\dot{u}_j - \dot{u}_p) \right] \quad (2)$$

where A is the area of the quad element, $z_{jm} = z_j - z_m$, $z_{mi} = z_m - z_i$, and $\dot{u}_i, \dot{u}_j, \dot{u}_m, \dot{u}_p$ are the x velocities of the nodes. This result is obtained by determining the x strain rates of triangles ijm and imp (per Equation 11 of subsection 3.4.4) and then weighting the individual triangle strain rates by the areas of the individual triangles. The same result is obtained by considering the alternate arrangement of triangles ijp and jmp.

Using this same approach, the other strain rates and rotational rate can be determined.

$$\dot{\epsilon}_z = \frac{1}{2A} \left[x_{jp} (\dot{v}_m - \dot{v}_i) + x_{mi} (\dot{v}_p - \dot{v}_j) \right] \quad (3)$$

$$\dot{\gamma}_{xz} = \frac{1}{2A} \left[x_{jp} (\dot{u}_m - \dot{u}_i) + x_{mi} (\dot{u}_p - \dot{u}_j) + z_{jp} (\dot{v}_i - \dot{v}_j) + z_{mi} (\dot{v}_j - \dot{v}_p) \right] \quad (4)$$

$$\dot{\epsilon}_\theta = (\dot{u}_i + \dot{u}_j + \dot{u}_m + \dot{u}_p) / (x_i + x_j + x_m + x_p) \quad (5)$$

$$\omega_{xz} = \frac{1}{4A} \left[z_{jp} (\dot{v}_i - \dot{v}_m) + z_{mi} (\dot{v}_j - \dot{v}_p) - x_{jp} (\dot{u}_m - \dot{u}_i) - x_{mi} (\dot{u}_p - \dot{u}_j) \right] \quad (6)$$

The forces are determined in the same manner as the masses. The forces at node i are half the forces at node i from triangles ijm, imp, and ijp.

$$F_x^i = -\frac{\pi}{2} \left[\bar{x}_{ijm} (z_{jm} \sigma_x + x_{mj} \tau_{xz}) + \bar{x}_{imp} (z_{mp} \sigma_x + x_{pm} \tau_{xz}) + \bar{x}_{ijp} (z_{jp} \sigma_x + x_{pj} \tau_{xz}) - \sigma_\theta A \right] \quad (7)$$

$$F_z^i = -\frac{\pi}{2} \left[\bar{x}_{ijm} (x_{mj} \sigma_z + z_{jm} \tau_{xz}) + \bar{x}_{imp} (x_{pm} \sigma_z + z_{mp} \tau_{xz}) + \bar{x}_{ijp} (x_{pj} \sigma_z + z_{jp} \tau_{xz}) \right] \quad (8)$$

where \bar{x}_{ijm} is the average x coordinate of triangle ijm, and the other terms are as defined previously.

There is an additional force required for quad elements that is not required for triangular elements. The lower half of Figure 9 shows how hourglassing can occur in a quad element. This mode of deformation can occur without inducing any normal or shear strain rates. It is detected by evaluating the difference in the rotational rates of the opposite sides of the quad.

The rotational rates of the four sides are

$$\omega_{mp} = \left[(\dot{v}_m - \dot{v}_p)x_{pm} + (\dot{u}_p - \dot{u}_m)z_{pm} \right] \ell_{pm} \quad (9)$$

$$\omega_{pi} = \left[(\dot{v}_p - \dot{v}_i)x_{pi} + (\dot{u}_i - \dot{u}_p)z_{pi} \right] \ell_{pi} \quad (10)$$

$$\omega_{ji} = \left[(\dot{v}_j - \dot{v}_i)x_{ij} + (\dot{u}_i - \dot{u}_j)z_{ij} \right] \ell_{ji} \quad (11)$$

$$\omega_{mj} = \left[(\dot{v}_m - \dot{v}_j)x_{jm} + (\dot{u}_j - \dot{u}_m)z_{jm} \right] \ell_{mj} \quad (12)$$

where ℓ_{ij} is the length of side ij and the other terms are as defined previously.

A viscous stress is used to resist the hourglassing (Reference 19) as shown in Figure 9. The stress varies from $\pm q_{\max}$ on each of the opposite sides. For sides ij and mp

$$q_{\max}^{ij-mp} = C_H c_s \rho h_{\min} (\omega_{mp} + \omega_{ji}) \quad (13)$$

where C_H is an input hourglass viscosity coefficient, c_s is the second velocity of the material, ρ is the density of the material and h_{\min} is a characteristic minimum length (area/largest diagonal).

For the other two sides

$$q_{\max}^{jm-pi} = C_H c_s \rho h_{\min} (\omega_{pi} + \omega_{mj}) \quad (14)$$

These stresses are then converted to equivalent nodal forces using the form

$$F_{x(hg)}^i = -\pi \bar{x} (q_{\max}^{ij-mp} z_{ij} + q_{\max}^{jm-pi} z_{pi}) / 3 \quad (15)$$

$$F_{z(hg)}^i = -\pi \bar{x} (q_{\max}^{ij-mp} x_{ij} + q_{\max}^{jm-pi} x_{pi}) / 3 \quad (16)$$

Both the hourglass forces and the internal stress forces of Equations 7 and 8 are then added to the appropriate nodes.

The heat conduction algorithm for quad elements is derived from the triangular element algorithm in a similar manner. The heat flow in the two directions is

$$q_x = k \frac{\partial T}{\partial x} = -k \left[z_{jp} (T_i - T_m) + z_{mi} (T_j - T_p) \right] / 2A \quad (17)$$

$$q_z = k \frac{\partial T}{\partial z} = -k \left[x_{jp} (T_m - T_i) + x_{mi} (T_p - T_j) \right] / 2A \quad (18)$$

and the incremental increase in thermal energy at node i is

$$\Delta Q_i = \frac{\pi}{2} \left[\bar{x}_{ijm} (z_{jm} q_x + x_{mj} q_z) + \bar{x}_{imp} (z_{mp} q_x + x_{pm} q_z) + \bar{x}_{ijp} (z_{jp} q_x + x_{pj} q_z) \right] \Delta t + \alpha_i \Delta Q_e \quad (19)$$

where $\bar{x}_{ijm}, z_{jm}, x_{mj}$, etc., are as defined in Equation 7, Δt is the integration time increment, ΔQ_e is the internal energy generated by the element during the previous time increment, and α_i is the fraction of ΔQ_e distributed to node i. The temperature and internal energy update are similar to those described for the triangular elements in subsection 3.4.4.

3.4.6 Bending Shell Elements

A 2D axisymmetric bending shell element is shown in Figures 10 and 11. The concepts for this element are provided in Reference 20. The approach taken is to consider the bending shell to be represented by three or five layered elements that share the same two nodes. This subsection provides the algorithm for the three layer shell, and the five layer algorithm is similar.

Bending moments about the two end nodes are induced by allowing the in-plane stresses in the outer layers to be different from one another. This is accomplished by allowing the in-plane strain rates in the outer layers to be different from one another. These strain rates are dependent on the nodal velocities, as well as the nodal rotational rates and the offset from the center layer.

This algorithm is valid for small volumetric strains and thin shells (where the thickness is much less than the length). These assumptions lead to approximately equal lengths ($L_1 \approx L_2 \approx L_3 \approx L$),

thicknesses $(T_1 \approx T_2 \approx T_3 \approx T/3)$, and offsets $(H_1 \approx H_2 \approx H \approx T/3)$ for each of the three layers. Note that T is the total thickness of all three layers and that T_1 , T_2 , and T_3 are the thicknesses of the individual layers.

The shell element at the top of Figure 10 is in a general orientation at an angle ϕ from the x axis. The algorithm is performed in the $x' - z'$ coordinate system as shown in the lower portions of Figure 10.

The masses at nodes i and j are

$$M_i = \alpha_i \rho_o V_o \quad (1)$$

$$M_j = \alpha_j \rho_o V_o \quad (2)$$

where ρ_o is the initial density of the element and V_o is the initial volume of the composite element (all three layers). The fractions of the initial mass that are assigned to nodes i and j are

$$\alpha_i = (2x_i + x_j) / 3(x_i + x_j) \quad (3)$$

$$\alpha_j = 1.0 - \alpha_i \quad (4)$$

The initial volume is

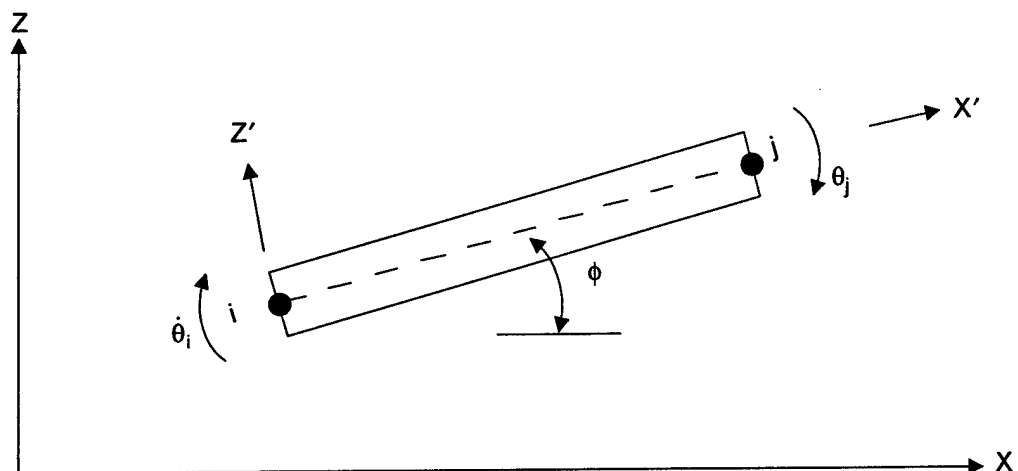
$$V_o = 2\pi \bar{x} A_o = 2\pi \bar{x} L_o T_o \quad (5)$$

where \bar{x} is the average initial x coordinate of nodes i and j , A_o is the initial area, L_o is the initial length, and T_o is the initial total thickness.

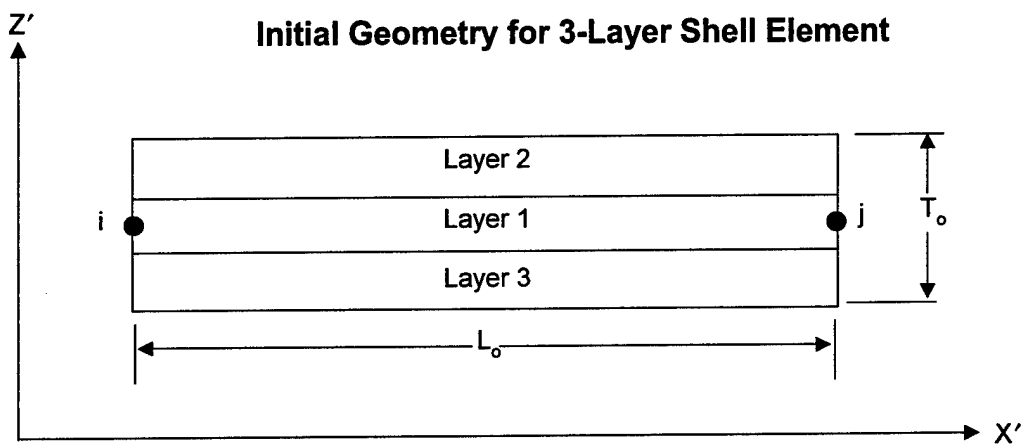
The mass moment of rotational inertia is required, and it is expressed as

$$I_y^i = M_i (L^2 + T^2) / 24 \quad (6)$$

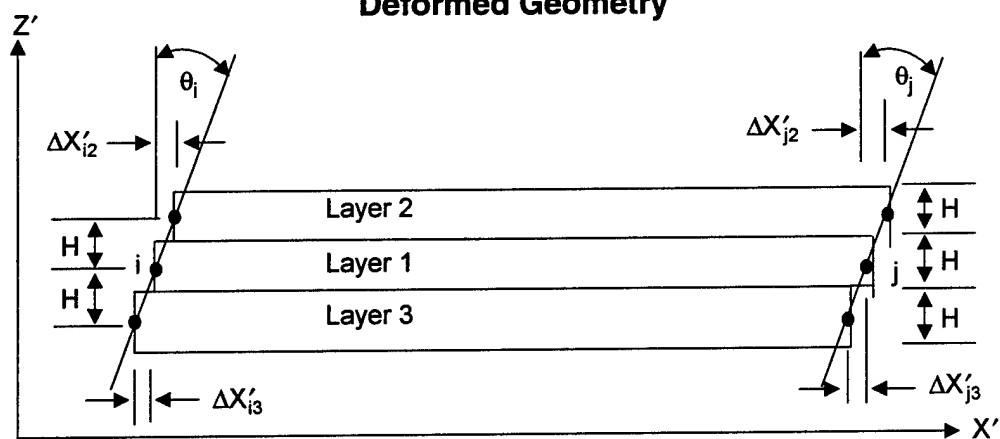
Note that the current (not initial) values of the length and thickness (L and T) are used, and this requires I_y^i to be updated every cycle.



Initial Geometry for 3-Layer Shell Element



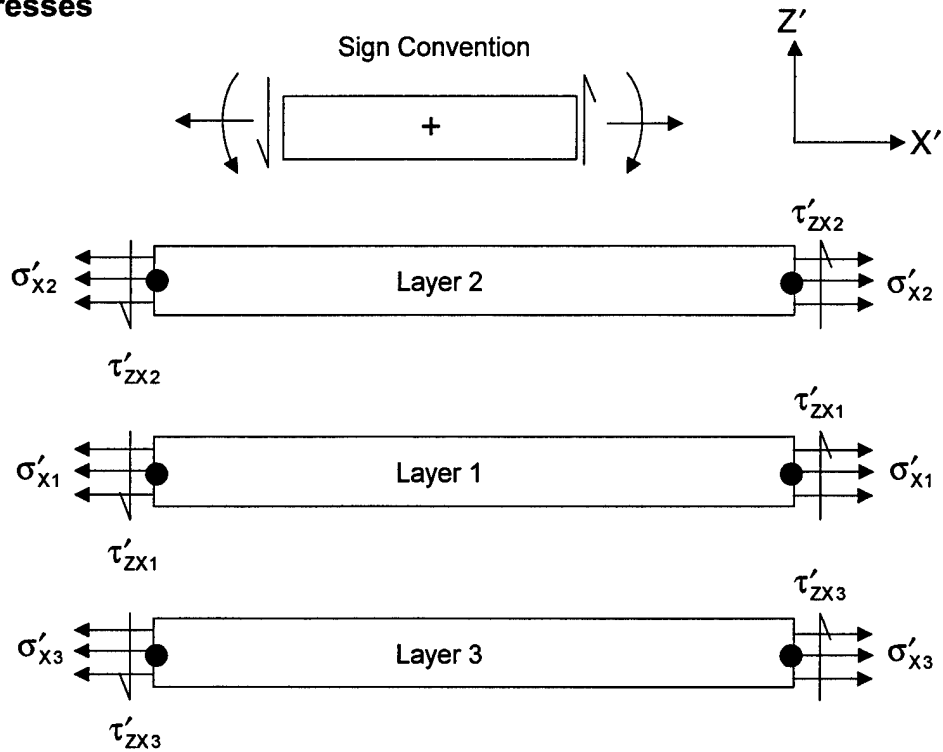
Deformed Geometry



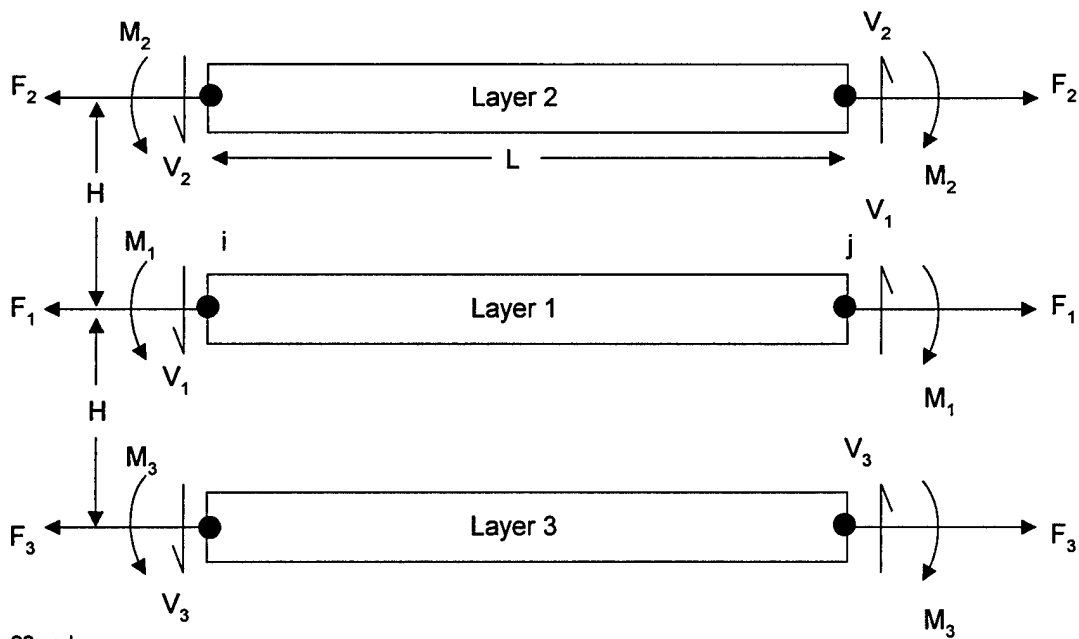
21.vsd
T19616

Figure 10. Description of the 2D Bending Shell Element

Stresses



Forces and Moments



22.vsd
T19616

Figure 11. Stresses, Forces, and Moments for the 2D Bending Shell Element

The offset of the center of layer 2 (above the center of layer 1), as well as the offset of layer 3 below layer 1, is expressed as

$$H = V_o / 6\pi\bar{x}L \quad (7)$$

where V_o is the initial volume of the composite element, \bar{x} is the average x coordinate of the nodes, and L is the current length of the element (distance between nodes). This is a good approximation if the volumetric strains are small and the offsets are small ($\Delta x'_{i2}$, $\Delta x'_{j2}$, $\Delta x'_{i3}$, $\Delta x'_{j3}$ in Figure 10). H is also the thickness of each of the layers.

The rigid body rate of rotation (clockwise positive) of the composite element is

$$\dot{\phi} = (\dot{z}'_i - \dot{z}'_j) / L \quad (8)$$

where the in-plane (\dot{x}'_i and \dot{x}'_j) and normal (\dot{z}'_i and \dot{z}'_j) velocity components of the center layer are

$$\dot{x}'_i = \dot{z}_i \sin \phi + \dot{x}_i \cos \phi \quad (9)$$

$$\dot{x}'_j = \dot{z}_j \sin \phi + \dot{x}_j \cos \phi \quad (10)$$

$$\dot{z}'_i = \dot{z}_i \cos \phi - \dot{x}_i \sin \phi \quad (11)$$

$$\dot{z}'_j = \dot{z}_j \cos \phi - \dot{x}_j \sin \phi \quad (12)$$

The nodal velocities at nodes i and j are \dot{x}_i , \dot{z}_i , \dot{x}_j , and \dot{z}_j .

The in-plane velocities of the top and bottom layers can now be determined.

$$\dot{x}'_{i2} = \dot{x}'_i + H(\dot{\theta}_i + \dot{\phi}) \quad (13)$$

$$\dot{x}'_{i3} = \dot{x}'_i - H(\dot{\theta}_i + \dot{\phi}) \quad (14)$$

$$\dot{x}'_{j2} = \dot{x}'_j + H(\dot{\theta}_j + \dot{\phi}) \quad (15)$$

$$\dot{x}'_{j3} = \dot{x}'_j - H(\dot{\theta}_j + \dot{\phi}) \quad (16)$$

where the in-plane (x') velocities at node i are \dot{x}'_i , \dot{x}'_{i2} , and \dot{x}'_{i3} , the rotational velocity of node i is $\dot{\theta}_i$, and the rigid body rotational velocity of the element is $\dot{\phi}$. For nomenclature consistency, the nodal x velocities will be designated \dot{u}'_i , \dot{u}'_{i2} , and \dot{u}'_{i3} , and the z velocities will be designated \dot{v}'_i , \dot{v}'_{i2} , and \dot{v}'_{i3} . The velocities at node j have similar notations.

The normal velocities of the three layers are equal at node i ($\dot{v}'_i = \dot{v}'_{i2} = \dot{v}'_{i3}$) and at node j ($\dot{v}'_j = \dot{v}'_{j2} = \dot{v}'_{j3}$).

The in-plane strain rates in the x' direction are

$$\dot{\epsilon}'_{x1} = (\dot{u}'_j - \dot{u}'_i) / L \quad (17)$$

$$\dot{\epsilon}'_{x2} = (\dot{u}'_{j2} - \dot{u}'_{i2}) / L \quad (18)$$

$$\dot{\epsilon}'_{x3} = (\dot{u}'_{j3} - \dot{u}'_{i3}) / L \quad (19)$$

The hoop strain rates are

$$\dot{\epsilon}_{\theta 1} = \bar{\dot{u}}_1 / \bar{x} \quad (20)$$

$$\dot{\epsilon}_{\theta 2} = \bar{\dot{u}}_2 / \bar{x} \quad (21)$$

$$\dot{\epsilon}_{\theta 3} = \bar{\dot{u}}_3 / \bar{x} \quad (22)$$

where $\bar{\dot{u}}_1$, $\bar{\dot{u}}_2$, $\bar{\dot{u}}_3$ are the average x velocities of the two ends of the three shell layers, and \bar{x} is the average x coordinate of the composite element.

The shear strain rates for all three layers are identical

$$\dot{\gamma}'_{xz1} = \frac{1}{2} \left(\frac{\partial \dot{v}'}{\partial x'} + \dot{\theta}_y \right) = \frac{1}{2} \left(\frac{\dot{v}'_j - \dot{v}'_i}{L} + \frac{\dot{\theta}_i + \dot{\theta}_j}{2} \right) \quad (23)$$

$$\dot{\gamma}'_{xz2} = \dot{\gamma}_{xz1} \quad (24)$$

$$\dot{\gamma}'_{xz3} = \dot{\gamma}_{xz1} \quad (25)$$

where $\dot{v}'_i = \dot{z}'_i$ and $\dot{v}'_j = \dot{z}'_j$ are from Equations 11 and 12.

After the in-plane strain rate, $\dot{\epsilon}'_x$, the hoop strain rate $\dot{\epsilon}_\theta$, and the shear strain rate, $\dot{\gamma}'_{xz}$, have been determined, the through-thickness strain rate, $\dot{\epsilon}'_z$, must be determined. The plane stress condition of the shell requires the through-thickness stress to be $\sigma'_z = 0$. Therefore, it is necessary to iterate to find the strain rate that produces the correct stress ($\sigma'_z = 0$).

The iteration algorithm is shown in Figure 12. The initial through-thickness strain rate and stress [$\dot{\epsilon}'_z(1)$ and $\sigma'_z(1)$] come from assuming incompressible flow during the previous cycle. The two in-plane normal strain rates ($\dot{\epsilon}'_x$ and $\dot{\epsilon}_\theta$) are obtained in the standard manner, and then the through-thickness strain rate is set to

$$\dot{\epsilon}'_z(1) = -(\dot{\epsilon}'_x + \dot{\epsilon}_\theta) \quad (26)$$

which results in incompressible flow for the cycle ($\dot{\epsilon}'_x + \dot{\epsilon}'_z + \dot{\epsilon}_\theta = 0$).

From the current strain rates, the previous stresses, and the previous volumetric strain, the net through-thickness stress is

$$\sigma'_z = s'_z - P \quad (27)$$

where s'_z is the deviator stress, determined from the current strain rates and the previous stresses. The pressure is determined from $P = -K\varepsilon_v$ where K is the bulk modulus and ε_v is the previous volumetric strain. The strain rate and stress for the incompressible condition are represented by $\dot{\epsilon}'_z(1)$ and $\sigma'_z(1)$ in Figure 12.

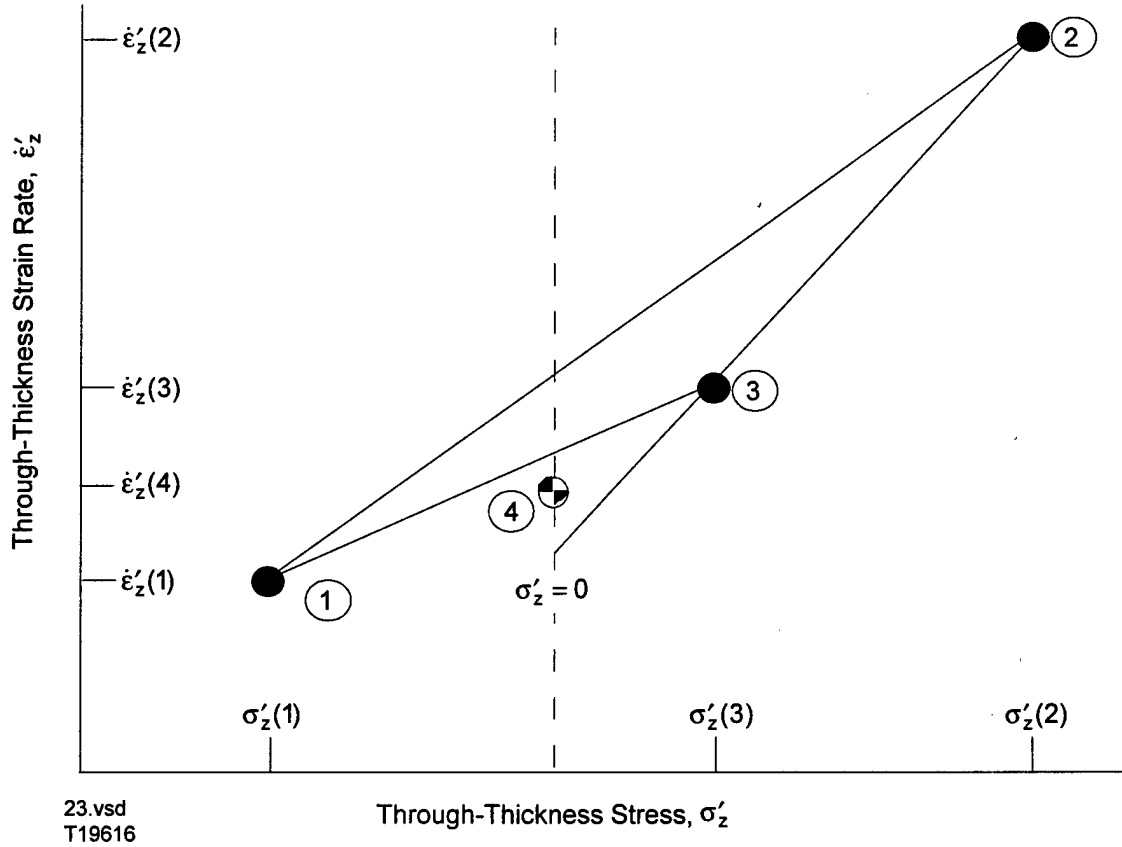


Figure 12. Normal Stress Iteration Algorithm for 2D and 3D Bending Shells, and Plane Stress Geometry

The next step is to determine $\dot{\epsilon}'_z(2)$ and $\sigma'_z(2)$, as shown in Figure 12. This condition is assumed to be that which would result from a compressible elastic strain rate of

$$\dot{\epsilon}'_z(2) = -v(\dot{\epsilon}'_x + \dot{\epsilon}'_\theta) / (1 - v) \quad (28)$$

where v is Poissons ratio, and $\dot{\epsilon}'_x$ and $\dot{\epsilon}'_\theta$ are identical to those of Equation 26.

Using the new strain rate it is possible to determine a new normal stress from Equation 27. Both the deviator stress and the pressure are different from the incompressible step. The pressure is different because the volumetric strain has been modified to:

$$\epsilon_v(2) = \epsilon_v(1) + [\dot{\epsilon}'_z(2) - \dot{\epsilon}'_z(1)]\Delta t \quad (29)$$

where Δt is the integration time increment.

Now by linear interpolation it is possible to determine $\dot{\epsilon}'_z(3)$ for $\sigma'_z = 0$. The new computed value of $\sigma'_z(3)$ will generally be close to $\sigma'_z = 0$, but an additional iteration may be required. This is represented by $\dot{\epsilon}'_z(4)$, and it is the average $\dot{\epsilon}'_z$ computed from interpolation/extrapolation of points 1 and 3, and 2 and 3.

The resulting stresses are shown on the upper half of Figure 11. These stresses are integrated over the appropriate areas to obtain the forces on the lower half of Figure 11.

For layer 1, the in-plane force, the shear force, and the bending moment are given by

$$F_1^i = F_1^j = 2\pi\bar{x}H\sigma'_{x1} \quad (30)$$

$$V_1^i = V_1^j = 2\pi\bar{x}H\tau'_{xz} \quad (31)$$

$$M_1^i = -V_1L/2 \quad (32)$$

$$M_1^j = V_1L/2 \quad (33)$$

where \bar{x} is the average x coordinate of nodes i and j, H is the thickness of the individual element layer from Equation 7, and L is the current length. These forces do not include the force due to the hoop stress. The in-plane forces, the shear forces, and the bending moments for layers 2 and 3 are determined in a similar manner. The moment component (M_1^i and M_1^j) is included to keep the element in equilibrium.

The net forces and moments on nodes i and j (from all three layers) are as follows:

$$F_x^i = F_x^j = F_1 + F_2 + F_3 \quad (34)$$

$$F_z^i = F_z^j = (V_1 + V_2 + V_3) \quad (35)$$

$$M^i = M_1^i + M_2^i + M_3^i + F_2H - F_3H \quad (36)$$

$$M^j = M_1^j + M_2^j + M_3^j + F_2H - F_3H \quad (37)$$

These are per the sign convention at the top of Figure 11, and in the element (local) coordinate system.

The net forces on node i, in the system coordinate system, are

$$F_x^i = -F_{x'}^i \cos \phi + F_{z'}^i \sin \phi - \pi A (\sigma_{\theta 1} + \sigma_{\theta 2} + \sigma_{\theta 3}) \quad (38)$$

$$F_z^i = -F_{x'}^i \sin \phi - F_{z'}^i \cos \phi \quad (39)$$

where A is the cross-sectional area of each individual shell layer and $\sigma_{\theta 1}$, $\sigma_{\theta 2}$, and $\sigma_{\theta 3}$ are the hoop stresses for each of the three layers. The net nodal force on node j is determined in a similar manner.

An assessment of the accuracy of the three and five layer shell algorithms is shown in Figure 13. The errors are 11 percent for the three layer algorithm and 4 percent for the five layer algorithm.

The heat conduction algorithm is similar to the 1D algorithms, except the cross-sectional area (in the x' direction) is

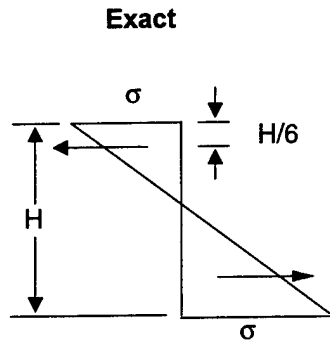
$$A = 2\pi \bar{x} H \quad (40)$$

where \bar{x} is the average x coordinate of the nodes and H is the thickness of the individual layer. For the heat conduction option all three layers will have equal temperatures because all layers are attached to the same nodes.

3.4.7 Membrane Shell Elements

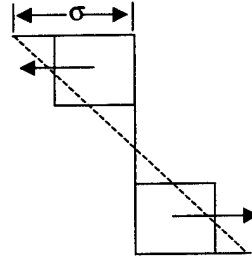
The 2D membrane shell elements are a simplified form of the bending shell elements presented in subsection 3.4.6 and shown in Figure 10. The membrane shell element has only in-plane stresses and is composed of only a single layer. It cannot produce bending or transverse shear stresses. Furthermore it is assumed to be incompressible, and this eliminates the need to iterate to obtain the through-thickness stress. This algorithm is presented in Reference 21 for plane stress geometry.

Elastic Bending



$$M = H^2 \sigma / 6 = .167 \sigma H^2$$

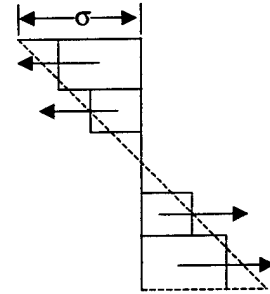
3 Point Integration (3 Layers)



$$M = 4/27 \sigma H^2 = .148 \sigma H^2$$

11% Low

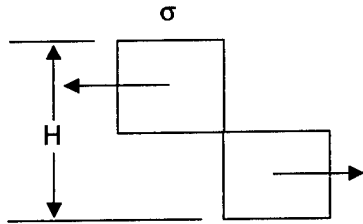
5 Point Integration (5 Layers)



$$M = 20/125 \sigma H^2 = .160 \sigma H^2$$

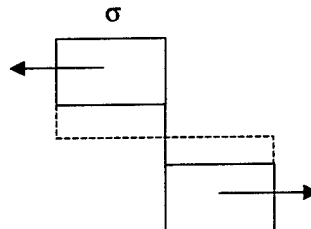
4% Low

Plastic Bending



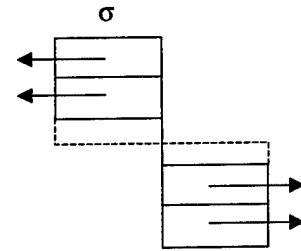
$$M = \sigma H^2 / 4 = .25 \sigma H^2$$

24.vsd
T19616



$$M = 2/9 \sigma H^2 = .222 \sigma H^2$$

11% Low



$$M = 6/25 \sigma H^2 = .240 \sigma H^2$$

4% Low

Figure 13. Accuracy Assessment for Bending Shells

Referring back to Equation 23 of subsection 3.4.6, the through-thickness strain rate for incompressible deformation is

$$\dot{\epsilon}'_z = -(\dot{\epsilon}'_x + \dot{\epsilon}'_\theta) \quad (1)$$

where $\dot{\epsilon}'_x$ is the in-plane strain rate and $\dot{\epsilon}'_\theta$ is the hoop strain rate.

The deviator stresses (s'_x, s'_z, s'_θ) can then be determined from $\dot{\epsilon}'_x, \dot{\epsilon}'_z, \dot{\epsilon}'_\theta$, which give the net stresses

$$\sigma'_x = s'_x - P \quad (2)$$

$$\sigma'_z = s'_z - P \quad (3)$$

$$\sigma'_\theta = s'_\theta - P \quad (4)$$

In Equation 3, setting $\sigma'_z = 0$ gives $P = s'_z$, and this provides an explicit determination of the stresses in Equations 2–4.

3.4.8 Nonreflective Boundary Elements

Nonreflective boundary elements (References 8 and 9) have been available historically to provide nonreflective damping for the modeling of large infinite bodies such as soil or water. They are intended primarily to absorb elastic waves, but they are also effective for other applications (Reference 10). The 2D nonreflective boundary elements are incorporated as two-node, infinitely-thin, massless elements, as shown in Figure 14.

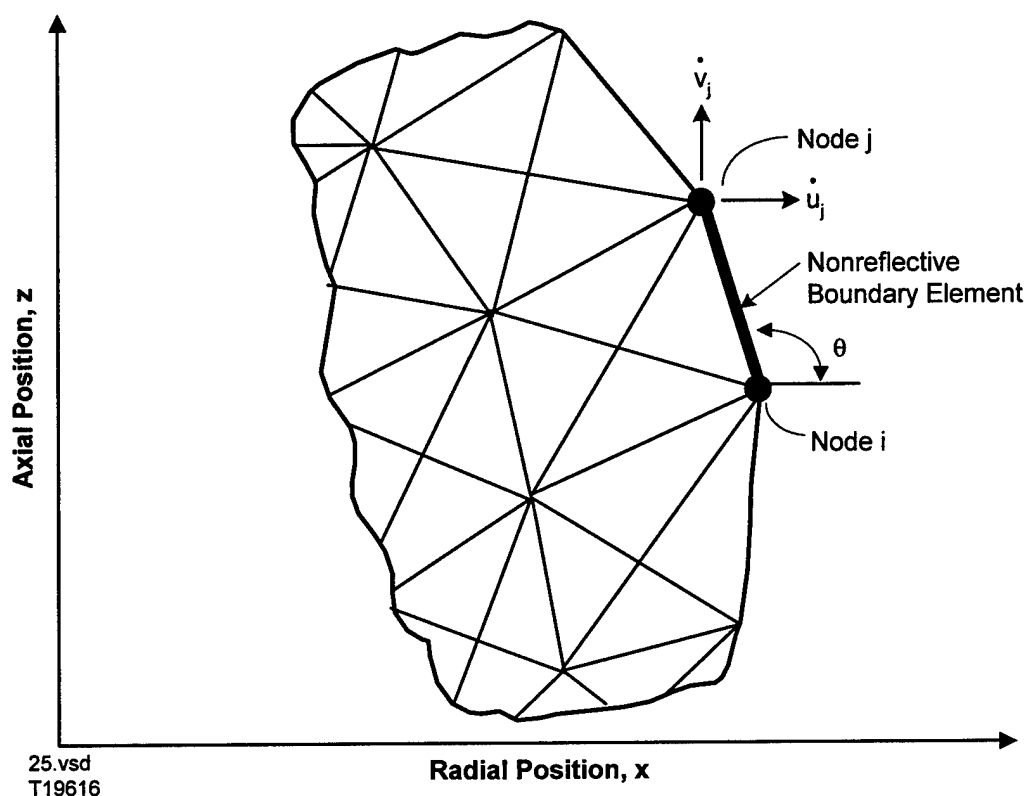


Figure 14. Description of the 2D Nonreflective Boundary Element

The average velocity normal to the boundary element is

$$V_N = \bar{u} \sin \theta - \bar{v} \cos \theta \quad (1)$$

where $\bar{u} = (\dot{u}_i + \dot{u}_j) / 2$ is the average velocity in the x direction, \bar{v} is the average velocity in the z direction, and θ is the angle between the element and the x axis.

The average velocity parallel to the element (from node i to node j) is

$$V_P = \bar{u} \cos \theta + \bar{v} \sin \theta \quad (2)$$

The total normal and parallel forces are

$$F_N = -\rho_o c_s A V_N \quad (3)$$

$$F_P = -\rho_o c_{\text{shear}} A V_P \quad (4)$$

where ρ_o is the initial density of the material, $A = 2\pi\bar{x}$ is the surface area of the element, and V_N and V_P are the velocities. The longitudinal and shear velocities are

$$c_s = \sqrt{(K_1 + 4G/3) / \rho_o} \quad (5)$$

$$c_{\text{shear}} = \sqrt{G / \rho_o} \quad (6)$$

where K_1 is the bulk modulus and G is the shear modulus.

Now the total forces must be aligned with the two principal axes and distributed to the two nodes

$$F_x^i = F_x^j = (F_N \sin \theta + F_P \cos \theta) / 2 \quad (7)$$

$$F_z^i = F_z^j = (F_N \cos \theta + F_P \sin \theta) / 2 \quad (8)$$

3.5 2D AXISYMMETRIC GEOMETRY WITH SPIN

The 2D axisymmetric geometry with spin is identical to the 2D axisymmetry geometry described previously in subsection 3.4, except that this geometry allows the nodes to experience rotations (or spin) about the axis of revolution, as shown in Figure 15.

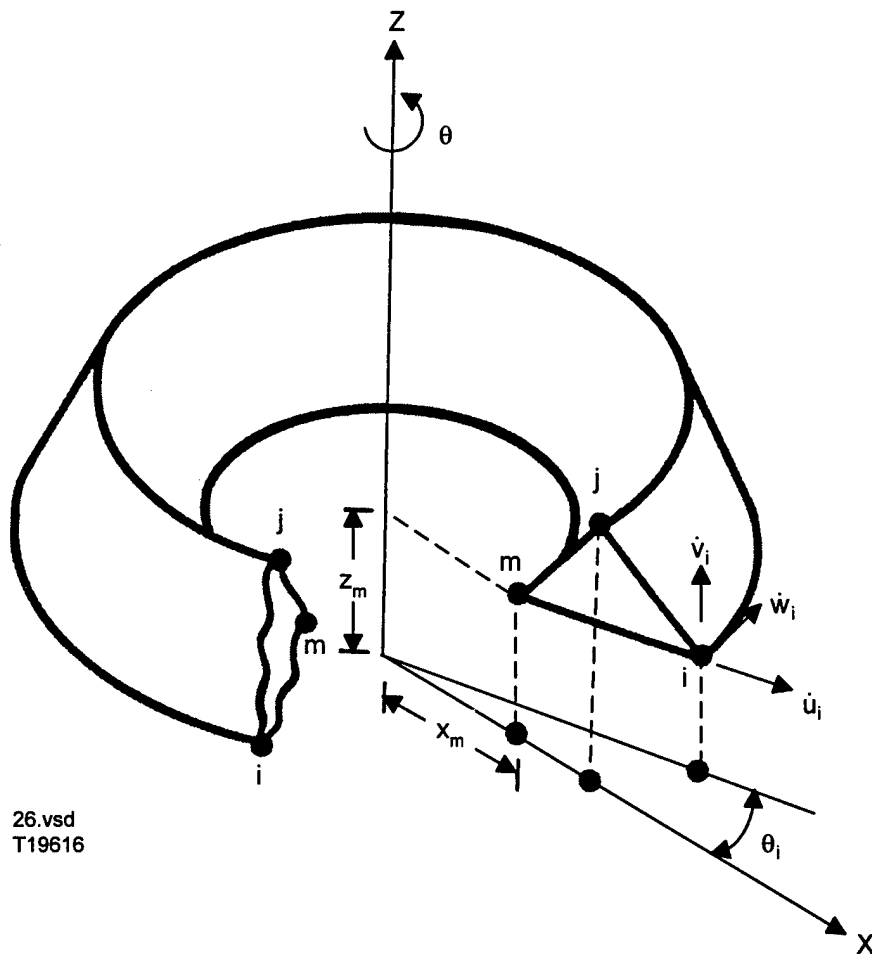


Figure 15. Description of the 2D Axisymmetric Triangular Element with Spin

For this geometry the concentrated masses at the nodes can be visualized as concentric circular rings contained in planes that are perpendicular to the axis of revolution. These rings can move up and down along the axial direction, they can expand and contract in the radial direction, and they can rotate about the axis of revolution. This additional spinning degree of freedom introduces centrifugal forces, and also allows for two additional shear strain rates and shear stresses. The algorithm is reported in References 3 and 11.

The three normal strain rates $(\dot{\epsilon}_x, \dot{\epsilon}_z, \dot{\epsilon}_\theta)$ and the shear strain rate in the x-z plane $(\dot{\gamma}_{xz})$ for a triangular element are identical to those described in subsection 3.4. The two additional shear strain rates are

$$\dot{\gamma}_{x\theta} = \frac{\partial \dot{w}}{\partial x} - \frac{\bar{\dot{w}}}{\bar{x}} \quad (1)$$

$$\dot{\gamma}_{z\theta} = \frac{\partial \dot{w}}{\partial z} \quad (2)$$

where $\dot{w}_i = x_i \dot{\theta}_i$ is the tangential velocity of node i under a rotational rate $\dot{\theta}_i$. The derivatives $\left(\frac{\partial \dot{w}}{\partial x} \text{ and } \frac{\partial \dot{w}}{\partial z}\right)$ are obtained in the same manner as the other derivatives were obtained in subsection 3.4. In Equation 1, $\bar{\dot{w}}$ is the average tangential velocity of the three nodes and \bar{x} is the average x coordinate.

The shear strain rates in Equations 1 and 2 lead to two new shear stresses $(\tau_{x\theta} \text{ and } \tau_{z\theta})$, that are obtained in the same manner as described in subsection 3.4. The resulting tangential force is

$$F_\theta^i = -\pi \bar{x} \left[\left(\frac{\bar{x}}{x_i} \right) b_i \tau_{x\theta} + c_i \tau_{z\theta} \right] \quad (3)$$

where $b_i = z_j - z_m$ and $c_i = x_m - x_j$, as defined previously. The factor $\left(\frac{\bar{x}}{x_i} \right)$ is required to maintain equilibrium in the θ direction.

The equations of motion are modified and expanded for this geometry. The radial acceleration (given previously in subsection 3.4.1) is expanded to include centrifugal force due to spin.

$$\ddot{x}_i^t = \bar{F}_x^i / \bar{M}_i + x_i^t (\dot{\theta}^{t-})^2 \quad (4)$$

where \bar{F}_x^i and \bar{M}_i are the force and mass described in subsection 3.4.1, x_i^t is the radial coordinate at time = t and $\dot{\theta}^{t-}$ is the rotation velocity before it is updated at time = t.

The updated radial velocity is

$$\dot{x}_i^{t+} = (\dot{x}_i^{t-} + \ddot{x}_i^t \overline{\Delta t}) (1 - C_D \overline{\Delta t} / x_i^t) \quad (5)$$

where \dot{x}_i^{t-} is the constant velocity for the previous time increment and $\overline{\Delta t}$ is the average of the two integration time increments about time = t. The expression in the second set of parentheses can be used to damp out the radial velocities to give steady-state solutions for spinning bodies. If the constant, C_D , is set equal to twice the sound velocity of the material, the system will be approximately critically damped and the steady-state solution will be rapidly attained.

For the rotational equations of motion it is necessary to consider the angular momentum, H , of each concentrated mass. This gives

$$H_i^{t+} = H_i^{t-} + x_i^t \overline{F}_\theta^i \overline{\Delta t} \quad (6)$$

By substituting $H_i = \dot{\theta}_i x_i^2 \overline{M}_i$ into Equation (6), it is possible to determine the updated rotation velocity.

$$\dot{\theta}_i^{t+} = \dot{\theta}_i^{t-} \left(\frac{x_i^t}{x_i^{t+\Delta t}} \right)^2 + \frac{x_i^t \overline{\Delta t}}{(x_i^{t+\Delta t})^2} \left(\frac{\overline{F}_\theta^i}{\overline{M}_i} \right) \quad (7)$$

It should be noted that even if the net circumferential force, \overline{F}_θ^i is equal to zero, it is possible for the spin to change if the radius changes between times t and t+ Δt . It is therefore necessary to obtain the new radial position at t+ Δt before obtaining the new rotation velocity at t+ Δt .

3.6 2D PLANE STRAIN GEOMETRY

The 2D plane strain geometry is a simplified form of the 2D axisymmetric geometry. The primary difference is that the plane strain geometry is for a unit thickness and has no hoop strains or strain rates.

Referring back to subsection 3.4.4 and Figure 4 for 2D axisymmetric triangular elements, some of the revised equations are as follows:

The mass at node i is

$$M_i = \rho_o V_o / 3 \quad (1)$$

where ρ_o is the initial density of the material and V_o is the initial volume of the element. The initial volume is

$$V_o = A_o \Delta y \quad (2)$$

where A_o is the initial area and $\Delta y \equiv 1.0$ is the unchanging unit thickness.

The strain rates and rotational rate for $\dot{\epsilon}_x$, $\dot{\epsilon}_z$, $\dot{\gamma}_{xz}$, and ω_{xz} are identical to those of Equations 11, 12, 14, and 15 of subsection 3.4.4. The hoop strain rate ($\dot{\epsilon}_\theta$) in Equation 13 of subsection 3.4.4 is replaced by the through-thickness strain rate, which is

$$\dot{\epsilon}_y \equiv 0 \quad (3)$$

After the stresses have been determined, the forces in node i are

$$F_x^i = -(b_i \sigma_x + c_i \tau_{xz}) / 2 \quad (4)$$

$$F_z^i = -(c_i \sigma_z + b_i \tau_{xz}) / 2 \quad (5)$$

where $b_i = z_j - z_m$, $c_i = x_m - x_j$, and σ_x , σ_z , and τ_{xz} are the two normal stresses and shear stress.

3.7 2D PLANE STRESS GEOMETRY

The 2D plane stress geometry is similar to the 2D plane strain geometry. The difference is that for plane strain geometry all of the strain is in the x-z plane and there is no strain normal to the plane ($\epsilon_y \equiv \dot{\epsilon}_y \equiv 0$). For plane stress geometry, all the stress is in the x-z plane and there is no stress normal to the plane ($\sigma_y \equiv 0$). The initial plane stress geometry has an initial thickness of $\Delta y_o = 1.0$, but the thickness can change as the grid is deformed. The original algorithm was for incompressible flow (Reference 21), but the current algorithm includes compressibility.

The plane stress algorithm is identical to the plane strain algorithm, except for the determination of the through-thickness strain rate, and the determination of the forces. Because the through-thickness stress must be $\sigma_y = 0$ it is necessary to iterate $\dot{\epsilon}_y$ to determine this stress. This is accomplished by using the iteration algorithm described in subsection 3.4.6 and shown in Figure 12. For bending shells the known strain rates are $\dot{\epsilon}'_x$ and $\dot{\epsilon}_\theta$, and the through-thickness strain rate (to be determined) is $\dot{\epsilon}'_z$. For plane stress geometry, the known strain rates are $\dot{\epsilon}_x$ and $\dot{\epsilon}_z$, and the through-thickness strain rate (to be determined) is $\dot{\epsilon}_y$. Other than the change in nomenclature, the algorithms for the two cases are identical.

The forces are slightly modified from those of the plane strain geometry

$$F_x^i = -\Delta y (b_i \sigma_x + c_i \tau_{xz}) / 2 \quad (1)$$

$$F_z^i = -\Delta y (c_i \sigma_x + b_i \tau_{xz}) / 2 \quad (2)$$

where Δy is the current thickness and the other terms are identical to those of the plane strain geometry given in Equations 4 and 5 of subsection 3.6. The current thickness is

$$\Delta y = V / A = V_o (1 + \epsilon_v) / A \quad (3)$$

where V is the current volume, A is the current area, V_o is the initial volume, and ϵ_v is the current volumetric strain.

3.8 3D GEOMETRY

A description of 3D geometry is shown in Figure 16. This figure shows a tetrahedral element, but brick elements, bar elements, bending shell elements, membrane shell elements, and nonreflective boundary elements are also available. The early developments of this work are reported in References 2, 4, 14, and 22–24.

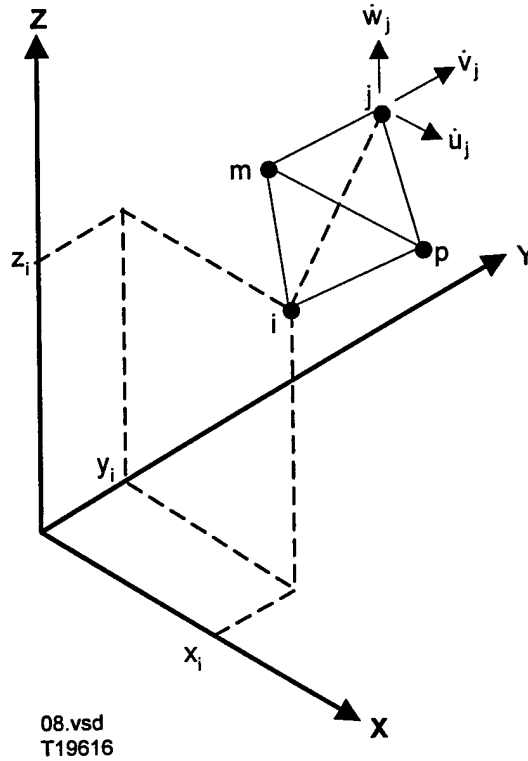


Figure 16. Description of the 3D Tetrahedral Element

3.8.1 Equations of Motion

The accelerations, velocities, and positions are determined as follows:

$$\ddot{x}_i^t = \overline{F}_x^i / \overline{M}_i \quad (1)$$

$$\ddot{y}_i^t = \overline{F}_y^i / \overline{M}_i \quad (2)$$

$$\ddot{z}_i^t = \overline{F}_z^i / \overline{M}_i \quad (3)$$

$$\dot{x}_i^{t+} = \dot{x}_i^{t-} + \ddot{x}_i^t \overline{\Delta t} \quad (4)$$

$$\dot{y}_i^{t+} = \dot{y}_i^{t-} + \ddot{y}_i^t \overline{\Delta t} \quad (5)$$

$$\dot{z}_i^{t+} = \dot{z}_i^{t-} + \ddot{z}_i^t \overline{\Delta t} \quad (6)$$

$$x_i^{t+\Delta t} = x_i^t + \dot{x}_i^{t+} \Delta t \quad (7)$$

$$y_i^{t+\Delta t} = y_i^t + \dot{y}_i^{t+} \Delta t \quad (8)$$

$$z_i^{t+\Delta t} = z_i^t + \dot{z}_i^{t+} \Delta t \quad (9)$$

Equations 1–3 provide the x, y, and z accelerations at time = t. \bar{F}_x^i , \bar{F}_y^i , and \bar{F}_z^i are the net x, y, and z direction forces on node i. These forces are contributed to by all of the elements that contain node i, and are obtained from the element computations in the previous cycle of integration. \bar{M}_i is the total mass at node i, and it contains a fraction of the mass of all elements that contain node i. Although Figure 16 shows only a tetrahedral element, a node can have various element types attached to it. This means it is possible for an individual node to have masses and forces from different element types. The specific algorithms for masses and forces are provided in subsections 3.8.4–3.8.9.

The updated velocities in Equations 4–6 are constant for the interval between time = t and time = t+Δt. The constant velocities for the previous time increment are \dot{x}_i^{t-} , \dot{y}_i^{t-} , and \dot{z}_i^{t-} , and $\bar{\Delta t}$ is the average of the two integration time increments about time = t.

The integration time increment is limited to

$$\Delta t = C_1 \left[h / \left(\sqrt{g^2} + \sqrt{g^2 + c_s^2} \right) \right] \quad (10)$$

where $g^2 = C_Q Q / \rho$, h is a characteristic length (described later for each element type), and c_s is the sound velocity of the material (References 2 and 5). Q is the artificial viscosity, and C_Q is a constant for the artificial viscosity. These are described in Section 6. The Courant sound speed fraction, C_1 , must be less than unity ($C_1 \leq 1.0$) to ensure numerical stability. $C_1 = 0.9$ is a typical value.

For 3D bending shell elements there are also rotational degrees of freedom on each node. The rotational velocities of node i are updated in the same general manner as the translational velocities in Equations 1–6, except that they are coupled, and therefore more complex (Reference 25). The system of equations to be solved is as follows:

$$\begin{bmatrix} I_{xx} & I_{xy} & I_{xz} \\ I_{yx} & I_{yy} & I_{yz} \\ I_{zx} & I_{zy} & I_{zz} \end{bmatrix} \begin{Bmatrix} \ddot{\theta}_x \\ \ddot{\theta}_y \\ \ddot{\theta}_z \end{Bmatrix} = \begin{bmatrix} \overline{M}_x + (I_{yy} - I_{zz})\dot{\theta}_y\dot{\theta}_z + (I_{yx}\dot{\theta}_z - I_{zx}\dot{\theta}_y)\dot{\theta}_x + I_{yz}(\dot{\theta}_z^2 - \dot{\theta}_y^2) \\ \overline{M}_y + (I_{zz} - I_{xx})\dot{\theta}_x\dot{\theta}_z + (I_{zy}\dot{\theta}_x - I_{xy}\dot{\theta}_z)\dot{\theta}_y + I_{xz}(\dot{\theta}_x^2 - \dot{\theta}_z^2) \\ \overline{M}_z + (I_{xx} - I_{yy})\dot{\theta}_x\dot{\theta}_y + (I_{xz}\dot{\theta}_y - I_{yz}\dot{\theta}_x)\dot{\theta}_z + I_{xy}(\dot{\theta}_y^2 - \dot{\theta}_x^2) \end{bmatrix} \quad (11)$$

The rotational accelerations $(\ddot{\theta}_x, \ddot{\theta}_y, \ddot{\theta}_z)$, the moments of inertia $(I_{xx} \dots I_{zz})$ and the net moments $(\overline{M}_x, \overline{M}_y, \overline{M}_z)$ are acting on node i at time $= t$. The rotational velocities $(\dot{\theta}_x, \dot{\theta}_y, \dot{\theta}_z)$ are for the time increment prior to time $= t$.

The updated accelerations are determined from Equation 11 and are designated $\ddot{\theta}_x^t, \ddot{\theta}_y^t, \ddot{\theta}_z^t$. The updated velocities for the next time increment are

$$\dot{\theta}_x^{t+} = \dot{\theta}_x^{t-} + \ddot{\theta}_x^t \Delta t \quad (12)$$

$$\dot{\theta}_y^{t+} = \dot{\theta}_y^{t-} + \ddot{\theta}_y^t \Delta t \quad (13)$$

$$\dot{\theta}_z^{t+} = \dot{\theta}_z^{t-} + \ddot{\theta}_z^t \Delta t \quad (14)$$

The rotational displacements $(\theta_x, \theta_y, \theta_z)$ are not required.

3.8.2 Sliding Interfaces

The 3D sliding interface algorithm is similar to the 2D sliding algorithm described in subsection 3.4.2, but it does not have the order independent algorithm for automatic sliding. Although an automatic sliding algorithm is available in 3D, the searching time can be excessive and it is usually more computationally efficient for the user to specify the master and slave regions. Although the 3D sliding algorithm has been improved in recent years, the early algorithms are reported in References 14 and 22–24.

The interface determination algorithm and the search algorithm will not be described herein, except to note that they are analogous to the 2D algorithms described in subsection 3.4.2.

Figure 17 shows a slave node in contact with a triangular master surface defined by nodes i, j , and k . The normal velocities of the slave node and the three master nodes are adjusted first.

Three of the four conditions required to determine these new velocities involve conservation of linear momentum normal to the master plane and conservation of angular momenta about the two axes in the plane. These conditions define the fractions (R_i, R_j, R_k) of linear momenta transferred from the slave node to the three master nodes. The resulting momenta-conserving relationships between the instantaneous normal velocity changes of the slave node (ΔV_s^N) and the master nodes ($\Delta V_i^N, \Delta V_j^N, \Delta V_k^N$) have the form

$$\Delta V_i^N = -R_i M_s \Delta V_s^N / M_i \quad (1)$$

where M_s and M_i represent the mass of the slave node and the master node i .

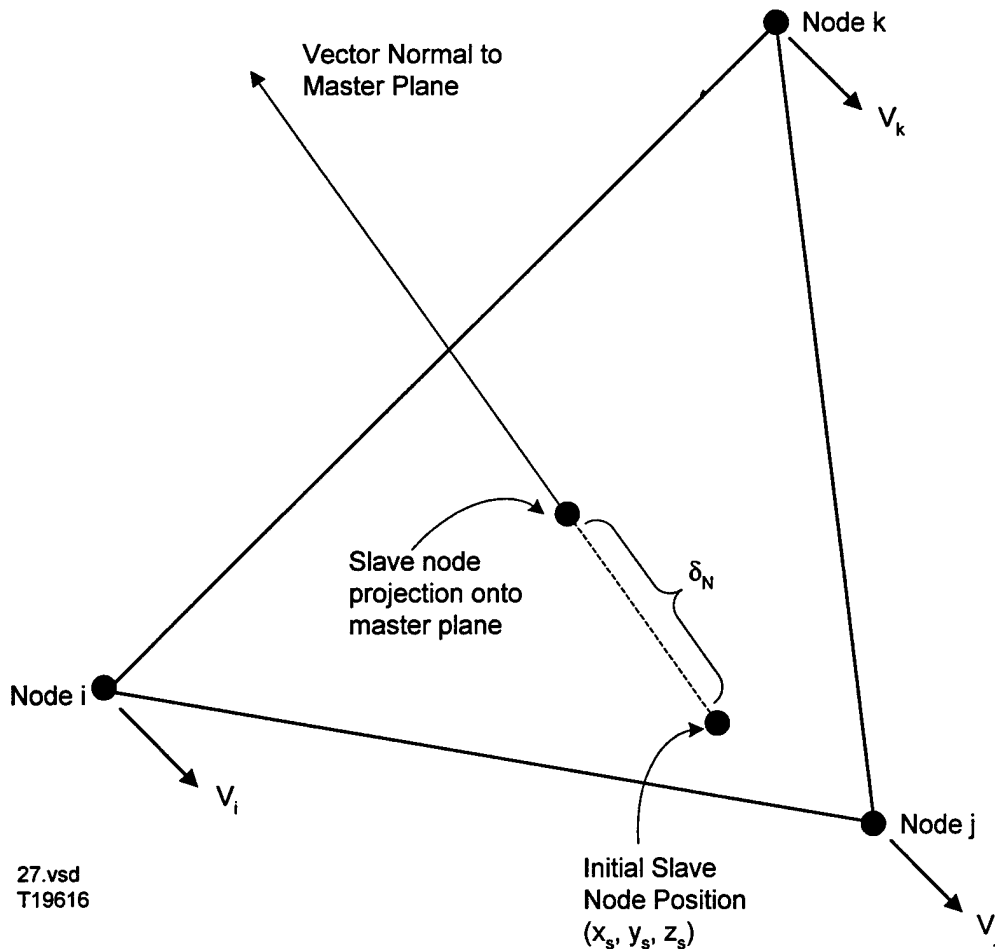


Figure 17. Description of the 3D Sliding Interface Contact Algorithm

The final condition involves equating the normal velocities of the slave node and the master surface at the slave node position. For this case, it is necessary to determine the velocity of the master surface at the slave node location. Here the velocity is determined within a two-dimensional triangle. The resulting master surface velocity in the x direction, at the slave node position, is

$$\dot{u}_m = q_i \dot{u}_i + q_j \dot{u}_j + q_k \dot{u}_k \quad (2)$$

The other velocity components (\dot{v}_m and \dot{w}_m) have similar form to Equation 2 and the geometry constants (q_i, q_j, q_k), have the form

$$q_i = \frac{1}{2A_{xy}} [x_j y_k - x_k y_j + (y_j - y_k)x_s + (x_k - x_j)y_s] \quad (3)$$

where A_{xy} is the projected cross-sectional area of the triangular master surface on the x-y plane, and the other terms represent the coordinates of the master and slave nodes. The projections could also be on the x-z or y-z plane depending on the orientation of the master plane.

By equating the normal velocities and substituting the relationships of Equation 1, the normal velocity change imposed on the slave node is defined as

$$\Delta V_s^N = \frac{V_m^N - V_s^N}{1 + q_i R_i M_s / M_i + q_j R_j M_s / M_j + q_k R_k M_s / M_k} \quad (4)$$

where the slave node velocity normal to the master surface is

$$V_s^N = A\dot{u}_s + B\dot{v}_s + C\dot{w}_s \quad (5)$$

where A, B, C are direction cosines of the vector normal to the master surface. The normal velocity of the master surface, V_m^N , has the same form as Equation 5 and the velocity changes to the three master nodes can be defined from Equation 1. The specific velocity changes in the x, y, and z directions are obtained by multiplying ΔV by the appropriate direction cosines.

Frictional effects are constrained to the plane of the master surface and the direction opposes the relative motion. The net magnitude of the frictional velocity change to the slave node is proportional to the normal velocity change to the slave node, or

$$\Delta V_s^P = f_s \Delta V_s^N \quad (6)$$

where f_s is the coefficient of friction.

The velocity components in the plane of the master surface are obtained by subtracting the velocity components normal to the master plane, from the total velocity components. These velocity components for the slave node are expressed as

$$\dot{u}_s^P = \dot{u}_s - A V_s^N \quad (7)$$

$$\dot{v}_s^P = \dot{v}_s - B V_s^N \quad (8)$$

$$\dot{w}_s^P = \dot{w}_s - C V_s^N \quad (9)$$

The in-plane velocities of the master surface $(\dot{u}_m^P, \dot{v}_m^P, \dot{w}_m^P)$ are obtained in a similar manner.

The relative velocity components $(\dot{u}_{rel}^P, \dot{v}_{rel}^P, \dot{w}_{rel}^P)$ are then obtained in the form of

$$\dot{u}_{rel}^P = \dot{u}_m^P - \dot{u}_s^P \quad (10)$$

Finally, the friction induced velocity changes $(\Delta \dot{u}_s^P, \Delta \dot{v}_s^P, \Delta \dot{w}_s^P)$ to the slave node have the form

$$\Delta \dot{u}_s^P = \left(\frac{\dot{u}_{rel}^P}{\sqrt{[(\dot{u}_{rel}^P)^2 + (\dot{v}_{rel}^P)^2 + (\dot{w}_{rel}^P)^2]}} \right) \Delta V_s^P \quad (11)$$

The momentum change of the master nodes, due to the frictional force, gives in-plane velocity changes to master node $i(\Delta \dot{u}_i^P, \Delta \dot{v}_i^P, \Delta \dot{w}_i^P)$ of the form

$$\Delta \dot{u}_i^P = -R_i M_s \Delta \dot{u}_s^P / M_i \quad (12)$$

For the standard (not automatic) sliding algorithm the slave nodes cannot also be master nodes (for a given interface). Here the velocity changes are collected after all slave nodes have been processed and there is no order dependence.

For the automatic sliding algorithm the slave and master node velocities are updated as they are processed, and this results in some order dependence.

Future plans are to incorporate a new 3D algorithm that is analogous to the current 2D algorithm.

3.8.3 Erosion

The three-dimensional algorithm that follows should be applied only to problems in which erosion is the primary mode of penetration. It is reported in Reference 16. It is only available for tetrahedral elements. For many problems, the master surface is initially on the top (or any other side) of a plate and it cannot involve other sides (except as special cases) during erosion. The precise restriction for the general algorithm to follow is that no element with a free surface can be eroded unless that free surface was initially designated as a master surface. The two exceptions are for a free surface on the $y = 0$ plane of symmetry, and for a free surface on the bottom of the plate.

Figure 18 shows a partially eroded master surface defined as a set of adjacent triangles. The initial master surface included the entire top surface of the plate. The slave nodes are essentially above the master surface and must always view the associated master triangles so that the nodes of the triangles (M1, M2, M3) are in a counterclockwise order. The slave nodes can be randomly ordered and are not allowed to penetrate through the master surface. The master surface is allowed to erode by totally failing tetrahedral elements which have one, two, three or four sides on the master surface. Totally failed elements do not develop stresses or pressures; they essentially disappear except that mass is retained at the nodes.

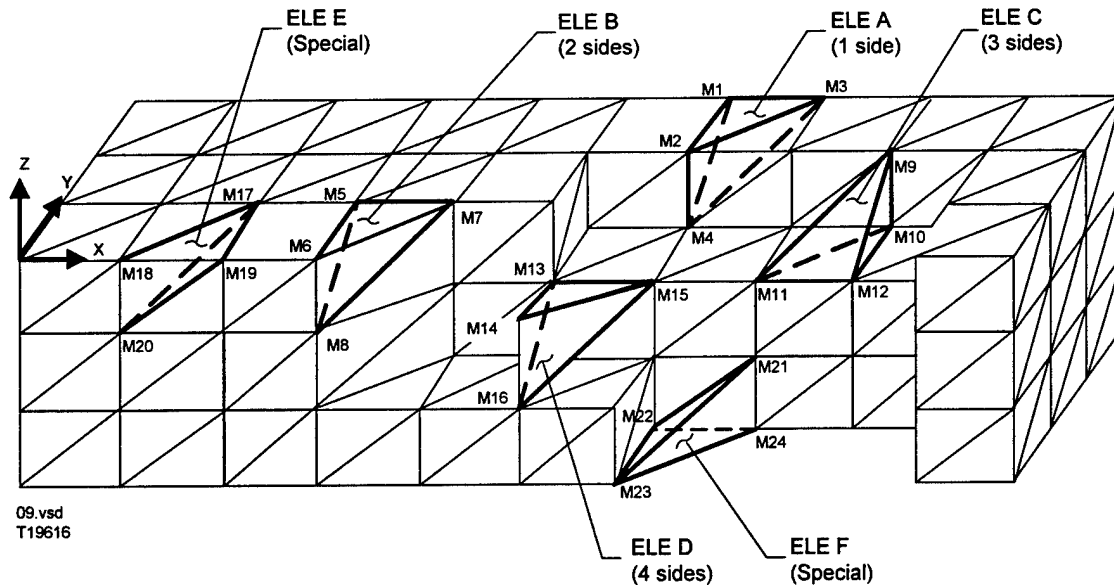


Figure 18. Description of the 3D Erosion Algorithm

Before the computations begin, the preprocessor must store the groups of three nodes defining the individual triangular master planes. It must also permanently mark each node contained on the master surface, and it must count and store the number of elements attached to each node. If three or four nodes of an element are marked, then the element is on the master surface and is eligible for failure if it exceeds the specified erosion strain. When an element is totally failed, the element count for each of the four nodes is decremented, so that the count reflects the number of unfailed elements attached to the node. When the count reaches zero, the node is made a slave node because it is no longer associated with the master surface. This new slave node (which continues to have mass, momentum, and kinetic energy) can then interact with the master surface but cannot pass through it.

The six elements in Figure 18 (elements, A, B, C, D, E, F) have three or four nodes on the master surface and have one, two, three or four sides on the master surface. The following describes the changes necessary to redefine the master surface and the slave nodes:

- Element A has one side (M1-M2-M3) on the master surface. All four nodes (M1, M2, M3, and M4) are marked. Because only one side (M1-M2-M3) is contained in the list of master triangles, it is known that the other three sides are not on the master surface. If the equivalent plastic strain or volumetric strain of element A exceeds the erosion strain, the element is totally failed. The updated master surface has one triangular side (M1-M2-M3) removed and three triangular sides of adjacent elements (M1-M2-M4,

M1-M4-M3, M2-M3-M4) added. The nodes of the new sides must be given in the proper order so that the slave nodes see a counterclockwise ordering. The element counts of nodes M1, M2, M3, M4 are decremented, but all four nodes remain on the master surface because none of the element counts goes to zero.

- Element B has two sides (M5-M6-M7, M6-M8-M7) on the master surface. The four nodes M5, M6, M7, and M8 are marked. If the equivalent plastic strain or volumetric strain of element B exceeds the erosion strain, the element is totally failed. The previous master surface has two sides (M5-M6-M7, M6-M8-M7) removed and two other surfaces (M5-M6-M8, M5-M8-M7) added. The element counts of nodes M5, M6, M7 and M8 are decremented, but none of the counts goes to zero.
- Element C has three sides (M9-M10-M11, M9-M11-M12, M9-M12-M10) on the master surface. The four nodes M9, M10, M11, and M12 are marked. If the equivalent plastic strain or volumetric strain of element C exceeds the erosion strain, the element is totally failed. The previous master surface has three sides (M9-M10-M11, M9-M11-M12, M9-M12-M10) removed and one other surface (M10-M11-M12) added. The element counts of nodes M9, M10, M11, and M12 are decremented, but none of the counts goes to zero.
- Element D has four sides (M13-M14-M15, M13-M16-M14, M14-M16-M15, M13-M15-M16) on the master surface. The four nodes M13, M14, M15, and M16 are marked. If the equivalent plastic strain or volumetric strain of element D exceeds the erosion strain, the element is totally failed. The previous master surface has all four sides removed and none added. The element count of nodes M13, M14, M15, and M16 are decremented. The element counts of nodes M13, M15, and M16 do not go to zero and therefore remain on the master surface. The element count on node M14 does go to zero, however, so it is designated to be a slave node.
- Element E is a special case because it has one side (M18, M19, M20) on a plane of symmetry at $y = 0$, which was not initially designated as a master surface. The general algorithm would indicate one side (M17-M18-M19) to be deleted and three sides to be added (M17-M18-M20, M17-M20, M19, M18-M19-M20). The side on the plane of symmetry at $y = 0$ (M18-M19-M20) should not be added, however. This side is readily identified and deleted by noting that $y = 0$ for nodes M18, M19, and M20. For this case the element counts of nodes M17, M18, M19, and M20 are again decremented. Node

M20 was not previously marked and must therefore be marked to identify it as a part of the updated master surface. It should be noted that the general algorithm would handle this special case if the triangular element sides on the plane of symmetry would initially be designated as part of the master surface. Because this would significantly increase the size of the master surface (and the associated searching time), it is instead treated as a special case.

- Element F is another special case because it is eroded through a free surface (bottom of the plate) which was not initially designated as a master surface. Here the general algorithm would remove two sides (M21-M22-M23, M21-M23-M24) and add two new sides (M21-M22-M24, M22-M23-M24). The side on the bottom of the plate (M22-M23-M24) should not be added, however. This side can be readily identified if the nodal numbering system proceeds downward by layers, thus placing the highest node numbers on the bottom surface of the plate. Under these conditions, node numbers M22, M23, and M24 would all be greater than (or equal to) the lowest node number on the bottom of the plate, and that triangle would therefore not be added to the list of master triangles. Other approaches could be used for different nodal numbering systems. Again it should be noted that the general algorithm would handle this special case if the element sides on the bottom of the plate would initially be designated as part of the master surface.

To ensure that there is no cross-over of material between the two surfaces (such as a projectile and a target), a two-step approach (two separate sliding interfaces) is used with the standard (not automatic) sliding algorithm. For the first interface, all of the projectile nodes and the eroded target nodes are slave to the master surface in the target. For the second interface, all of the nodes in the center of the target, and the eroded projectile nodes, are slave to the master surface on the projectile. The eroded nodes are therefore restrained from passing through either the projectile or the target. The automatic sliding algorithm handles both surfaces automatically.

3.8.4 Tetrahedral Elements

A typical tetrahedral element is shown in Figure 16. It is geometrically defined by nodes i , j , m , and p . The formulation is based on nodes i , j , and m being positioned in a counterclockwise manner when viewed from node p . The coordinates of node i are designated x_i , y_i , z_i , and the corresponding velocities are designated \dot{u}_i , \dot{v}_i , \dot{w}_i (which are identical to \dot{x}_i , \dot{y}_i , \dot{z}_i used previously). This algorithm is reported in References 2, 4, 14, and 23.

The algorithm that follows is for a single tetrahedral element. The arrangement of the elements, however, can have a significant effect on the computed response (References 16 and 18). There are also some mixed (average volumetric strain, or average pressure) algorithms that provide improved accuracy for various arrangements of elements (Reference 16).

The mass at node i , for an individual tetrahedral element, is simply

$$M_i = \rho_o V_o / 4 \quad (1)$$

where ρ_o is the initial density of the material and V_o is the initial volume of the element. The general expression for the volume is

$$V = \frac{1}{6} \begin{vmatrix} 1 & x_i & y_i & z_i \\ 1 & x_j & y_j & z_j \\ 1 & x_m & y_m & z_m \\ 1 & x_p & y_p & z_p \end{vmatrix} \quad (2)$$

When the elements are incorporated into an assemblage of elements, then the total mass at node i contains individual element masses from all elements that contain that node.

$$\bar{M}_i = \sum M_i \quad (3)$$

The volumetric strain and strain rate are obtained in the same manner as used for the 1D and 2D elements.

$$\epsilon_v = V / V_o - 1 \quad (4)$$

$$\dot{\epsilon}_v = (\epsilon_v^{t+\Delta t} - \epsilon_v^t) / \Delta t \quad (5)$$

In Equation 4, V and V_o are the current and initial element volumes; and in Equation 5, $\epsilon_v^{t+\Delta t}$ and ϵ_v^t are the volumetric strains at time $t + \Delta t$ and time t . The volumetric strains and strain rates are based on the initial configuration, as opposed to the shear and deviator strain rates which are based on the current configuration.

The strain rates are obtained from the current geometry of the element and the velocities of the nodes. If it is assumed the velocities vary linearly between the nodes, the x, y, and z velocities ($\dot{u}, \dot{v}, \dot{w}$) within each element can be expressed as

$$\dot{u} = \alpha_1 + \alpha_2 x + \alpha_3 y + \alpha_4 z \quad (6)$$

$$\dot{v} = \alpha_5 + \alpha_6 x + \alpha_7 y + \alpha_8 z \quad (7)$$

$$\dot{w} = \alpha_9 + \alpha_{10} x + \alpha_{11} y + \alpha_{12} z \quad (8)$$

where $\alpha_1 \dots \alpha_{12}$ are geometry and velocity-dependent constants for each element. It is possible to solve for $\alpha_1 \dots \alpha_4$ by substituting the x velocities and coordinates of the four nodes into Equation 6. This gives four equations and four unknowns so that the constants ($\alpha_1 \dots \alpha_4$) can be evaluated.

Equation 6 can then be expressed in terms of element geometry and nodal velocities.

$$\dot{u} = \frac{1}{6V} \left[(a_i + b_i x + c_i y + d_i z) \dot{u}_i + (a_j + b_j x + c_j y + d_j z) \dot{u}_j + (a_m + b_m x + c_m y + d_m z) \dot{u}_m + (a_p + b_p x + c_p y + d_p z) \dot{u}_p \right] \quad (9)$$

where V is the volume from Equation 2 and the geometry constants have the form

$$a_i = \begin{vmatrix} x_j & y_j & z_j \\ x_m & y_m & z_m \\ x_p & y_p & z_p \end{vmatrix} \quad (10)$$

$$b_i = - \begin{vmatrix} 1 & y_j & z_j \\ 1 & y_m & z_m \\ 1 & y_p & z_p \end{vmatrix} \quad (11)$$

$$c_i = \begin{vmatrix} 1 & x_j & z_j \\ 1 & x_m & z_m \\ 1 & x_p & z_p \end{vmatrix} \quad (12)$$

$$d_i = - \begin{vmatrix} 1 & x_j & y_j \\ 1 & x_m & y_m \\ 1 & x_p & y_p \end{vmatrix} \quad (13)$$

The remaining geometry-dependent constants (a_j , b_j , c_j , d_j , etc.) are obtained by a systematic interchange of signs and subscripts. The y and z velocities in Equations 7 and 8 are obtained in a similar manner and are identical to Equation 6 except the x velocities at the four nodes are replaced by the y and z velocities.

Another geometry constant is the altitude of the tetrahedral element. The altitude from node i to the plane defined by the other three nodes of the tetrahedron is

$$h_i = \frac{6V}{\sqrt{b_i^2 + c_i^2 + d_i^2}} \quad (14)$$

The other altitudes (h_j , h_m , h_p) are obtained by appropriately changing the subscripts of the geometry-dependent constants. The minimum of the four altitudes is designated as h , and it is used for the characteristic length in Equation 10 of subsection 3.8.1, for the integration time increment.

After the velocities are obtained, it is possible to determine the normal strain rates ($\dot{\epsilon}_x$, $\dot{\epsilon}_y$, $\dot{\epsilon}_z$), the shear strain rates ($\dot{\gamma}_{xy}$, $\dot{\gamma}_{xz}$, $\dot{\gamma}_{yz}$) and the spin rates (ω_x , ω_y , ω_z) of the element.

$$\dot{\epsilon}_x = \frac{\partial \dot{u}}{\partial x} = \frac{1}{6V} (b_i \dot{u}_i + b_j \dot{u}_j + b_m \dot{u}_m + b_p \dot{u}_p) \quad (15)$$

$$\dot{\epsilon}_y = \frac{\partial \dot{v}}{\partial y} = \frac{1}{6V} (c_i \dot{v}_i + c_j \dot{v}_j + c_m \dot{v}_m + c_p \dot{v}_p) \quad (16)$$

$$\dot{\epsilon}_z = \frac{\partial \dot{w}}{\partial z} = \frac{1}{6V} (d_i \dot{w}_i + d_j \dot{w}_j + d_m \dot{w}_m + d_p \dot{w}_p) \quad (17)$$

$$\dot{\gamma}_{xy} = \frac{\partial \dot{u}}{\partial y} + \frac{\partial \dot{v}}{\partial x} \quad (18)$$

$$\dot{\gamma}_{xz} = \frac{\partial \dot{u}}{\partial z} + \frac{\partial \dot{w}}{\partial x} \quad (19)$$

$$\dot{\gamma}_{yz} = \frac{\partial \dot{v}}{\partial z} + \frac{\partial \dot{w}}{\partial y} \quad (20)$$

$$\omega_x = \frac{1}{2} \left(\frac{\partial \dot{w}}{\partial y} - \frac{\partial \dot{v}}{\partial z} \right) \quad (21)$$

$$\omega_y = \frac{1}{2} \left(\frac{\partial \dot{u}}{\partial z} - \frac{\partial \dot{w}}{\partial x} \right) \quad (22)$$

$$\omega_z = \frac{1}{2} \left(\frac{\partial \dot{v}}{\partial x} - \frac{\partial \dot{u}}{\partial y} \right) \quad (23)$$

It can be seen that Equations 15–23 are derivatives of linear functions and therefore give constant values within the element.

The equivalent strain rate ($\bar{\dot{\epsilon}}$) and deviator strain rates ($\dot{\epsilon}_x, \dot{\epsilon}_y, \dot{\epsilon}_z$) are determined in an identical manner as shown previously for 1D and 2D geometry.

$$\bar{\dot{\epsilon}} = \sqrt{\frac{2}{9} \left[(\dot{\epsilon}_x - \dot{\epsilon}_y)^2 + (\dot{\epsilon}_x - \dot{\epsilon}_z)^2 + (\dot{\epsilon}_y - \dot{\epsilon}_z)^2 + \frac{3}{2} (\dot{\gamma}_{xy}^2 + \dot{\gamma}_{xz}^2 + \dot{\gamma}_{yz}^2) \right]} \quad (24)$$

The constitutive models also require deviator strain rates, which are expressed as

$$\dot{\epsilon}_x = \dot{\epsilon}_x - \dot{\epsilon}_{ave} \quad (25)$$

$$\dot{\epsilon}_y = \dot{\epsilon}_y - \dot{\epsilon}_{ave} \quad (26)$$

$$\dot{\epsilon}_z = \dot{\epsilon}_z - \dot{\epsilon}_{ave} \quad (27)$$

where $\dot{\epsilon}_{ave} = (\dot{\epsilon}_x + \dot{\epsilon}_y + \dot{\epsilon}_z) / 3$. Note that the sum of the deviator strain rates is $\dot{\epsilon}_x + \dot{\epsilon}_y + \dot{\epsilon}_z = 0$.

The stresses in the elements are determined from the strains, strain rates, temperatures, pressures, internal energies, and material constants. This is identical to the 1D and 2D algorithms for solid elements, except that all three shear stresses are present. The three normal stresses are generally expressed as

$$\sigma_x = s_x - (P + Q) \quad (28)$$

$$\sigma_y = s_y - (P + Q) \quad (29)$$

$$\sigma_z = s_z - (P + Q) \quad (30)$$

where s_x , s_y , and s_z are the normal deviator stresses, P is the hydrostatic pressure and Q is the artificial viscosity. These are described in detail in Section 6.

Trial values of the deviator stresses and shear stresses at time $t + \Delta t$ are

$$s_x^{t+\Delta t} = s_x^t + 2G\dot{e}_x\Delta t + \Delta s_x \quad (31)$$

$$s_y^{t+\Delta t} = s_y^t + 2G\dot{e}_y\Delta t + \Delta s_y \quad (32)$$

$$s_z^{t+\Delta t} = s_z^t + 2G\dot{e}_z\Delta t + \Delta s_z \quad (33)$$

$$\tau_{xy}^{t+\Delta t} = \tau_{xy}^t + G\dot{\gamma}_{xy}\Delta t + \Delta\tau_{xy} \quad (34)$$

$$\tau_{xz}^{t+\Delta t} = \tau_{xz}^t + G\dot{\gamma}_{xz}\Delta t + \Delta\tau_{xz} \quad (35)$$

$$\tau_{yz}^{t+\Delta t} = \tau_{yz}^t + G\dot{\gamma}_{yz}\Delta t + \Delta\tau_{yz} \quad (36)$$

In Equation 31 the first term (s_x^t) is the normal stress at the previous time and the second term ($2G\dot{e}_x\Delta t$) is the incremental stress due to the incremental strain ($\dot{e}_x\Delta t$) during that time increment, where G is the elastic shear modulus and Δt is the integration time increment. The third term (Δs_x) is due to shear stresses from the previous time increment, which now act as normal stresses due to the new orientation of the element caused by an incremental rotation ($\omega_y\Delta t, \omega_z\Delta t$) during the time increment. The remaining normal stresses and shear stresses have a similar form.

The correction terms for element rotations are

$$\Delta s_x = 2 \left(\omega_y \tau_{xz}^t - \omega_z \tau_{xy}^t \right) \Delta t \quad (37)$$

$$\Delta s_y = 2 \left(\omega_z \tau_{xy}^t - \omega_x \tau_{yz}^t \right) \Delta t \quad (38)$$

$$\Delta s_z = 2 \left(\omega_x \tau_{yz}^t - \omega_y \tau_{xz}^t \right) \Delta t \quad (39)$$

$$\Delta \tau_{xy} = \left[\omega_z \left(s_x^t - s_y^t \right) + \omega_y \tau_{yz}^t - \omega_x \tau_{xz}^t \right] \Delta t \quad (40)$$

$$\Delta \tau_{xz} = \left[\omega_y \left(s_z^t - s_x^t \right) + \omega_x \tau_{xy}^t - \omega_z \tau_{yz}^t \right] \Delta t \quad (41)$$

$$\Delta \tau_{yz} = \left[\omega_x \left(s_y^t - s_z^t \right) + \omega_z \tau_{xz}^t - \omega_y \tau_{xy}^t \right] \Delta t \quad (42)$$

Equations 31–36 assume an elastic response of the material. If the strength of the material is exceeded, then plastic flow (or fracture) will occur. The Von Mises yield criterion is used to determine an equivalent stress, $\bar{\sigma}$, that can be compared to the uniaxial tensile (or compressive) strength of the material. The general form of the equivalent stress is

$$\bar{\sigma} = \sqrt{\frac{1}{2} \left[\left(\sigma_x - \sigma_y \right)^2 + \left(\sigma_x - \sigma_z \right)^2 + \left(\sigma_y - \sigma_z \right)^2 + 6 \left(\tau_{xy}^2 + \tau_{xz}^2 + \tau_{yz}^2 \right) \right]} \quad (43)$$

Using deviator stresses (instead of total stresses), Equation 43 can be rewritten as

$$\bar{\sigma} = \sqrt{\frac{3}{2} \left(s_x^2 + s_y^2 + s_z^2 \right) + 3 \left(\tau_{xy}^2 + \tau_{xz}^2 + \tau_{yz}^2 \right)} \quad (44)$$

If $\bar{\sigma}$ is not greater than the equivalent tensile strength of the material, σ , the final deviator and shear stresses are as given in Equations 31–36. If $\bar{\sigma}$ is greater than σ , then the stresses in Equations 31–36 are multiplied by the factor $(\sigma / \bar{\sigma})$. When the reduced deviator and shear stresses are put into Equation 44, the result is always $\bar{\sigma} = \sigma$. This is known as the radial return algorithm. The various material strength models for σ are presented in Section 6.

During plastic flow, it is sometimes necessary to determine the equivalent plastic strain for strain hardening effects on the strength of the material or to determine if the material has failed. The first step in this process is to adjust the total strain rates to plastic strain rates by subtracting out the elastic portion of the strain rates.

$$\dot{\epsilon}_x^p = \dot{\epsilon}_x - (\dot{s}_x^{t+\Delta t} - s_x^t - \Delta s_x) / 2G\Delta t \quad (45)$$

$$\dot{\epsilon}_y^p = \dot{\epsilon}_y - (\dot{s}_y^{t+\Delta t} - s_y^t - \Delta s_y) / 2G\Delta t \quad (46)$$

$$\dot{\epsilon}_z^p = \dot{\epsilon}_z - (\dot{s}_z^{t+\Delta t} - s_z^t - \Delta s_z) / 2G\Delta t \quad (47)$$

$$\dot{\gamma}_{xy}^p = \dot{\gamma}_{xy} - (\dot{\tau}_{xy}^{t+\Delta t} - \tau_{xy}^t - \Delta \tau_{xy}) / G\Delta t \quad (48)$$

$$\dot{\gamma}_{xz}^p = \dot{\gamma}_{xz} - (\dot{\tau}_{xz}^{t+\Delta t} - \tau_{xz}^t - \Delta \tau_{xz}) / G\Delta t \quad (49)$$

$$\dot{\gamma}_{yz}^p = \dot{\gamma}_{yz} - (\dot{\tau}_{yz}^{t+\Delta t} - \tau_{yz}^t - \Delta \tau_{yz}) / G\Delta t \quad (50)$$

The general expression for the equivalent plastic strain rate is

$$\bar{\dot{\epsilon}}_p = \sqrt{\frac{2}{9} \left[(\dot{\epsilon}_x^p - \dot{\epsilon}_y^p)^2 + (\dot{\epsilon}_x^p - \dot{\epsilon}_z^p)^2 + (\dot{\epsilon}_y^p - \dot{\epsilon}_z^p)^2 + \frac{3}{2} (\dot{\gamma}_{xy}^p{}^2 + \dot{\gamma}_{xz}^p{}^2 + \dot{\gamma}_{yz}^p{}^2) \right]} \quad (51)$$

The equivalent plastic strain, $\bar{\epsilon}_p$, is then obtained by integrating $\bar{\dot{\epsilon}}_p$ with respect to time.

$$\bar{\epsilon}_p^{t+\Delta t} = \bar{\epsilon}_p^t + \bar{\dot{\epsilon}}_p \Delta t \quad (52)$$

After the element stresses are determined, the concentrated nodal forces can be obtained. These forces are statically equivalent to the distributed stresses within the element. They are dependent on the displaced element geometry and the magnitude of the stresses. The forces in the x, y and z directions at node i of an element are given by

$$F_x^i = -\frac{1}{6} (b_i \sigma_i + c_i \tau_{xy} + d_i \tau_{xz}) \quad (53)$$

$$F_y^i = -\frac{1}{6}(c_i\sigma_y + b_i\tau_{xy} + d_i\tau_{yz}) \quad (54)$$

$$F_z^i = -\frac{1}{6}(d_i\sigma_z + c_i\tau_{yz} + b_i\tau_{xz}) \quad (55)$$

The geometry-dependent constants (b_i , c_i , d_i) are again identical to those used for calculation of the strain rates and altitudes. The forces at the other nodes are readily obtained by changing subscripts.

Note that $F_x^i + F_x^j + F_x^m + F_x^p \equiv 0$ for each element, and this ensures equilibrium in the system. A similar equilibrium exists in the y and z directions. This results in conservation of momentum if there are no external forces or restraints. The final net forces on node i are

$$\bar{F}_x^i = \sum F_x^i \quad (56)$$

$$\bar{F}_y^i = \sum F_y^i \quad (57)$$

$$\bar{F}_z^i = \sum F_z^i \quad (58)$$

It is also possible to add external forces through applied pressures.

The heat conduction algorithm can be obtained straightforwardly from the 1D heat conduction algorithm (subsection 3.1.3) and the strain rate equations in this subsection. The 2D algorithm is reported in Reference 7. Substituting temperatures for velocities in Equation 9 gives

$$T = \frac{1}{6V} \left[(a_i + b_i x + c_i y + d_i z)T_i + (a_j + b_j x + c_j y + d_j z)T_j \right. \\ \left. + (a_m + b_m x + c_m y + d_m z)T_m + (a_p + b_p x + c_p y + d_p z)T_p \right] \quad (59)$$

Other than the nodal temperatures (T_i , T_j , T_m , T_p) all of the other terms are as described for Equation 9.

The instantaneous heat flows in the x, y, z directions can then be obtained from

$$q_x = -k \frac{\partial T}{\partial x} = -k(b_i T_i + b_j T_j + b_m T_m + b_p T_p) / 6V \quad (60)$$

$$q_y = -k \frac{\partial T}{\partial y} = -k(c_i T_i + c_j T_j + c_m T_m + c_p T_p) / 6V \quad (61)$$

$$q_z = -k \frac{\partial T}{\partial z} = -k(d_i T_i + d_j T_j + d_m T_m + d_p T_p) / 6V \quad (62)$$

The incremental increase in thermal energy at the nodes can be obtained by integrating the heat flow with respect to area and time.

$$\Delta Q_i = \frac{1}{6} (q_x b_i + q_y c_i + q_z d_i) \Delta t + \Delta Q_e / 4 \quad (63)$$

Note that the internal energy generated in the element during the previous time increment, ΔQ_e , is distributed equally ($\Delta Q_e/4$) to all four nodes.

The remaining equations are similar to those in 1D and 2D. The updated temperatures of the nodes have the form

$$T_i^{t+\Delta t} = T_i^t + \sum \Delta Q_i / \bar{M}_i c_{pi} \quad (64)$$

where $T_i^{t+\Delta t}$ and T_i^t are the temperatures of the nodes at times $t+\Delta t$ and t , $\sum \Delta Q_i$ is the sum of the incremental heat contributed by all elements that contain node i , \bar{M}_i is the total mass of node i , and c_{pi} is the specific heat of node i .

The internal energy in an element can be used to compute element pressures. To account for the flow of internal energy through the grid, the element temperature is assumed to be the average of the nodal temperatures.

$$\bar{T} = (T_i + T_j + T_m + T_p) / 4 \quad (65)$$

The internal energy (per initial volume) is given by

$$E_s = (\bar{T} - T_o) \rho_o c_p \quad (66)$$

where T_0 is the initial temperature (where $E_s = 0$), ρ_0 is the initial density, and c_p is the specific heat of the element material.

The integration time increment must also be bounded to ensure that the computations remain stable for heat conduction (References 6 and 7). The heat conduction portion requires

$$\Delta t \leq \rho c_p h_{\min}^2 / 4k \quad (67)$$

where h_{\min} is the minimum altitude of the element (as provided in Equation 14) and the other terms recently have been defined. This is analogous to the time increment restriction for wave propagation in Equation 10 of subsection 3.8.1. Unless h_{\min} is very small, the wave propagation restriction is much more severe than the heat conduction restriction.

3.8.5 Brick Elements

The 3D brick element is shown in Figure 19. This element was developed by Flanagan and Belytschko (Reference 26) and the nodal numbering in Figure 19 is as used in their paper. The EPIC code uses a different nodal numbering arrangement for the user, and the transformation is made within the code. In Figure 19, nodes 5, 6, 7, and 8 are clockwise when viewed from node 1. The coordinates of node 1 are x_1, y_1, z_1 , and the corresponding velocities are $\dot{u}_1, \dot{v}_1, \dot{w}_1$ (which are identical to $\dot{x}_1, \dot{y}_1, \dot{z}_1$).

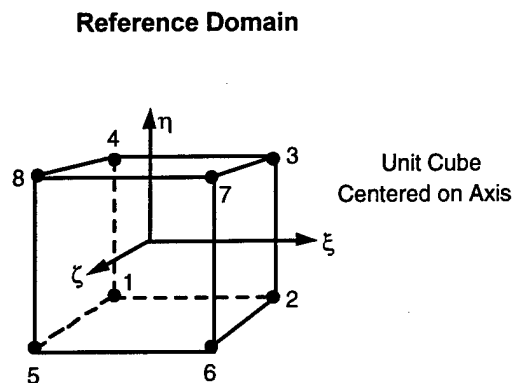
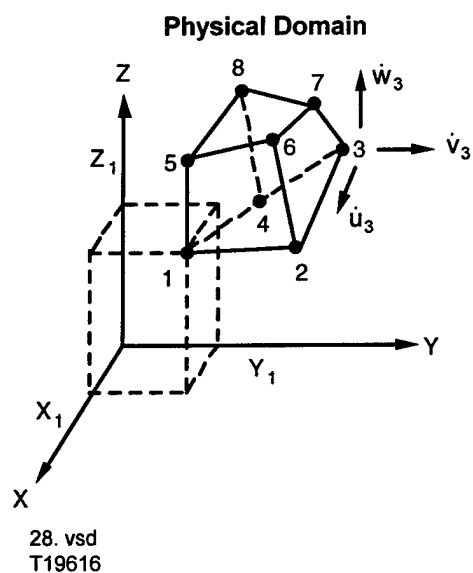
The mass at node i , for an individual brick element, is simply

$$M_i = \rho_0 V_0 / 8 \quad (1)$$

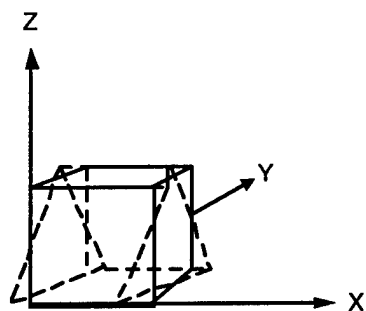
where ρ_0 is the initial density of the material and V_0 is the initial volume of the element. The volume is a complex expression that is presented later.

The strain rates are obtained from the current geometry of the element and the velocities of the nodes. Note that the geometry is expressed in a reference domain coordinate system as a unit cube, as shown in the upper right portion of Figure 19. The velocity in the x direction is

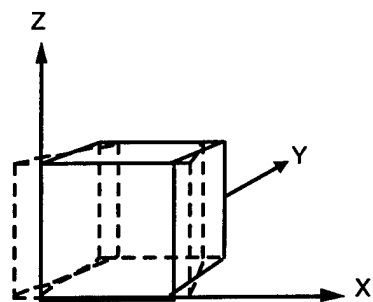
$$\dot{u} = \phi_1 \dot{u}_1 + \phi_2 \dot{u}_2 + \phi_3 \dot{u}_3 + \phi_4 \dot{u}_4 + \phi_5 \dot{u}_5 + \phi_6 \dot{u}_6 + \phi_7 \dot{u}_7 + \phi_8 \dot{u}_8 \quad (2)$$



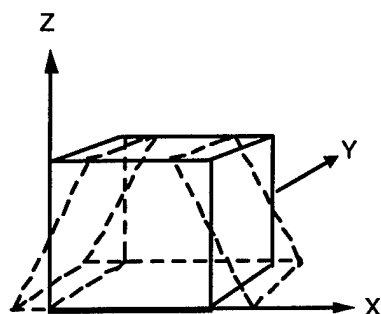
Hourglass Modes



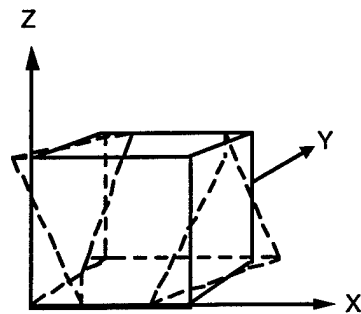
Mode 1 (X)



Mode 2 (X)



Mode 3 (X)



Mode 4 (X)

29.vsd
T19616

Figure 19. Description of the 3D Brick Element

where the shape functions are

$$\phi_1 = \frac{1}{8} - \frac{1}{4}\xi + \frac{1}{4}\eta - \frac{1}{4}\zeta - \frac{1}{2}\eta\zeta + \frac{1}{2}\zeta\xi - \frac{1}{2}\xi\eta + \xi\eta\zeta \quad (3a)$$

$$\phi_2 = \frac{1}{8} + \frac{1}{4}\xi + \frac{1}{4}\eta - \frac{1}{4}\zeta - \frac{1}{2}\eta\zeta - \frac{1}{2}\zeta\xi + \frac{1}{2}\xi\eta - \xi\eta\zeta \quad (3b)$$

$$\phi_3 = \frac{1}{8} + \frac{1}{4}\xi + \frac{1}{4}\eta + \frac{1}{4}\zeta + \frac{1}{2}\eta\zeta + \frac{1}{2}\zeta\xi + \frac{1}{2}\xi\eta + \xi\eta\zeta \quad (3c)$$

$$\phi_4 = \frac{1}{8} - \frac{1}{4}\xi + \frac{1}{4}\eta + \frac{1}{4}\zeta + \frac{1}{2}\eta\zeta - \frac{1}{2}\zeta\xi - \frac{1}{2}\xi\eta - \xi\eta\zeta \quad (3d)$$

$$\phi_5 = \frac{1}{8} - \frac{1}{4}\xi - \frac{1}{4}\eta - \frac{1}{4}\zeta + \frac{1}{2}\eta\zeta + \frac{1}{2}\zeta\xi + \frac{1}{2}\xi\eta - \xi\eta\zeta \quad (3e)$$

$$\phi_6 = \frac{1}{8} + \frac{1}{4}\xi - \frac{1}{4}\eta - \frac{1}{4}\zeta + \frac{1}{2}\eta\zeta - \frac{1}{2}\zeta\xi - \frac{1}{2}\xi\eta + \xi\eta\zeta \quad (3f)$$

$$\phi_7 = \frac{1}{8} + \frac{1}{4}\xi - \frac{1}{4}\eta + \frac{1}{4}\zeta - \frac{1}{2}\eta\zeta + \frac{1}{2}\zeta\xi - \frac{1}{2}\xi\eta - \xi\eta\zeta \quad (3g)$$

$$\phi_8 = \frac{1}{8} - \frac{1}{4}\xi - \frac{1}{4}\eta + \frac{1}{4}\zeta - \frac{1}{2}\eta\zeta - \frac{1}{2}\zeta\xi + \frac{1}{2}\xi\eta + \xi\eta\zeta \quad (3h)$$

where ζ , ξ , and η are the coordinates of the reference domain as shown in Figure 19. The y and z velocities (\dot{v} and \dot{w}) have the same form as Equation 2. The x nodal velocities ($\dot{u}_1 \dots \dot{u}_8$) are simply replaced by the y nodal velocities ($\dot{v}_1 \dots \dot{v}_8$) and the z nodal velocities ($\dot{w}_1 \dots \dot{w}_8$).

For the physical domain it is necessary to determine the [B] matrix for the geometry constants.

$$[B] = \begin{bmatrix} B_{x1} & B_{x2} & B_{x3} & B_{x4} & B_{x5} & B_{x6} & B_{x7} & B_{x8} \\ B_{y1} & B_{y2} & B_{y3} & B_{y4} & B_{y5} & B_{y6} & B_{y7} & B_{y8} \\ B_{z1} & B_{z2} & B_{z3} & B_{z4} & B_{z5} & B_{z6} & B_{z7} & B_{z8} \end{bmatrix} \quad (4)$$

where

$$B_{x1} = y_2[(z_6 - z_3) + (z_5 - z_4)] + y_3(z_2 - z_4) + y_4[(z_3 - z_8) + (z_2 - z_5)] \\ + y_5[(z_8 - z_6) + (z_4 - z_2)] + y_6(z_5 - z_2) + y_8(z_4 - z_5) \quad (5a)$$

$$B_{x2} = y_3[(z_7 - z_4) + (z_6 - z_1)] + y_4(z_3 - z_1) + y_1[(z_4 - z_5) + (z_3 - z_6)] \\ + y_6[(z_5 - z_7) + (z_1 - z_3)] + y_7(z_6 - z_3) + y_5(z_1 - z_6) \quad (5b)$$

$$B_{x3} = y_4[(z_8 - z_1) + (z_7 - z_2)] + y_1(z_4 - z_2) + y_2[(z_1 - z_6) + (z_2 - z_7)] \\ + y_7[(z_6 - z_8) + (z_2 - z_4)] + y_8(z_7 - z_4) + y_6(z_2 - z_7) \quad (5c)$$

$$B_{x4} = y_1[(z_5 - z_2) + (z_8 - z_3)] + y_2(z_1 - z_3) + y_3[(z_2 - z_7) + (z_1 - z_8)] \\ + y_8[(z_7 - z_5) + (z_3 - z_1)] + y_5(z_8 - z_1) + y_7(z_3 - z_8) \quad (5d)$$

$$B_{x5} = y_8[(z_4 - z_5) + (z_1 - z_6)] + y_7(z_8 - z_6) + y_6[(z_7 - z_2) + (z_8 - z_1)] \\ + y_1[(z_2 - z_4) + (z_6 - z_8)] + y_4(z_1 - z_8) + y_2(z_6 - z_1) \quad (5e)$$

$$B_{x6} = y_5[(z_1 - z_8) + (z_2 - z_7)] + y_8(z_5 - z_7) + y_7[(z_8 - z_3) + (z_5 - z_2)] \\ + y_2[(z_3 - z_1) + (z_7 - z_5)] + y_1(z_2 - z_5) + y_3(z_7 - z_2) \quad (5f)$$

$$B_{x7} = y_6[(z_2 - z_5) + (z_3 - z_8)] + y_5(z_6 - z_8) + y_8[(z_5 - z_4) + (z_6 - z_3)] \\ + y_3[(z_4 - z_2) + (z_8 - z_6)] + y_2(z_3 - z_6) + y_4(z_8 - z_3) \quad (5g)$$

$$B_{x8} = y_7[(z_3 - z_6) + (z_4 - z_5)] + y_6(z_7 - z_5) + y_5[(z_6 - z_1) + (z_7 - z_4)] \\ + y_4[(z_1 - z_3) + (z_5 - z_7)] + y_3(z_4 - z_7) + y_1(z_5 - z_4) \quad (5h)$$

For $B_{y1} \dots B_{y8}$ replace y and z with z and x , and for $B_{z1} \dots B_{z8}$ replace y and z with x and y .

The volume can now be determined using any of the following three expressions.

$$V = \frac{1}{12} \{ B_{x1}x_1 + B_{x2}x_2 + B_{x3}x_3 + B_{x4}x_4 + B_{x5}x_5 + B_{x6}x_6 + B_{x7}x_7 + B_{x8}x_8 \} \quad (6a)$$

$$V = \frac{1}{12} \{ B_{y1}y_1 + B_{y2}y_2 + B_{y3}y_3 + B_{y4}y_4 + B_{y5}y_5 + B_{y6}y_6 + B_{y7}y_7 + B_{y8}y_8 \} \quad (6b)$$

$$V = \frac{1}{12} \{ B_{z1}z_1 + B_{z2}z_2 + B_{z3}z_3 + B_{z4}z_4 + B_{z5}z_5 + B_{z6}z_6 + B_{z7}z_7 + B_{z8}z_8 \} \quad (6c)$$

The final geometric term is the characteristic element length, h , that is used for the artificial viscosity and the integration time increment.

$$h = 12V \sqrt{\frac{1}{2B_{xyz}}} \quad (7)$$

where V is the element volume and

$$\begin{aligned} B_{xyz} = & B_{x1}^2 + B_{x2}^2 + B_{x3}^2 + B_{x4}^2 + B_{x5}^2 + B_{x6}^2 + B_{x7}^2 + B_{x8}^2 \\ & + B_{y1}^2 + B_{y2}^2 + B_{y3}^2 + B_{y4}^2 + B_{y5}^2 + B_{y6}^2 + B_{y7}^2 + B_{y8}^2 \\ & + B_{z1}^2 + B_{z2}^2 + B_{z3}^2 + B_{z4}^2 + B_{z5}^2 + B_{z6}^2 + B_{z7}^2 + B_{z8}^2 \end{aligned} \quad (8)$$

The three normal strain rates $(\dot{\epsilon}_x, \dot{\epsilon}_y, \dot{\epsilon}_z)$ are obtained by taking derivatives of the velocity fields in the physical domain.

$$\dot{\epsilon}_x = \frac{\partial \dot{u}}{\partial x} = \frac{1}{12V} [B_{x1}\dot{u}_1 + B_{x2}\dot{u}_2 + B_{x3}\dot{u}_3 + B_{x4}\dot{u}_4 + B_{x5}\dot{u}_5 + B_{x6}\dot{u}_6 + B_{x7}\dot{u}_7 + B_{x8}\dot{u}_8] \quad (9)$$

$$\dot{\epsilon}_y = \frac{\partial \dot{v}}{\partial y} = \frac{1}{12V} [B_{y1}\dot{v}_1 + B_{y2}\dot{v}_2 + B_{y3}\dot{v}_3 + B_{y4}\dot{v}_4 + B_{y5}\dot{v}_5 + B_{y6}\dot{v}_6 + B_{y7}\dot{v}_7 + B_{y8}\dot{v}_8] \quad (10)$$

$$\begin{aligned} \dot{\epsilon}_z = \frac{\partial \dot{w}}{\partial z} = & \frac{1}{12V} [B_{z1}\dot{w}_1 + B_{z2}\dot{w}_2 + B_{z3}\dot{w}_3 + B_{z4}\dot{w}_4 + B_{z5}\dot{w}_5 + B_{z6}\dot{w}_6 \\ & + B_{z7}\dot{w}_7 + B_{z8}\dot{w}_8] \end{aligned} \quad (11)$$

The x velocity in Equation 9 is expressed as a function of the reference domain coordinates in Equation 2. The derivatives of the terms in Equation 2 $\left(\frac{\partial\phi_1}{\partial x} \dots \frac{\partial\phi_8}{\partial x}\right)$ are replaced by the physical domain geometry constants in Equation 9 $\left(\frac{B_{x1}}{12V} \dots \frac{B_{x8}}{12V}\right)$. For the y direction, $\frac{\partial\phi_1}{\partial y} \dots \frac{\partial\phi_8}{\partial y}$ are replaced by $\frac{B_{y1}}{12V} \dots \frac{B_{y8}}{12V}$ in Equation 10 and for the z direction, $\frac{\partial\phi_1}{\partial z} \dots \frac{\partial\phi_8}{\partial z}$ are replaced by $\frac{B_{z1}}{12V} \dots \frac{B_{z8}}{12V}$ in Equation 11.

The three shear strain rates $(\dot{\gamma}_{xy}, \dot{\gamma}_{xz}, \dot{\gamma}_{yz})$ and the three rotational spin rates $(\dot{\omega}_x, \dot{\omega}_y, \dot{\omega}_z)$ are determined in a similar manner.

$$\dot{\gamma}_{xy} = \frac{\partial \dot{u}}{\partial y} + \frac{\partial \dot{v}}{\partial x} \quad (12)$$

$$\dot{\gamma}_{xz} = \frac{\partial \dot{u}}{\partial z} + \frac{\partial \dot{w}}{\partial x} \quad (13)$$

$$\dot{\gamma}_{yz} = \frac{\partial \dot{v}}{\partial z} + \frac{\partial \dot{w}}{\partial y} \quad (14)$$

$$\dot{\omega}_x = \frac{1}{2} \left(\frac{\partial \dot{w}}{\partial y} - \frac{\partial \dot{v}}{\partial z} \right) \quad (15)$$

$$\dot{\omega}_y = \frac{1}{2} \left(\frac{\partial \dot{u}}{\partial z} - \frac{\partial \dot{w}}{\partial x} \right) \quad (16)$$

$$\dot{\omega}_z = \frac{1}{2} \left(\frac{\partial \dot{v}}{\partial x} - \frac{\partial \dot{u}}{\partial y} \right) \quad (17)$$

The stresses are determined with exactly the same procedures used for the tetrahedral elements in subsection 3.8.4.

The x direction forces on each of the eight nodes are as follows:

$$F_{x1} = -\frac{1}{12} [B_{x1}\sigma_x + B_{y1}\tau_{xy} + B_{z1}\tau_{xz}] - F_{x1}^{HG} \quad (18)$$

$$F_{x2} = -\frac{1}{12} [B_{x2}\sigma_x + B_{y2}\tau_{xy} + B_{z2}\tau_{xz}] - F_{x2}^{HG} \quad (19)$$

$$F_{x3} = -\frac{1}{12} [B_{x3}\sigma_x + B_{y3}\tau_{xy} + B_{z3}\tau_{xz}] - F_{x3}^{HG} \quad (20)$$

$$F_{x4} = -\frac{1}{12} [B_{x4}\sigma_x + B_{y4}\tau_{xy} + B_{z4}\tau_{xz}] - F_{x4}^{HG} \quad (21)$$

$$F_{x5} = -\frac{1}{12} [B_{x5}\sigma_x + B_{y5}\tau_{xy} + B_{z5}\tau_{xz}] - F_{x5}^{HG} \quad (22)$$

$$F_{x6} = -\frac{1}{12} [B_{x6}\sigma_x + B_{y6}\tau_{xy} + B_{z6}\tau_{xz}] - F_{x6}^{HG} \quad (23)$$

$$F_{x7} = -\frac{1}{12} [B_{x7}\sigma_x + B_{y7}\tau_{xy} + B_{z7}\tau_{xz}] - F_{x7}^{HG} \quad (24)$$

$$F_{x8} = -\frac{1}{12} [B_{x8}\sigma_x + B_{y8}\tau_{xy} + B_{z8}\tau_{xz}] - F_{x8}^{HG} \quad (25)$$

where $B_{x1} \dots B_{z8}$ are the geometry constants, σ_x is the normal stress in the x direction and τ_{xy} and τ_{xz} are shear stresses. The hourglass forces ($F_{x1}^{HG} \dots F_{x8}^{HG}$) are required to resist hourglassing deformations and they are presented later. The y-direction forces ($F_{y1} \dots F_{y8}$) are obtained by replacing σ_x , τ_{xy} , and τ_{xz} by τ_{xy} , σ_y , and τ_{yz} respectively, and the z-direction forces ($F_{z1} \dots F_{z8}$) are obtained by replacing σ_x , τ_{xy} , and τ_{xz} with τ_{xz} , τ_{yz} , and σ_z , respectively.

A 3D brick element can experience hourglass deformations in a manner similar to a 2D quad element. In 3D, however, it is much more complex. The lower portion of Figure 19 shows four hourglass modes in the x direction. The same four modes occur in the y direction and in the z direction, for a total of 12 hourglass modes.

The following four steps are required for the hourglass algorithm:

- Compute the hourglass shape vector (γ)
- Compute the hourglass modal velocity (\dot{q})
- Compute the hourglass resistance stress (Q)
- Compute the hourglass resistance force (F^{HG}).

The hourglass shape vector for mode 1 is

$$\gamma_{11} = 1 - \frac{1}{12V} [B_{x1}\bar{x} + B_{y1}\bar{y} + B_{z1}\bar{z}] \quad (26a)$$

$$\gamma_{12} = 1 - \frac{1}{12V} [B_{x2}\bar{x} + B_{y2}\bar{y} + B_{z2}\bar{z}] \quad (26b)$$

$$\gamma_{13} = -1 - \frac{1}{12V} [B_{x3}\bar{x} + B_{y3}\bar{y} + B_{z3}\bar{z}] \quad (26c)$$

$$\gamma_{14} = -1 - \frac{1}{12V} [B_{x4}\bar{x} + B_{y4}\bar{y} + B_{z4}\bar{z}] \quad (26d)$$

$$\gamma_{15} = -1 - \frac{1}{12V} [B_{x5}\bar{x} + B_{y5}\bar{y} + B_{z5}\bar{z}] \quad (26e)$$

$$\gamma_{16} = -1 - \frac{1}{12V} [B_{x6}\bar{x} + B_{y6}\bar{y} + B_{z6}\bar{z}] \quad (26f)$$

$$\gamma_{17} = 1 - \frac{1}{12V} [B_{x7}\bar{x} + B_{y7}\bar{y} + B_{z7}\bar{z}] \quad (26g)$$

$$\gamma_{18} = 1 - \frac{1}{12V} [B_{x8}\bar{x} + B_{y8}\bar{y} + B_{z8}\bar{z}] \quad (26h)$$

where $B_{x1} \dots B_{z8}$ are the geometry constants and

$$\bar{x} = x_1 + x_2 - x_3 - x_4 - x_5 - x_6 + x_7 + x_8 \quad (27)$$

$$\bar{y} = y_1 + y_2 - y_3 - y_4 - y_5 - y_6 + y_7 + y_8 \quad (28)$$

$$\bar{z} = z_1 + z_2 - z_3 - z_4 - z_5 - z_6 + z_7 + z_8 \quad (29)$$

The shape vectors $(\gamma_{11} \dots \gamma_{18})$ in Equation 26 are not related to the shear strain rates $(\dot{\gamma}_{xy}, \dot{\gamma}_{xz}, \dot{\gamma}_{yz})$ in Equations 10–12. The shape vectors for modes 2, 3, and 4 ($\gamma_{21} \dots \gamma_{28}$, $\gamma_{31} \dots \gamma_{38}$, and $\gamma_{41} \dots \gamma_{48}$) are obtained in a similar manner.

The hourglass modal velocities for the four x modes in Figure 19 are

$$\dot{q}_{x1} = \frac{1}{\sqrt{8}} [\gamma_{11} \dot{u}_1 + \gamma_{12} \dot{u}_2 + \gamma_{13} \dot{u}_3 + \gamma_{14} \dot{u}_4 + \gamma_{15} \dot{u}_5 + \gamma_{16} \dot{u}_6 + \gamma_{17} \dot{u}_7 + \gamma_{18} \dot{u}_8] \quad (30)$$

$$\dot{q}_{x2} = \frac{1}{\sqrt{8}} [\gamma_{21} \dot{u}_1 + \gamma_{22} \dot{u}_2 + \gamma_{23} \dot{u}_3 + \gamma_{24} \dot{u}_4 + \gamma_{25} \dot{u}_5 + \gamma_{26} \dot{u}_6 + \gamma_{27} \dot{u}_7 + \gamma_{28} \dot{u}_8] \quad (31)$$

$$\dot{q}_{x3} = \frac{1}{\sqrt{8}} [\gamma_{31} \dot{u}_1 + \gamma_{32} \dot{u}_2 + \gamma_{33} \dot{u}_3 + \gamma_{34} \dot{u}_4 + \gamma_{35} \dot{u}_5 + \gamma_{36} \dot{u}_6 + \gamma_{37} \dot{u}_7 + \gamma_{38} \dot{u}_8] \quad (32)$$

$$\dot{q}_{x4} = \frac{1}{\sqrt{8}} [\gamma_{41} \dot{u}_1 + \gamma_{42} \dot{u}_2 + \gamma_{43} \dot{u}_3 + \gamma_{44} \dot{u}_4 + \gamma_{45} \dot{u}_5 + \gamma_{46} \dot{u}_6 + \gamma_{47} \dot{u}_7 + \gamma_{48} \dot{u}_8] \quad (33)$$

The y modal velocities $(\dot{q}_{y1} \dots \dot{q}_{y4})$ are obtained by replacing \dot{u} with \dot{v} , and the z modal velocities $(\dot{q}_{z1} \dots \dot{q}_{z4})$ are obtained by replacing \dot{u} with \dot{w} .

The resisting stress for the first x mode is

$$Q_{x1} = C_H \rho c_s \dot{q}_{x1} \sqrt{B_x / 864} \quad (34)$$

where C_H is an input hourglass viscosity coefficient, c_s is the sound velocity of the material, ρ is the density of the material, and

$$B_x = [B_{x1}^2 + B_{x2}^2 + B_{x3}^2 + B_{x4}^2 + B_{x5}^2 + B_{x6}^2 + B_{x7}^2 + B_{x8}^2] \quad (35)$$

The resistance stresses for the other three x modes (Q_{x2} , Q_{x3} , Q_{x4}) are obtained by replacing \dot{q}_{x1} by the other modal velocities $(\dot{q}_{x2}$, \dot{q}_{x3} , $\dot{q}_{x4})$. The y and z modes are obtained in a similar manner.

Now the forces to resist hourglassing can be determined and substituted into Equations 18–25.

$$F_{x1}^{HG} = \frac{1}{\sqrt{8}} [Q_{x1}\gamma_{11} + Q_{x2}\gamma_{21} + Q_{x3}\gamma_{31} + Q_{x4}\gamma_{41}] \quad (36)$$

$$F_{x2}^{HG} = \frac{1}{\sqrt{8}} [Q_{x1}\gamma_{12} + Q_{x2}\gamma_{22} + Q_{x3}\gamma_{32} + Q_{x4}\gamma_{42}] \quad (37)$$

$$F_{x3}^{HG} = \frac{1}{\sqrt{8}} [Q_{x1}\gamma_{13} + Q_{x2}\gamma_{23} + Q_{x3}\gamma_{33} + Q_{x4}\gamma_{43}] \quad (38)$$

$$F_{x4}^{HG} = \frac{1}{\sqrt{8}} [Q_{x1}\gamma_{14} + Q_{x2}\gamma_{24} + Q_{x3}\gamma_{34} + Q_{x4}\gamma_{44}] \quad (39)$$

$$F_{x5}^{HG} = \frac{1}{\sqrt{8}} [Q_{x1}\gamma_{15} + Q_{x2}\gamma_{25} + Q_{x3}\gamma_{35} + Q_{x4}\gamma_{45}] \quad (40)$$

$$F_{x6}^{HG} = \frac{1}{\sqrt{8}} [Q_{x1}\gamma_{16} + Q_{x2}\gamma_{26} + Q_{x3}\gamma_{36} + Q_{x4}\gamma_{46}] \quad (41)$$

$$F_{x7}^{HG} = \frac{1}{\sqrt{8}} [Q_{x1}\gamma_{17} + Q_{x2}\gamma_{27} + Q_{x3}\gamma_{37} + Q_{x4}\gamma_{47}] \quad (42)$$

$$F_{x8}^{HG} = \frac{1}{\sqrt{8}} [Q_{x1}\gamma_{18} + Q_{x2}\gamma_{28} + Q_{x3}\gamma_{38} + Q_{x4}\gamma_{48}] \quad (43)$$

For $F_{y1}^{HG} \dots F_{y8}^{HG}$ replace $Q_{x1} \dots Q_{x4}$ with $Q_{y1} \dots Q_{y4}$, and for $F_{z1}^{HG} \dots F_{z8}^{HG}$ replace $Q_{x1} \dots Q_{x4}$ with $Q_{z1} \dots Q_{z4}$.

Both the hourglass forces and the internal stress forces are then added together as shown in Equations 18–25.

The heat conduction algorithm follows the same pattern as used for the other elements. The heat flow in the three directions is

$$\begin{aligned}
q_x &= -k \frac{\partial T}{\partial x} \\
&= -k [B_{x1}T_1 + B_{x2}T_2 + B_{x3}T_3 + B_{x4}T_4 + B_{x5}T_5 + B_{x6}T_6 + B_{x7}T_7 + B_{x8}T_8] / 12V
\end{aligned} \tag{44}$$

$$\begin{aligned}
q_y &= -k \frac{\partial T}{\partial y} \\
&= -k [B_{y1}T_1 + B_{y2}T_2 + B_{y3}T_3 + B_{y4}T_4 + B_{y5}T_5 + B_{y6}T_6 + B_{y7}T_7 + B_{y8}T_8] / 12V
\end{aligned} \tag{45}$$

$$\begin{aligned}
q_z &= -k \frac{\partial T}{\partial z} \\
&= -k [B_{z1}T_1 + B_{z2}T_2 + B_{z3}T_3 + B_{z4}T_4 + B_{z5}T_5 + B_{z6}T_6 + B_{z7}T_7 + B_{z8}T_8] / 12V
\end{aligned} \tag{46}$$

The increase in thermal energy at node 1 is $\Delta Q_1 = \frac{1}{12} (B_{x1}q_x + B_{y1}q_y + B_{z1}q_z) \Delta t + \Delta Q_e / 8$, where B_{x1} , B_{y1} , and B_{z1} are as described previously, Δt is the integration time increment, and ΔQ_e is the internal energy generated by the element during the previous time increment. The temperature and internal energy update are similar to those described for the tetrahedral elements in subsection 3.8.4.

3.8.6 Bar Elements

The 3D bar element is a simple element that is incompressible and carries only axial loads. It is described in Reference 27. A summary of the 3D bar element algorithm is shown in Figure 20. The bar is geometrically determined by nodes i and j (whose positions define the length, ℓ), and the cross-sectional area, A . By assuming the material is incompressible, the area is determined from

$$A = V_o / \ell = A_o \ell_o / \ell \tag{1}$$

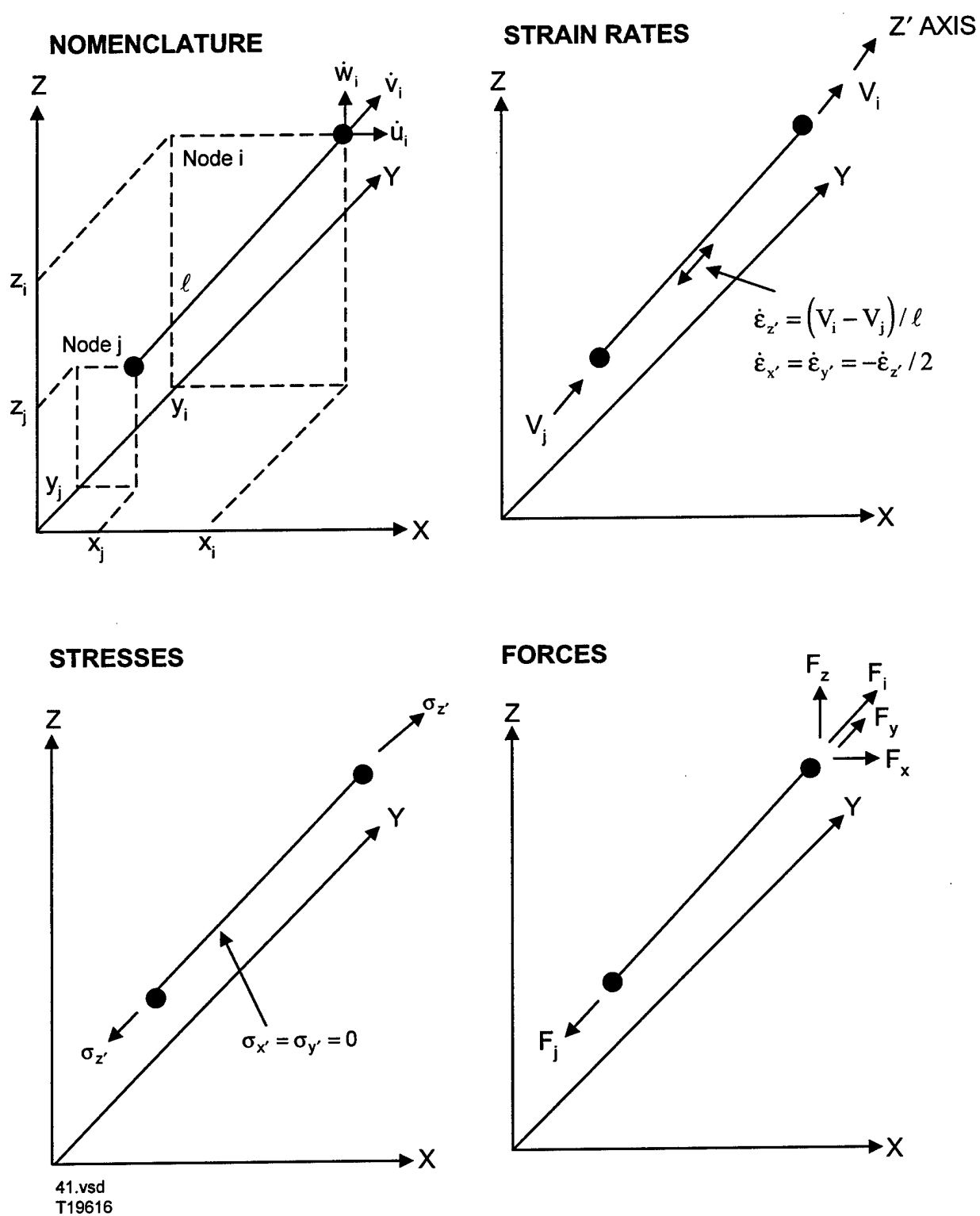


Figure 20. Description of the 3D Bar Element

where V_o , A_o , and ℓ_o are the initial volume, initial cross-sectional area, and initial length, respectively. The mass is equally distributed to the two nodes.

$$M_i = M_j = \rho_o V_o / 2 \quad (2)$$

where ρ_o and V_o are the initial density and volume.

If the z' axis is assumed to coincide with the axis of the bar, the axial strain rate is given by

$$\dot{\epsilon}_{z'} = (V_i - V_j) / \ell \quad (3)$$

where V_i and V_j are the velocity components of nodes i and j , along the axis of the rod. Specifically

$$V_i = (\dot{u}_i \ell_x + \dot{v}_i \ell_y + \dot{w}_i \ell_z) \quad (4)$$

where \dot{u}_i , \dot{v}_i , and \dot{w}_i are the x , y , and z components of the velocity at node i and ℓ_x , ℓ_y , ℓ_z are the direction cosines of the bar.

Incompressibility requires that

$$\dot{\epsilon}_{x'} + \dot{\epsilon}_{y'} + \dot{\epsilon}_{z'} = 0 \quad (5)$$

where $\dot{\epsilon}_{x'}$ and $\dot{\epsilon}_{y'}$ are the strain rates normal to the longitudinal axis of the bar. This gives

$$\dot{\epsilon}_{x'} = \dot{\epsilon}_{y'} = -\dot{\epsilon}_{z'} / 2 \quad (6)$$

With the strain rates defined, the deviator stresses can be determined by the standard method.

The net stresses are a function of both the deviator stresses $(s_{z'}, s_{x'}, s_{y'})$ and the pressure (P).

$$\sigma_{z'} = s_{z'} - P \quad (7)$$

$$\sigma_{x'} = s_{x'} - P = 0 \quad (8)$$

$$\sigma_{y'} = s_{y'} - P = 0 \quad (9)$$

Because the net normal stresses must vanish ($\sigma_{x'} = \sigma_{y'} = 0$), the pressure is defined as

$$P = s_{x'} = s_{y'} \quad (10)$$

The net nodal forces act along the axis of the bar and are determined from

$$F_i = F_j = \sigma_{z'} A \quad (11)$$

The components in the x, y, and z directions are given by

$$F_x^i = F_i \ell_x \quad (12)$$

$$F_y^i = F_i \ell_y \quad (13)$$

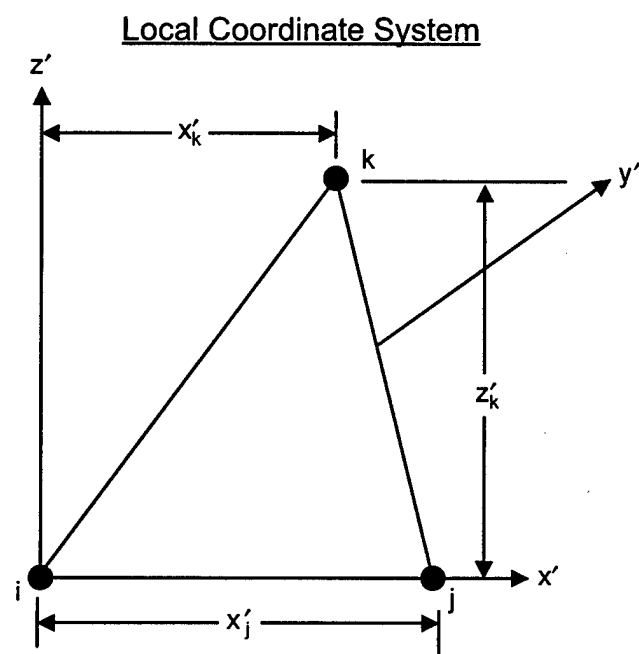
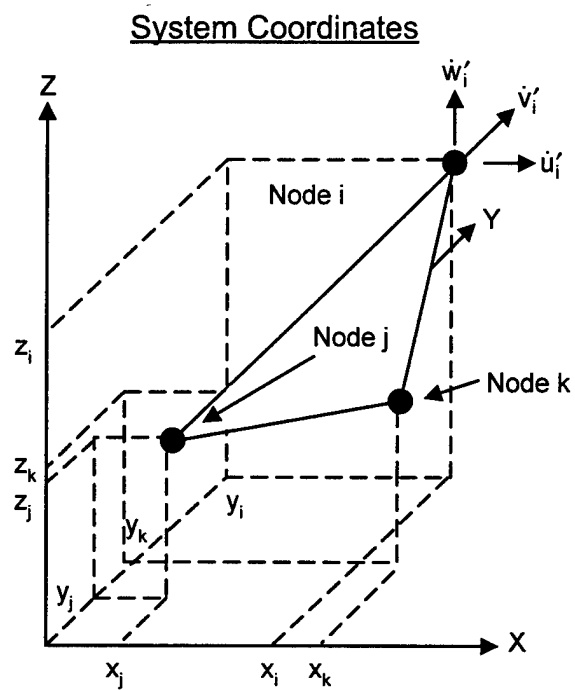
$$F_z^i = F_i \ell_z \quad (14)$$

where ℓ_x , ℓ_y , ℓ_z are the direction cosines of the bar.

The heat conduction algorithm is identical to the 1D heat conduction algorithm in subsection 3.1.3, except the area for the 3D bar is given by Equation 1.

3.8.7 Bending Shell Elements

A 3D bending shell element is shown in Figures 21–25. The concepts for the algorithm are presented in Reference 20. As was the case for the 2D bending shell element, described in subsection 3.4.6, the 3D bending shell is represented by three or five layered elements that share the same nodes. Each of the three or five layered elements is a triangle defined by nodes i, j, k.



42.vsd
T19616

Figure 21. Description of the 3D Bending Shell Element

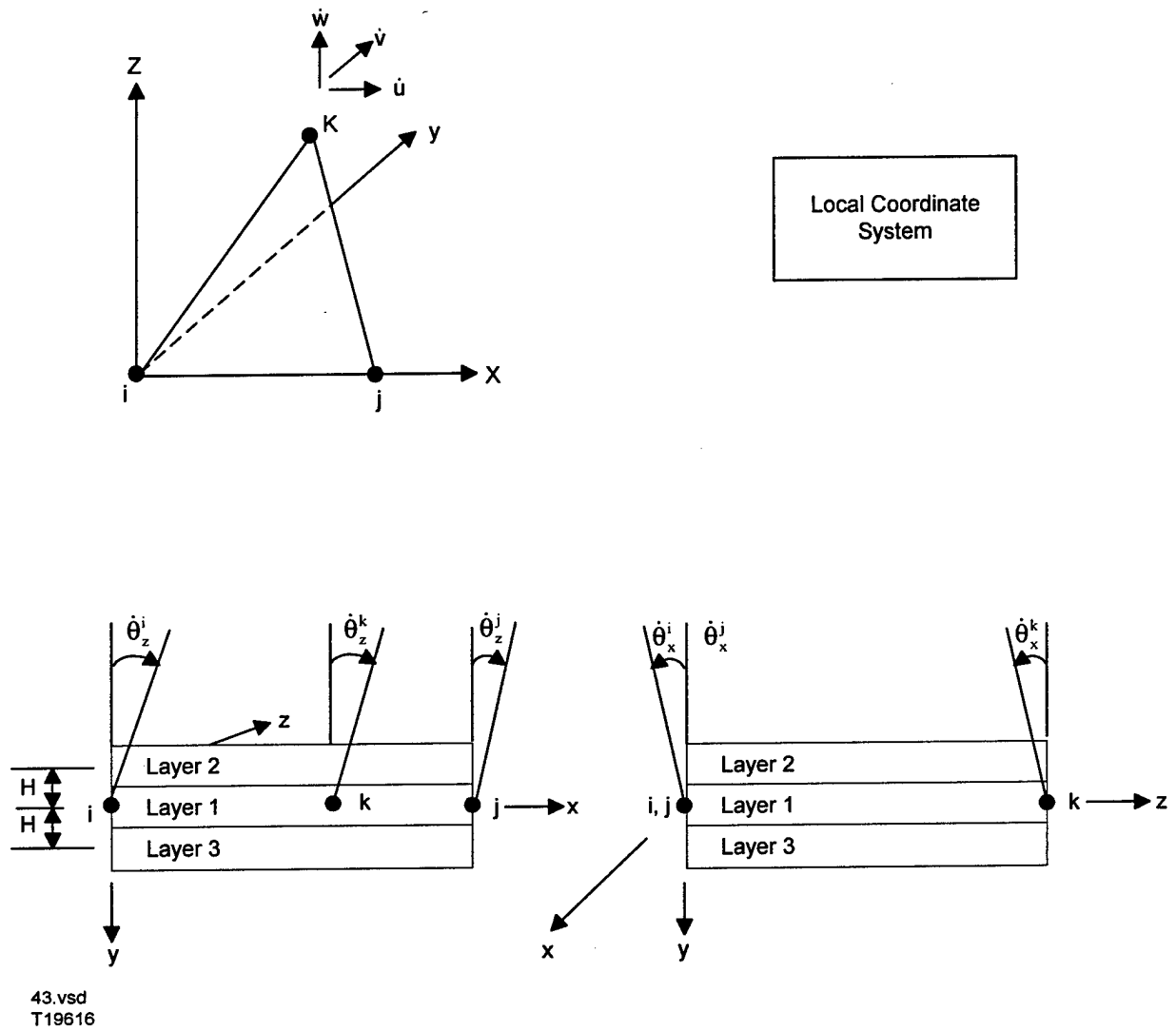


Figure 22. Description of the Geometry and Velocities for the 3D Bending Shell Element

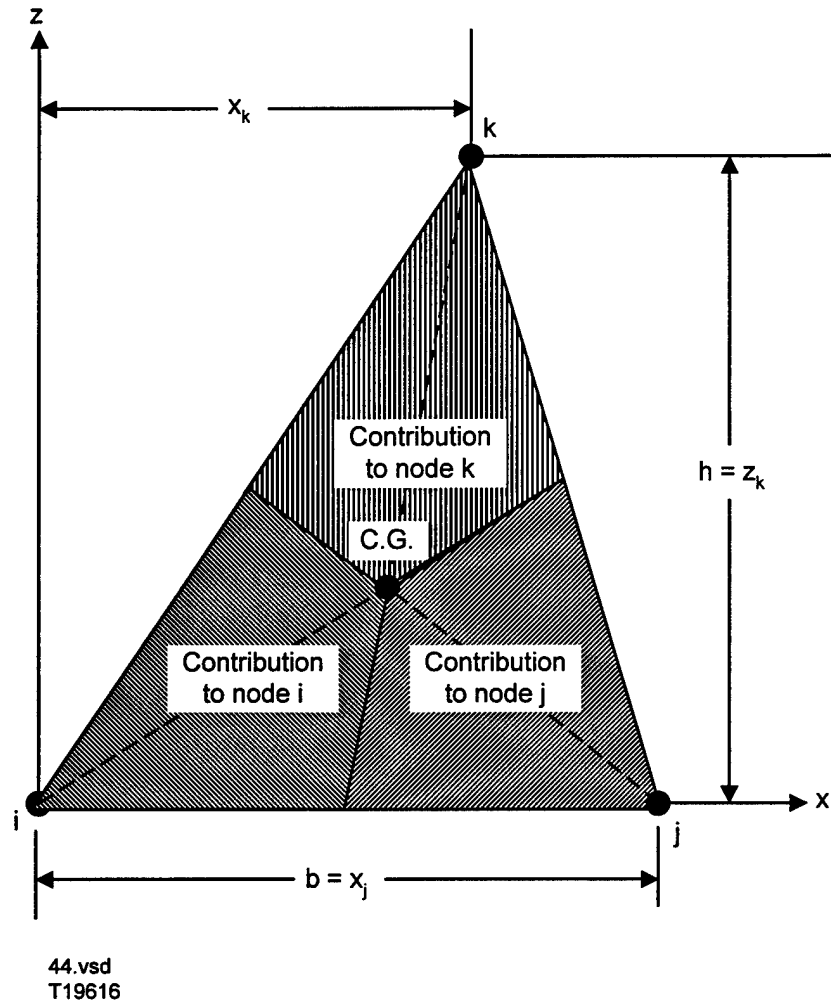
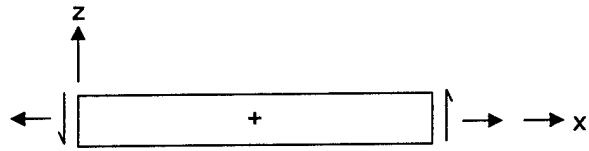


Figure 23. Description of the Mass Distribution for the 3D Bending Shell Element

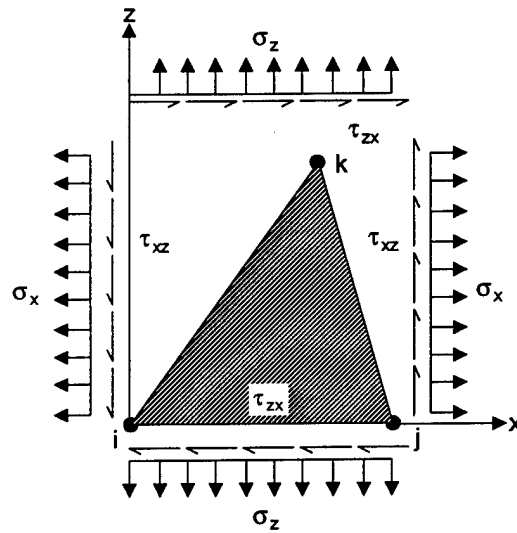
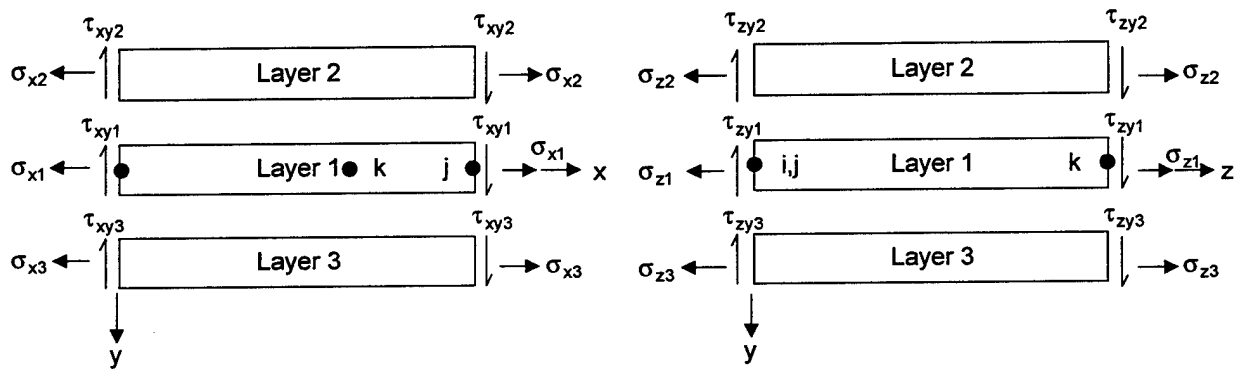


Sign Convention

Positive stress on positive face \rightarrow positive sign

Positive stress on negative face \rightarrow negative sign

Positive moment about axis \rightarrow right hand rule



45.vsd
T19616

Figure 24. Description of the Stresses for the 3D Bending Shell Element

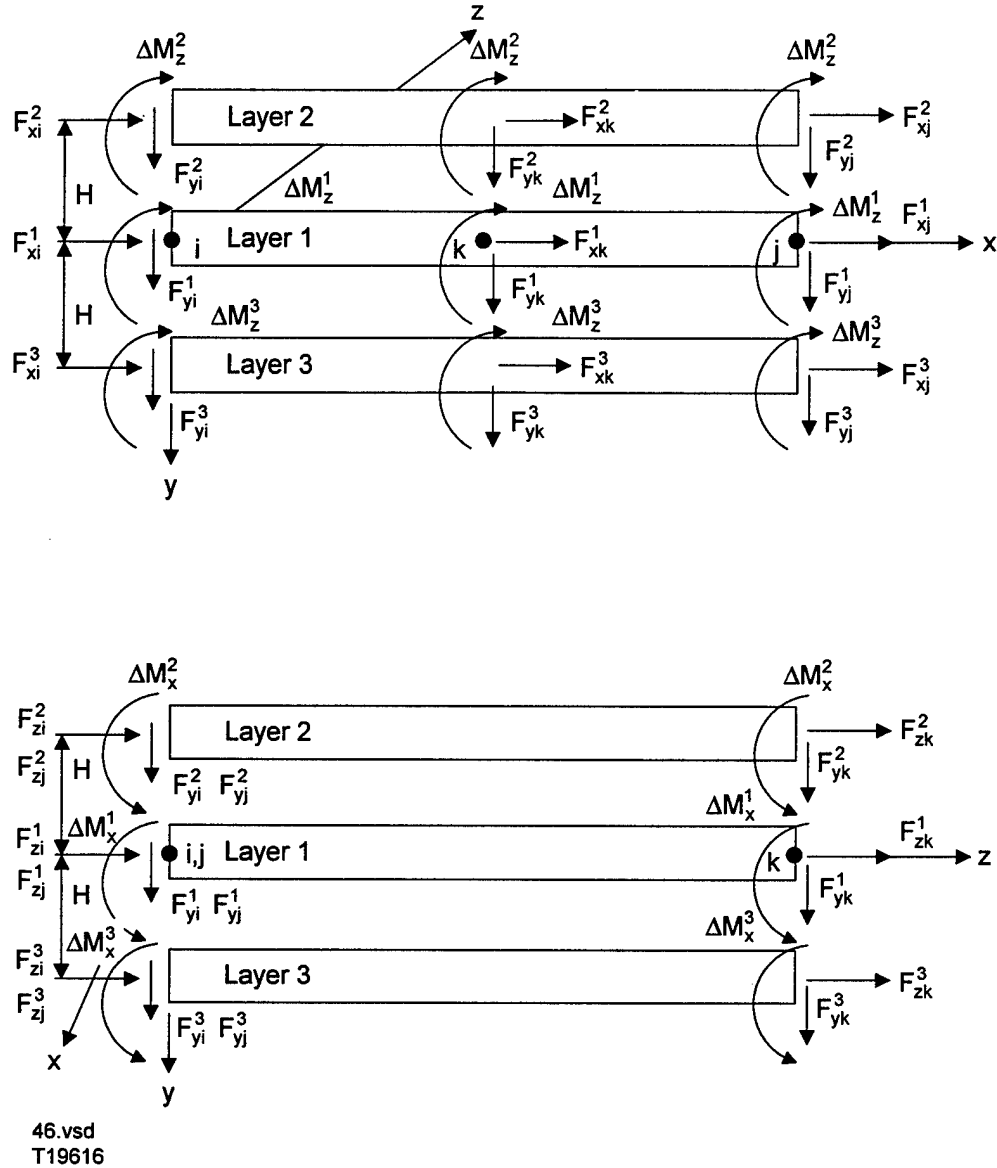


Figure 25. Description of the Forces and Moments for the 3D Bending Shell Element

The first step is to perform a coordinate transformation into a local coordinate system, as shown in Figure 21. Each triangle is put into the $x' - z'$ plane at $y' = 0$, where node i is at $x' = y' = z' = 0$, and node j is on the positive x' axis at $y' = z' = 0$. The transformations are not presented herein. They are partially provided in Reference 27.

Unless noted otherwise, the remainder of this subsection is presented in the local coordinate system, and the x' , y' , z' coordinates will be represented as x , y , z for simplicity.

Bending moments in the shell element are induced by allowing the in-plane stresses in the outer layers to be different from one another. This is accomplished by allowing the in-plane strain rates to be different from one another. These strain rates are dependent on the nodal velocities, as well as the nodal rotational rates and offset from the center layer, as shown in Figure 22.

The masses at the three nodes of an element are equal.

$$M_i = M_j = M_k = \rho_o V_o / 3 \quad (1)$$

where ρ_o is the initial density and V_o is the initial volume. The initial volume is simply $V_o = A_o T_o$, where A_o is the initial area and T_o is the initial total thickness (of all layers).

The mass moments of inertia are required for the rotational rates at the nodes. Figure 23 shows how the mass is distributed to the three nodes for the inertia computations. The mass moments of inertia for node i are as follows:

$$I_{xx}^i = \rho b h T \left\{ \frac{23h^2}{2592} + \frac{T^2}{72} \right\} \quad (2)$$

$$I_{yy}^i = \rho b h T \left\{ \frac{69b^2 + 69h^2 + 84bx_k + 69x_k^2}{7776} \right\} \quad (3)$$

$$I_{zz}^i = \rho b h T \left\{ \frac{(69b^2 + 84bx_k + 69x_k^2)}{7776} + \frac{T^2}{72} \right\} \quad (4)$$

$$I_{xz}^i = I_{zx}^i = -\rho b h T \left\{ \frac{14bh + 23hx_k}{2592} \right\} \quad (5)$$

$$I_{xy}^i = I_{yx}^i = 0 \quad (6)$$

$$I_{yz}^i = I_{zy}^i = 0 \quad (7)$$

where ρ is the current density, T is the current total thickness of the element (all layers), and b , h , and x_k are geometric distances provided in Figure 23.

The moments of inertia for node j are

$$I_{xx}^j = \rho b h T \left\{ \frac{23h^2}{2592} + \frac{T^2}{72} \right\} \quad (8)$$

$$I_{yy}^j = \rho b h T \left\{ \frac{222b^2 + 69h^2 - 222bx_k + 69x_k^2}{7776} \right\} \quad (9)$$

$$I_{zz}^j = \rho b h T \left\{ \frac{(222b^2 - 222bx_k + 69x_k^2)}{7776} + \frac{T^2}{72} \right\} \quad (10)$$

$$I_{xz}^j = I_{zx}^j = \rho b h T \left\{ \frac{37bh - 23hx_k}{2592} \right\} \quad (11)$$

$$I_{xy}^j = I_{yx}^j = 0 \quad (12)$$

$$I_{yz}^j = I_{zy}^j = 0 \quad (13)$$

and the moments of inertia for node k are

$$I_{xx}^k = \rho b h T \left\{ \frac{37h^2}{1296} + \frac{T^2}{72} \right\} \quad (14)$$

$$I_{yy}^k = \rho b h T \left\{ \frac{46b^2 + 148h^2 - 148bx_k + 148x_k^2}{5184} \right\} \quad (15)$$

$$I_{zz}^k = \rho b h T \left\{ \frac{(46b^2 - 148bx_k + 148x_k^2)}{5184} + \frac{T^2}{72} \right\} \quad (16)$$

$$I_{xz}^k = I_{zx}^k = \rho b h T \left\{ \frac{37h(b - 2x_k)}{2592} \right\} \quad (17)$$

$$I_{xy}^k = I_{yx}^k = 0 \quad (18)$$

$$I_{yz}^k = I_{zy}^k = 0 \quad (19)$$

Note that the current (not initial) geometry must be used and this requires $I_{xx} \dots I_{zz}$ to be updated every cycle.

In Figure 22 the three corner velocities of layer 1 are identical to the nodal velocities, because the nodes are positioned in the plane of layer 1. For nomenclature consistency, the nodal x velocities at node i are designated \dot{u}_i , \dot{u}_{i2} , \dot{u}_{i3} , the y velocities are \dot{v}_i , \dot{v}_{i2} , \dot{v}_{i3} , and the z velocities are \dot{w}_i , \dot{w}_{i2} , \dot{w}_{i3} . For layers 2 and 3, the x, y, and z velocities at node i are

$$\dot{u}_{i2} = \dot{u}_i + H\dot{\theta}_z^i \quad (20)$$

$$\dot{u}_{i3} = \dot{u}_i - H\dot{\theta}_z^i \quad (21)$$

$$\dot{v}_{i2} = \dot{v}_i \quad (22)$$

$$\dot{v}_{i3} = \dot{v}_i \quad (23)$$

$$\dot{w}_{i2} = \dot{w}_i - H\dot{\theta}_x^i \quad (24)$$

$$\dot{w}_{i3} = \dot{w}_i + H\dot{\theta}_x^i \quad (25)$$

The offset between layers is simply

$$H = V_o / 3A \quad (26)$$

where V_o is the initial volume and A is the current area of the triangular element. The x, y, and z velocities for nodes j and k can be obtained in a similar manner.

The in-plane strain rates ($\dot{\epsilon}_x$, $\dot{\epsilon}_z$, $\dot{\gamma}_{xz}$) are obtained in exactly the same manner as for 2D triangular elements. See Equations 11, 12, and 14 in subsection 3.4.4. The rotational velocities are assumed to vary linearly between the nodes in the same manner as the translational velocities. The final strain rates, for the local coordinate system in Figure 21, are as follows:

$$\dot{\epsilon}_x = \frac{z_k}{2A} \left[(\dot{u}_j + y\dot{\theta}_z^j) - (\dot{u}_i + y\dot{\theta}_z^i) \right] \quad (27)$$

$$\dot{\epsilon}_z = \frac{1}{2A} \left[(x_k - x_j) (\dot{w}_i - y \dot{\theta}_x^i) - x_k (\dot{w}_j - y \dot{\theta}_x^j) + x_j (\dot{w}_k - y \dot{\theta}_x^k) \right] \quad (28)$$

$$\dot{\epsilon}_y = f(\dot{\epsilon}_x, \dot{\epsilon}_y) \quad (29)$$

$$\dot{\gamma}_{xy} = \frac{1}{2A} \left[z_k (\dot{v}_j - \dot{v}_i) \right] + \frac{1}{3} (\dot{\theta}_z^i + \dot{\theta}_z^j + \dot{\theta}_z^k) \quad (30)$$

$$\dot{\gamma}_{xz} = \frac{1}{2A} \left[(x_k - x_j) \dot{v}_i - x_k \dot{v}_j + x_j \dot{v}_k \right] - \frac{1}{3} (\dot{\theta}_x^i + \dot{\theta}_x^j + \dot{\theta}_x^k) \quad (31)$$

$$\dot{\gamma}_{zx} = \frac{1}{2A} \left[z_k (\dot{w}_j - y \dot{\theta}_x^j) - z_k (\dot{w}_i - y \dot{\theta}_x^i) + (x_k - x_j) (\dot{u}_i + y \dot{\theta}_z^i) - x_k (\dot{u}_j + y \dot{\theta}_z^j) + x_j (\dot{u}_k + y \dot{\theta}_z^k) \right] \quad (32)$$

The through thickness strain rate, $\dot{\epsilon}_y$, cannot be determined explicitly, but must be iterated to provide $\sigma_y = 0$ through the thickness. Also note that for layer 1 (center) $y = 0$, for layer 2 (top) $y = H$, and for layer 3 (bottom) $y = -H$.

The determination of the in-plane shear and deviator stresses is similar to that used for the 2D bending shells. Because the stress normal to the plane is $\sigma_y = 0$, an iteration procedure must be used. The iteration begins by assuming incompressible flow, which gives

$$\dot{\epsilon}_y = -(\dot{\epsilon}_x + \dot{\epsilon}_z) \quad (33)$$

Now that all the strain rates are defined $(\dot{\epsilon}_x, \dot{\epsilon}_y, \dot{\epsilon}_z, \dot{\gamma}_{xy}, \dot{\gamma}_{xz}, \dot{\gamma}_{yz})$ the shear and deviator stresses can be determined in the standard manner, as provided in subsection 3.8.4. The iteration on the volumetric strain, to obtain $\sigma_y = 0$, is almost identical to that presented in subsection 3.4.6 and shown in Figure 12. For 2D bending shells the known normal strain rates are $\dot{\epsilon}_x'$ and $\dot{\epsilon}_\theta$, and the through thickness strain rate (to be determined) is $\dot{\epsilon}_z'$. For 3D bending shells (as well as plane stress elements), the known normal strain rates are $\dot{\epsilon}_x$ and $\dot{\epsilon}_z$, and the through-thickness strain rate (to be determined) is $\dot{\epsilon}_y$. Other than the change in nomenclature, the algorithms for the three cases (2D bending shells, plane stress elements, 3D bending shells) are identical.

The stresses acting on the elements are shown in Figure 24, and the resulting forces are shown in Figure 25. The x, y, and z forces on nodes i, j, and k (for each layer) are as follows:

$$F_x^i = \frac{H}{2} \left[\tau_{xz} (x_k - x_j) - \sigma_x z_k \right] \quad (34)$$

$$F_y^i = \frac{H}{2} \left[\tau_{yz} (x_k - x_j) - \tau_{xy} z_k \right] \quad (35)$$

$$F_z^i = \frac{H}{2} \left[\sigma_z (x_k - x_j) - \tau_{xz} z_k \right] \quad (36)$$

$$F_x^j = \frac{H}{2} \left[\sigma_x z_k - \tau_{xz} x_k \right] \quad (37)$$

$$F_y^j = \frac{H}{2} \left[\tau_{xy} z_k - \tau_{yz} x_k \right] \quad (38)$$

$$F_z^j = \frac{H}{2} \left[\tau_{xz} z_k - \sigma_z x_k \right] \quad (39)$$

$$F_x^k = \frac{H}{2} (\tau_{xz} x_j) \quad (40)$$

$$F_y^k = \frac{H}{2} (\tau_{yz} x_j) \quad (41)$$

$$F_z^k = \frac{H}{2} (\sigma_z x_j) \quad (42)$$

where the stresses are for the specific layer being considered.

Because there are shear forces in each layer, it is necessary to have concentrated moments on the nodes of each layer to provide equilibrium. Summing moments about the z axes at node i gives

$$3\Delta M_z + F_y^k x_k + F_y^j x_j = 0 \quad (43)$$

The resulting concentrated moments are

$$\Delta M_z = - (F_y^k x_k + F_y^j x_j) / 3 \quad (44)$$

Summing about the x axis at node i gives

$$\Delta M_x = F_y^k z_k / 3 \quad (45)$$

Again, the concentrated moments for each layer must use the appropriate force for the specific layer being considered.

The next step is to sum the forces and moments from each layer onto the three nodes.

For node i, the three forces are

$$F_x^i = F_{x(1)}^i + F_{x(2)}^i + F_{x(3)}^i \quad (46)$$

$$F_y^i = F_{y(1)}^i + F_{y(2)}^i + F_{y(3)}^i \quad (47)$$

$$F_z^i = F_{z(1)}^i + F_{z(2)}^i + F_{z(3)}^i \quad (48)$$

In Equation 34, F_x^i is for a generalized single layer, but in Equation 46 it represents the forces for all three layers. $F_{x(1)}^i$ in Equation 46 is F_x^i from Equation 34 for layer 1. The forces on nodes j and k are determined in a similar manner.

The net moments on node i are

$$M_z^i = \Delta M_{z(1)} + \Delta M_{z(2)} + \Delta M_{z(3)} + F_{x(2)}^i H - F_{x(3)}^i H \quad (49)$$

$$M_x^i = \Delta M_{x(1)} + \Delta M_{x(2)} + \Delta M_{x(3)} - F_{z(2)}^i H + F_{z(3)}^i H \quad (50)$$

The net moments on nodes j and k are determined in a similar manner.

The final step is to convert the forces and moments back to the system coordinates, from the local coordinate system.

The heat conduction algorithm is identical to the 2D heat conduction algorithm for triangular elements. For the heat conduction option all three layers will have equal temperatures because all layers are attached to the same nodes.

3.8.8 Membrane Shell Elements

The 3D membrane shell elements are a simplified form of the 3D bending shell elements presented in subsection 3.8.7 and shown in Figure 21. The membrane shell element has only in-plane stresses and is composed of only a single layer. It cannot produce bending or transverse shear stresses. Furthermore it is assumed to be incompressible, and this eliminates the need to iterate to obtain the through-thickness stress. This algorithm is presented in Reference 21 for plane stress geometry.

Referring back to Equation 29 of subsection 3.8.7, the through-thickness strain rate for incompressible deformation is

$$\dot{\epsilon}_y = -(\dot{\epsilon}_x + \dot{\epsilon}_z) \quad (1)$$

where $\dot{\epsilon}_x$ and $\dot{\epsilon}_z$ are the in-plane strain rates in the local coordinate system.

The deviator stresses (s_x, s_y, s_z) can then be determined from $\dot{\epsilon}_x, \dot{\epsilon}_y, \dot{\epsilon}_z$, which gives the net stresses

$$\sigma_x = s_x - P \quad (2)$$

$$\sigma_y = s_y - P \quad (3)$$

$$\sigma_z = s_z - P \quad (4)$$

In Equation 3, setting $\sigma_y = 0$ gives $P = s_y$, and this provides an explicit determination of the stresses in Equations 2–4.

3.8.9 Nonreflective Boundary Elements

The 3D nonreflective boundary elements are incorporated as infinitely thin, triangular, massless elements as shown in Figure 26. They can be used to absorb elastic waves to represent infinite media, and they can also be used to reduce the size of the model for other applications such as for penetration problems (References 8–10).

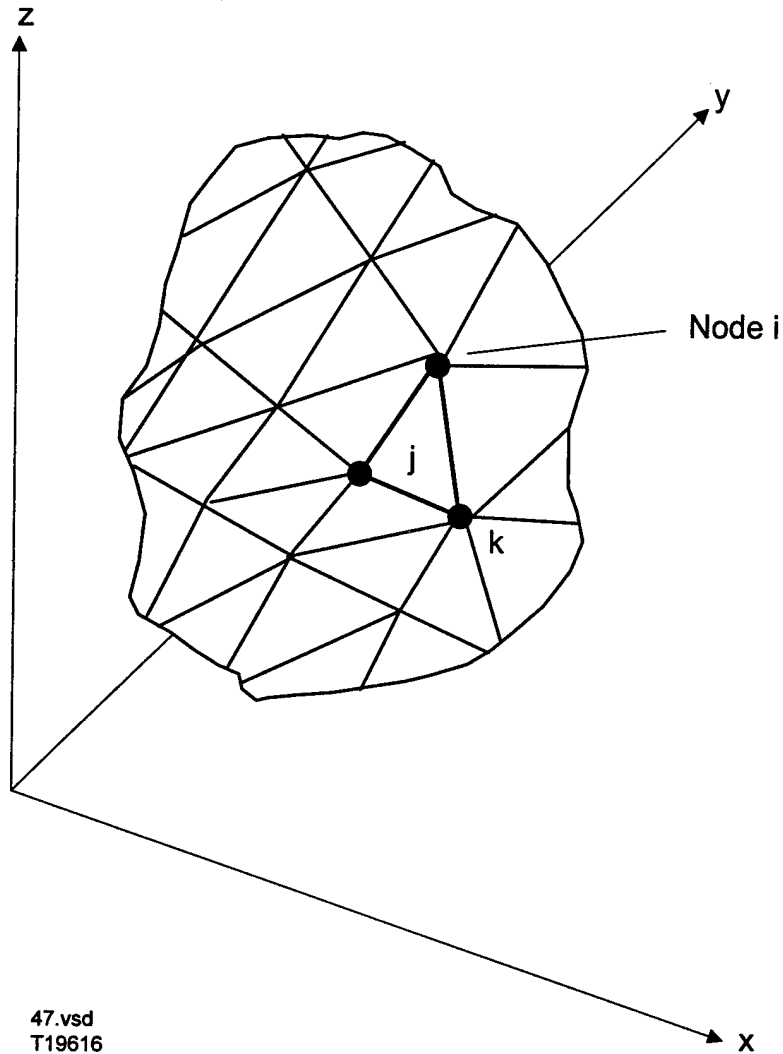


Figure 26. Description of the 3D Nonreflective Boundary Element

The average velocity normal to the triangular face is

$$V_N = \bar{u}\ell_x + \bar{v}\ell_y + \bar{w}\ell_z \quad (1)$$

where $\bar{u} = (\dot{u}_i + \dot{u}_j + \dot{u}_k)/3$ is the average velocity in the x direction, and \bar{v} and \bar{w} are the average velocities in the y and z directions. The direction cosines normal to the surface are

$$\ell_x = A_x / A \quad (2)$$

$$\ell_y = A_y / A \quad (3)$$

$$\ell_z = A_z / A \quad (4)$$

where A_x , A_y , and A_z are the projected areas on the yz , xz , and xy planes when viewed along the x , y , and z axes, and A is the total area.

$$A_x = \frac{1}{2} \left[(y_i - y_j)(z_k - z_j) - (y_k - y_j)(z_i - z_j) \right] \quad (5)$$

$$A_y = \frac{1}{2} \left[(z_i - z_j)(x_k - x_j) - (z_k - z_j)(x_i - x_j) \right] \quad (6)$$

$$A_z = \frac{1}{2} \left[(x_i - x_j)(y_k - y_j) - (x_k - x_j)(y_i - y_j) \right] \quad (7)$$

$$A = \sqrt{A_x^2 + A_y^2 + A_z^2} \quad (8)$$

In addition to the normal velocity it is necessary to determine two velocities in the plane of the element. The first of the in-plane velocities is in the direction along the line connecting nodes j and k .

$$V_1 = \bar{u} \ell_{x1} + \bar{v} \ell_{y1} + \bar{w} \ell_{z1} \quad (9)$$

where V_1 is the in-plane velocity, \bar{u} , \bar{v} , and \bar{w} are the average nodal velocities as defined previously, and the directions cosines are

$$\ell_{x1} = (x_k - x_j) / d \quad (10)$$

$$\ell_{y1} = (y_k - y_j) / d \quad (11)$$

$$\ell_{z1} = (z_k - z_j) / d \quad (12)$$

where d is the distance between nodes j and k .

The other in-plane velocity is perpendicular to both V_N and V_1 . It is expressed as

$$V_2 = \bar{u}\ell_{x2} + \bar{v}\ell_{y2} + \bar{w}\ell_{z2} \quad (13)$$

where the direction cosines are

$$\ell_{x2} = \ell_y\ell_{z1} - \ell_z\ell_{y1} \quad (14)$$

$$\ell_{y2} = \ell_z\ell_{x1} - \ell_x\ell_{z1} \quad (15)$$

$$\ell_{z2} = \ell_x\ell_{y1} - \ell_y\ell_{x1} \quad (16)$$

The total normal resisting force on the element is

$$F_N = -\rho_o c_s A V_N \quad (17)$$

and the total in-plane forces are

$$F_1 = -\rho_o c_{\text{shear}} A V_1 \quad (18)$$

$$F_2 = -\rho_o c_{\text{shear}} A V_2 \quad (19)$$

where ρ_o is the initial density of the material, A is the total area and V_N , V_1 and V_2 are the velocities. The longitudinal and shear sound velocities are

$$c_s = \sqrt{(K_1 + 4G/3)/\rho_o} \quad (20)$$

$$c_{\text{shear}} = \sqrt{G/\rho_o} \quad (21)$$

where K_1 is the bulk modulus and G is the shear modulus.

Now the total forces must be aligned with the three principal axes and distributed equally to the three nodes.

$$F_x^i = F_x^j = F_x^k = (F_N\ell_x + F_1\ell_{x1} + F_2\ell_{x2})/3 \quad (22)$$

$$F_y^i = F_y^j = F_y^k = (F_N \ell_y + F_1 \ell_{y1} + F_2 \ell_{y2})/3 \quad (23)$$

$$F_z^i = F_z^j = F_z^k = (F_N \ell_z + F_1 \ell_{z1} + F_2 \ell_{z2})/3 \quad (24)$$

SECTION 4

SPH ALGORITHMS

During the past few years SPH (Smooth Particle Hydrodynamics) methods have been developed and applied to problems involving high velocity impact. The appeal of SPH for high velocity impact is that it is a Lagrangian technique and that it has variable connectivity to allow for severe distortions. The Lagrangian feature is desired because it allows the grid to be embedded in the material and this reduces some of the material interface and material history problems associated with Eulerian codes. Furthermore, the ability to handle severe distortions allows the SPH technique to be applied to problems that historically have been reserved for Eulerian approaches.

Although SPH approaches can be applied to severe distortions, they are generally not as good as standard finite elements for structural response applications. These same characteristics are held by Eulerian techniques. The important advantage of SPH, however, is that its Lagrangian formulation allows it to be straightforwardly linked to standard finite element Lagrangian formulations. This means that it is possible for both severe distortions and structural response computations to be performed with a single Lagrangian code, and that both severe distortions and structural responses can occur in the same problem. A long term objective is to allow the user to define almost any impact problem with a standard finite element grid, and then to allow the standard elements to be converted to SPH nodes as the standard elements become distorted. Although this approach has been demonstrated, more work is required to increase the accuracy and robustness for a wider range of problems. The algorithms that follow are reported in References 28–31.

4.1 2D AXISYMMETRIC GEOMETRY

A schematic overview of the structure of the EPIC code is shown in Figure 27. It is very similar for both standard elements and SPH nodes, with the primary differences being the computations of the strains, strain rates and nodal forces. The determination of the nodal displacements and velocities, as well as the stresses, is identical for both approaches and is not included here. A description of the basic 2D axisymmetric finite element algorithm is provided in subsection 3.4.

Figure 28 represents some features of the SPH technique. Node i is designated as the center node and the neighbor nodes are designated as nodes j . The distance between nodes is r_{ij} , the

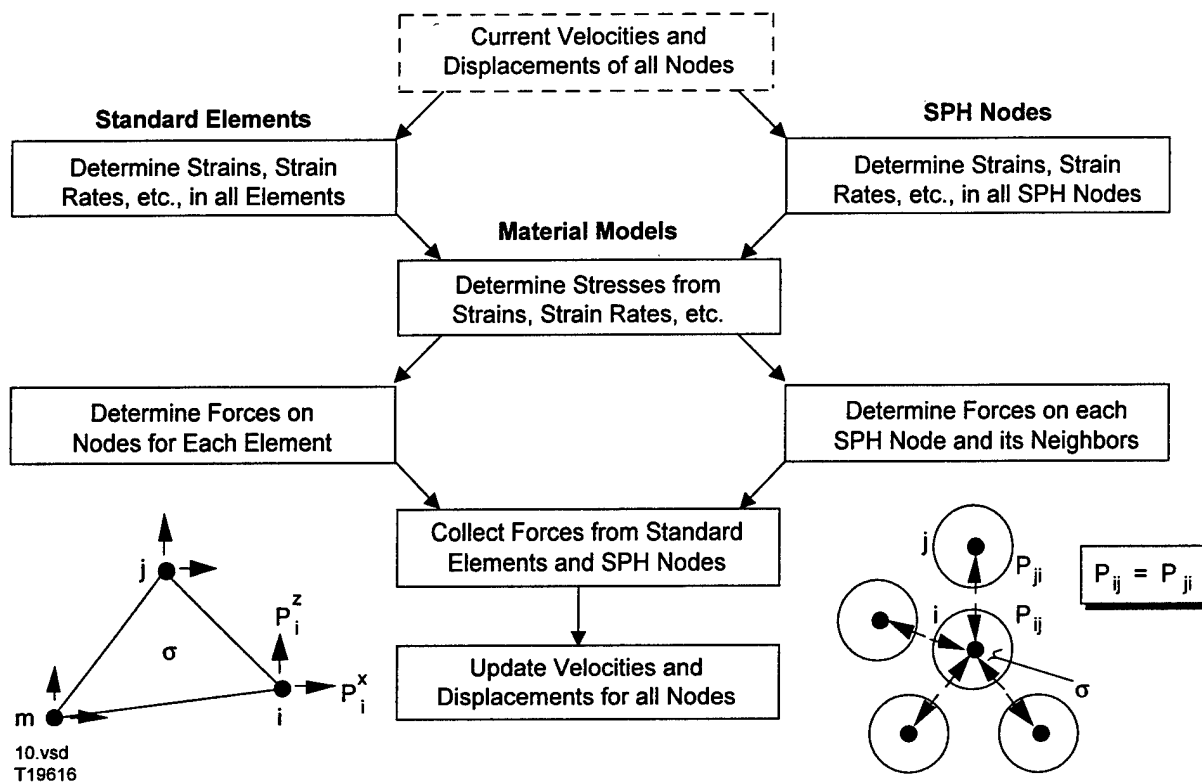


Figure 27. EPIC Code Structure for Standard Elements and SPH Nodes

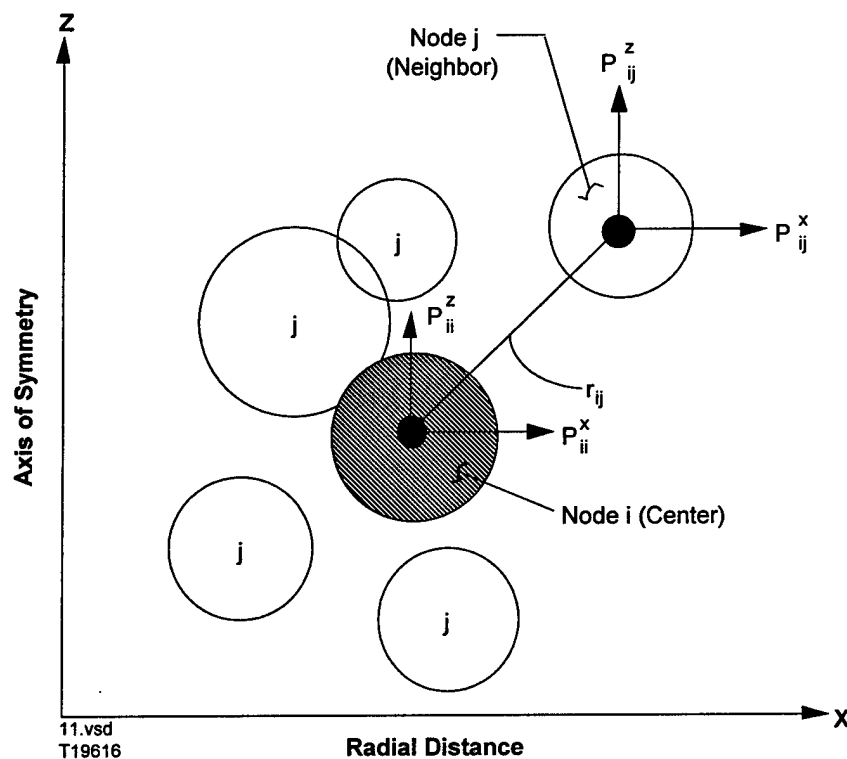


Figure 28. SPH Characteristics

diameters of the nodes are d_i and d_j , and the masses of the nodes are M_i and M_j . The masses remain constant throughout the computation, and are obtained from $M = \rho_o V_o$ where ρ_o and V_o represent the initial density of the material and the initial volume represented by the node.

The SPH approach allows for variable nodal connectivity, and this means that it is necessary for each center node i to search and find the closest neighbor nodes j . This searching time can be significant, especially for larger problems, and several approaches have been tried. The EPIC code currently uses a bucket searching algorithm (Reference 13).

4.1.1 Smoothing Functions

The smoothing function is an important part of the SPH algorithm. Two smoothing functions and their derivatives are shown in Figure 29. These smoothing functions can be used for both plane strain and axisymmetric geometries. The B-Spline has been a commonly used smoothing function in the past, but the recently introduced Quadratic smoothing function appears to have some advantages (Reference 30).

The B-Spline smoothing function is expressed as

$$W_{ij} = \frac{1}{\pi h_{ij}^2} \left[\frac{15}{7} \left(\frac{2}{3} - v_{ij}^2 + \frac{1}{2} v_{ij}^3 \right) \right] \quad 0 \leq v_{ij} \leq 1 \quad (1a)$$

$$W_{ij} = \frac{1}{\pi h_{ij}^2} \left[\frac{5}{14} (2 - v_{ij})^3 \right] \quad 1 \leq v_{ij} \leq 2 \quad (1b)$$

where $v_{ij} = r_{ij}/h_{ij}$, and the smoothing distance is

$$h_{ij} = \alpha (d_i + d_j) / 2 \quad (2)$$

The dimensionless smoothing distance, α , is a user supplied input. It is usually taken as $\alpha = 1.0$, but other values can be used ($0.8 \leq \alpha \leq 1.2$). The diameters, d_i and d_j , can be obtained (for axisymmetric geometry) from

$$d = d_o \sqrt{(1 + \epsilon_v) x_o / x} \quad (3)$$

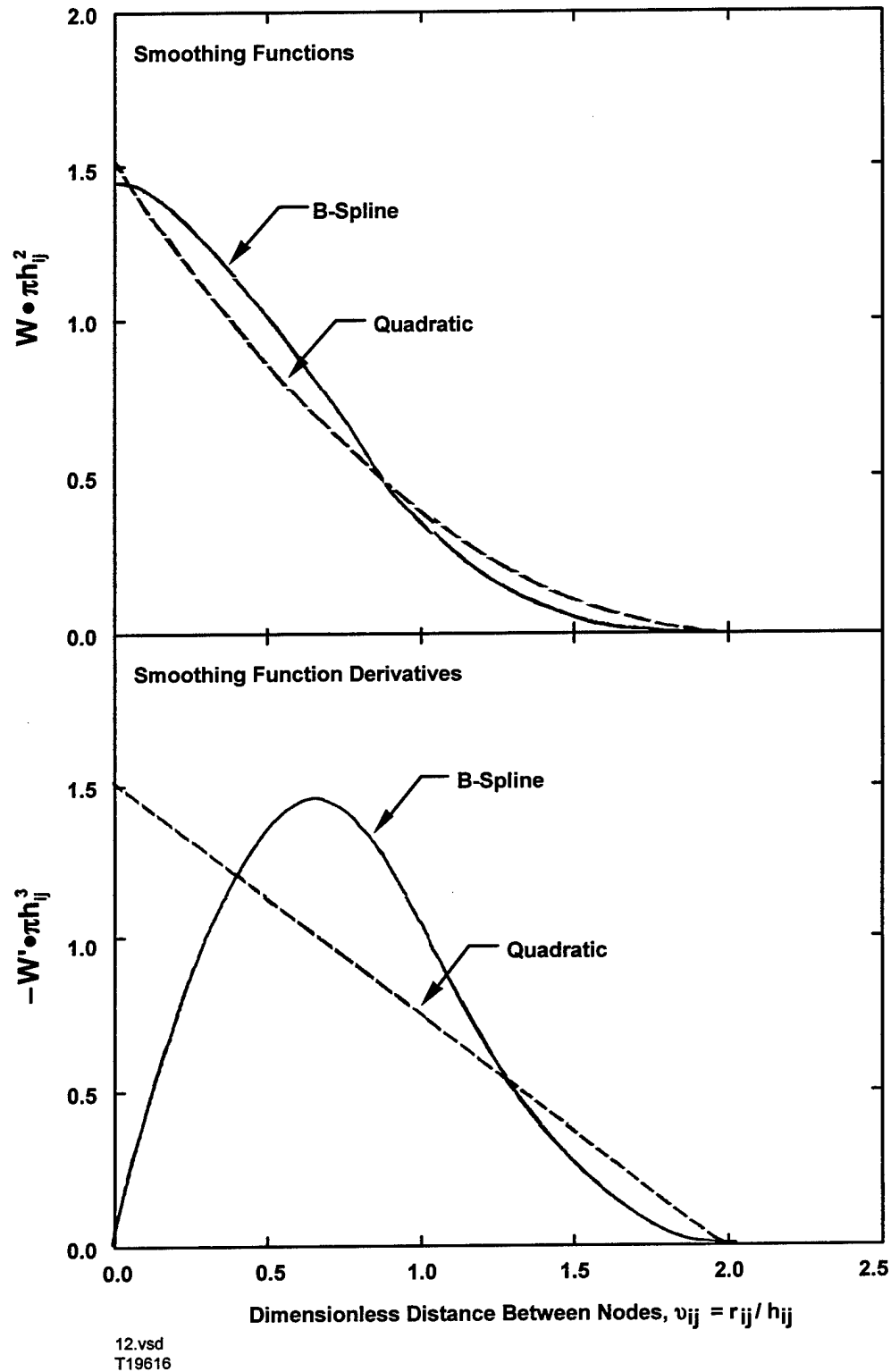


Figure 29. 2D B-Spline and Quadratic Smoothing Functions and Their Derivatives

where ε_v is the volumetric strain (defined later), d_0 is the initial node diameter, and x_0 and x are the initial and current x (radial) coordinates.

A requirement of the smoothing function is that it exhibits the characteristics of a Dirac delta function as h_{ij} approaches zero. It will be shown later that it is the derivative, W'_{ij} , of the smoothing function that actually provides the weighting function for the strain rates and forces. The negative value of the B-Spline derivative, $-W'_{ij}$, is shown in Figure 29 and is expressed as

$$W'_{ij} = \frac{1}{\pi h_{ij}^3} \left[-\frac{30}{7} v_{ij} + \frac{45}{14} v_{ij}^2 \right] \quad 0 \leq v_{ij} \leq 1 \quad (4a)$$

$$W'_{ij} = \frac{1}{\pi h_{ij}^3} \left[-\frac{15}{14} (2 - v_{ij})^2 \right] \quad 1 \leq v_{ij} \leq 2 \quad (4b)$$

The interesting feature of the B-Spline derivative is that $-W'_{ij}$ exhibits a maximum at $v_{ij} = 2/3$ and decreases for both smaller and larger values of v_{ij} . For $v_{ij} > 2/3$ it is logical that $-W'_{ij}$ decreases because it has less influence as the distance is increased. To have $-W'_{ij}$ decrease for $v_{ij} < 2/3$ is not intuitively satisfying because the closer neighbor node j comes to center node i , the less influence it has. This can also lead to instabilities in compression (Reference 32).

The Quadratic smoothing function is also shown in Figure 29. It is expressed as

$$W_{ij} = \frac{1}{\pi h_{ij}^2} \left[\frac{3}{8} v_{ij}^2 - \frac{3}{2} v_{ij} + \frac{3}{2} \right] \quad 0 \leq v_{ij} \leq 2 \quad (5)$$

The derivative is

$$W'_{ij} = \frac{1}{\pi h_{ij}^3} \left[\frac{3}{4} v_{ij} - \frac{3}{2} \right] \quad 0 \leq v_{ij} \leq 2 \quad (6)$$

For the Quadratic smoothing function derivative, the weighting function, $-W'_{ij}$, always increases as the nodes move closer together, and always decreases as they move apart. This intuitively appears to be more realistic than the B-Spline derivative. It is also more simple than the B-Spline and does not have the compressive softening that can lead to compressive instabilities.

Based on these arguments alone, it would appear that the newer Quadratic smoothing function is an improvement over the traditional B-Spline.

4.1.2 Strain Rates

For 2D axisymmetric geometry, the three normal strain rates $(\dot{\epsilon}_x, \dot{\epsilon}_z, \dot{\epsilon}_\theta)$, the shear strain rate, $\dot{\gamma}_{xz}$, the rotational rate, ω_{xz} , and the volumetric strain rate, $\dot{\epsilon}_v$, for center node i, are as follows.

$$\dot{\epsilon}_x = -\sum_j \beta_x W'_{ij} V_j (\dot{u}_j - \dot{u}_i) \ell_x / 2\pi x_j \quad (1)$$

$$\dot{\epsilon}_z = -\sum_j \beta_z W'_{ij} V_j (\dot{v}_j - \dot{v}_i) \ell_z / 2\pi x_j \quad (2)$$

$$\dot{\epsilon}_\theta = -\sum_j \beta_\theta W'_{ij} V_j r_{ij} \dot{u}_j / 4\pi x_j^2 \quad (3)$$

$$\dot{\gamma}_{xz} = -\sum_j W'_{ij} V_j [\beta_z (\dot{u}_j - \dot{u}_i) \ell_z + \beta_x (\dot{v}_j - \dot{v}_i) \ell_x] / 2\pi x_j \quad (4)$$

$$\omega_{xz} = \sum_j W'_{ij} V_j [\beta_z (\dot{u}_j - \dot{u}_i) \ell_z - \beta_x (\dot{v}_j - \dot{v}_i) \ell_x] / 4\pi x_j \quad (5)$$

$$\dot{\epsilon}_v = \dot{\epsilon}_x + \dot{\epsilon}_z + \dot{\epsilon}_\theta \quad (6)$$

where $W'_{ij} = \partial W_{ij} / \partial r$ is the derivative of the smoothing function, V_j is the current volume of the node j, \dot{u}_i and \dot{u}_j are the x velocities of nodes i and j, \dot{v}_i and \dot{v}_j are the z velocities, ℓ_x and ℓ_z are the direction cosines from node i to node j, and x_j is the x coordinate of node j. The updated volumetric strain is obtained by integrating the volumetric strain rate.

$$\epsilon_v^{t+\Delta t} = \epsilon_v^t + \dot{\epsilon}_v^t \Delta t (1 + \epsilon_v^t) \quad (7)$$

where Δt is the integration time increment, and the factor $(1 + \epsilon_v^t)$ converts the strain rate from the current configuration back to the initial configuration.

The three β factors are used to normalize the smoothing functions such that they will provide the exact strain rates in the three principal directions for states of constant strain rates. They are

obtained from Equations 1–3 by setting $\dot{u}_j - \dot{u}_i \equiv \dot{\epsilon}_x r_{ij} \ell_x$ for a constant strain rate in the x direction, $\dot{v}_j - \dot{v}_i \equiv \dot{\epsilon}_x r_{ij} \ell_z$ for a constant strain rate in the z direction, and $\dot{u}_j \equiv \dot{\epsilon}_\theta x_j$ for a constant hoop strain rate. The resulting normalizing factors are

$$\beta_x = \frac{-1}{\sum W_{ij} V_j r_{ij} \ell_x^2 / 2\pi x_j} \quad (8)$$

$$\beta_z = \frac{-1}{\sum W_{ij} V_j r_{ij} \ell_z^2 / 2\pi x_j} \quad (9)$$

$$\beta_\theta = \frac{-1}{\sum W_{ij} V_j r_{ij} / 4\pi x_j} \quad (10)$$

The effect of using the Normalized Smoothing Function (NSF) algorithm can be significant. Figure 30 shows a cross-section of an axisymmetric ring of material represented by 25 SPH nodes (5 x 5). The two cross-sections on the left side are for the Standard Smoothing Functions, which means that they do not use the NSF algorithm. The two on the right side do use the NSF algorithm. The top two use the B-Spline smoothing function and the bottom two use the Quadratic smoothing function. The numbers in the centers of the circular SPH nodes represent the equivalent strain rate in the node when the axisymmetric cross-section is subjected to a stretching radial velocity of

$$\dot{u}_i = 3x_i / 2 \quad (11)$$

where x_i is the radial coordinate. The resulting uniform strain rates are

$$\dot{\epsilon}_x = \partial \dot{u} / \partial x = 3/2 \quad (12)$$

$$\dot{\epsilon}_\theta = \dot{u} / x = 3/2 \quad (13)$$

$$\dot{\epsilon}_z = \dot{\gamma}_{xz} = 0 \quad (14)$$

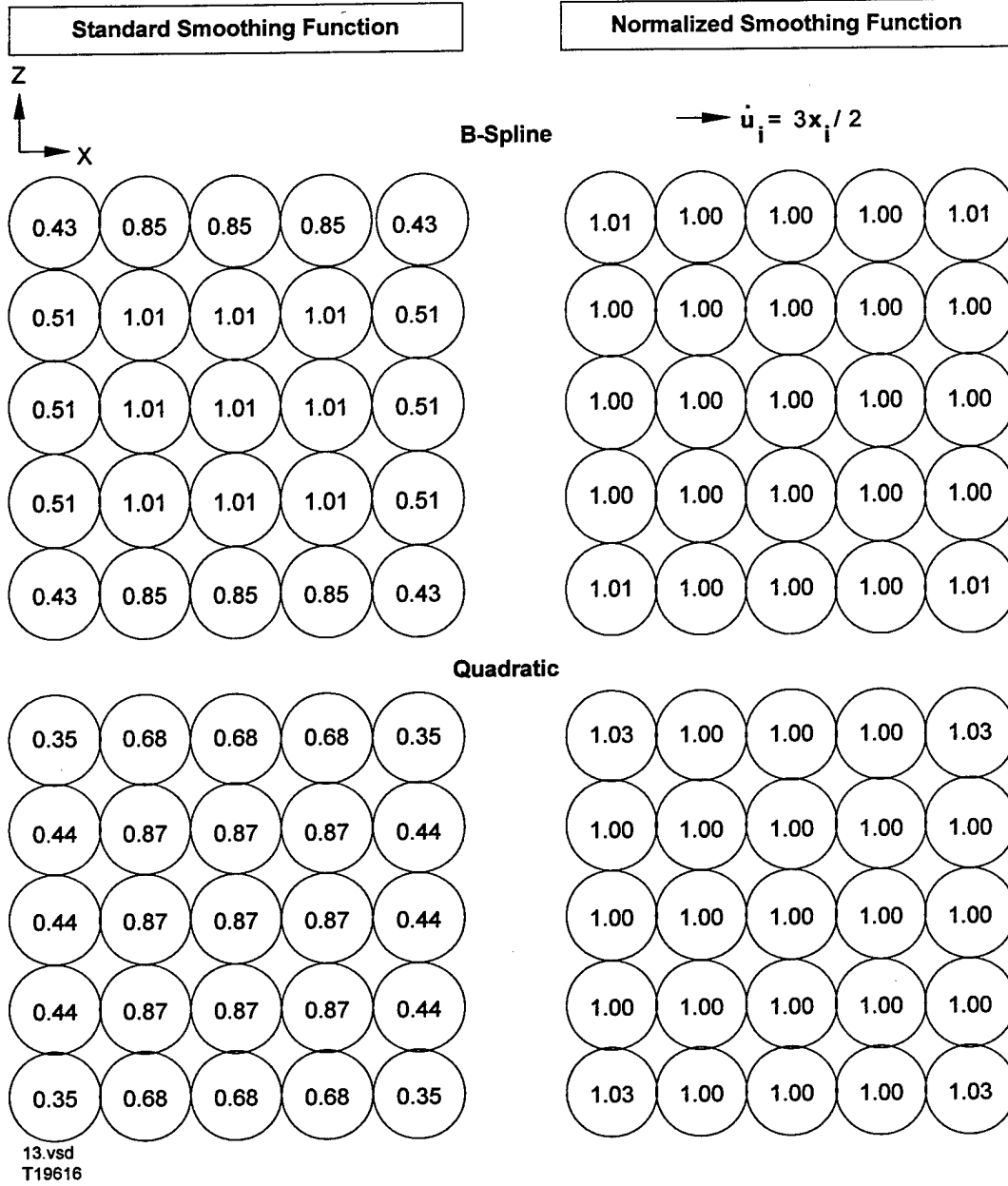


Figure 30. Equivalent Strain Rates in Radially Stretching Cross-Sections With a Uniform Arrangement of SPH Nodes

The equivalent strain rate is defined as

$$\bar{\epsilon} = \sqrt{\frac{2}{9} \left[(\dot{\epsilon}_x - \dot{\epsilon}_z)^2 + (\dot{\epsilon}_x - \dot{\epsilon}_\theta)^2 + (\dot{\epsilon}_z - \dot{\epsilon}_\theta)^2 + \frac{3}{2} \dot{\gamma}_{xz} \right]} \quad (15)$$

Substituting Equations 12–14 into Equation 15 gives

$$\bar{\dot{\epsilon}} \equiv 1.0 \quad (16)$$

The upper left cross-section in Figure 30 (B-Spline without NSF) shows good accuracy in the center region ($\bar{\dot{\epsilon}} = 1.01$), but the side boundaries and corners are significantly low ($0.43 \leq \bar{\dot{\epsilon}} \leq 0.85$). The reason for the low strain rates at the boundaries is that the basic SPH algorithm is for an interior node, which assumes there is a full distribution of neighbor nodes. When the distribution of neighbor nodes is not full, inaccuracies are introduced. The lower left in Figure 30 (Quadratic without NSF) has a similar pattern, but the interior nodes have a lower strain rate ($\bar{\dot{\epsilon}} \leq 0.87$). This does not necessarily mean that the B-Spline is more accurate than the Quadratic smoothing function, because the results in Figure 30 are specifically for a uniform grid with a dimensionless smoothing distance of $\alpha = 1.0$. For some other conditions (such as $\alpha = 0.8$) the Quadratic smoothing function is more accurate, as will be shown later. At larger smoothing distances the interior nodes approach an equivalent strain rate of $\bar{\dot{\epsilon}} = 1.0$, and at lower smoothing distances ($\alpha < 0.8$) the strain rates decrease to $\bar{\dot{\epsilon}} = 0$ at $\alpha = 0.5$. This effect is illustrated in Figure 31, where the equivalent strain rate of an interior node is shown as a function of the dimensionless smoothing distance, α . Note that the B-Spline is more accurate at $\alpha = 1.0$ and the Quadratic is more accurate at $\alpha = 0.8$. The sharp slope changes for the Quadratic smoothing function at $\alpha = 0.707, 1.000, 1.118$, etc., occur when the expanding smoothing distance encounters additional nodes at $v_{ij} = 2.0$. The Quadratic smoothing function derivative, W'_{ij} , has a finite slope at $v_{ij} = 2.0$ (and therefore has a noticeable effect) whereas the slope of W'_{ij} for the B-Spline is zero at $v_{ij} = 2.0$. When the NSF algorithm is applied, as shown on the right side of Figure 30 and in Figure 31, then the results are much improved. The NSF algorithm is also very effective when the nodes are in a non-uniform arrangement, and it is shown to provide excellent results for several cylinder impact examples (Reference 30).

4.1.3 Forces

After the strain rates, rotational rate, and volumetric strain in Equations 1–7 of subsection 4.1.2 are determined, it is possible to determine the shear and deviator stresses, the pressure, and the nodal artificial viscosity in the standard manner, as provided in subsection 3.4.4. These stresses must then be converted to forces as shown in Figure 27.

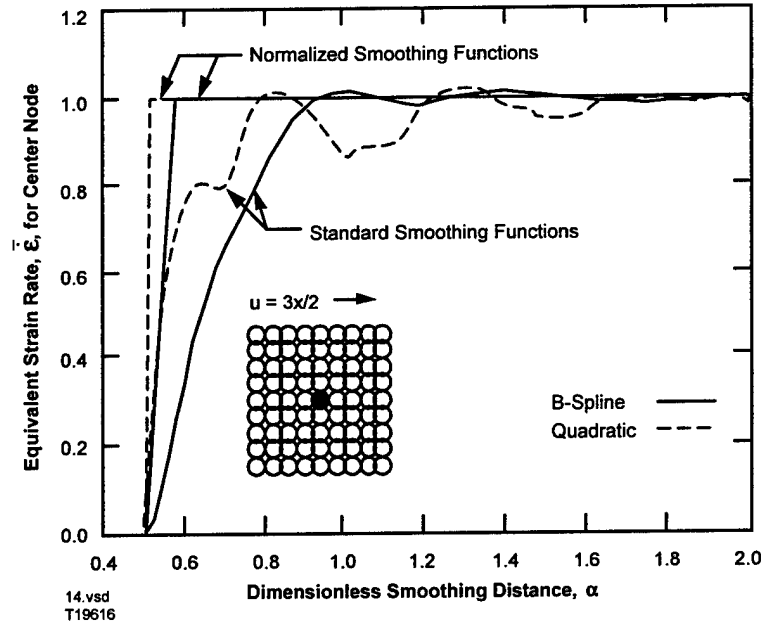


Figure 31. Equivalent Strain Rate Versus Dimensionless Smoothing Distance for an Interior SPH Node in a Radial Stretching Cross-Section

The nodal force in the x direction on node j, due to the stress of node i, is

$$P_x^{ij} = P_x^{ij(\text{plane})} + P_x^{ij(\text{hoop})} \quad (1)$$

The force due to the in-plane stresses is

$$P_x^{ij(\text{plane})} = W_{ij} V_i V_j [\beta_x (\sigma_x^i - Q_{ij}) \ell_x + \beta_z \tau_{xz}^i \ell_z] / 2\pi x_j \quad (2)$$

where $\sigma_x^i = s_x^i - (P_i + Q_i)$ is the net normal stress in the x direction, composed of the deviator stress, pressure, and nodal artificial viscosity, and τ_{xz}^i is the shear stress.

There is also an artificial viscosity, Q_{ij} , which is dependent on the relative velocities of nodes i and j. It is intended to stabilize the grid and keep adjacent nodes from becoming too close to one another. This will be designated as a bond viscosity, because it acts on the bond between nodes i and j. It can also introduce a significant amount of artificial strength.

The force due to the hoop stress is

$$P_x^{ij(\text{hoop})} = \beta_\theta W_{ij} V_j^2 r_{ij} \sigma_\theta^i / 4\pi r_j^2 \quad (3)$$

and the force in the z direction is

$$P_z^{ij} = W_{ij} V_i V_j \left[\beta_z (\sigma_z^i - Q_{ij}) \ell_z + \beta_x \tau_{xz}^i \ell_x \right] / 2\pi x_j \quad (4)$$

Equations 2–4 provide the forces only on the neighbor nodes j. The forces on center node i, due to the stresses in node i, are equal and opposite to the in-plane forces in the x and z directions.

$$P_x^{ii} = - \sum_j P_x^{ij(\text{plane})} \quad (5)$$

$$P_z^{ii} = - \sum_j P_z^{ij} \quad (6)$$

4.1.4 Artificial Viscosity

There are two forms of artificial viscosity; the nodal viscosity, Q_i , and the bond viscosity, Q_{ij} . The important distinction between Q_i (nodal) and Q_{ij} (bond) is that Q_i can only be activated during volumetric strain rate, but Q_{ij} can be activated even if there is no volumetric strain rate (such as pure shear or incompressible flow). The net effect is that Q_{ij} can introduce additional (artificial) strength into the computed results.

The nodal viscosity is identical to that used in standard finite element and finite difference methods (References 5 and 33):

$$Q_i = C_L \rho_i c_i h_i |\dot{\epsilon}_v| + C_Q \rho_i h_i^2 \dot{\epsilon}_v^2 \quad (1)$$

for $\dot{\epsilon}_v < 0$. C_L and C_Q are the linear and quadratic coefficients, ρ_i is the density of node i, c_i is the sound velocity of node i, and h_i is the minimum smoothing distance between node i and neighbor nodes j.

The bond viscosity of Monaghan and Gingold (Reference 34) can be expressed in the following form:

$$Q_{ij} = C_L \rho_i c_i |\mu_{ij}| + C_Q \rho_i \mu_{ij}^2 \quad (2)$$

for $\mu_{ij} < 0$, and

$$\mu_{ij} = \frac{h_{ij} (\dot{u}_{ij} x_{ij} + \dot{v}_{ij} z_{ij})}{r_{ij}^2 + \epsilon_o h_{ij}^2} \quad (3)$$

where $\dot{u}_{ij} = \dot{u}_i - \dot{u}_j$ is the x velocity difference between nodes i and j, and $x_{ij} = x_i - x_j$ is the x coordinate difference. The analogous terms for the z components are \dot{v}_{ij} and z_{ij} . The distance between nodes is $r_{ij} = \sqrt{x_{ij}^2 + z_{ij}^2}$, and ϵ_o is a small number ($\epsilon_o \approx 0.01$) that acts to limit μ_{ij} as r_{ij} becomes small.

Equation 2 can be rewritten in the following form (for $\epsilon_o = 0$):

$$Q_{ij} = C_L \rho_i c_i h_{ij} |\dot{\epsilon}_{ij}| + C_Q \rho_i h_{ij}^2 \dot{\epsilon}_{ij}^2 \quad (4)$$

for $\dot{\epsilon}_{ij} < 0$. This looks very similar to the nodal artificial viscosity of Equation 1, except the volumetric strain rate, $\dot{\epsilon}_v$, of Equation 1 is replaced with a linear strain rate, $\dot{\epsilon}_{ij}$, in Equation 4. This linear strain rate is simply the strain rate along the bond between nodes:

$$\dot{\epsilon}_{ij} = (V_j^N - V_i^N) / r_{ij} \quad (5)$$

where V_i^N is the velocity of node i along the bond from node i to node j, and V_j^N is the velocity of node j in the same direction. A similar form of this bond viscosity was developed previously for the NABOR particle method algorithm (References 35 and 36).

It should be noted that most of the SPH literature (Reference 34) describes the bond viscosity term as

$$\Pi_{ij} = (C_L c_{ij} |\mu_{ij}| + C_Q \mu_{ij}^2) / \rho_{ij} \quad (6)$$

for $\mu_{ij} < 0$. Here C_L , C_Q , and μ_{ij} are as defined previously, c_{ij} is the average sound velocity at nodes i and j , and ρ_{ij} is the average density at nodes i and j . Also, Π_{ij} is the viscosity for both nodes i and j . In the algorithms of Equations 1–5, Q_{ij} is based on the density and sound velocity of node i only. The relationship between the two forms is approximated by

$$Q_{ij} \approx \Pi_{ij} \rho_i^2 / 2 \quad (7)$$

For identical sound velocities and densities at nodes i and j , the relationship of Equation 7 is exact. The factor 2 in the denominator occurs because Π_{ij} is for both nodes whereas Q_{ij} is only for node i (and there is another Q_{ji} at node j).

4.1.5 Material Interfaces

Figure 32 shows a material interface represented by SPH nodes. If the two materials are not bonded together, the standard SPH algorithm introduces unacceptably large errors because nodes from material A influence the strain rates in nodes from material B, and vice versa. Also, shear and tensile stresses are developed between the two materials such that sliding and separation are significantly inhibited. If SPH approaches are to be applied to problems involving sliding interfaces, then specialized interface algorithms must be developed.

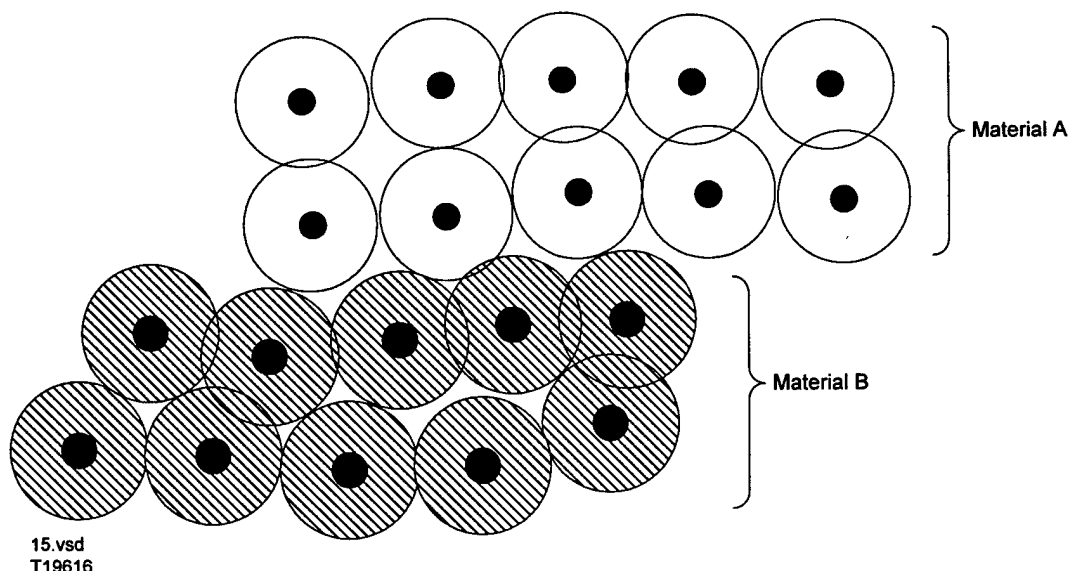


Figure 32. Material Interface With SPH Nodes

4.2 2D PLANE STRAIN GEOMETRY

The 2D plane strain geometry is a simplified form of the 2D axisymmetric geometry. The primary difference is that the plane strain geometry is for a unit thickness and has no hoop strains or strain rates.

Using the same notation as for the axisymmetric geometry in subsection 4.1.2, the two normal strain rates ($\dot{\epsilon}_x$, $\dot{\epsilon}_z$), the shear strain rate, $\dot{\gamma}_{xz}$, and the rotation rate, ω_{xz} , for center node i , are as follows:

$$\dot{\epsilon}_x = -\sum_j \beta_x W_{ij}' V_j (\dot{u}_j - \dot{u}_i) \ell_x \quad (1)$$

$$\dot{\epsilon}_z = -\sum_j \beta_z W_{ij}' V_j (\dot{v}_j - \dot{v}_i) \ell_z \quad (2)$$

$$\dot{\gamma}_{xz} = -\sum_j W_{ij}' V_j [\beta_z (\dot{u}_j - \dot{u}_i) \ell_z + \beta_x (\dot{v}_j - \dot{v}_i) \ell_x] \quad (3)$$

$$\omega_{xz} = \sum_j W_{ij}' V_j [\beta_z (\dot{u}_j - \dot{u}_i) \ell_z - \beta_x (\dot{v}_j - \dot{v}_i) \ell_x] / 2 \quad (4)$$

One of the differences is that the volume of node j is now identical to the area ($V_j = A_j$) because the plane strain geometry is for a unit thickness. Also, the axisymmetric hoop strain rate ($\dot{\epsilon}_\theta$) is replaced by the through-thickness strain rate, which is

$$\dot{\epsilon}_y \equiv 0 \quad (5)$$

The normalizing factors are also modified.

$$\beta_x = \frac{-1}{\sum W_{ij}' V_j r_{ij}^2 \ell_x^2} \quad (6)$$

$$\beta_z = \frac{-1}{\sum W_{ij}' V_j r_{ij}^2 \ell_z^2} \quad (7)$$

After the stresses have been determined, the forces on node j, due to stresses on node i, are as follows:

$$P_x^{ij} = W_{ij}' V_i V_j \left[\beta_x (\sigma_x^i - Q_{ij}) \ell_x + \beta_z \tau_{xz}^i \ell_z \right] \quad (8)$$

$$P_z^{ij} = W_{ij}' V_i V_j \left[\beta_z (\sigma_z^i - Q_{ij}) \ell_z + \beta_x \tau_{xz}^i \ell_x \right] \quad (9)$$

Here the notation is as provided in subsection 4.1.3.

4.3 3D GEOMETRY

There is very little additional complexity in going from 2D to 3D geometry. Again, there is similarity between the 3D SPH and the 3D standard element algorithms provided in subsection 3.8. The B-Spline smoothing function in 3D is

$$W_{ij} = \frac{1}{\pi h_{ij}^3} \left(1 - \frac{3}{2} v_{ij}^2 + \frac{3}{4} v_{ij}^3 \right) \quad 0 \leq v_{ij} \leq 1 \quad (1a)$$

$$W_{ij} = \frac{1}{\pi h_{ij}^3} \left[\frac{1}{4} (2 - v_{ij})^3 \right] \quad 1 \leq v_{ij} \leq 2 \quad (1b)$$

and the derivative is

$$W_{ij}' = \frac{1}{\pi h_{ij}^4} \left(-3v_{ij} + \frac{9}{4} v_{ij}^2 \right) \quad 0 \leq v_{ij} \leq 1 \quad (2a)$$

$$W_{ij}' = \frac{1}{\pi h_{ij}^4} \left[-\frac{3}{4} (2 - v_{ij})^2 \right] \quad 1 \leq v_{ij} \leq 2 \quad (2b)$$

The 3D B-Spline smoothing function and its derivative are simply $7/10h_{ij}$ times the corresponding 2D functions given in Equations 1 and 4 of subsection 4.1.1, and shown in Figure 29.

The 3D form of the Quadratic smoothing function is

$$W_{ij} = \frac{1}{\pi h_{ij}^3} \left[\frac{5}{8} \left(\frac{3}{8} v_{ij}^2 - \frac{3}{2} v_{ij} + \frac{3}{2} \right) \right] \quad 0 \leq v_{ij} \leq 2 \quad (3)$$

and the derivative is

$$W'_{ij} = \frac{1}{\pi h_{ij}^4} \left[\frac{15}{16} \left(\frac{1}{2} v_{ij} - 1 \right) \right] \quad 0 \leq v_{ij} \leq 2 \quad (4)$$

Here again, the 3D Quadratic smoothing function and its derivative are simply $5/8h_{ij}$ times the corresponding 2D functions given in Equations 5 and 6 of subsection 4.1.1, and shown in Figure 29.

The three normal strain rates $(\dot{\epsilon}_x, \dot{\epsilon}_y, \dot{\epsilon}_z)$, the three shear strain rates $(\dot{\gamma}_{xy}, \dot{\gamma}_{xz}, \dot{\gamma}_{yz})$, and the three rotational rates $(\omega_{xy}, \omega_{xz}, \omega_{yz})$ for the center node i , are as follows:

$$\dot{\epsilon}_x = -\sum_j \beta_x W'_{ij} V_j (\dot{u}_j - \dot{u}_i) \ell_x \quad (5)$$

$$\dot{\epsilon}_y = -\sum_j \beta_y W'_{ij} V_j (\dot{v}_j - \dot{v}_i) \ell_y \quad (6)$$

$$\dot{\epsilon}_z = -\sum_j \beta_z W'_{ij} V_j (\dot{w}_j - \dot{w}_i) \ell_z \quad (7)$$

$$\dot{\gamma}_{xy} = -\sum_j W'_{ij} V_j [\beta_y (\dot{u}_j - \dot{u}_i) \ell_y + \beta_x (\dot{v}_j - \dot{v}_i) \ell_x] \quad (8)$$

$$\dot{\gamma}_{xz} = -\sum_j W'_{ij} V_j [\beta_x (\dot{w}_j - \dot{w}_i) \ell_x + \beta_z (\dot{u}_j - \dot{u}_i) \ell_z] \quad (9)$$

$$\dot{\gamma}_{yz} = -\sum_j W'_{ij} V_j [\beta_z (\dot{v}_j - \dot{v}_i) \ell_z + \beta_y (\dot{w}_j - \dot{w}_i) \ell_y] \quad (10)$$

$$\omega_{xy} = \sum_j W'_{ij} V_j [\beta_y (\dot{u}_j - \dot{u}_i) \ell_y - \beta_x (\dot{v}_j - \dot{v}_i) \ell_x] / 2 \quad (11)$$

$$\omega_{xz} = \sum_j W'_{ij} V_j [\beta_x (\dot{w}_j - \dot{w}_i) \ell_x - \beta_z (\dot{u}_j - \dot{u}_i) \ell_z] / 2 \quad (12)$$

$$\omega_{yz} = \sum_j W'_{ij} V_j [\beta_z (\dot{v}_j - \dot{v}_i) \ell_z - \beta_y (\dot{w}_j - \dot{w}_i) \ell_y] / 2 \quad (13)$$

There is a change in nomenclature for the 3D algorithm when compared to the 2D algorithm. For the 2D strain rates and rotational rates in Equations 1–5 of subsection 4.1.2, \dot{u}_i and \dot{v}_i are the velocities corresponding to the x (radial) and z (axial) directions, respectively. For the 3D algorithm of Equations 5–13, the x, y, and z velocities are represented by \dot{u}_i , \dot{v}_i , and \dot{w}_i , respectively. This is consistent with the 3D finite element algorithms of subsection 3.8.

The three β factors are obtained in the same manner as the 2D geometry and are expressed as

$$\beta_x = \frac{-1}{\sum W'_{ij} V_j r_{ij} \ell_x^2} \quad (14)$$

$$\beta_y = \frac{-1}{\sum W'_{ij} V_j r_{ij} \ell_y^2} \quad (15)$$

$$\beta_z = \frac{-1}{\sum W'_{ij} V_j r_{ij} \ell_z^2} \quad (16)$$

There is an additional complexity in applying the NSF algorithm in 3D geometry. For 2D axisymmetric geometry there is only one possible orientation of axes because the z axis represents the axis of rotation. For 3D geometry the β factors are determined along the three principal axes. If the axes are changed, then the β factors may change and the computed results may also change. Additional work is required to examine the magnitude of this potential problem.

Finally, the nodal forces are as follows:

$$P_x^{ij} = W'_{ij} V_i V_j [\beta_x (\sigma_x^i - Q_{ij}) \ell_x + \beta_y \tau_{xy}^i \ell_y + \beta_z \tau_{xz}^i \ell_z] \quad (17)$$

$$P_y^{ij} = W'_{ij} V_i V_j [\beta_y (\sigma_y^i - Q_{ij}) \ell_y + \beta_x \tau_{xy}^i \ell_x + \beta_z \tau_{yz}^i \ell_z] \quad (18)$$

$$P_z^{ij} = W'_{ij} V_i V_j [\beta_z (\sigma_z^i - Q_{ij}) \ell_z + \beta_x \tau_{xz}^i \ell_x + \beta_y \tau_{yz}^i \ell_y] \quad (19)$$

SECTION 5

LINKING OF FINITE ELEMENTS AND SPH NODES

It has been noted previously that a desirable characteristic of the SPH approach is that it can be linked to standard finite element grids. This allows highly distorted materials to be considered together with structural response materials. Also, as shown in Figure 27, a single material model subroutine can be used for both the standard elements and the SPH nodes. This means that a material model needs to be incorporated and validated only one time, and that the user can be assured that the identical material model is used for both the standard elements and the SPH nodes. This work has been reported in References 28, 29, and 31.

Figure 33 shows how SPH nodes can be attached to a standard finite element grid. The broken circle around node i represents the effective region ($0 \leq v_{ij} \leq 2$) for SPH nodes on node i . The size of the SPH interface nodes is equal to the size of the interface elements. The mass of the SPH interface nodes comes from the SPH nodes only, and this ensures that the mass on all nodes is essentially equal.

The current approach for this type of linkage is to determine the strain rates for SPH node i only from nodes n_1, \dots, n_5 . The standard nodes in the effective region (n_6, \dots, n_9) are not included because of the complexity they would introduce into the numerical algorithm. The strain rates can be accurately computed on the interface by using the NSF algorithm, but the resulting forces appear to be in error.

The forces on SPH nodes i come from SPH nodes n_1, \dots, n_5 and from interface elements B and C. There is no direct force contribution from standard nodes n_6, \dots, n_9 , other than through the interface elements. Improvements could include consideration of standard nodes (n_6, \dots, n_9) or generation of ghost nodes on the standard node side of the interface.

Figure 34 shows how SPH nodes interact with a standard grid on a sliding interface. The SPH nodes are designated as slave nodes and the standard elements form the master surface. As was the case for the attached interface, the standard nodes (m_2, m_3, n_6) do not directly affect the strain rates in SPH node i , and do not directly affect the forces on node i . The maximum allowable overlap of an SPH node and slave node i , with master surface $m_2 - m_3$, is shown as δ_0 . When the SPH nodes are initially defined as SPH nodes, then $\delta_0 = 0$. When the SPH nodes are converted

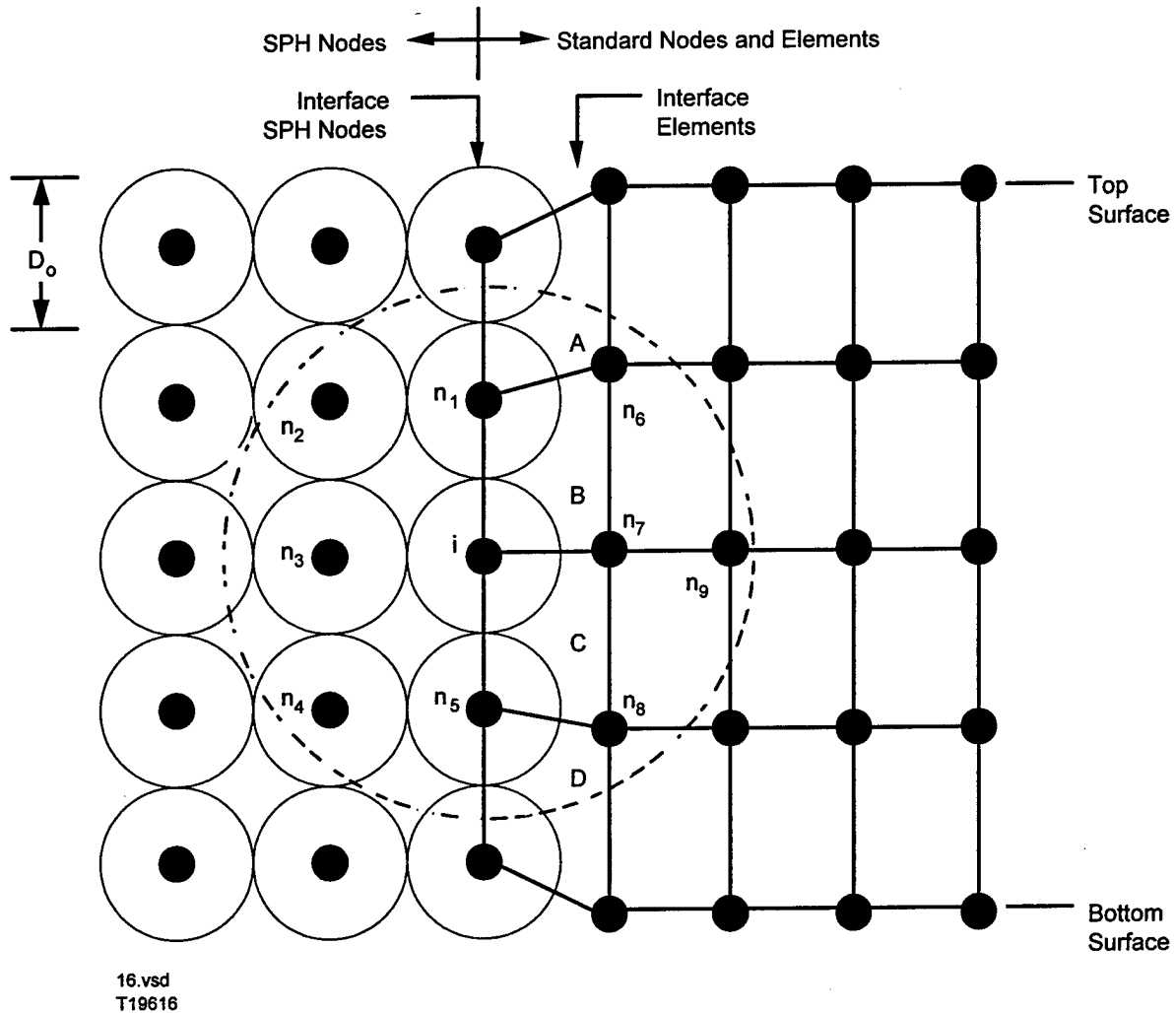


Figure 33. SPH Node Attachment to a Standard Grid

from standard elements, δ_0 can be a small fraction of the SPH node diameter. The approximations for the sliding interface are similar to those of the attached interface, but more research is required to evaluate and improve the existing algorithm. The specific equations are presented in subsection 3.4.2.

When slave node i overlaps ($\delta \geq \delta_0$) master segment $m_2 - m_3$, then the three normal velocities of nodes i , m_2 , and m_3 are adjusted to (1) conserve linear momentum, (2) conserve angular momentum and (3) provide a normal velocity match of node i on master segment $m_2 - m_3$. The positions of the nodes are adjusted to be consistent with the velocity changes. The specific equations are presented in subsection 3.4.2.

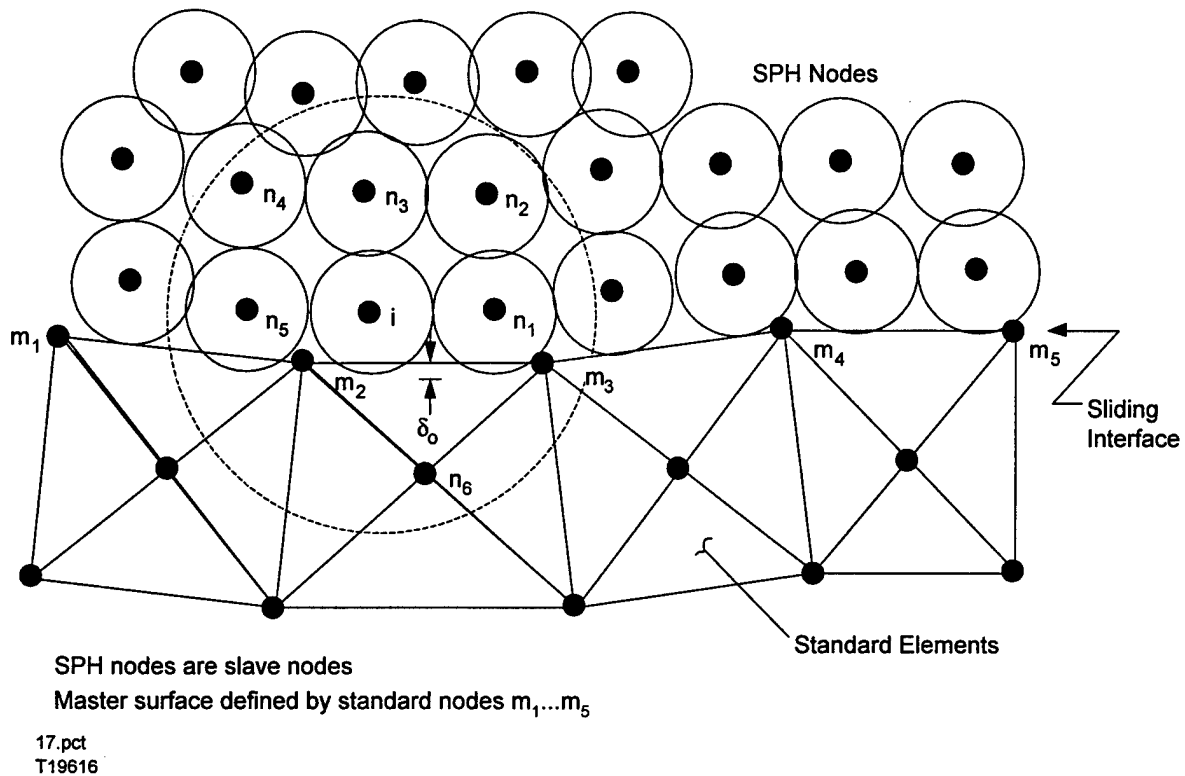


Figure 34. SPH Node Sliding on a Standard Grid

It is also possible to generate SPH nodes from a standard finite element grid. Figure 8 shows an illustration of a standard erosion algorithm, as described in subsection 3.4.3, and Figure 35 shows the SPH node generation algorithm. The standard algorithm removes (erodes) elements from the sliding interface when the elements are strained to an equivalent plastic strain of $\bar{\epsilon}_p \approx 1.5$, and it then redefines the master surface and slave nodes. Although the mass is retained at the nodes, the volumes of the eroded elements are discarded, and this introduces inaccuracies into the algorithm.

The SPH generation algorithm is similar, except it replaces the highly strained elements on the master surface with equivalent SPH nodes. Because the SPH nodes replace both the mass and volume of the eroded elements, this is a more accurate algorithm. Here the elements are converted to SPH nodes at an equivalent plastic strain of $\bar{\epsilon}_p \approx 0.5$.

When a standard triangular element is replaced by a circular SPH node, the circle will extend beyond the replaced triangular element by a distance δ_0 , as shown in Figure 35. For the subsequent sliding interface computations, an effective crossover distance is defined as $\delta_{\text{eff}} = \delta - \delta_0$, where δ is the current crossover distance and δ_0 is the initial crossover distance.

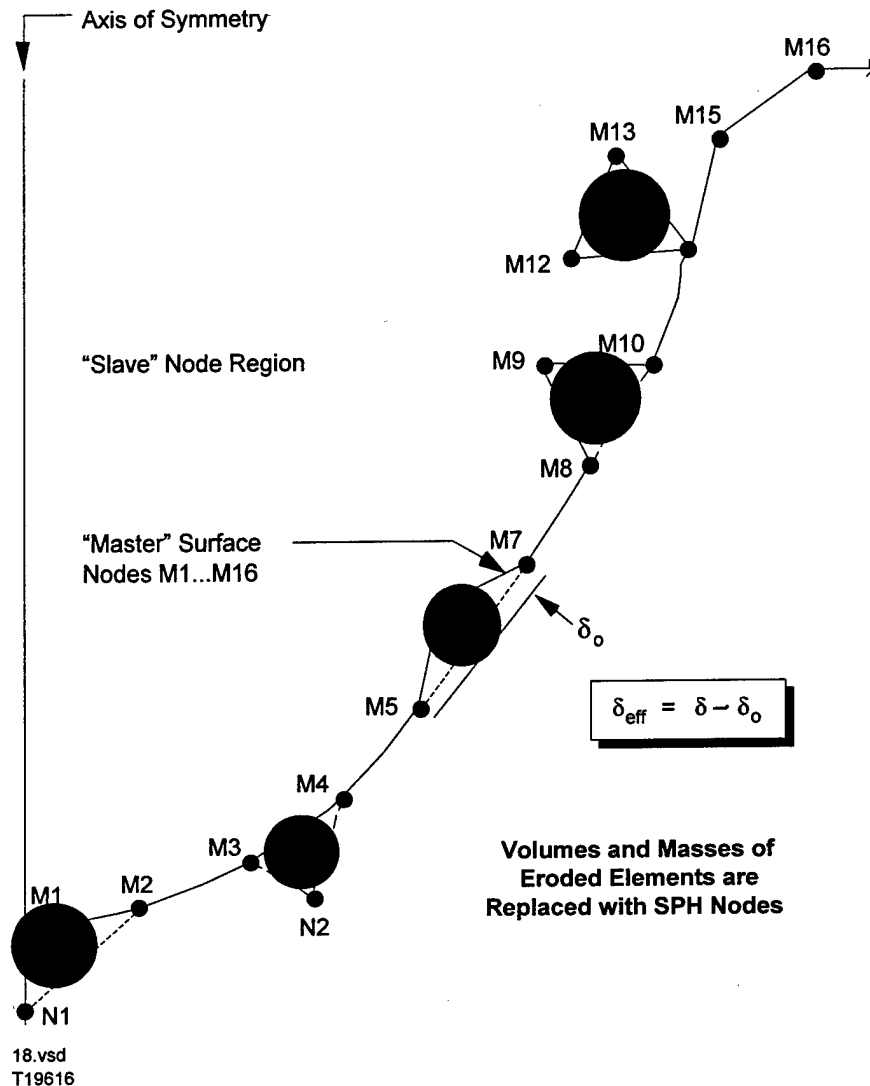


Figure 35. Description of the SPH Node Generation Algorithm

This effective distance is then used to determine contact ($\delta_{\text{eff}} \geq 0$), and to adjust the velocities and displacements of the master and slave nodes as discussed previously.

The current SPH generation algorithm has a significant approximation in that the generated SPH nodes are allowed to slide along the standard elements, instead of being attached to the elements. Future effort is required to develop an interface algorithm that will allow the SPH node to be attached to the standard finite element grid after it has been generated.

SECTION 6

MATERIAL MODELS

This section describes the material models that are available. The basic material types are as follows:

- Solid (metal) materials
- Explosive materials
- Crushable/concrete materials
- Liquid materials
- Brittle (ceramic) materials
- Reactive explosive materials
- RDG solid (metal) materials.

The solid (metal) material models and algorithms are presented in detail and the unique portions of the others are also presented. In some instances, there are many models available for a material type, and in other cases there is only a single model.

6.1 SOLID MATERIALS

The solid material models are generally used for metals, although some of the models can be used for nonmetallic materials. The stress determination algorithms for 1D, 2D, and 3D are provided in subsections 3.1.3 (1D), 3.4.4 (2D), and 3.8.4 (3D).

The 3D stresses, as presented previously in subsection 3.8.4, are composed of three normal stresses $(\sigma_x, \sigma_y, \sigma_z)$ and three shear stresses $(\tau_{xy}, \tau_{xz}, \tau_{yz})$. The three normal stresses are expressed as

$$\sigma_x = s_x - (P + Q) \quad (1)$$

$$\sigma_y = s_y - (P + Q) \quad (2)$$

$$\sigma_z = s_z - (P + Q) \quad (3)$$

where s_x , s_y , and s_z are the normal deviator stresses, P is the hydrostatic pressure, and Q is the artificial viscosity.

Trial values of the deviator stresses and shear stresses at time $t + \Delta t$ are

$$s_x^{t+\Delta t} = s_x^t + 2G\dot{e}_x\Delta t + \Delta s_x \quad (4)$$

$$s_y^{t+\Delta t} = s_y^t + 2G\dot{e}_y\Delta t + \Delta s_y \quad (5)$$

$$s_z^{t+\Delta t} = s_z^t + 2G\dot{e}_z\Delta t + \Delta s_z \quad (6)$$

$$\tau_{xy}^{t+\Delta t} = \tau_{xy}^t + G\dot{\gamma}_{xy}\Delta t + \Delta\tau_{xy} \quad (7)$$

$$\tau_{xz}^{t+\Delta t} = \tau_{xz}^t + G\dot{\gamma}_{xz}\Delta t + \Delta\tau_{xz} \quad (8)$$

$$\tau_{yz}^{t+\Delta t} = \tau_{yz}^t + G\dot{\gamma}_{yz}\Delta t + \Delta\tau_{yz} \quad (9)$$

In Equation 4 the first term (s_x^t) is the normal stress at the previous time and the second term ($2G\dot{e}_x\Delta t$) is the incremental stress due to the incremental strain ($\dot{e}_x\Delta t$) during that time increment, where G is the elastic shear modulus and Δt is the integration time increment. The third term (Δs_x) is due to shear stresses from the previous time increment, which now act as normal stresses due to the new orientation of the element caused by an incremental rotation ($\omega_y\Delta t, \omega_z\Delta t$) during the time increment. The remaining normal stresses and shear stresses have a similar form.

The correction terms for element rotations are given in Equations 37–42 of subsection 3.8.4.

Equations 4–9 assume an elastic response of the material. If the strength of the material is exceeded, then plastic flow (or fracture) will occur. The Von Mises yield criterion is used to determine an equivalent stress, $\bar{\sigma}$, that can be compared to the uniaxial tensile (or compressive) strength of the material. The general form of the equivalent stress is

$$\bar{\sigma} = \sqrt{\frac{1}{2} \left[(\sigma_x - \sigma_y)^2 + (\sigma_x - \sigma_z)^2 + (\sigma_y - \sigma_z)^2 + 6(\tau_{xy}^2 + \tau_{xz}^2 + \tau_{yz}^2) \right]} \quad (10)$$

Using deviator stresses (instead of total stresses), Equation 10 can be rewritten as

$$\bar{\sigma} = \sqrt{\frac{3}{2}(s_x^2 + s_y^2 + s_z^2) + 3(\tau_{xy}^2 + \tau_{xz}^2 + \tau_{yz}^2)} \quad (11)$$

If $\bar{\sigma}$ is not greater than the equivalent tensile strength of the material, σ , the final deviator and shear stresses are as given in Equations 4–9. If $\bar{\sigma}$ is greater than σ , then the stresses in Equations 4–9 are multiplied by the factor $(\sigma / \bar{\sigma})$. When the reduced deviator and shear stresses are put into Equation 11, the result is always $\bar{\sigma} = \sigma$. This is known as the radial return algorithm.

In the following subsections, models are presented for the strength of the material (σ), the pressure (P) and artificial viscosity (Q). Additional subsections address a 2D orthotropic algorithm, the internal energy algorithm, fracture models, and a fragmentation model.

6.1.1 Johnson-Cook Strength Model

The Johnson-Cook strength model (Reference 37) is expressed as

$$\sigma = [C_1 + C_2 \varepsilon^N] [1 + C_3 \ln \dot{\varepsilon}^*] [1 - T^{*M}] + C_4 P \quad (1)$$

Where ε is the equivalent plastic strain, $\dot{\varepsilon}^* = \dot{\varepsilon} / \dot{\varepsilon}_0$ is the dimensionless strain rate for $\dot{\varepsilon}_0 = 1.0s^{-1}$, T^* is the homologous temperature, and P is the hydrostatic pressure. This model is valid only for $0 \leq T^* \leq 1.0$. The material constants are C_1 , C_2 , N, C_3 , M, and C_4 . C_1 and C_2 have units of stress and the others are dimensionless. The original model did not include the pressure term ($C_4 P$).

Although this model is empirical, it is flexible, robust, and contains the effects of the important parameters. The strength goes to zero as the temperature approaches melting ($T^* = 1.0$). It is also relatively easy to obtain constants for this model (References 37 and 38).

A constant flow stress ($\sigma = C_1$) can be obtained by setting $C_2 = C_3 = C_4 = T^{*M} = 0$, a linear strain hardening model ($\sigma = C_1 + C_2 * \varepsilon$) can be obtained by setting $C_3 = C_4 = T^{*M} = 0$, and a pressure hardening model ($\sigma = C_1 + C_4 P$) can be obtained by setting $C_2 = C_3 = T^{*M} = 0$.

6.1.2 Modified Johnson-Cook Strength Model

The modified Johnson-Cook strength model (Reference 38) is expressed as

$$\sigma = [C_1 + C_2 \dot{\epsilon}^N] [\dot{\epsilon}^{*C_3}] [1 - T^{*M}] + C_4 P \quad (1)$$

This is identical to the Johnson-Cook model in subsection 6.1.1, except that the strain rate effect $[\dot{\epsilon}^{*C_3}]$ is different. This model provides an enhanced strain rate effect at high strain rates.

6.1.3 Zerilli-Armstrong Strength Model for FCC Metals

The Zerilli-Armstrong strength model (Reference 39) for FCC metals is expressed as

$$\sigma = C_0 + C_2 \epsilon^N \exp(-C_3 \cdot T + C_4 T \ln \dot{\epsilon}) \quad (1)$$

Where ϵ is the equivalent plastic strain, T is the absolute temperature, and $\dot{\epsilon}$ is the equivalent strain rate. The material constants are C_0 , C_2 , N , C_3 , and C_4 . C_0 and C_2 have units of stress, and C_3 and C_4 have units of (temperature)⁻¹. The grain size is not represented as a variable (as it is in Reference 39) but is included in C_0 .

6.1.4 Zerilli-Armstrong Strength Model for BCC Metals

The Zerilli-Armstrong model (Reference 39) for BCC metals is expressed as

$$\sigma = C_0 + C_1 \exp(-C_3 T + C_4 T \ln \dot{\epsilon}) + C_5 \epsilon^N \quad (1)$$

This is similar to the Zerilli-Armstrong FCC model in subsection 6.1.3. C_0 , C_1 , and C_5 have units of stress, and C_3 and C_4 have units of (temperature)⁻¹.

6.1.5 Bodner-Partom Strength Model

The Bodner-Partom model (References 40, 41, and 42) is expressed as

$$\sigma = Z \left[- \left(\frac{2N}{N+1} \right) \bullet \ln \left(\frac{\sqrt{3}\dot{\epsilon}_p}{2D_0} \right) \right]^{\left(\frac{1}{2N} \right)} \quad (1)$$

where $\dot{\epsilon}_p$ is the equivalent plastic strain rate and D_0 is an input constant representing the maximum allowable plastic strain rate. The other input constants are Z_0 , Z_1 , N_0 , N_1 , M_0 , M_1 , and α .

For constants $M_1 = \alpha = 0$

$$Z = Z_1 - (Z_1 - Z_0) \exp(-M_0 W_p) \quad (2)$$

where W_p is the plastic work per unit volume.

For constants $M_1 > 0$ and $\alpha > 0$ an expanded form is used.

$$Z = Z_1 - (Z_1 - Z_0) \exp(-M_0 W_p) \exp(-(M_0 + M_1 - M)/\alpha) \quad (3)$$

where

$$M = M_0 + M_1 \exp(-\alpha W_p) \quad (4)$$

For $N_1 = T_{\text{zero}}$

$$N = N_0 \quad (5)$$

and for $N_1 > T_{\text{zero}}$

$$N = N_0 + \left(\frac{N_1 - T_{\text{zero}}}{T - T_{\text{zero}}} \right) \quad (6)$$

where T is the absolute temperature and T_{zero} is the absolute zero temperature.

This constitutive model requires an iterative solution because the strength, σ , and the plastic strain rate, $\dot{\epsilon}_p$, are dependent upon one another. This results in increased CPU time. Also, this model is more complex than the Johnson-Cook and Zerilli-Armstrong models, and References 40, 41, and 42 should be consulted for more information.

6.1.6 MTS Strength Model

The MTS model is presented in References 43 and 44. The following description is an edited version provided by P.J. Maudlin of Los Alamos National Laboratory. The material strength is

$$\sigma = \hat{\sigma}_a + \frac{G}{G_0} (s_{th} \hat{\sigma} + s_{th,i} \hat{\sigma}_i + s_{th,s} \hat{\sigma}_s) \quad (1)$$

which contains the constants $\hat{\sigma}_a$ (which represents dislocation interactions with long-range barriers), $\hat{\sigma}_i$ (which represents dislocation interactions with interstitial atoms, and $\hat{\sigma}_s$ (which represents dislocation interactions with solute atoms).

The first product in the equation for σ contains a micro-structure evolution variable, i.e., $\hat{\sigma}$, called the mechanical threshold stress, that is multiplied by a constant-structure deformation variable s_{th} ; s_{th} is a function of absolute temperature T and plastic strain-rate $\dot{\epsilon}_p$. The evolution equation for $\hat{\sigma}$ is a differential hardening law representing dislocation-dislocation interaction:

$$\frac{\partial \hat{\sigma}}{\partial \epsilon_p} = \Theta_0 \left[1 - \frac{\tanh\left(\alpha \frac{\hat{\sigma}}{\hat{\sigma}_s}\right)}{\tanh(\alpha)} \right] \quad (2)$$

where $\hat{\sigma}_s$ is the value of $\hat{\sigma}$ at large plastic strain and α is a material constant.

In the equation for $\frac{\partial \hat{\sigma}}{\partial \epsilon_p}$, Θ_0 represents hardening due to dislocation generation and the stress ratio represents softening due to dislocation recovery. The threshold stress at zero strain-hardening $\hat{\sigma}_s$ is called the saturation threshold stress. Relationships for Θ_0 , $\hat{\sigma}_s$ are:

$$\Theta_0 = a_0 + a_1 \ln(\dot{\epsilon}_p) + a_2 \sqrt{\dot{\epsilon}_p} \quad (3)$$

which contains the dislocation generation material constants a_1 , a_2 , and a_3 .

Also

$$\hat{\sigma}_s = \hat{\sigma}_{s0} \left(\frac{\dot{\epsilon}_p}{\dot{\epsilon}_{s0}} \right)^{kT/Gb^3A} \quad (4)$$

where $\hat{\sigma}_{s0}$ is the saturation stress at zero degrees kelvin, $\dot{\epsilon}_{s0}$ is a reference strain rate, b is the magnitude of Burgers vector (inter-atomic slip distance), A is another material constant, and K is Boltzmanns constant.

The shear modulus in these equations is assumed to be a function of the temperature and is expressed as

$$G = b_0 - b_1 / (\exp(b_2 T) - 1) \quad (5)$$

where b_0 is the shear modulus at zero degrees Kelvin, and b_1 and b_2 are constants.

For thermal-activation controlled deformation s_{th} is evaluated via an Arrhenius rate equation:

$$s_{th} = \left[1 - \left(\frac{kT \ln(\dot{\epsilon}_0 / \dot{\epsilon}_p)}{Gb^3 g_0} \right)^{\frac{1}{q}} \right]^{\frac{1}{p}} \quad (6)$$

where $\dot{\epsilon}_0$ is a reference strain rate, g_0 is the normalized activation energy for a dislocation interaction, and p and q are additional constants.

Expressions for $s_{th,i}$ and $s_{th,s}$ are identical to the equation for s_{th} in form but use the constants $\dot{\epsilon}_{0,i}$, $g_{0,i}$, p_i , q_i (for $s_{th,i}$) and $\dot{\epsilon}_{0,s}$, $g_{0,s}$, p_s , q_s (for $s_{th,s}$).

The MTS model is much more complex than the Johnson-Cook and Zerilli-Armstrong models, and References 43 and 44 should be consulted for more information.

6.1.7 Steinberg-Guinan-Lund Strength Model

The Steinberg-Guinan-Lund models are described in References 45 and 46. A rate independent model is given in Reference 45 and a rate dependent model is provided in Reference 46. In this subsection the material strength is represented by Y instead of σ .

The strain-rate dependent form of the SGL model defines the yield stress as

$$Y = \left[Y_T(\dot{\epsilon}_p, T) + Y_A f(\dot{\epsilon}_p) \right] \frac{G(P, T)}{G_0} \quad (1)$$

where the athermal and thermally activated components $Y_A f(\epsilon_p)$ and Y_T are defined by

$$Y_A f(\epsilon_p) = Y_A \left\{ 1 + \beta(\epsilon_p + \epsilon_i) \right\}^n \quad (2)$$

and

$$\dot{\epsilon}_p = \left(\frac{1}{C_1} \exp \left[\frac{2U_K}{T} \left(1 - \frac{Y_T}{Y_P} \right)^2 \right] + \frac{C_2}{Y_T} \right)^{-1} \quad (3)$$

In these equations, P and T are the pressure and temperature, ϵ_p and $\dot{\epsilon}_p$ are the equivalent plastic strain and equivalent plastic strain rate, Y_A is the yield strength at the Hugoniot elastic limit (HEL) and $f(\epsilon_p)$ is the work-hardened function with $\{\beta, \epsilon_i, \text{ and } n\}$ as fitting parameters. G_0 is the initial shear modulus, Y_P is the Peierls stress, and $2U_K$ is the energy necessary to form a pair of kinks in a dislocation segment. The quantities C_1 and C_2 are defined in terms of various dislocation mechanics parameters and are specific to the material being modeled. The shear modulus G is defined by

$$G(P, T) = G_0 \left[1 + \frac{AP}{\eta^{1/3}} - B(T - T_{\text{room}}) \right] \quad (4)$$

with A and B treated as material constants and $\eta(\rho/\rho_0)$ denoting the compression. Melting is modeled using a modified Lindemann law, where the melt temperature T_m is defined as

$$T_m = T_{mo} \exp \left[2\alpha \left(1 - \frac{1}{\eta} \right) \right] \eta^{2(\gamma_0 - \alpha - 1/3)} \quad (5)$$

T_{mo} is the melt temperature at constant volume, γ_0 is the initial Gruneisen coefficient, and α is a material constant. For any compression η in which the temperature T exceeds T_m , melting is considered to have occurred, resulting in the loss of yield strength and shear strength. In addition, there are two limits imposed.

$$Y_A f(\epsilon_p) \leq Y_{max}^0 \quad (6)$$

And

$$Y_T \leq Y_p \quad (7)$$

where Y_{max}^0 is the work-hardening maximum in the rate-dependent version of the model. The rate-dependent form of the SGL model is treated as a special case of the more general form for yield stress with Y_T set to zero. In particular, the rate-independent model assumes the form

$$Y = Y_0 f(\epsilon_p) G(P, T) / G_0 \quad (8)$$

where $f(\epsilon_p)$ and $G(P, T)$ are defined as before. Here, however, the following limit applies:

$$Y_0 f(\epsilon_p) \leq Y_{max} \quad (9)$$

These models are more complex than the Johnson-Cook and Zerilli-Armstrong models, and References 45 and 46 should be consulted for more information.

6.1.8 2D Orthotropic Model

This is a simplified anisotropic model that is anisotropic only in the plastic response. The elastic response remains isotropic. It essentially expands and contracts the yield surface in the three primary axes and allows for initial orientation of the material axes with the system coordinate axes. It is described in detailed in Reference 47. The description that follows is an edited version provided by P.J. Maudlin of Los Alamos National Laboratory.

The 1948 Hill yield function (Reference 48) written in terms of total stress (σ_{ij}) is

$$f = \frac{1}{2} \left\{ F(\sigma_{22} - \sigma_{33})^2 + G(\sigma_{33} - \sigma_{11})^2 + H(\sigma_{11} - \sigma_{22})^2 + 2N\sigma_{12}^2 + 2M\sigma_{13}^2 + 2L\sigma_{23}^2 \right\} - \sigma^2 = 0 \quad (1)$$

where the quantity σ is a flow stress that is assumed to be a function of strain, strain rate, and temperature invariants. Expressing Hill's Quadratic in terms of deviatoric stress (s_{ij}) gives

$$f = \frac{1}{2} \left\{ (G + H)s_{11}^2 + (F + H)s_{22}^2 + (F + G)s_{33}^2 - 2Hs_{11}s_{22} - 2Gs_{11}s_{33} - 2Fs_{22}s_{33} + 2Ns_{12}^2 + 2Ms_{13}^2 + 2Ls_{23}^2 \right\} - s^2 = 0 \quad (2)$$

The physical interpretation and measurement of the parameters in Equation 2 are discussed by Hill in some detail. This function is conveniently analytic and can be used for three-dimensional problems. In terms of independent stress components it represents a five-dimensional stress space.

For a two-dimensional problem, recalling that the trace of the deviatoric stress tensor is zero, Hill's yield function reduces to

$$f = \frac{1}{2} \left\{ (4G + H + F)s_{11}^2 + (4F + H + G)s_{22}^2 + (4F + 4G - 2H)s_{11}s_{22} + 2N s_{12}^2 \right\} - \sigma^2 = 0 \quad (3)$$

The yield surface actually implemented in EPIC is a π -plane transformation (useful for yield surface data fitting) of Equation 3 defined in terms of three new variables (s_x, s_y, s_z) which are linear combinations of the deviatoric stress components.

$$\begin{pmatrix} s_x \\ s_y \\ s_z \end{pmatrix} \equiv \begin{pmatrix} \frac{-\sqrt{3}}{2} & -\sqrt{3} & 0 \\ \frac{3}{2} & 0 & 0 \\ 0 & 0 & -\sqrt{3} \end{pmatrix} \begin{pmatrix} s_{11} \\ s_{22} \\ s_{12} \end{pmatrix} \quad (4)$$

These transformed stresses represent an orthogonal reference frame whose $s_x - s_y$ plane is coincident with the π -plane in the principle axes space for deviatoric stress. Substituting

Equation 4 into Equation 3, assuming that the rotational term $s_x s_y$ is insignificant, and collecting terms, gives the form that is used in EPIC for two-dimensional problems.

$$f = A s_x^2 + B s_y^2 + C s_z^2 - \sigma^2 = 0 \quad (5a)$$

Or

$$f = A \left(-\frac{\sqrt{3}}{2} s_{11} - \sqrt{3} s_{22} \right)^2 + B \left(\frac{3}{2} s_{11} \right)^2 + C \left(-\sqrt{3} s_{12} \right)^2 - \sigma^2 = 0 \quad (5b)$$

where the shape factor constants A, B, and C can be constructed from the Hill constants F, G, H, and N. For the special case where the shape factors $A = B = C = 1$, Equation 5 simplifies to the von Mises yield function.

The yield function given by Equation 5 may contain an implied normalization in the quantity σ . As it appears in Equation 5, σ represents a directionally averaged flow stress. If the flow stress is constructed solely from uniaxial stress data in a given material direction, such as “1” for example, then the flow stress function σ_{us} (in equivalent stress units) is conceptually different from the quantity appearing in Equation 5 and needs to be renormalized, i.e.,

$$\sigma = \sigma_{us} / \bar{M} \quad (6)$$

in order to recover the uniaxial stress result:

$$s_{11} = \pm \frac{2}{3} \sigma_{us} \quad (7)$$

Substitution of Equations 6 and 7 into the yield function given by Equation 5 and solving for the normalization constant \bar{M} under the assumption of uniaxial stress in the “1” direction gives

$$\bar{M} = \frac{1}{\sqrt{B}} \quad (8)$$

The important point here is that if a flow stress function like Johnson-Cook is used for σ in Equation 5, where the model coefficients have been characterized from data measured in a

certain direction, then renormalization of the flow stress model by some \bar{M} is necessary. Obviously as the yield function tends to isotropy, Equation 8 indicates that \bar{M} goes to unity.

The yield function given by Equation 5 is cast in a reference frame that rotates and translates with an element of material relative to the laboratory frame. From the point of view of an observer in this material frame, the material element experiences only deformation without rigid body motion (pure stretch). For two-dimensional problems the rigid body rotations are planar occurring in the x-z plane, and are described by the angle θ . An initial value for this angle, i.e., $\theta(t=0)$, can be specified that measures the initial orientation difference between the z axis in the laboratory frame and the z axis in the material frame. Thus, the material constants for Equation 5 (i.e., A, B, C) can be measured in a reference frame initially different from the reference frame that EPIC uses for some application calculation.

6.1.9 Internal Energy

The shear and deviator stresses, together with the shear and deviator strain rates, generate internal energy in the material. This energy leads to increased temperatures (that affect the strength models) and it is also used in the Equation of State model for the pressures. This incremental internal energy (for a cycle of integration) is

$$\Delta E_d = (\bar{s}_x \dot{e}_x + \bar{s}_y \dot{e}_y + \bar{s}_z \dot{e}_z + \bar{\tau}_{xy} \dot{\gamma}_{xy} + \bar{\tau}_{xz} \dot{\gamma}_{xz} + \bar{\tau}_{yz} \dot{\gamma}_{yz}) (\bar{V} / V_o) \Delta t \quad (1)$$

The bars on the deviator and shear stresses, and the volume, represent averages of these values at times t and $t + \Delta t$. The factor \bar{V} / V_o converts the energy to internal energy per initial volume.

6.1.10 Artificial Viscosity

The artificial viscosity is an important term in the representations for the normal stresses, as shown in Equations 1–3 in subsection 6.1. It is combined with the normal stresses to damp out localized oscillations of the concentrated masses. It tends to eliminate spurious oscillations which would otherwise occur for wave propagation problems. This technique was originally proposed by Von Neumann and Richtmyer (Reference 33) and has been expanded for use in various computer codes (Reference 5). It is expressed in terms of linear and quadratic components and is applied only when the volumetric strain rate (\dot{e}_v) is negative.

$$Q = C_L \rho c_s h |\dot{\epsilon}_v| + C_Q \rho h^2 (\dot{\epsilon}_v)^2 \text{ for } \dot{\epsilon}_v < 0 \quad (1)$$

$$Q = 0 \text{ for } \dot{\epsilon}_v \geq 0$$

where c_s is the sound velocity of the material, ρ is the density, and h is a characteristic dimension (such as minimum altitude) of the element. C_L and C_Q are the linear and quadratic dimensionless coefficients.

6.1.11 Mie-Gruneisen Equation of State

The Mie-Gruneisen Equation of State (Reference 49) is used to compute the pressure term in Equations 1–3 of subsection 6.1. The pressure is a function of the volumetric strain and the internal energy.

$$P = P_v + \Gamma E_s (1 + \mu) \quad (1)$$

where

$$P_v = (K_1 \mu + K_2 \mu^2 + K_3 \mu^3) \left(1 - \frac{\Gamma \mu}{2} \right) \quad (2)$$

Substituting Equation 2 into Equation 1 gives the complete expression for the pressure.

$$P = (K_1 \mu + K_2 \mu^2 + K_3 \mu^3) \left(1 - \frac{\Gamma \mu}{2} \right) + \Gamma E_s (1 + \mu) \quad (3)$$

where $\mu = V_0/V - 1$, K_1 , K_2 , and K_3 are material-dependent constants and Γ is the Gruneisen coefficient. V_0 and V are the initial and current element volumes.

Since the pressure can be significantly affected by the internal energy E_s , it is desirable to solve the pressure and energy equations simultaneously. This gives

$$E_s^{t+\Delta t} = \frac{E_s^t - .5 \left[(P + Q)^t + Q^{t+\Delta t} + P_v^{t+\Delta t} \right] \dot{\epsilon}_v \Delta t + \Delta E_d}{1 + .5 \Gamma (1 + \mu) \dot{\epsilon}_v \Delta t} \quad (4)$$

where $\dot{\epsilon}_v$ is the volumetric strain rate and ΔE_d is the internal energy generated by the deviator and shear stresses during the previous cycle. E_s is the total internal energy per initial unit volume.

Substituting Equation 4 into Equation 3 gives the pressure at time = $t + \Delta t$ for the internal energy at time = $t + \Delta t$.

It is interesting that Equation 3 reduces to $P = K_1\mu$ for small strains and spherical stress (no shear). The higher order terms ($K_2\mu^2$ and $K_3\mu^3$) go to zero and the internal energy is $K_1\mu^2/2$. This shows that K_1 is consistent with an elastic bulk modulus.

Another form of the Mie-Gruneisen Equation of State is

$$P = \frac{\rho_0 c_s^2 \eta}{(1 - S\eta)^2} \left(1 - \frac{\Gamma\eta}{2} \right) + \Gamma E_s \quad (5)$$

where ρ_0 is the initial density, $\eta = 1 - \rho_0/\rho$, E_s is the internal energy per initial unit volume, c_s is the bulk sound velocity, Γ is the Gruneisen coefficient, and s is the slope of the $U_s - U_p$ relationship. $U_s - U_p$ are the sound velocity and particle velocity, respectively. Again the pressure-energy equations are solved simultaneously as they are in Equations 1 – 4.

6.1.12 Johnson-Cook Fracture Model

The Johnson-Cook fracture model (Reference 50) is based on accumulated damage. When the damage approaches unity ($D = 1.0$), the element has failed. After the element has failed the material essentially behaves as a liquid because it has no strength (no shear and deviator stresses) and it cannot develop hydrostatic tension. A failed element can produce only hydrostatic compression. It is also possible to soften (weaken) the strength as the damage increases, such that the failure is gradual rather than instantaneous.

The damage to an element is defined as

$$D = \sum \frac{\Delta \epsilon_p}{\epsilon_p^f} \quad (1)$$

where $\Delta \epsilon_p$ is the increment of equivalent plastic strain which occurs during an integration cycle, ϵ_p^f is the equivalent strain to fracture, under the current conditions of strain rate, temperature, pressure, and equivalent stress. Fracture is then allowed to occur when $D = 1.0$.

To illustrate, assume the fracture strain in Figure 36 is a function of only the pressure-stress ratio, σ^* , which will be defined later. This assumed relationship indicates the material can be more severely strained when it is under hydrostatic compression. The example shows how damage is accumulated under compression. When the pressure is released to $\sigma^* = 0$, $D = 0.75$ even though the plastic strain, ϵ_p , is greater than ϵ_p^f at $\sigma^* = 0$. The importance of path-dependency is evident since a model based only on current conditions would incorrectly predict fracture for these conditions.

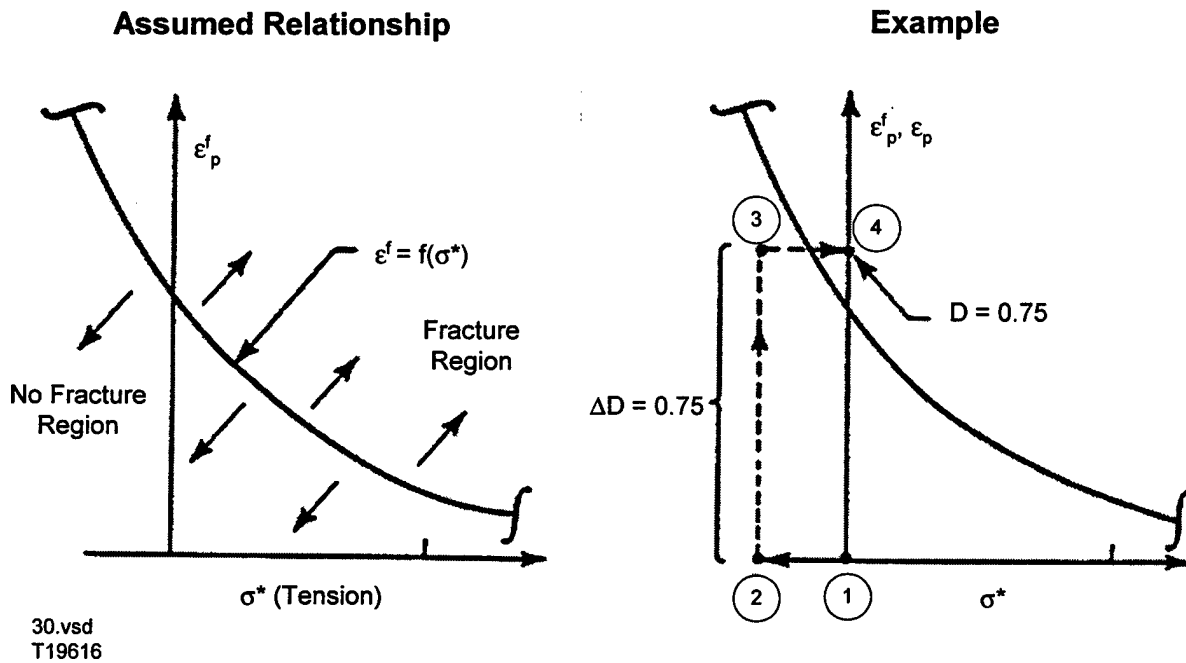


Figure 36. Description of the Johnson-Cook Fracture Model

The general expression for the strain at fracture is given by

$$\epsilon_p^f = [D_1 + D_2 \exp^{D_3 \sigma^*}] [1 + D_4 \ln \dot{\epsilon}^*] [1 + D_5 T^*] \quad (2)$$

for constant values of the variables (σ^* , $\dot{\epsilon}^*$, T^*) and for $\sigma^* \leq 1.5$. The dimensionless pressure-stress ratio is defined as $\sigma^* = \sigma_m / \bar{\sigma}$ where σ_m is the average of the three normal stresses and $\bar{\sigma}$

is the von Mises equivalent stress. The dimensionless strain rate, $\dot{\epsilon}^*$, and homologous temperature, T^* , are identical to those used in the strength models presented in the previous subsections.

The five dimensionless constants are $D_1 \dots D_5$. The expression in the first set of brackets follows the form presented by Hancock and Mackenzie (Reference 51). It essentially says that the strain to fracture decreases as the hydrostatic tension, σ_m , increases. The expression in the second set of brackets represents the effect of strain rate, and that in the third set of brackets represents the effect of temperature. For high values of hydrostatic tension ($\sigma^* > 1.5$) a different relationship is used.

It is clear from Figure 36 that less damage is accumulated when the material is in compression ($\sigma^* < 0$). At the other extreme, however, when there is significant hydrostatic tension, the strain to fracture drops rapidly. Figure 37 shows the relationship which is used for large values of the pressure-stress ratio ($\sigma^* > 1.5$). The fracture strain varies in a linear manner, from $\sigma^* = 1.5$ to σ_{spall}^* at ϵ_{min}^f . The model constants are the spall stress, σ_{spall} , and the minimum fracture strain, ϵ_{min}^f . The dimensionless σ_{spall}^* is computed from σ_{spall} and the current value of the von Mises flow stress, $\bar{\sigma}$.

6.1.13 Modified Johnson-Cook Fracture Model

The modified Johnson-Cook fracture model is similar to the Johnson-Cook fracture model (presented in subsection 6.1.12) except the Tuler-Butcher time-dependent spall model (Reference 52) is used for the high tensile regions. For mean tensile pressures less than σ_{mo} , the damage and fracture strain are determined from Equations 1 and 2 of subsection 6.1.12. For mean tensile stresses $\sigma_m > \sigma_{mo}$, the damage is

$$D = \frac{\sum (\sigma_m^* - 1)^\lambda \Delta t}{K^*} \quad (1)$$

where $\sigma_m^* = \sigma_m / \sigma_{mo}$, Δt is the integration time increment, and λ and K^* are material constants.

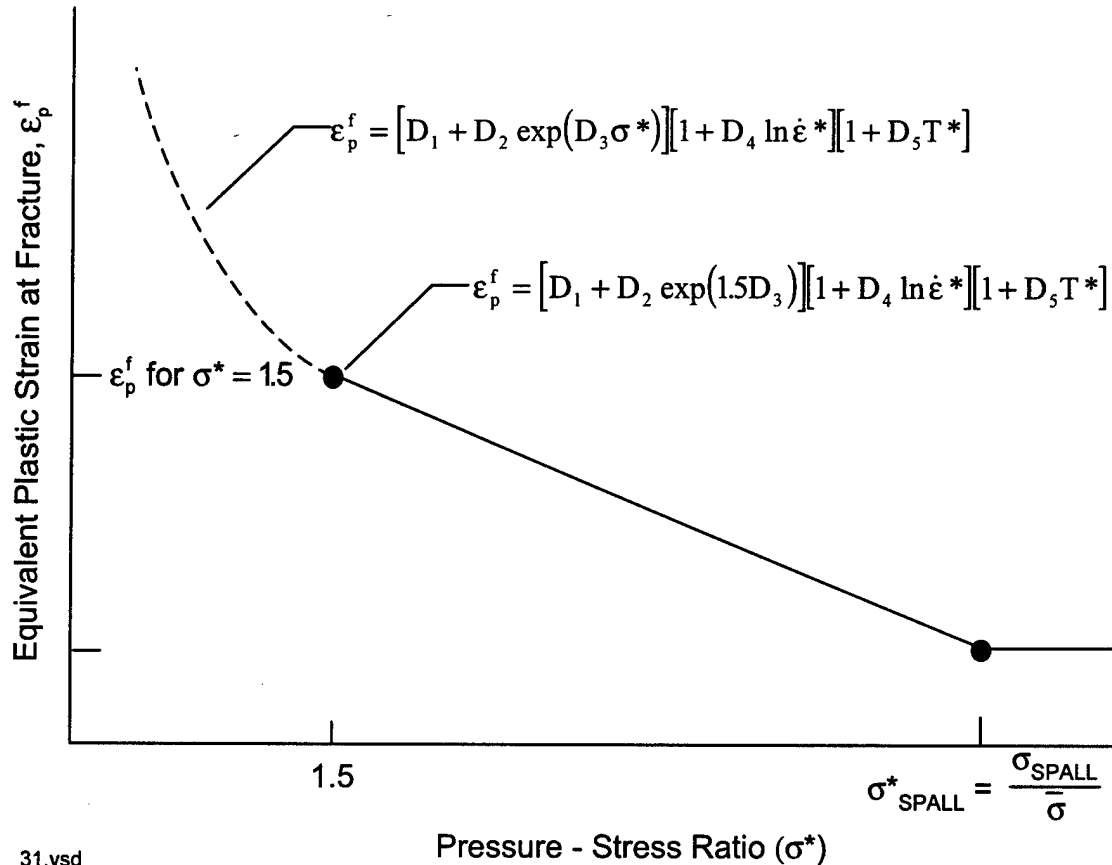


Figure 37. Description of Fracture Strains at Large Tensile Pressure-Stress Ratios for the Johnson-Cook Fracture Model

6.1.14 Fragmentation Model

The fragmentation model is presented in Reference 18. The theoretical approach for this work is an extension of work developed by Grady (References 53, 54, and 55) on the fragmentation of stretching jets and expanding sheets. Fragment sizes for one-dimensional stretching jets and two-dimensional expanding sheets were developed using energy principles. These theories are based on a ductile mode of failure. Fragment sizes are determined by equating the internal kinetic energy of the flowing fragment material with the plastic strain energy used during the fragmentation process. The following discussion takes Grady's theory and extends it to three-dimensional ductile fragmentation, with considerations being taken to ensure computational compatibility.

Consider, prior to fragmentation, a rapidly flowing mass of material from which a cubical fragment of size b will be formed as shown in Figure 38. To simplify the development, assume

that the x, y, and z axes correspond to those of the principal strain rates. The theoretical approach is to equate the kinetic energy of a fragment's flowing material about its center of mass (local kinetic energy), with the plastic work occurring during the fragmentation process. If it is assumed that all of the internal kinetic energy is consumed during fragmentation, an equality can be developed and solved directly for the fragment size.

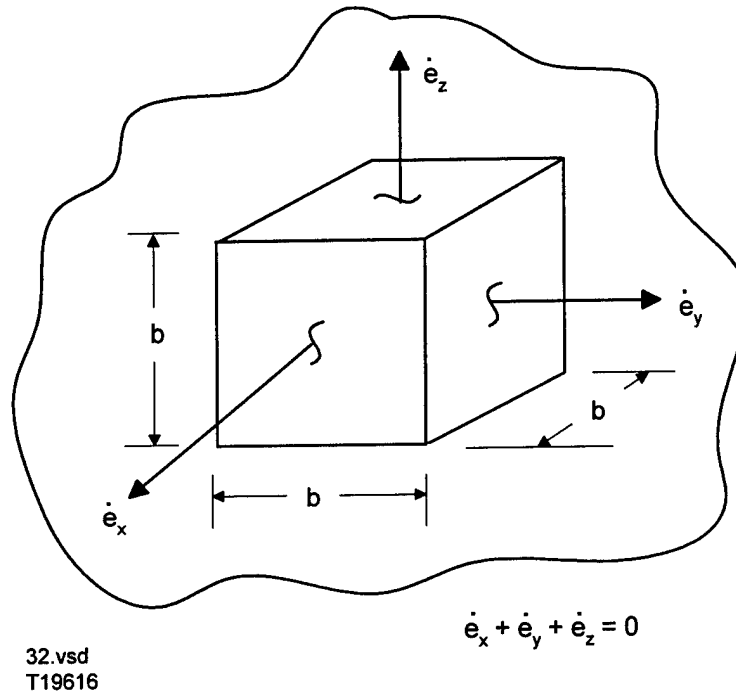


Figure 38. Fragment Characteristics

The local kinetic energy for the flowing fragment material can be determined explicitly by summing the local kinetic energy in each direction:

$$KE = \frac{1}{2} \int v(x)^2 dm + \frac{1}{2} \int v(y)^2 dm + \frac{1}{2} \int v(z)^2 dm \quad (1)$$

The local kinetic energy in the x-direction, about the fragment's center of mass can be expressed as

$$(KE)_x = \frac{1}{2} \int v(x)^2 dm \quad (2)$$

where the incremental mass is

$$dm = b^2 \rho \, dx \quad (3)$$

and where ρ is the density of the material.

For a linear velocity gradient across the fragment, with local face velocities of $\pm V_x$ (about the CG velocity), the x velocity distribution is

$$v(x) = V_x \left(\frac{2x}{b} - 1 \right) \quad \text{for } 0 \leq x \leq b \quad (4)$$

The local kinetic energy in the x -direction is then

$$(KE)_x = \int_0^b \frac{1}{2} b^2 \rho V_x^2 \left(\frac{2x}{b} - 1 \right)^2 dx \quad (5)$$

$$(KE)_x = \frac{b^3 \rho}{6} V_x^2 \quad (6)$$

Since $v(x)$ is linear, the deviator strain rate, \dot{e}_x , is constant within the fragment and can be expressed as a function of the velocity

$$\dot{e}_x = \frac{2V_x}{b} \quad (7)$$

The local kinetic energy in terms of the deviator strain rate and fragment size is then

$$(KE)_x = \frac{b^5 \rho \dot{e}_x^2}{24} \quad (8)$$

The same approach is used to determine the local kinetic energy in the y and z directions, which gives a total local kinetic energy of the fragment of

$$KE = \frac{b^5 \rho}{24} (\dot{e}_x^2 + \dot{e}_y^2 + \dot{e}_z^2) \quad (9)$$

The deviator strain rates can be expressed in terms of an equivalent strain rate

$$\bar{\dot{\epsilon}} = \sqrt{\frac{2}{3}(\dot{\epsilon}_x^2 + \dot{\epsilon}_y^2 + \dot{\epsilon}_z^2)} \quad (10)$$

and the total kinetic energy becomes

$$KE = \frac{b^3 \rho \bar{\dot{\epsilon}}^2}{16} \quad (11)$$

The plastic work generated for each fragment during the fragmentation process can be expressed in the following form:

$$PW = b^3 (s_x e_x^f + s_y e_y^f + s_z e_z^f) \quad (12)$$

where s_x , s_y , and s_z are constant deviator stresses and e_x^f , e_y^f , and e_z^f are the deviator strains occurring from void initiation to material separation.

Equation 12 can be expressed in terms of equivalent stress and strain to obtain the following relationship for plastic work:

$$PW = b^3 \bar{\sigma} \bar{\epsilon}_f \quad (13)$$

Equation 13 represents the total plastic work needed for fragmentation to occur, where $\bar{\epsilon}_f$ is analogous to the equivalent strain rate of Equation 10, and the von Mises equivalent stress is

$$\bar{\sigma} = \sqrt{\frac{3}{2}(s_x^2 + s_y^2 + s_z^2)} \quad (14)$$

Equating Equations 11 and 13 and solving for b , the fragment size is expressed as

$$b = \sqrt{\frac{16 \bar{\sigma} \bar{\epsilon}_f}{\rho \bar{\dot{\epsilon}}^2}} = A \sqrt{\frac{\bar{\sigma}}{\rho \bar{\dot{\epsilon}}^2}} \quad (15)$$

The dimensionless constant, $A = 4\sqrt{\bar{\epsilon}_f}$, can be approximated by establishing bounds for $\bar{\epsilon}_f$. Grady (Reference 54) estimated that the strains which occur from void initiation to material separation are between 0.01 and 0.10. Substituting $0.01 \leq \bar{\epsilon}_f \leq 0.10$ gives $0.40 \leq A \leq 1.26$.

Equation 15 is expressed in terms of equivalent strain rate and equivalent stress for computational compatibility. As applied numerically, the fragment size calculation takes the following form:

$$\bar{b} = \frac{\sum b \Delta \bar{\epsilon}_p}{\sum \Delta \bar{\epsilon}_p} \quad (16)$$

where b is the fragment size computed for the current element condition of $\bar{\sigma}$, ρ , and $\bar{\epsilon}$ from Equation 15; and $\Delta \bar{\epsilon}_p$ is the increment of plastic strain occurring during an integration cycle. The total plastic strain is represented by $\bar{\epsilon}_p = \sum \Delta \bar{\epsilon}_p$.

This calculation is performed for every element at each integration cycle until the element fails. Here the failure does not refer to the fragmentation presented herein, but to fracture due to damage or erosion. Under both of these conditions, the equivalent stress is set to $\bar{\sigma} = 0$.

When an element fails, a fragment of size \bar{b} is saved in an element array for post-processing. The calculated fragment size is an average based on the amount of element strain that occurs for each cycle as shown in Equation 16.

This is a deviation from the theoretical approach that states the calculation should start at the initiation of fragmentation and continue until complete separation. Due to the difficulty in determining when the initiation of fragmentation begins, the approach here is to calculate an average fragment size based on the element history, and to later apply a factor A to the fragment size during post-processing. Equation 16 is the only addition to the main routine in EPIC which is required to calculate the fragment size, and the increased computational time is negligible.

The remainder of the fragment computations are performed in the Postprocessor. The final fragment size associated with each failed element is obtained by applying the factor A to the calculated value determined from Equation 16, during post-processing.

The number of fragments for each failed element is determined by dividing the element volume by the fragment volume. Mass is conserved, and thus, the number of fragments calculated will generally not be a whole number. A velocity vector is defined for the fragments by using an average of the nodal velocities associated with the element. All the fragments that are determined from a specific failed element will have the same velocity vector. For each failed element, a fragment size, velocity, and number of fragments will be known. The fragment mass, kinetic energy, and momentum are determined straightforwardly.

The EPIC Postprocessor can plot, in bar graph form, the number of fragments versus fragment mass, momentum, kinetic energy, and size. The advantage of presenting the data in this form is that the results are relatively mesh independent.

6.2 EXPLOSIVE MATERIALS

The materials identified as Explosive Materials are designated to detonate at a predetermined time, based on the point (or points) of detonation and the distance from the initial detonation point (Reference 19). There are also Reactive Explosive Materials (described in subsection 6.6) that do not detonate at a specified time, but rather are detonated when the proper conditions (generally the pressure history) have been experienced.

6.2.1 Gamma Law Model

The Gamma law explosives model determines the pressure from

$$P = F(\gamma - 1)E / \bar{V} \quad (1)$$

where F is the burn fraction ($0 \leq F \leq 1.0$), γ is a material constant, and E is the internal energy per initial unit volume. The relative volume is $\bar{V} = V / V_0$, where V and V_0 represent the current and initial element volumes, respectively.

The explosive is effectively initiated with the burn fraction, which is dependent on the time for the detonation wave to arrive and travel through the element, or the compressed state of the element. The burn fractions for these two conditions are

$$F = \frac{(t - t_s)D + b / 2}{b} \quad (2a)$$

$$F = \frac{1 - \bar{V}}{1 - V_{CJ}} \quad (2b)$$

In Equation (2a), t is the current time and t_s is the time required for the detonation wave to reach the center of the element when traveling at the detonation velocity, D . A reference distance, b , is used to spread the wave front over a limited number of elements. For 1D elements $b = \Delta z_0$ (where Δz_0 is the initial length of the element), for 2D triangular elements $b = 3\sqrt{A_0}$ (where A_0 is the initial area of the element), and for 3D tetrahedral elements $b = 2 V_0^{1/3}$ (where V_0 is the initial volume of the element). Equation (2b) gives the burn fraction in terms of the compressed state, where $V_{CJ} = \gamma/(\gamma + 1)$ is the Chapman-Jouquet relative volume. This allows a converging detonation wave to travel at a velocity greater than D . The maximum value of F from Equations (2a) and (2b) is selected, if it is within the limits, $0 \leq F \leq 1.0$. If F is negative or greater than unity, then F is set to 0 or 1.0, respectively.

Because the pressure, P , is directly proportional to the internal energy, E , the pressure-energy equations are solved simultaneously in a manner similar to that used for the Mie-Gruneisen Equation of State in subsection 6.1.11.

It is possible to determine γ as a function of the other material parameters.

$$\gamma = \sqrt{1 + D^2 \rho_0 / 2E_0} \quad (3)$$

where D is the detonation velocity, ρ_0 is the initial density, and E_0 is the initial internal energy per initial unit volume.

6.2.2 JWL Model

The JWL explosives model (Reference 56) also is commonly used. Here the pressure is expressed as

$$P = F \left[C_1 (1 - C_5 / C_2 \bar{V}) \exp (-C_2 \bar{V}) + C_3 (1 - C_5 / C_4 \bar{V}) \exp (-C_4 \bar{V}) + C_5 E / \bar{V} \right] \quad (1)$$

where F is the burn fraction from subsection 6.2.1, E is the internal energy per initial unit volume, and $\bar{V} = V / V_0$ is the relative volume. C_1 , C_2 , C_3 , C_4 , and C_5 are material constants. Again the pressure-energy equations are solved simultaneously.

6.3 CRUSHABLE/CONCRETE MATERIALS

There are two models available for crushable/concrete materials. Both models were developed for concrete, but they also can be used for other crushable materials. For the solid (metal) materials under subsection 6.1, it is possible to use combinations of various strength, pressure, and fracture models. For the concrete models, however, the strength, pressure and damage act together to form a single model.

6.3.1 Modified Osborn Model

The Osborn concrete model (Reference 57) is composed of a pressure-hardening strength model and a crushable pressure model. The strength is expressed as

$$\sigma = [C_1(1 - D) + C_4 P] [1 + C_3 \ln \dot{\epsilon}^*] \quad (1)$$

The softening due to damage $(1 - D)$ and the strain rate effect $[1 + C_3 \ln \dot{\epsilon}^*]$ are modifications made to the original Osborn model. It is recommended that the damage model not be used, and it is therefore not described herein.

In Equation 1, D is the damage (not used and set to $D = 0$), P is the pressure, and $\dot{\epsilon}^* = \dot{\epsilon} / \dot{\epsilon}_0$ is the dimensionless strain rate for $\dot{\epsilon}_0 = 1.0 \text{ s}^{-1}$. The three constants are C_1 , C_4 , and C_3 , where C_1 has units of stress and the other (C_4 and C_3) are dimensionless.

The model for the pressure is shown in Figure 39. The constants are P_{crush} , μ_{crush} , K_1 , K_2 , K_3 , K_{lock} , and μ_{lock} as shown in Figure 39. The maximum hydrostatic tension is P_{min} . For increasing μ the material behaves in a linear elastic manner for $\mu \leq \mu_{\text{crush}}$. The transition region is for $\mu_{\text{crush}} < \mu < \mu_{\text{lock}}$, where the pressure is expressed as

$$P = P_{\text{crush}} + K_1 \bar{\mu} + K_2 \bar{\mu}^2 + K_3 \bar{\mu}^3 \quad (2)$$

where $\bar{\mu} = \mu - \mu_{\text{crush}}$. For $\mu \geq \mu_{\text{lock}}$ the pressure is determined from K_{lock} as shown in Figure 39.

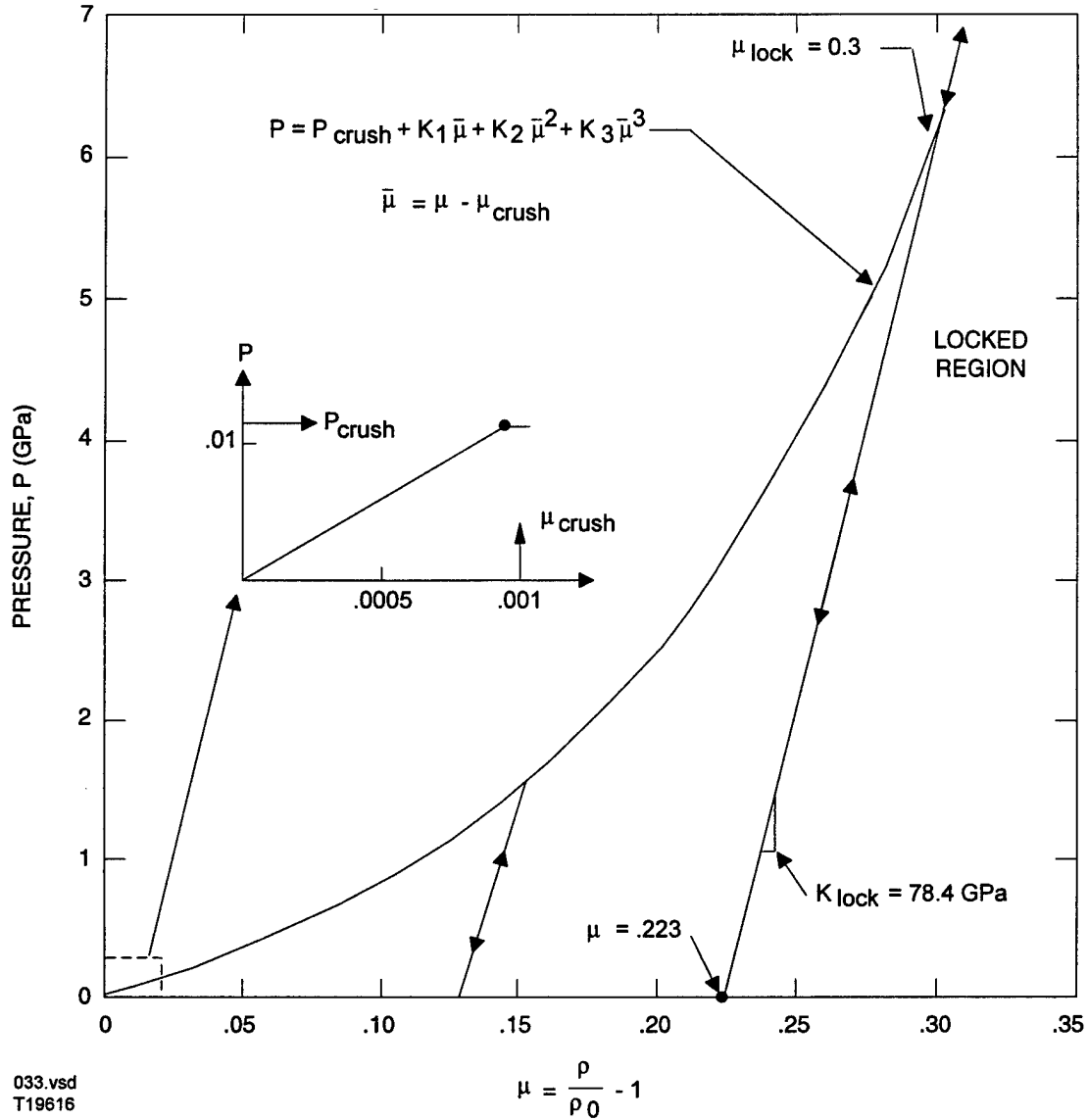


Figure 39. Description of the Pressure-Volume Relationship for the Osborn Concrete Model (Specific Data Shown are for a Typical Concrete)

For decreasing μ in the transition region, the pressure unloads along an interpolated bulk modulus (between elastic and locked).

For the pressure model, P_{crush} , K_1 , K_2 , K_3 , K_{lock} , and P_{min} have units of stress (or pressure), and the others (μ_{crush} and μ_{lock}) are dimensionless.

6.3.2 Holmquist-Johnson-Cook Model

The Holmquist-Johnson-Cook concrete model (Reference 58) is summarized in Figure 40. The strength portion of the model is shown at the top of Figure 40. The normalized equivalent stress is defined as $\sigma^* = \sigma / f'_c$, where σ is the actual equivalent stress and f'_c is the quasi-static uniaxial compressive strength. The specific expression is

$$\sigma^* = [A(1 - D) + B P^{*N}] [1 + C \ln \dot{\epsilon}^*] \quad (1)$$

where D is the damage ($0 \leq D \leq 1.0$), $P^* = P / f'_c$ is the normalized pressure (where P is the actual pressure), and $\dot{\epsilon}^* = \dot{\epsilon} / \dot{\epsilon}_0$ is the dimensionless strain rate (where $\dot{\epsilon}$ is the actual strain rate and $\dot{\epsilon}_0 = 1.0s^{-1}$ is the reference strain rate). The normalized maximum tensile hydrostatic pressure is $T^* = T / f'_c$, where T is the maximum tensile hydrostatic pressure the material can withstand.

The material constants are A , B , N , C and σ_{max}^* , where A is the σ^* intercept at $P^* = 0$, B is the normalized pressure hardening coefficient, N is the pressure hardening exponent, C is the strain rate coefficient, and σ_{max}^* is the normalized maximum strength that can be developed.

The damage for fracture is shown in the lower left corner of Figure 40. It is accumulated from both equivalent plastic strain and plastic volumetric strain, and is expressed as

$$D = \sum \frac{\Delta \epsilon_p + \Delta \mu_p}{\epsilon_p^f + \mu_p^f} \quad (2)$$

where $\Delta \epsilon_p$ and $\Delta \mu_p$ are the equivalent plastic strain and plastic volumetric strain, respectively, during a cycle of integration; and $\epsilon_p^f + \mu_p^f = f(P)$ is the plastic strain to fracture under a constant pressure, P . The specific expression is

$$\epsilon_p^f + \mu_p^f = D_1 (P^* + T^*)^{D_2} \quad (3)$$

where D_1 and D_2 are constants and P^* and T^* are as defined previously. As is evident from Equation 3, the concrete material cannot undergo any plastic strain at $P^* = -T^*$ without fracturing, and alternatively, the plastic strain to fracture increases as P^* increases. A third damage constant, $(\epsilon_p^f + \mu_p^f)_{min}$, is provided to allow for a finite amount of plastic strain to fracture the material. This is included to suppress fracture from low magnitude tensile waves.

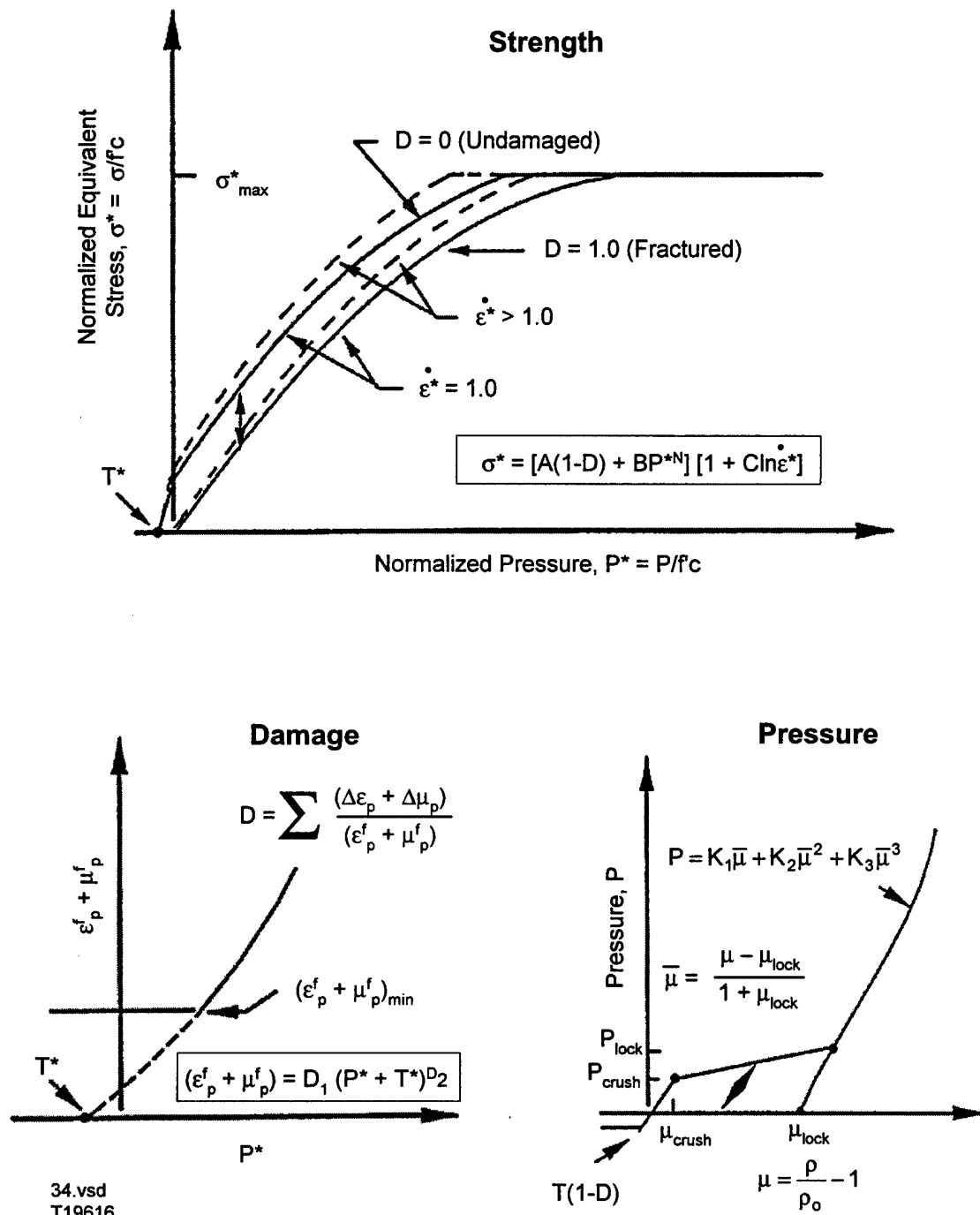


Figure 40. Description of the Holmquist-Johnson-Cook (HJC) Concrete Model

Damage due to plastic volumetric strain is included in Equations 2 and 3 because the concrete will lose cohesive strength during air void collapse. Under most circumstances, the majority of the damage will occur from equivalent plastic strain.

The hydrostatic pressure-volume relationship is presented in the lower right corner of Figure 40. This pressure-volume response is separated into three response regions. The first region is linear elastic and occurs at $P \leq P_{crush}$, where P_{crush} and μ_{crush} are the pressure and volumetric strain that occur in a uniaxial stress compression test, and T is as previously defined. The elastic bulk modulus is $K_{elastic} = P_{crush} / \mu_{crush}$.

The second region is referred to as the transition region and occurs at $P_{crush} < P < P_{lock}$. In this region, the air voids are gradually compressed out of the concrete producing plastic volumetric strain. Unloading in this region occurs along a modified path that is interpolated from the adjacent regions.

The third region defines the relationship for fully dense material (all air voids removed from the concrete). The air voids are completely removed from the material when the pressure reaches P_{lock} and the relationship is expressed as

$$P = K_1 \bar{\mu} + K_2 \bar{\mu}^2 + K_3 \bar{\mu}^3 \quad (4)$$

where

$$\bar{\mu} = \frac{\mu - \mu_{lock}}{1 + \mu_{lock}} \quad (5)$$

The modified volumetric strain, $\bar{\mu}$, is used so that the constants (K_1 , K_2 , and K_3) are equivalent to those used for material with no voids. The standard volumetric strain for this model is $\mu = \rho / \rho_0 - 1$ for current density ρ and initial density ρ_0 . The locking volumetric strain is $\mu_{lock} = \rho_{grain} / \rho_0 - 1$ where ρ_{grain} is the grain density. This is identical to the density of the material with no air voids.

For tensile pressure, $P = K_{elastic} \mu$ in the elastic region, $P = K_1 \bar{\mu}$ in the fully dense region, and the pressures are interpolated in the transition region. The interpolation factor is

$F = (\mu_{max} - \mu_{crush}) / (\mu_{plock} - \mu_{crush})$ where μ_{max} is the maximum volumetric strain reached prior to unloading and μ_{plock} is the volumetric strain at P_{lock} . A similar method is used for compressive

unloading except that the higher order terms ($K_2\bar{\mu}^2$ and $K_3\bar{\mu}^3$) are included. The tensile pressure is limited to $T(1 - D)$.

An addition to the model, subsequent to Reference 58, is that the shear modulus varies in a manner proportional to the current bulk modulus, which is identical to using a constant Poisson's ratio.

6.4 LIQUID MATERIALS

For liquid materials the three normal stress components are expressed as

$$\sigma_x = 2\mu\dot{\epsilon}_x - (P + Q) \quad (1)$$

$$\sigma_y = 2\mu\dot{\epsilon}_y - (P + Q) \quad (2)$$

$$\sigma_z = 2\mu\dot{\epsilon}_z - (P + Q) \quad (3)$$

where μ is the viscosity coefficient and $\dot{\epsilon}_x$, $\dot{\epsilon}_y$, and $\dot{\epsilon}_z$ are the normal strain rates. P is the pressure and Q is the artificial viscosity as described in subsections 6.1.10 and 6.1.11. For liquids the pressure is usually limited to compression only.

The three shear stress are

$$\tau_{xy} = \mu\dot{\gamma}_{xy} \quad (4)$$

$$\tau_{xz} = \mu\dot{\gamma}_{xz} \quad (5)$$

$$\tau_{yz} = \mu\dot{\gamma}_{yz} \quad (6)$$

where $\dot{\gamma}_{xy}$, $\dot{\gamma}_{xz}$, and $\dot{\gamma}_{yz}$ are the shear strain rates.

6.5 BRITTLE MATERIALS

There are two models available for brittle/ceramic materials, the original Johnson-Holmquist (JH-1) model and the improved Johnson-Holmquist (JH-2) model. Both models were developed

for ceramic materials, but they can also be used for other brittle materials such as glass. As was the case for the crushable/concrete models under subsection 6.3, the strength, pressure, and damage act together to form a single model.

6.5.1 Johnson-Holmquist JH-1 Model

The original Johnson-Holmquist brittle/ceramic material model (Reference 59) is summarized in Figure 41. The available strength (equivalent stress), σ , is dependent on the pressure, P , the dimensionless strain rate, $\dot{\epsilon}^* = \dot{\epsilon} / \dot{\epsilon}_0$ (for $\dot{\epsilon}_0 = 1.0 \text{ s}^{-1}$), and the damage, D . For undamaged material, $D = 0$; for partially damaged material, $0 < D < 1.0$; and for totally damaged (fractured) material, $D = 1.0$. Note that the strength is significantly reduced for fractured material ($D = 1.0$).

T is the maximum tensile hydrostatic pressure the material can experience, and S_1 and S_2 are the strengths of the intact material (for $\dot{\epsilon}^* = 1.0$) at the compressive pressures P_1 and P_2 , respectively. After the material has fractured ($D = 1.0$), the slope of the strength is given by C_6 , and the maximum fracture strength is S_3 (for $\dot{\epsilon}^* = 1.0$).

The strain rate constant is C_3 . If σ_0 is the available strength at $\dot{\epsilon}^* = 1.0$, then the strength at the other strain rates is

$$\sigma = \sigma_0 (1 + C_3 \ln \dot{\epsilon}^*) \quad (1)$$

It can be seen that the strength increases significantly with pressure, which is consistent with the well-known fact that brittle materials are much stronger in compression than they are in tension. The constants, T , S_1 , and P_1 can generally be determined from quasi-static and/or dynamic (Hopkinson bar) tension, torsion, or compression tests; and the strain rate constant, C_3 , can be determined from comparable quasi-static and dynamic (Hopkinson bar) tests.

The higher pressure constants, S_2 and P_2 , generally require plate impact tests. The interpretation of these tests can be difficult because generally only the net uniaxial stress can be measured. To accurately obtain the constants, it is necessary to determine both the hydrostatic and deviatoric components of stress.

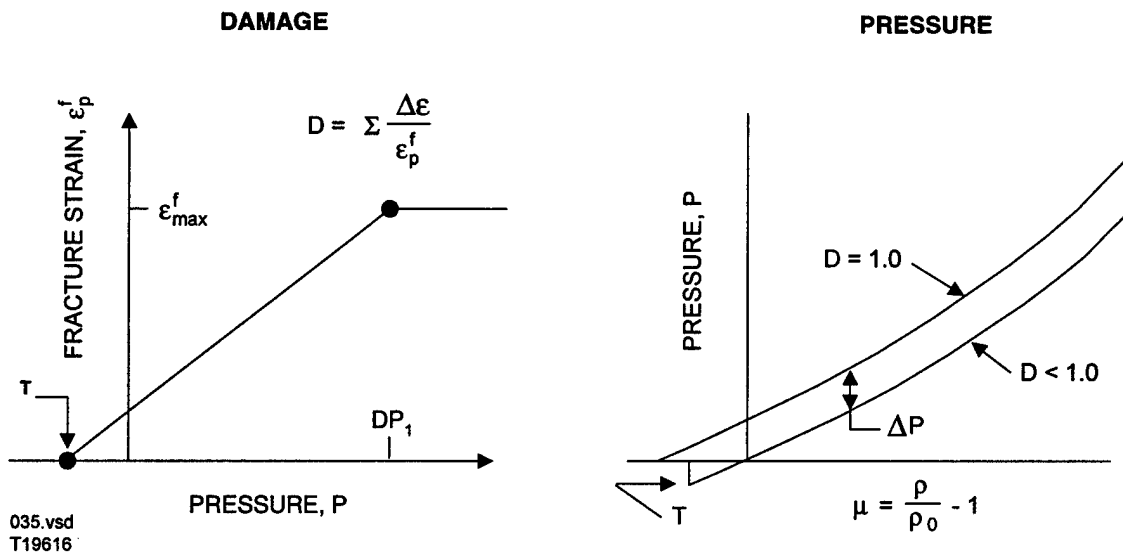
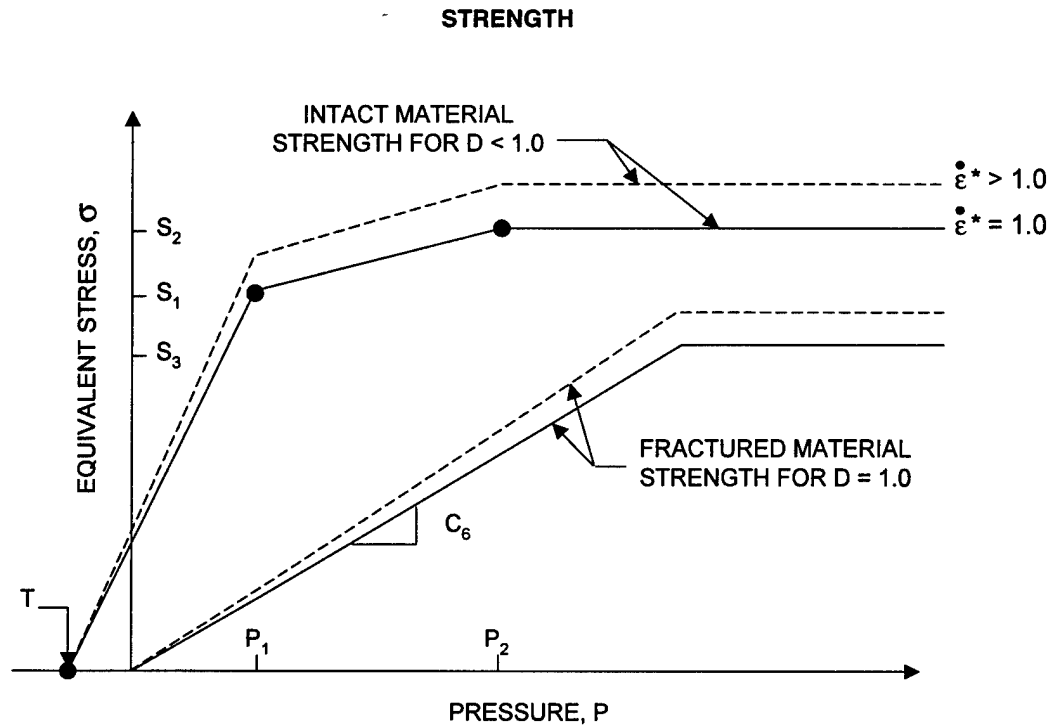


Figure 41. Description of the Original Johnson-Holmquist (JH-1) Ceramic Model

The post-fracture constant, C_6 , can be bounded by two different types of tests. A lower bound can be established by axial compression testing of a powdered material which has radial pressure confinement, and an upper bound can be established by axial compression testing of intact material (using displacement control) with radial pressure confinement. For the latter technique,

it is the strength after fracture which is of interest. The maximum strength of the fractured material, S_3 , may sometimes be obtained from these tests, but it usually requires plate impact testing.

The damage for fracture is accumulated in a manner similar to that used in the Johnson-Cook fracture model, presented in subsection 6.1.12. It is expressed as

$$D = \sum \Delta \epsilon_p / \epsilon_p^f \quad (2)$$

where $\Delta \epsilon_p$ is the plastic strain during a cycle of integration and $\epsilon_p^f = f(P)$ is the plastic strain to fracture under a constant pressure, P . Referring to Figure 41, the material cannot undergo any plastic strain at the maximum hydrostatic tension, T , but it increases to $\epsilon_p^f = \epsilon_{\max}^f$ at a compressive pressure of $P = DP_1$.

The hydrostatic pressure before fracture ($D < 1.0$) is simply

$$P = K_1 \mu + K_2 \mu^2 + K_3 \mu^3 \quad (3)$$

where K_1 , K_2 , and K_3 are constants (K_1 is the bulk modulus); and $\mu = \rho/\rho_0 - 1$ for current density ρ and initial density ρ_0 . For tensile pressures ($\mu < 0$), Equation 3 is replaced by $P = K_1 \mu$.

Energy effects are not included.

After fracture ($D = 1.0$), bulking (pressure increase and/or volumetric strain increase) can occur. Now an additional incremental pressure, ΔP , is added, such that

$$P = K_1 \mu + K_2 \mu^2 + K_3 \mu^3 + \Delta P \quad (4)$$

The pressure increment is determined from energy considerations. Looking back to the strength model in Figure 41, there is a drop in strength when the material goes from an intact state ($D < 1.0$) to a fractured state ($D = 1.0$). This represents a loss in the elastic internal energy of the deviator and shear stresses. The general expression for this internal energy is

$$U = \sigma^2 / 6G \quad (5)$$

where σ is the equivalent plastic flow stress and G is the shear modulus of elasticity.

The loss in this elastic internal energy can be expressed as

$$\Delta U = U_i - U_f \quad (6)$$

where U_i is the elastic energy of the intact material before fracture ($D < 1.0$) and U_f is the elastic energy immediately after fracture ($D = 1.0$).

This energy loss (of deviator and shear stresses) can be converted to potential hydrostatic internal energy by adding ΔP . An approximate equation for the energy conservation is

$$\Delta P \mu_f + \Delta P^2 / (2K_1) = \beta \Delta U \quad (7)$$

where μ_f is μ at fracture and β is the fraction ($0 \leq \beta \leq 1.0$) of the elastic energy loss converted to potential hydrostatic energy.

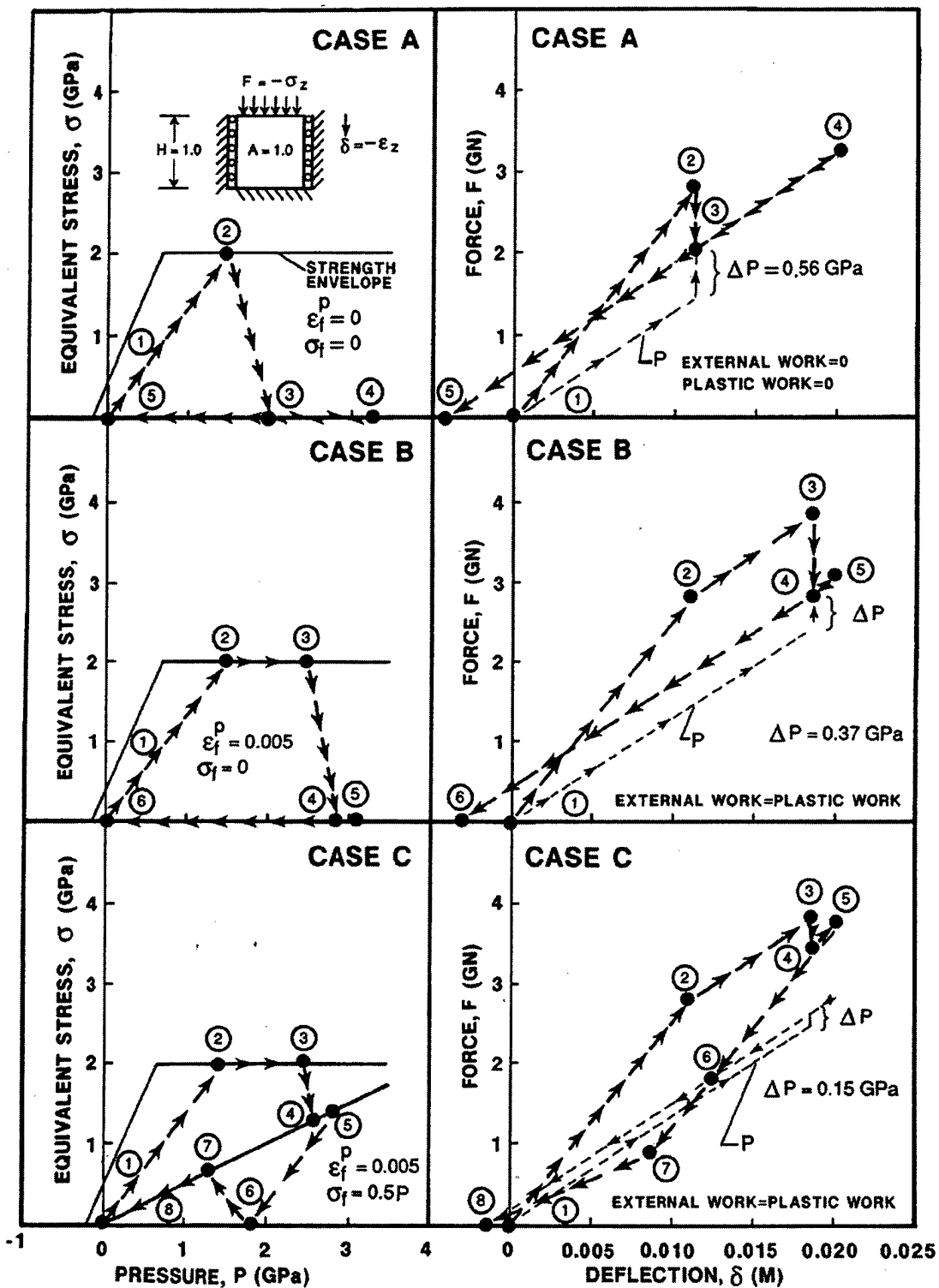
The first term ($\Delta P \mu_f$) is the approximate potential energy for $\mu > 0$, and the second term $[\Delta P^2 / (2K_1)]$ is the corresponding potential energy for $\mu < 0$.

Solving for ΔP gives

$$\Delta P = -K_1 \mu_f + \sqrt{(K_1 \mu_f)^2 + 2\beta K_1 \Delta U} \quad (8)$$

Note that $\Delta P = 0$ for $\beta = 0$, and that ΔP increases as ΔU increases and/or μ_f decreases.

Various features of this model can be illustrated by the three examples shown in Figure 42. The tensile strength of the material is $T = 0.2$ GPa, the unconfined compressive strength is $S_1 = S_2 = 2.0$ GPa, the modulus of elasticity is $E = 220$ GPa and Poisson's ratio is $\nu = 0.22$. Because the height is $H = 1.0$ m and the area is $A = 1.0$ m², the deflection is $\delta = -\epsilon_z$ and the force is $F = -\sigma_z$. For all three cases, the force, F , is slowly applied until $\delta = 0.02$ m, and then it is slowly released until $F = 0$. The paths are shown for strength versus pressure and for force versus deflection.



36.doc
T19616

Figure 42. Examples of Material Responses with the JH-1 Ceramic Model

For Case A, the material cannot develop any plastic strain ($\epsilon_p^f = 0$) or any strength after fracture ($\sigma_f = 0$ for $C_6 = 0$). All of the elastic energy loss (of deviator and shear stresses) is converted to potential hydrostatic energy ($\beta = 1.0$). Because there is no plastic work, the external work must also vanish. This is clearly shown in the force versus deflection relationship for Case A. The pressure jump at fracture ($\Delta P = 0.56$ GPa) provides for this conservation of energy.

Case B is similar to Case A except that the material is allowed to undergo a small amount of plastic strain ($\epsilon_p^f = 0.005$) prior to fracture. Even though the elastic energy loss at fracture, ΔU , is equal to that of Case A, the pressure jump ($\Delta P = 0.37$ GPa) is less because μ_f is greater at fracture.

Case C is similar to Case B except that there is strength after the material has fractured ($\sigma_f = 0.5P$ for $C_6 = 0.5$). Here, the pressure jump ($\Delta P = 0.15$ GPa) is reduced from that of Case B because the elastic energy loss at fracture, ΔU , is less. The loading/unloading path is very complex. Of special interest is the elastic unloading between points 5 and 7. Between points 5 and 6, the axial deviator stress, s_z , is in compression; but between points 6 and 7, the same deviator stress is in tension. The net stress, σ_z , which includes the hydrostatic pressure, remains in compression. At point 7, the elastic unloading is complete and the material flows plastically between points 7 and 8.

6.5.2 Johnson-Holmquist JH-2 Model

The improved Johnson-Holmquist brittle/ceramic model (Reference 60) is summarized in Figure 43. The original Johnson-Holmquist (JH-1) model for brittle materials includes pressure-dependent strength, damage and fracture, significant strength after fracture, bulking, and strain rate effects, as presented in subsection 6.5.1. After the model was first reported, it was implemented into several codes and applied to a variety of applications. It soon became apparent that there were several concerns.

The JH-1 model does not allow for gradual softening, and some materials clearly show a gradual softening during flyer plate impact tests. Also, results for some applications are very sensitive to the constants used in the model and there is not a straightforward process available to determine accurate constants. Finally, the jump conditions between fractured material (damage = $D = 1.0$) and intact material ($D < 1.0$) caused some problems for Eulerian codes, whereby the material could tend to heal itself after fracture had occurred.

The new model was developed to address these concerns. Reference 61 provides a description of a procedure to obtain constants for glass, as well as some plate impact and penetration computations.

A general overview of the JH-2 model is shown in Figure 43. Although it is very similar to the JH-1 model, there are several differences.

- The material begins to soften when the damage begins to accumulate ($D > 0$). This allows for gradual softening of the material under increasing plastic strain. (The JH-1 model does not soften until $D = 1.0$, and then the softening occurs instantaneously.)
- The strength and pressure are normalized by the strength and pressure components of the Hugoniot Elastic Limit (HEL), which allows for many of the constants to be dimensionless. This can be very helpful when comparing different materials, and when estimating constants for materials which have an insufficient database to determine constants.
- The strength and damage are analytic functions of the pressure and other variables. This allows for parametric variation of the constants in a more systematic manner. (The JH-1 model uses multiple linear segments.)
- The strength generally is a smoothly varying function of the intact strength, fracture strength, strain rate, and damage. It is well-suited for implementation into Eulerian codes.

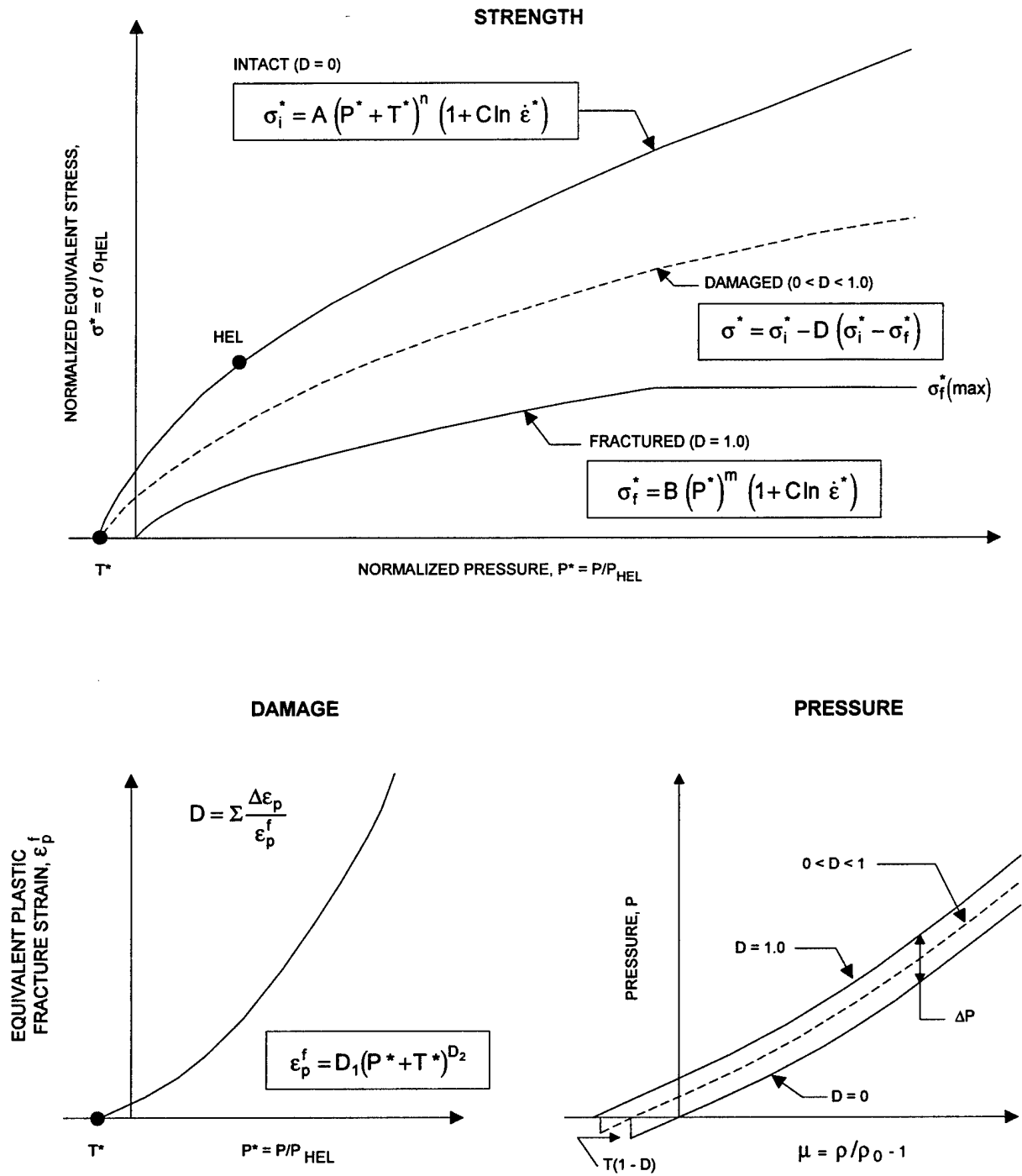
Returning to Figure 43, the normalized equivalent stress is

$$\sigma^* = \sigma_i^* - D(\sigma_i^* - \sigma_f^*), \quad (1)$$

where σ_i^* is the normalized intact equivalent stress, σ_f^* is the normalized fracture stress, and D is the damage ($0 \leq D \leq 1.0$).

The normalized equivalent stresses (σ^* , σ_i^* , σ_f^*) have the general form

$$\sigma^* = \sigma / \sigma_{HEL}, \quad (2)$$



037.vsd
T19616

Figure 43. Description of the Improved Johnson-Holmquist (JH-2) Ceramic Model

where σ is the actual equivalent stress and σ_{HEL} is the equivalent stress at the HEL.

The normalized intact strength is given by

$$\sigma_i^* = A(P^* + T^*)^N (1 + C \ln \dot{\epsilon}^*), \quad (3)$$

and the normalized fracture strength is given by

$$\sigma_f^* = B(P^*)^M (1 + C \ln \dot{\epsilon}^*). \quad (4)$$

Note that the normalized fracture strength can be limited by $\sigma_f^* \leq \sigma_f^*(\text{max})$. This optional fracture strength parameter is included to provide more flexibility in defining the important fracture strength. It also allows the user to use the same fracture strength as used for the JH-1 model (when $M = 1.0$).

The material constants are A , B , C , M , N , and $\sigma_f^*(\text{max})$. The normalized pressure is $P^* = P/P_{\text{HEL}}$, where P is the actual pressure and P_{HEL} is the pressure at the HEL. The normalized maximum tensile hydrostatic pressure is $T^* = T/P_{\text{HEL}}$, where T is the maximum tensile hydrostatic pressure the material can withstand. The dimensionless strain rate is $\dot{\epsilon}^* = \dot{\epsilon} / \dot{\epsilon}_0$, where $\dot{\epsilon}$ is the actual strain rate and $\dot{\epsilon}_0 = 1.0 \text{ s}^{-1}$ is the reference strain rate.

The damage for fracture is accumulated in a manner similar to that used in the JH-1 model in subsection 6.5.1, and the Johnson-Cook fracture model in subsection 6.1.12. It is expressed as

$$D = \sum \Delta \epsilon_p / \epsilon_p^f, \quad (5)$$

where $\Delta \epsilon_p$ is the plastic strain during a cycle of integration and $\epsilon_p^f = f(P)$ is the plastic strain to fracture under a constant pressure, P . The specific expression is

$$\epsilon_p^f = D_1 (P^* + T^*)^{D_2} \quad (6)$$

where D_1 and D_2 are constants and P^* and T^* are as defined previously in Equation 3. Again, the material cannot undergo any plastic strain at $P^* = -T^*$, but ϵ_p^f increases as P^* increases.

A physical explanation of damage and fracture is shown in Figure 44. If the material is held under a constant pressure and then subjected to a straining deformation at a constant strain rate, the damage begins to accumulate when the material begins to flow plastically (at $\sigma = \sigma_i$). The material then begins to soften (relative to the intact strength). This softening could be related to the material going from a larger particle size to a smaller particle size under increased plastic strain. When the material is completely damaged ($D = 1.0$), the strength does not decrease with increased plastic strain (at $\sigma = \sigma_f$).

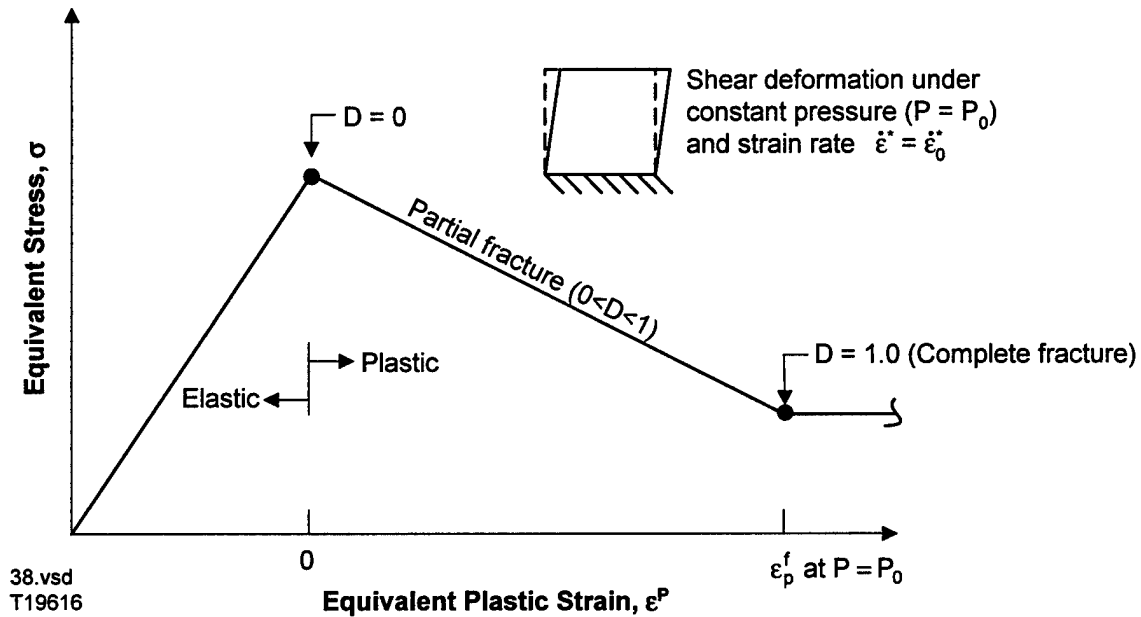


Figure 44. Strength, Damage, and Fracture Under a Constant Pressure and Strain Rate for the JH-2 Model

Unfortunately, it is not generally possible to perform these tests at sufficiently high pressures of interest. As a result, the damage functions and fracture strength must be inferred from other data.

The hydrostatic pressure before fracture begins ($D = 0$) is simply

$$P = K_1\mu + K_2\mu^2 + K_3\mu^3 \quad (7)$$

where K_1 , K_2 , and K_3 are constants (K_1 is the bulk modulus); and $\mu = \rho/\rho_0 - 1$ for current density ρ and initial density ρ_0 . For tensile pressure ($\mu < 0$), Equation 7 is replaced by $P = K_1\mu$. Energy effects are assumed to be insignificant.

After damage begins to accumulate ($D > 0$), bulking (pressure increase and/or volumetric strain increase) can occur. Now an additional incremental pressure, ΔP , is added, such that

$$P = K_1\mu + K_2\mu^2 + K_3\mu^3 + \Delta P. \quad (8)$$

The pressure increment is determined from energy considerations; it varies from $\Delta P = 0$ at $D = 0$ to $\Delta P = \Delta P_{\max}$ at $D = 1.0$. Figure 45 shows how ΔP increases as D increases. The incremental internal elastic energy decrease (due to decreased shear and deviator stresses) is converted to potential internal energy by incrementally increasing ΔP . The decrease in the shear and deviator stresses occurs because the strength, σ , decreases as the damage, D , increases, as shown in Figure 43 and Equation 1.

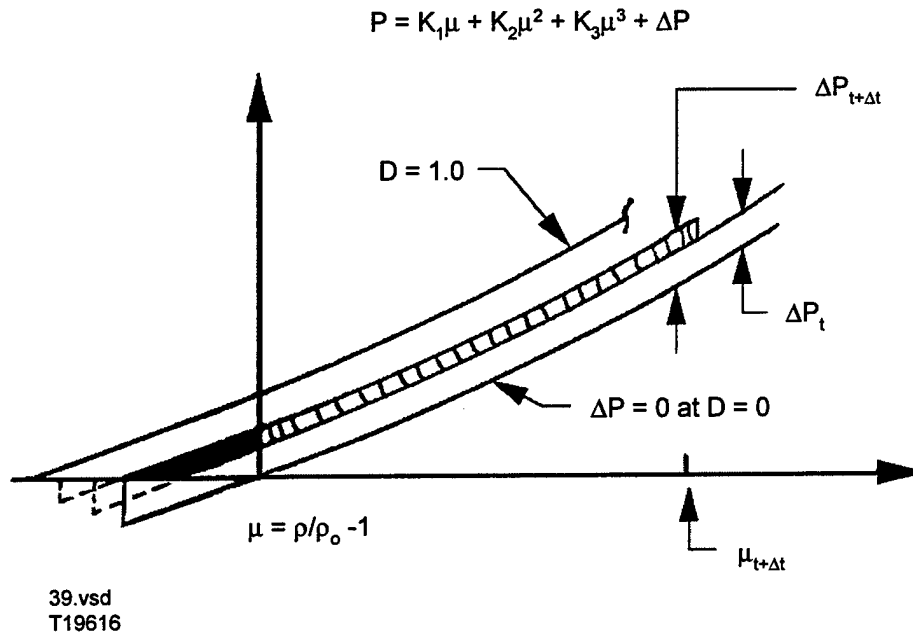


Figure 45. Description of Incremental Bulking Pressure for the JH-2 Model

The general expression for the elastic internal energy of the shear and deviator stresses is

$$U = \sigma^2/6G \quad (9)$$

where σ is the equivalent plastic flow stress and G is the shear modulus of elasticity.

The incremental energy loss is

$$\Delta U = U_{D(t)} - U_{D(t+\Delta t)} \quad (10)$$

where $U_{D(t)}$ and $U_{D(t+\Delta t)}$ are computed from Equation 9 using $\sigma_{t+\Delta t}$ for both energies.

If the energy loss, ΔU , is converted to potential hydrostatic energy through ΔP , an approximate equation for this energy conservation is

$$(\Delta P_{t+\Delta t} - \Delta P_t) \mu_{t+\Delta t} + (\Delta P_{t+\Delta t}^2 - \Delta P_t^2) / 2K_1 = \beta \Delta U. \quad (11)$$

The first term $[(\Delta P_{t+\Delta t} - \Delta P_t) \mu_{t+\Delta t}]$ is the approximate potential energy for $\mu > 0$ and the second term $[(\Delta P_{t+\Delta t}^2 - \Delta P_t^2) / 2K_1]$ is the corresponding potential energy for $\mu < 0$.

Solving for the updated ΔP gives

$$\Delta P_{t+\Delta t} = -K_1 \mu_{t+\Delta t} + \sqrt{(K_1 \mu_{t+\Delta t} + \Delta P_t)^2 + 2\beta K_1 \Delta U}. \quad (12)$$

As was the case for the JH-1 model, the JH-2 model also gives $\Delta P = 0$ when $\beta = 0$, where β is the fraction ($0 \leq \beta \leq 1$) of the elastic energy loss converted to potential hydrostatic energy.

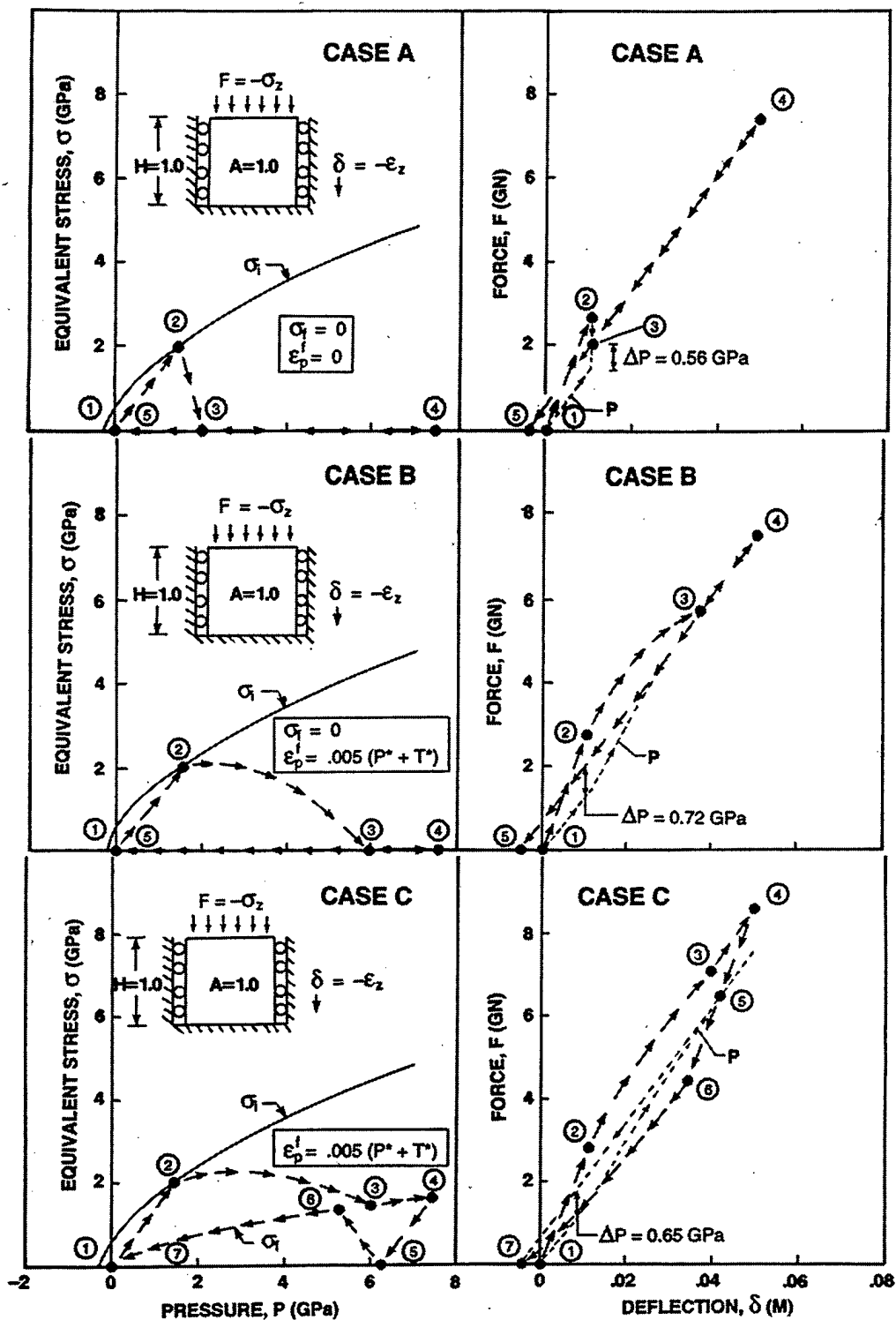
Various features of the JH-2 model can be illustrated by the three examples shown in Figure 46. The tensile strength of the material is $T = 0.2$ GPa, the HEL = 2.79 GPa, the intact strength is assumed to be $\sigma_i^* = 0.93 (P^* + T^*)^{0.6}$, the modulus of elasticity is $E = 220$ GPa, and Poisson's ratio is $\nu = 0.22$. There is no strain rate effect so that $C = 0$ in Equations 3 and 4. From the preceding constants, the following additional constants can be obtained:

$$K_1 = \frac{E}{3(1-2\nu)} = 130.95 \text{ GPa}, \quad (13)$$

$$G = \frac{E}{2(1+\nu)} = 90.16 \text{ GPa}, \quad (14)$$

$$P_{\text{HEL}} = K_1 \mu_{\text{HEL}} + K_2 \mu_{\text{HEL}}^2 + K_3 \mu_{\text{HEL}}^3 = 1.46 \text{ GPa}, \quad (15)$$

$$\sigma_{\text{HEL}} = \frac{3}{2} (\text{HEL} - P_{\text{HEL}}), \quad (16)$$



40.vsd
T19616

Figure 46. Examples of Material Responses with the JH-2 Ceramic Model

where HEL is the net axial stress for the Hugoniot Elastic Limit, P_{HEL} is the pressure component of the HEL, and $\mu_{HEL} = 0.01117$ is the corresponding μ at P_{HEL} (for $K_2 = K_3 = 0$). For a known HEL and G, μ_{HEL} can be obtained iteratively from

$$HEL = K_1\mu_{HEL} + K_2\mu_{HEL}^2 + K_3\mu_{HEL}^3 + \frac{4}{3}G\left(\frac{\mu_{HEL}}{1+\mu_{HEL}}\right). \quad (17)$$

Because the height is $H = 1.0\text{m}$ and the area is $A = 1.0\text{m}^2$, the deflection is $\delta = -\epsilon_z$ and the force is $F = -\sigma_z$. For all three cases, the force, F , is slowly applied until $\delta = 0.05\text{m}$, and then it is slowly released until $F = 0$. The paths are shown for strength versus pressure and for force versus deflection.

For Case A, the material cannot develop any plastic strain ($\epsilon_p^f = 0$) or any strength after fracture ($\sigma_f = 0$). All of the elastic energy loss (of deviator and shear stresses) is converted to potential hydrostatic energy ($\beta = 1.0$). Because there is no plastic work, the external work must also vanish. This is shown in the force versus deflection relationship for Case A. The pressure jump ($\Delta P = 0.56\text{ GPa}$) provides for this conservation of energy.

Case B is similar to Case A except the material is allowed to accumulate some plastic strain during fracture. Taking $D_1 = 0.005$ and $D_2 = 1.0$ in Equation 6 gives a pressure dependent fracture strain, ϵ_p^f . It can be seen in Figure 46 that the material gradually softens between point 2 (where the damage begins to accumulate) and point 3 (where the damage is complete and there is no strength). The bulking pressure, ΔP , is also generated between these two points.

Case C is similar to Case B except that there is strength in the fractured material [$\sigma_f^* = 0.31 (P^*)^{0.6}$]. The constants from Equation 4 are assumed to be $B = 0.31$, $m = 0.6$, and $C = 0$. Here the response is very complex, with the primary regions of interest as follows:

From Points 1 to 2 the material loads elastically until the intact strength, σ_i , is encountered at point 2. From Points 2 to 3 the material flows plastically, moving from the intact strength at point 2 to the fracture strength at point 3. The damage goes from $D = 0$ at point 2 to $D = 1.0$ at point 3. Similarly, the bulking pressure goes from $\Delta P = 0$ at point 2 to $\Delta P = 0.65\text{ GPa}$ at point 3. From Points 3 to 4 the material continues to flow plastically along the fracture strength envelope, σ_f . From Points 4 to 5 the loading direction is reversed at point 4 and the material unloads

elastically. At point 4, the axial deviator stress is in compression. At point 5, the axial deviator stress is completely unloaded such that the resulting stress is due only to the hydrostatic pressure. From Points 5 to 6 the elastic unloading continues and the axial deviator stress goes into tension. The net axial stress remains in compression, however, because the pressure is greater than the deviator stress. The fracture stress, σ_f , is encountered at point 6. From Points 6 to 7 the material unloads plastically along the fracture strength envelope. At point 7, both the pressure and the axial deviator stress (strength) go to zero.

6.6 REACTIVE EXPLOSIVE MATERIALS

For the Reactive Explosive materials the burn fraction is determined as a function of the pressure history. For the Explosive Materials (described previously in subsection 6.2) the burn fraction could be predetermined based on the detonation velocity and the point of detonation. The Reactive Explosive models generally require a very fine grid and significantly more CPU time.

6.6.1 Tarver Ignition and Growth Model

The Ignition and Growth model is presented in Reference 62. This reference uses the JWL Equation of State (presented previously in subsection 6.2.2) for both the pressure in the solid material and the gas products. The burn rate fraction, F , goes from $F = 0$ (solid only, no reaction) to $F = 1.0$ (complete reaction). The burn rate is

$$\dot{F} = \partial F / \partial t = I(1-F)^B (\rho / \rho_0 - 1 - A)^X + G_1(1-F)^C F^D P^Y + G_2(1-F)^E F^G P^Z \quad (1)$$

The three basic terms correspond to ignition, growth, and completion. F is the mass fraction of the explosive which has reacted, t is the time, ρ is the current density, ρ_0 is the initial density, and P is the pressure. The constants are I , G_1 , G_2 , A , B , C , D , E , G , X , Y , and Z . The dimensionless constant, A , prohibits ignition until $(\rho / \rho_0 - 1 - A) > 0$.

The burn rate, \dot{F} , is given by Equation 1, and the burn fraction, F , is numerically integrated as follows:

$$F^{t+\Delta t} = F^t + \dot{F}^t \Delta t \quad (2)$$

where Δt is the integration time increment and $\dot{F}^{t+\Delta t}$ is based on the volumetric strain at time = $t + \Delta t$ and the pressure at time = t . $F = 0$ indicates all solid behavior (no detonation), and $F = 1.0$ indicates all gas products behavior (complete detonation). The burn fraction is an element variable which must be carried from cycle to cycle.

There are two other element variables which must also be carried from cycle to cycle. VF_g is the fraction of the element volume which contains gas products, and ET_g is the total internal energy which has been added to the gas products.

$$ET_g = (E_g - E_o) V_o F \quad (3)$$

where E_g is the internal energy per initial volume in the gas products, E_o is the initial internal energy per initial volume in the explosive, V_o is the initial volume of the element, and F is the burn fraction.

The initial estimate for VF_g is given by

$$VF_g^{t+\Delta t} = VF_g^t + [\Delta F / (1 - F^t)] (1 - VF_g^t) \quad (4)$$

where $\Delta F = F^{t+\Delta t} - F^t$ is the incremental burn fraction between cycles. The quantity $\Delta F / (1 - F^t)$ is simply the fraction of unburned mass which was burned during the past cycle. Similarly, the quantity $(1 - VF_g^t)$ is the volume fraction of unburned material. This equation essentially converts the volume of solid burned during the past cycle to an equivalent volume of gas products. Equation 4 is only an estimate and is therefore altered in subsequent iterations.

The relative volumes for the entire element, solid portion, and gas products portion, are designated as \bar{V} , \bar{V}_s , and \bar{V}_g , respectively. They all have the form $\bar{V} = V / V_o$ where V is the current volume and V_o is the initial volume.

The relative volumes of the solid and gas products portions at time = t , are given by

$$\bar{V}_s^t = \bar{V}^t (1 - VF_g^t - \Delta VF) / (1 - F^{t+\Delta t}) \quad (5)$$

$$\bar{V}_g^t = \bar{V}^t (VF_g^t + \Delta VF) / F^{t+\Delta t} \quad (6)$$

where $\Delta VF = \left[\Delta F / (1 - F^t) \right] (1 - VF_g^t)$ is required to represent the volume of material which burned during the previous cycle.

Similarly, the relative volumes at time = $t + \Delta t$, are

$$\bar{V}_s^{t+\Delta t} = \bar{V}^{t+\Delta t} (1 - VF_g^{t+\Delta t}) / (1 - F^{t+\Delta t}) \quad (7)$$

$$\bar{V}_g^{t+\Delta t} = \bar{V}^{t+\Delta t} VF_g^{t+\Delta t} / F^{t+\Delta t} \quad (8)$$

For the first iteration, $VF_g^{t+\Delta t}$ is given by Equation 4; but in subsequent iterations, it is varied.

The corresponding volumetric strain rates are

$$\dot{\epsilon}_s = (\bar{V}_s^{t+\Delta t} - \bar{V}_s^t) / \Delta t \quad (9)$$

$$\dot{\epsilon}_g = (\bar{V}_g^{t+\Delta t} - \bar{V}_g^t) / \Delta t \quad (10)$$

The internal energy distributions must also be determined before the JWL Equation of State (EOS) can be applied.

The total added internal energy is given by

$$ET = (E - E_o) V_o \quad (11)$$

where E is the current internal energy per initial volume and E_o is the initial internal energy per initial volume in the explosive.

The total added energy in the gas products, ET_g , is given in Equation 3. The total added energy in the solid is then

$$ET_s = ET - ET_g \quad (12)$$

As the explosive burns, the internal energy of the mass, which changes from solid to gas products during an integration cycle, must be transferred from the solid to the gas products.

$$ET_s^{t+} = ET_s^t - \Delta ET \quad (13)$$

$$ET_g^{t+} = ET_g^t + \Delta ET \quad (14)$$

where the energy change is given by

$$\Delta ET = ET_s \cdot \Delta F / (1 - F^t) \quad (15)$$

Now the internal energies, per initial volume, for the JWL EOS can be determined.

$$E_s = E_o^s + ET_s / [V_o \cdot (1 - F)] + \Delta E_d \quad (16)$$

$$E_g = E_o + ET_g / (V_o \cdot F) \quad (17)$$

where E_o^s and E_o are the initial internal energies per initial volume, for the solid and the gas products. In Equation 16, ΔE_d is the incremental internal energy, generated during the past cycle, due to the material strength (shear and deviator stresses) of the solid material. (As described in subsection 6.1.9).

The JWL EOS is given in subsection 6.2.2. After the pressures for both the solid and gas products have been computed, an equilibrium pressure difference is computed by

$$\Delta P = \frac{|P_s - P_g|}{|P_s| + |P_g|} \quad (18)$$

If $\Delta P < \Delta P_{\text{allowed}}$, then equilibrium has been attained. For $\Delta P > \Delta P_{\text{allowed}}$, a new value of VF_g is assumed (using a binary iteration) and the previous process is repeated. Limited experience indicates reasonable results are obtained using $\Delta P_{\text{allowed}} = 0.01$.

Although Reference 62 (and the discussion in this subsection) uses the JWL EOS for both the solid material and the gas products, it is possible to use other Equations of State with the burn rate given in Equation 1.

6.6.2 Mader Forest Fire Model

The Forest Fire model is presented in Reference 63. Here the burn rate is expressed as

$$\frac{\partial F}{\partial t} = (1 - F) \cdot \exp \left(C_0 + C_1 P + C_2 P^2 + \dots + C_{14} P^{14} \right) \quad (1)$$

where $C_0 \dots C_{14}$ are material constants and P is the pressure. The burn fraction, F , is as defined in subsection 6.6.1. $F = 0$ indicates all solid behavior (no detonation), and $F = 1.0$ indicates all gas products behavior (complete detonation). The numerical implementation is similar to that described in subsection 6.6.1.

6.7 RDG STRENGTH AND FRACTURE MODEL

The RDG strength and fracture model is described in References 64 and 65. This model uses either the Johnson-Cook or Bodner-Partom strength model and the Mie-Gruneisen Equation of State. These are coupled together with a void nucleation fracture model. The current strength and pressure are determined as a function of the intact material properties and the void volume fraction. The specific algorithm is not presented in this report. This is a complex model, and the References should be consulted for a detailed description.

SECTION 7

REFERENCES

1. G.R. Johnson, "Analysis of Elastic-Plastic Impact Involving Severe Distortions," *Journal of Applied Mechanics, ASME*, September 1976.
2. G.R. Johnson, "High Velocity Impact Computations in the Three Dimensions," *Journal of Applied Mechanics, ASME*, March 1977.
3. G.R. Johnson, *EPIC-2, A Computer Program for Elastic-Plastic Impact Computations in 2 Dimensions Plus Spin*, Honeywell Inc., Hopkins, Minnesota, Contract Report ARBRL-CR-00373, June 1978.
4. G.R. Johnson, *EPIC-3, A Computer Program for Elastic-Plastic Impact Computations in 3 Dimensions*, Honeywell Inc., Hopkins, Minnesota, Contract Report BRL-CR-343, July 1977.
5. R.T. Walsh, "Finite Difference Methods," *Dynamic Response of Materials to Intense Impulsive Loading*, Edited by P.C. Chou and A.K. Hopkins, Air Force Materials Laboratory, 1972.
6. G.E. Meyers, "The Critical Time Step for Finite Element Solutions to Two Dimensional Heat Conduction Transients," *Journal of Heat Transfer, ASME*, February 1978.
7. G.R. Johnson, "Dynamic Analysis of a Torsion Test Specimen Including Heat Conduction and Plastic Flow," *Journal of Engineering Materials and Technology, ASME*, July 1981.
8. J. Lysmer and R. Kuhlemeyer, "Finite Element Model for Infinite Media," *Journal of the Engineering Mechanics Division, ASCE*, Volume 95, 1969.
9. G.R. Johnson, E.H. Petersen, and R.A. Stryk, *Nonreflective Boundary Elements for the EPIC Code*, Honeywell Inc., Brooklyn Park, Minnesota, September 1990.

10. G.R. Johnson, "Lagrangian Computational Approaches for Penetration and Perforation of Solids," *Advances in Numerical Simulation, Techniques for Penetration and Perforation of Solids*, ADM-Volume 171, 1993.
11. G.R. Johnson, "Dynamic Response of Axisymmetric Solids Subjected to Impact and Spin," *AIAA Journal*, September 1979.
12. G.R. Johnson and R.A. Stryk, "An Automatic Sliding Interface Algorithm for Intense Impulsive Loading Computations," *Communications in Numerical Methods in Engineering*, December 1996.
13. D.J. Benson and J.O. Hallquist, "A Single Surface Contact Algorithm for the Post-Buckling Analysis of Shell Structures," *Computer Methods in Applied Mechanics and Engineering* 78, 1990.
14. G.R. Johnson, D.D. Colby, and D.J. Vavrick, "Three-Dimensional Computer Code for Dynamic Response of Solids to Intense Impulsive Loads," *International Journal for Numerical Methods in Engineering*, Volume 14, 1979.
15. F.P. Stecher and G.R. Johnson, "Lagrangian Computations for Projectile Penetration into Thick Plates," *Computers in Engineering 1984* — Volume 2, ASME, 1984.
16. G.R. Johnson and R.A. Stryk, "Eroding Interface and Improved Tetrahedral Element Algorithms for High Velocity Impact Computations in Three Dimensions," *International Journal of Impact Engineering*, Volume 5, 1987.
17. G.R. Johnson, "Recent Developments and Analyses Associated with the EPIC-2 and EPIC-3 Codes," *1981 Advances in Aerospace Structures and Materials-AD-01*, ASME, Edited by S.S. Wang and W.J. Renton, 1981.
18. G.R. Johnson, R.A. Stryk, T.J. Holmquist, and O.A. Souka, "Recent EPIC Code Developments for High Velocity Impact: 3D Element Arrangements and 2D Fragment Distributions," *International Journal of Impact Engineering*, Volume 8, 1990.
19. M.L. Wilkins, "Calculation of Elastic-Plastic Flow," *Methods in Computational Physics*, Volume 3, Edited by B. Alder, S. Fernbach, and M. Rotenberg, Academic Press, 1964.

20. T. Belytschko, J.I. Lin, and C.S. Tsay, "Explicit Algorithms for the Nonlinear Dynamics of Shells," *Computer Methods in Applied Mechanics and Engineering*, Volume 42, 1984.
21. G.R. Johnson, "Dynamic Plane Stress Computations for Large Plastic Deformations," *Communication in Applied Numerical Methods*, Volume 1, 1985.
22. G.R. Johnson, "Three-Dimensional Analysis of Sliding Surfaces During High Velocity Impact," *Journal of Applied Mechanics*, ASME, December 1977.
23. G.R. Johnson, D.D. Colby, and D.J. Vavrick, *Further Development of the EPIC-3 Computer Program for Three-Dimensional Analysis of Intense Impulsive Loading*, Honeywell Inc., Hopkins, Minnesota, Contract Report AFATL-TR-78-81, July 1978.
24. G.R. Johnson, "Dynamic Analysis of Explosive-Metal Interaction in Three Dimensions," *Journal of Applied Mechanics*, ASME, March 1981.
25. A.L. Fetter and J.D. Walecka, *Theoretical Mechanics of Particles and Continua*, McGraw-Hill, 1980.
26. D.P. Flanagan and T. Belytschko, "A Uniform Strain Hexahedron and Quadrilateral with Orthotropic Hourglass Control," *International Journal for Numerical Methods in Engineering*, Volume 17, 1981.
27. G.R. Johnson, R.A. Stryk, and E.H. Petersen, *3D Bar and Shell Elements for EPIC*, Alliant Techsystems Inc., Brooklyn Park, Minnesota, October 1991.
28. G.R. Johnson, E.H. Petersen, and R.A. Stryk, "Incorporation of an SPH Option into the EPIC Code for a Wide Range of High Velocity Impact Computations," *International Journal of Impact Engineering*, Volume 14, 1993.
29. G.R. Johnson, "Linking of Lagrangian Particle Methods to Standard Finite Element Methods for High Velocity Impact Computations," *Nuclear Engineering and Design*, Volume 150, 1994.

30. G.R. Johnson and S.R. Beissel, "Normalized Smoothing Functions for SPH Impact Computations," *International Journal for Numerical Methods in Engineering*, Volume 39, 1996.
31. G.R. Johnson, R.A. Stryk, and S.R. Beissel, "SPH for High Velocity Impact Computations," *Computer Methods in Applied Mechanics and Engineering*, Volume 139, 1996.
32. J.W. Swegle, S.W. Attaway, M.W. Heinstein, F.J. Mello, and D.L. Hicks, "An Analysis of Smoothed Particle Hydrodynamics," SAND93-2513, Sandia National Laboratories, Albuquerque, New Mexico, March 1994.
33. J. Von Neumann and R.D. Richtmeyer, "A Method for the Numerical Calculation of Hydrodynamic Shocks," *Journal of Applied Physics*, Volume 21, 1950.
34. J.J. Monaghan and R.A. Gingold, "Shock Simulation by the Particle Method SPH," *Journal of Computational Physics*, Volume 52, 1983.
35. G.R. Johnson, "Status of EPIC Codes, Material Characterization and New Computing Concepts at Honeywell," *Computational Aspects of Penetration Mechanics, Lecture Notes in Engineering* 3, 1983.
36. G.R. Johnson, R.A. Stryk, and J.G. Dodd, "Dynamic Lagrangian Computations for Solids with Variable Connectivity for Severe Distortions," *International Journal of Numerical Methods in Engineering*, Volume 23, 1986.
37. G.R. Johnson and W.H. Cook, "A Constitutive Model and Data for Metals Subjected to Large Strains, High Strain Rates, and High Temperatures," *Proceedings of Seventh International Symposium on Ballistics*, The Hague, The Netherlands, April 1983.
38. T.J. Holmquist and G.R. Johnson, "Determination of Constants and Comparison of Results for Various Constitutive Models," *Journal De Physique IV*, October 1991.
39. F.J. Zerilli and R.W. Armstrong, "Dislocation-Mechanics-Based Constitutive Relations for Material Dynamics Calculation," *Journal of Applied Physics*, Volume 61, 1987.

40. S.R. Bodner and Y. Partom, "Constitutive Equations for Elastic-Viscoplastic Strain-Hardening Materials," *Journal of Applied Mechanics*, June 1975.
41. S.R. Bodner and A. Merzer, "Viscoplastic Constitutive Equations for Copper with Strain Rate History and Temperature Effects," *Journal of Engineering Materials and Technology*, October 1978.
42. W.H. Cook, A.M. Rajendran, and D.J. Grove, "An Efficient Numerical Implementation of the Bodner-Partom Model in the EPIC-2 Code," *Engineering Fracture Mechanics*, Volume 41, 1992.
43. P.S. Follansbee and U.F. Kocks, "A Constitutive Description of the Deformation of Copper Based on the Use of Mechanical Threshold Stress as an Internal State Variable," *Acta Metall.*, Volume 36, 1988.
44. P.S. Follansbee and G.T. Gray III, "An Analysis of the Low Temperature, Low and High Strain Rate Deformation of Ti-6Al-4V," *Met. Trans.*, Volume 20A, 1989.
45. D.J. Steinberg, S.G. Cochran, and M.W. Guinan, "A Constitutive Model for Metals Applicable at High Strain Rate," *Journal of Applied Physics*, Volume 51, 1980.
46. D.J. Steinberg and C.M. Lund, "A Constitutive Model for Strain Rates from 10^{-4} to 10^6 s $^{-1}$," *Journal of Applied Physics*, Volume 65, 1989.
47. P.J. Maudlin and S.K. Schiffrl, "Computational Anisotropic Plasticity for High-Rate Forming Applications," *Computer Methods in Applied Mechanics and Engineering*, Volume 131, 1996.
48. R. Hill, "A Theory of the Yielding and Plastic Flow in Anisotropic Metals," *Proceedings of the Royal Society of London*, A193, 1948.
49. J.M. Walsh, et al., "Shock-Wave Compressions of Twenty-Seven Metals, Equation of State of Metals," *Physical Review*, October 1957.

50. G.R. Johnson and W.H. Cook, "Fracture Characteristics of Three Metals Subjected to Various Strains, Strain Rates, Temperatures, and Pressures," *Engineering Fracture Mechanics*, Volume 21, 1985.
51. J.W. Hancock and A.C. Mackenzie, "On the Mechanism of Ductile Failure in High-Strength Steels Subjected to Multi-Axial Stress States," *Journal of the Mechanics and Physics of Solids*, June 1976.
52. F.R. Tuler and B.M. Butcher, "A Criterion for the Time Dependence of Dynamic Fracture," *International Journal of Fracture Mechanics*, December 1968.
53. D.E. Grady, "Local Inertial Effects in Dynamic Fragmentation," *Journal of Applied Physics*, Volume 53, 1982.
54. D.E. Grady, "Fragmentation of Rapidly Expanding Jets and Sheets," *International Journal of Impact Engineering*, Volume 5, 1987.
55. D.E. Grady, "The Spall Strength of Condensed Matter," *Journal of the Mechanics and Physics of Solids*, Volume 36, 1988.
56. E.L. Lee, H.C. Horning, and J.W. Kury, "Adiabatic Expansion of High Explosive Detonation Products," UCRL-50422, Lawrence Livermore Laboratory, University of California, May 1968.
57. D.A. Matuska, R.E. Durrett, and J.J. Osborn, *Hull User Guide for Three Dimensional Linking with EPIC-3*, Orlando Technology, Inc., Shalimar, Florida, ARBRL-CR-00484, July 1982.
58. T.J. Holmquist, G.R. Johnson, and W.H. Cook, "A Computational Constitutive Model for Concrete Subjected to Large Strains, High Strain Rates and High Pressures," *Proceedings of Fourteenth International Symposium on Ballistics*, Quebec City, Canada, September 1993.
59. G.R. Johnson and T.J. Holmquist, "A Computational Constitutive Model for Brittle Materials Subjected to Large Strains, High Strain Rates, and High Pressures," *Shock Wave and High-Strain-Rate Phenomena in Materials*, 1992.

60. G.R. Johnson and T.J. Holmquist, "An Improved Computational Constitutive Model for Brittle Materials," *High Pressure Science and Technology — 1993*, AIP Press, 1994.
61. T.J. Holmquist, et al., "High Strain Rate Properties and Constitutive Modeling of Glass," *Proceedings of Fifteenth International Symposium on Ballistics*, Jerusalem, Israel, May 1995.
62. C.M. Tarver, J.O. Holmquist, and L.M. Erickson, "Modeling Short Pulse Duration Shock Initiation in Solid Explosives," *Proceedings of 8th Symposium (International) in Detonation*, Albuquerque, New Mexico, July 1985.
63. C.L. Mader, *Numerical Modeling of Detonation*, University of California Press, 1979.
64. A.M. Rajendran, M.A. Dietenberger, and D.J. Grove, "A Void Growth-Based Failure Model to Describe Spallation," *Journal of Applied Physics*, Volume 65, February 1989.
65. A.M. Rajendran, M.A. Dietenberger, and D.J. Grove, "Results from the Recently Developed Dynamic Failure Model," *Shock Compression of Condensed Matter—1989*, Elsevier Science Publishers, 1990.

DISTRIBUTION LIST
WL-TR-1997-7039

| | | | |
|---|---|---|---|
| Defense Tech Info Center ATTN: DTIC-OCP 8725 John J Kingman Road, Suite 0944 Fort Belvoir, VA 22060-6218 | 1 | R. Garrett Indian Head Division Naval Surface Warfare Center Indian Head, MD 20640 | 2 |
| Dr Gordon Johnson Alliant Techsystems Inc. 600 Second Street N. E Hopkins , MN 55345 | 5 | Eglin AFB Offices: | |
| | | WL/CA-N | 1 |
| | | WL/MNP-1 (Tech Library) | 1 |
| Dr Robert Stryk Alliant Techsystems Inc. 600 Second Street N. E Hopkins , MN 55345 | 2 | WL/MNSI (B. Aref) | 1 |
| | | WL/MNSI (Dr Belk) | 1 |
| | | WL/MNSI (E. Bradley) | 1 |
| | | WL/MNSI (Dr Cook) | 5 |
| | | WL/MNSI (R. Johnson) | 1 |
| T. Holmquist Alliant Techsystems Inc. 600 Second Street N. E Hopkins , MN 55345 | 2 | WL/MNSI (Lt McCann) | 1 |
| | | WL/MNSI (M. Nixon) | 1 |
| | | WL/MNSI (Dr Sidhu) | 1 |
| | | WL/MNSI (Dr Tu) | 1 |
| | | WL/MNSI (Dr Vanden) | 1 |
| Dr S. R. Beissel Alliant Techsystems Inc. 600 Second Street N. E Hopkins , MN 55345 | 2 | WL/MNS | 2 |
| J. Repa Los Alamos National Lab PO Box 1663 Los Alamos, NM 87545 | 2 | | |
| P. Yarrington Mail Stop 0820 Sandia National Lab PO Box 5800 Albuquerque, NM 87185-0820 | 2 | | |
| J. D. Cargile WES-SD 3909 Halls Ferry Road Vicksburg, MS 39180-6199 | 2 | | |